National Library of Canada

Acquisitions and Bibliographic Services Branch

395 Wellington Street
Ottawa, Ontario
K1A 0N4

Bibliothèque nationale du Canada

Direction des acquisitions et des services bibliographiques

395, rue Wellington
Ottawa (Ontario)
K1A 0N4

Your file Votre référence

Our file Notre référence

NOTICE

The quality of this microform is heavily dependent upon the quality of the original thesis submitted for microfilming. Every effort has been made to ensure the highest quality of reproduction possible.

If pages are missing, contact the university which granted the degree.

Some pages may have indistinct print especially if the original pages were typed with a poor typewriter ribbon or if the university sent us an inferior photocopy.

Reproduction in full or in part of this microform is governed by the Canadian Copyright Act, R.S.C. 1970, c. C-30, and subsequent amendments.

AVIS

La qualité de cette microforme dépend grandement de la qualité de la thèse soumise au microfilmage. Nous avons tout fait pour assurer une qualité supérieure de reproduction.

S'il manque des pages, veuillez communiquer avec l'université qui a conféré le grade.

La qualité d'impression de certaines pages peut laisser à désirer, surtout si les pages originales ont été dactylographiées à l'aide d'un ruban usé ou si l'université nous a fait parvenir une photocopie de qualité inférieure.

La reproduction, même partielle, de cette microforme est soumise à la Loi canadienne sur le droit d'auteur, SRC 1970, c. C-30, et ses amendements subséquents.

Canada

UNIVERSITY OF ALBERTA

MASS TRANSFER DUE TO ONE AND TWO CONFINED IMPINGING LAMINAR SLOT JETS

BY

XIAOSHENG FAN

A thesis submitted to the Faculty of Graduate Studies and Research in partial fulfilment of the requirements for the degree of **DOCTOR OF PHILOSOPHY**.

DEPARTMENT OF **CHEMICAL ENGINEERING**

Edmonton, Alberta

FALL 1994

National Library
of Canada

Acquisitions and
Bibliographic Services Branch

395 Wellington Street
Ottawa, Ontario
K1A 0N4

Bibliothèque nationale
du Canada

Direction des acquisitions et
des services bibliographiques

395, rue Wellington
Ottawa (Ontario)
K1A 0N4

Your file Votre référence

Our file Notre référence

The author has granted an irrevocable non-exclusive licence allowing the National Library of Canada to reproduce, loan, distribute or sell copies of his/her thesis by any means and in any form or format, making this thesis available to interested persons.

L'auteur a accordé une licence irrévocable et non exclusive permettant à la Bibliothèque nationale du Canada de reproduire, prêter, distribuer ou vendre des copies de sa thèse de quelque manière et sous quelque forme que ce soit pour mettre des exemplaires de cette thèse à la disposition des personnes intéressées.

The author retains ownership of the copyright in his/her thesis. Neither the thesis nor substantial extracts from it may be printed or otherwise reproduced without his/her permission.

L'auteur conserve la propriété du droit d'auteur qui protège sa thèse. Ni la thèse ni des extraits substantiels de celle-ci ne doivent être imprimés ou autrement reproduits sans son autorisation.

ISBN 0-315-95179-6

Canada

UNIVERSITY OF ALBERTA

RELEASE FORM

NAME OF AUTHOR: **Xiaosheng Fan**

TITLE OF THESIS: **Mass Transfer due to One and Two Confined Impinging Laminar Slot Jets**

DEGREE: **Doctor of Philosophy**

YEAR THIS DEGREE GRANTED: **1994**

Permission is hereby granted to the University of Alberta Library to reproduce single copies of this thesis and to lend or sell such copies for private, scholarly or scientific research purposes only.

The author reserves all other publication and other rights in association with the copyright in the thesis, and except as hereinbefore provided neither the thesis nor any substantial portion thereof may be printed or otherwise reproduced in any material form whatever without the author's prior written permission.

Jan Fan

Date: Aug. 30, 1994

302-10740-107 St
Edmonton, AB
Canada T5H 2Z1

UNIVERSITY OF ALBERTA

FACULTY OF GRADUATE STUDIES AND RESEARCH

The undersigned certify that they have read, and recommend to the Faculty of Graduate Studies and Research for acceptance, a thesis entitled **MASS TRANSFER DUE TO ONE AND TWO CONFINED IMPINGING LAMINAR SLOT JETS** submitted by **XIAOSHENG FAN** in partial fulfilment of the requirements for the degree of **DOCTOR OF PHILOSOPHY.**

J. H. Masliyah (Supervisor)

G. Hill (University of Saskatchewan)

Dr. K. Nandakumar

J.T. Ryan

D.J. Wilson

Date: June 17 ,1994

To my wife Hong, my daughter Jessica
and in memory of my parents

ABSTRACT

Local mass transfer from the impingement plate to the flow stream due to one and two confined impinging laminar slot jets has been investigated. For the cases of a single slot jet and two slot jets with symmetrical flow, both experimental and numerical studies were conducted. For the case of two slot jets with asymmetrical flow, only experimental investigations were carried out. With the single slot jets, three Reynolds numbers (200, 300, 400) and three nondimensional jet-to-plate spacings (2, 4 and 12) based on the width of the slot jet were studied. For the two slot jets, three Reynolds numbers (150, 300, 450), three nondimensional jet-to-plate spacings (2, 4, 8) and three nondimensional jet-to-jet spacings (10, 20, 30) were examined. The experiments were carried out using real-time holographic interferometry combined with the swollen polymer technique. All experimental runs were recorded by a high resolution video camera. Two-dimensional stream function-vorticity formulation was used for numerical computation.

Experimental results showed that for a single impinging slot jet, although the maximum mass transfer rate occurred at the stagnation point, a strong secondary peak existed downstream.

For the case of two symmetrical slot jets, because of the counteracting flows from the two jets, the central zone is essentially stagnant with extremely low mass transfer rate. Experimental results revealed that for the cases of small nondimensional jet-to-plate spacings (2 and 4), the mass transfer rate in the central region was about ten times lower than the maximum values. For a nondimensional jet-to-plate spacing of 8, the mass transfer rate in the central region was about 5 times lower than the maximum value.

For the case of two asymmetrical slot jets, the cross-flow from the stronger jet reduces

the mass transfer rate due to the weaker jet. When the flow rate ratio of the two jets is 2, the maximum mass transfer rate due to the weaker jet is about 4 times lower than that due to the stronger jet. With a flow rate ratio of 3, the influence of the weaker jet is almost swept out by the stronger jet and the mass transfer pattern is similar to that due to a single jet.

ACKNOWLEDGEMENT

I would like to express my gratitude to Dr. J.H. Masliyah, my supervisor, for his guidance and financial support throughout this long endeavour.

I would like to thank Dr. K. Nandakumar for several constructive discussions on the numerical scheme at the early stage of this work.

Keith Faulder and the staff of the Chemical Engineering Workshop provided indispensable and timely assistance to me for the experimental work and their effort is deeply appreciated.

Throughout the project, Bob Barton of DACS center has provided me with ever-ready and pleasant help with his highly regarded devotion and expertise in the computer work and he deserves my heartfelt respect and appreciation.

I would also like to acknowledge my officemate and personal friend, Dr. Shijie Liu, for his friendship and help in the numerical work; my personal friend, Dr. Shimin Tong, for his friendship and encouragement during the long course of the work.

Table of Contents

Chapter 1
Introduction 1
1.1 Background 1
1.2 Objectives of this work 2

Chapter 2
Literature Review 4
2.1 General Review 4
2.1.1 Flow Characteristics of Impinging Jets 4
2.1.2 Effect of Flow Media 6
2.1.3 Effect of Jet Shape 6
2.1.4 Effect of Confinement 7
2.1.5 Effect of Reynolds Numbers 8
2.1.6 Effect of Jet-to-Plate Spacing 10
2.1.7 Effect of Jet Exit Flow Conditions 12
2.1.8 Effect of Nozzle Size 13
2.1.9 Effect of Angle of Impact 14
2.1.10 Effect of Surface Movement, Crossflow and Throughflow . . 15
2.1.11 Multiple Impinging Jets 20
2.2 Impinging Jet Studies 21
2.2.1 Experimental Heat and Mass Transfer Studies 21
2.2.2 Theoretical and Numerical Studies 27
2.3 Heat and Mass Transfer due to Submerged Laminar Impinging Slot Jets 31
2.3.1 Unconfined Impinging Slot Jets 31
2.3.2 Confined Impinging Slot Jets 35
2.4 Conclusions 37

Chapter 3
Experimental Techniques 38
3.1 Swollen Polymer 38
3.2 Holographic Interferometry 40
3.2.1 Principles of Holography and Holographic Interferometry . . 40
3.2.2 Double-Exposure Holographic Interferometry 43

3.2.3 Real-Time Holographic Interferometry 44
3.3 Experimental Set-up 45
3.3.1 Optical Set-up 45
3.3.2 Mass Transfer Experimental Set-up 52
3.3.3 Recording and Other Equipment 54
3.4 Experimental Procedure 55
3.4.1 Preparation of the Polymer Coating 55
3.4.2 Making and Recording of Real-Time Holograms 56

Chapter 4
Validity of the Experimental Procedure 58

Chapter 5
Numerical Study 63
5.1 Governing Equations 63
5.2 Boundary Conditions 67
5.2.1 Boundary Conditions for Single Slot Jet 67
5.2.2 Boundary Conditions for Two Symmetrical Slot Jets 69
5.3 Numerical Formulation 72
5.3.1 Finite-Difference Equations 73
5.3.2 Boundary Conditions 78
5.3.2.1 Single Slot Jet Systems 78
5.3.2.2 Two Slot Jets Systems 81
5.4 Computational Procedure 82
5.4.1 Grid Design 82
5.4.2 Convergence Criterion 89
5.4.3 Solution of the Discretization Equations 90
5.4.4 Presentation of the Computed Results 92
5.5 Validation of the Numerical Solution 95

Chapter 6
Mass Transfer Due to One Confined Impinging Laminar Slot Jet 97
6.1 Flow Characteristics 97
6.1.1 Streamline Contours 98
6.1.2 Skin-Friction Factor along Impingement Plate 106
6.2 Mass Transfer Characteristics 111
6.2.1 Numerical Results 111
6.2.2 Experimental Results 113

6.2.2.1 Mass Transfer Pattern 113
6.2.2.2 Effect of Reynolds Numbers 120
6.2.2.3 Effect of Jet-to-Plate Spacing 122
6.2.3 Comparison Between Numerical and Experimental Results 122
6.2.4 Comparison with the Experimental Data in the Literature . 128
6.2.4.1 Comparison with the Data of Law 129
6.2.4.2 Comparison with the Data of Sparrow and Wong . . 129
6.2.4.3 Comparison with the Data of Gardon and Akfirat . . 134
6.2.5 Mass Transfer at the Stagnation Point 135

Chapter 7
Mass Transfer Due to Two Confined Impinging Laminar Slot Jets: Symmetrical Flow 136
7.1 Flow Characteristics 137
7.1.1 Streamline Contours 137
7.1.2 Skin-Friction Factor Along Impingement Plate 143
7.2 Mass Transfer Characteristics 146
7.2.1 Numerical Results 146
7.2.2 Experimental Results 152
7.2.2.1 Mass Transfer Pattern 152
7.2.2.2 Effect of Reynolds Number 160
7.2.2.3 Effect of Jet-to-Plate Spacing 163
7.2.2.4 Effect of Jet-to-Jet Spacing 163
7.2.3 Comparison Between Numerical and Experimental Results 166
7.2.4 Conclusions for the case of Two Symmetrical Slot Jets . . . 167

Chapter 8
Mass Transfer Due To Two Confined Impinging Laminar Slot Jets: Asymmetrical Flow 174
8.1 Mass Transfer Pattern 175
8.2 Mass Transfer Rate 180

Chapter 9
Conclusions 186
9.1 Mass Transfer due to One Confined Impinging Laminar Slot Jet . . 186

9.2 Mass Transfer due to Two Confined Impinging Laminar Slot Jets: Symmetrical Flow 187
9.3 Mass Transfer due to Two Confined Impinging Laminar Slot Jets: Asymmetrical Flow 188

Chapter 10
Recommendations 189

References 190

Appendix A
Physical Properties 202

Appendix B
Calibration of Rotameters 206

Appendix C
Computer Program for Computing the Experimental Sherwood Numbers 208

List of Tables

Table 5.1 Grid Design for Single Slot Jet Systems 89
Table 5.2 Grid Design for Two Slot Jets Systems 89

List of Figures

Figure 1.1 The three flow configurations studied 3
Figure 2.1 Flow field of an unconfined laminar impinging jet 5
Figure 2.2 Inclined Impinging Jet 15
Figure 2.3 Wall Jet Definition 32
Figure 3.1 Interference of Two Plane Waves 41
Figure 3.2 The Hologram of Two Plane Wavefronts 42
Figure 3.3 Reconstruction of Wave B 42
Figure 3.4 Experimental Set-up 46
Figure 3.5 Schematic of a Holographic System 48
Figure 3.6 The Holodiagram 48
Figure 3.7 Light Path Before and After a Thickness Change 51
Figure 3.8 Front and Top Views of Impingement Plate 52
Figure 3.9 Front and Top Views of the Confinement Plate with Slot Jets 53
Figure 4.1 Comparison with Law's Experimental Data for a Single Slot Jet with Re = 400 and H = 2 61
Figure 4.2 Comparison with Law's Experimental Data for a Single Slot Jet with Re = 400 and H = 4 61
Figure 5.1 Computational Domain for the Impinging Jet Systems 64
Figure 5.2 Grid Network for the Single Slot Jet System 74
Figure 5.3 A Typical Node of Computation 74
Figure 5.4 Effect of Number of Grid Points in X-Direction 84
Figure 5.5 X-Grid Distribution for One and Two Slot Jets 85
Figure 5.6 Effect of Number of Grid Points in Y-Direction: Single Slot Jet 87
Figure 5.7 Effect of Stretching Factor in Y-Coordinate: Single Slot Jet 88
Figure 5.8 Comparison of Local Skin Friction Factors 96
Figure 5.9 Comparison of Local Sherwood Numbers 96
Figure 6.1 Streamline Contours for H = 2: Single Jet 99
Figure 6.2 Streamline Contours for H = 4: Single Jet 100
Figure 6.3 Streamline Contours for H = 12: Single Jet 101
Figure 6.4 Locations of the Centres of Vortices for Single Jet 102
Figure 6.5 Streamline Contours Near the Stagnation Point for H = 2: Single Jet 103
Figure 6.6 Streamline Contours Near the Stagnation Point for H = 4: Single Jet 104
Figure 6.7 Streamline Contours Near the Stagnation Point for H = 12: Single Jet 105

Figure 6.8 Skin-Friction Factor for H = 2.0: Single Jet 108
Figure 6.9 Skin-Friction Factor for H = 4.0: Single Jet 108
Figure 6.10 Skin-Friction Factor for H = 12.0: Single Jet 109
Figure 6.11 Comparison of Skin-Friction Factor with the Results of Law: Single Jet 110
Figure 6.12 Effect of Reynolds Number on Mass Transfer Rate: Single Jet 112
Figure 6.13 Effect of Jet-to-Plate Spacing on Mass Transfer Rate: Single Jet . . . 113
Figure 6.14 Contours of Equal Mass Transfer Rate for H = 2: Single Jet 114
Figure 6.15 Contours of Equal Mass Transfer Rate for H = 4: Single Jet 115
Figure 6.16 Contours of Equal Mass Transfer Rate for H = 12: Single Jet 116
Figure 6.17 Digitized Contours of Sherwood Numbers for H = 2: Single Jet 117
Figure 6.18 Digitized Contours of Sherwood Numbers for H = 4: Single Jet 117
Figure 6.19 Digitized Contours of Sherwood Numbers for H = 12: Single Jet . . . 118
Figure 6.20 Effect of Reynolds Number on Experimental Mass Transfer Rate: Single Jet 121
Figure 6.21 Effect of Jet-to-Plate Spacing on Experimental Mass Transfer Rate: Single Jet 123
Figure 6.22 Comparison Between Numerical and Experimental Mass Transfer Rates for H = 2: Single Jet 124
Figure 6.23 Comparison Between Numerical and Experimental Mass Transfer Rates for H = 4: Single Jet 125
Figure 6.24 Comparison Between Numerical and Experimental Mass Transfer Rates for H = 12: Single Jet 126
Figure 6.25 Comparison with the Data of Law for H = 2: Single Jet 130
Figure 6.26 Comparison with the Data of Law for H = 4: Single Jet 131
Figure 6.27 Comparison with the Data of Law for H = 12: Single Jet 132
Figure 6.28 Comparison with the Data of Sparrow and Wong: Single Jet 133
Figure 6.29 Comparison with the Work of Gardon and Akfirat: Single Jet 134
Figure 6.30 Comparison of the Stagnation Mass Transfer Rate with the Experimental Data in the Literature 135
Figure 7.1 Streamline Contours for H = 2, S = 10: Symmetrical Flow 138
Figure 7.2 Streamline Contours for H = 4, S = 10: Symmetrical Flow 139
Figure 7.3 Streamline Contours for H = 4, S = 20: Symmetrical Flow 140
Figure 7.4 Streamline Contours for H = 4, S = 30: Symmetrical Flow 141
Figure 7.5 Streamline Contours for H = 8, S = 10: Symmetrical Flow 142
Figure 7.6 Skin-Friction Factor for S = 10: Symmetrical Flow 144
Figure 7.7 Skin-Friction Factor for H = 4: Symmetrical Flow 145
Figure 7.8 Effect of Reynolds Number on Numerical Mass Transfer Rate

for S = 10: Symmetrical Flow 147
Figure 7.9 Effect of Reynolds Number on Numerical Mass Transfer Rate for H = 4: Symmetrical Flow 148
Figure 7.10 Effect of Jet-to-Plate Spacing on Numerical Mass Transfer Rate for S = 10: Symmetrical Flow 149
Figure 7.11 Effect of Jet-to-Jet Spacing on Numerical Mass Transfer Rate for H = 4: Symmetrical Flow 150
Figure 7.12 Contours of Equal Mass Transfer Rate for H = 2, S = 10: Symmetrical Flow 154
Figure 7.13 Contours of Equal Mass Transfer Rate for H = 4, S = 10: Symmetrical Flow 155
Figure 7.14 Contours of Equal Mass Transfer Rate for H = 8, S = 10: Symmetrical Flow 156
Figure 7.15 Digitized Contours of Sherwood Numbers for H = 2, S = 10: Symmetrical Flow 159
Figure 7.16 Digitized Contours of Sherwood Numbers for H = 4, S = 10: Symmetrical Flow 159
Figure 7.17 Digitized Contours of Sherwood Numbers for H = 8, S = 10: Symmetrical Flow 160
Figure 7.18 Effect of Reynolds Number on the Experimental Mass Transfer Rate for S = 10: Symmetrical Flow 161
Figure 7.19 Effect of Sherwood Number on the Experimental Mass Transfer Rate for H = 4: Symmetrical Flow 162
Figure 7.20 Effect of Jet-to-Plate Spacing on the Experimental Mass Transfer Rate for S = 10: Symmetrical Flow 164
Figure 7.21 Effect of Jet-to-Jet Spacing on the Experimental Mass Transfer Rate for H = 4: Symmetrical Flow 165
Figure 7.22 Comparison Between Numerical and Experimental Mass Transfer Rates for H = 2 and S = 10: Symmetrical Flow 168
Figure 7.23 Comparison Between Numerical and Experimental Mass Transfer Rates for H = 4 and S = 10: Symmetrical Flow 169
Figure 7.24 Comparison Between Numerical and Experimental Mass Transfer Rates for H = 4 and S = 20: Symmetrical Flow 170
Figure 7.25 Comparison Between Numerical and Experimental Mass Transfer Rates for H = 4 and S = 30: Symmetrical Flow 171
Figure 7.26 Comparison Between Numerical and Experimental Mass Transfer Rates for H = 8 and S = 10: Symmetrical Flow 172
Figure 8.1 Contours of Equal Mass Transfer Rate for H = 2, S = 10 and a

Flow Ratio of 2 176
Figure 8.2 Contours of Equal Mass Transfer Rate for H = 2, S = 10 and a Flow Ratio of 3 177
Figure 8.3 Contours of Equal Mass Transfer Rate for H = 4, S = 10 and a Flow Ratio of 2 178
Figure 8.4 Contours of Equal Mass Transfer Rate for H = 4, S = 10 and Flow Ratio of 3 179
Figure 8.5 Digitized Contours of Sherwood Numbers for H = 2, S = 10 and a Flow Ratio of 3 181
Figure 8.6 Digitized Contours of Sherwood Numbers for H = 4, S = 10 and a Flow Ratio of 3 181
Figure 8.7 Mass Transfer Rate for H = 2, S = 10 and Flow Ratios of 2 and 3 . . 182
Figure 8.8 Mass Transfer Rate for H = 4, S = 10 and Flow Ratios of 2 and 3 . 183
Figure 8.9 Mass Transfer Rate for H 4, S = 20 and a Flow Ratio of 2 184
Figure B.1 Calibration Curve for the Rotameters 207

Nomenclature

a_E, a_N, a_P, a_S, a_W	discretization coefficients defined in Equation 5.51, dimensionless
B	constant of optical set-up defined in Equation 3.6, dimensionless
b	slot width, m
b_1	stretching factor for discretization in Y-direction, dimensionless
C	concentration of swelling agent defined in Equation 5.6, dimensionless
C_f	skin-friction factor defined in Equation 5.89, dimensionless
c	concentration of swelling agent, kmol/m^3
D	diffusion coefficient of the air-ethyl salicylate system, m^2/s
D_e, D_n, D_s, D_w	conductances defined in Equation 5.53, dimensionless
D_h	hydraulic diameter, m
d	jet diameter, m
F_e, F_n, F_s, F_w	mass flow rates defined in Equation 5.52, dimensionless
f	relative nozzle area defined as the cross-sectional area of the jet divided by the area directly influenced by the jet as used in Equation 2.8.
G	general coefficient used in Equation 5.47, dimensionless
H	jet-to-plate spacing defined in Equation 5.6, dimensionless
h	jet-to-plate spacing, m
k	local mass transfer coefficient defined in Equation 4.1, m/s
L	half distance between the two foci shown in Figure 3.6, m
M	momentum flow ratio defined in Equation 2.6, dimensionless
M_{cj}	velocity ratio of crossflow to jet flow, dimensionless
M_{jc}	mass velocity ratio of jet to crossflow, dimensionless
M_m	molar mass of the swelling agent, kg/kmol

M_{us}, M_{vs}	relative mass velocity of the throughflow and surface movement with respect to the average mass velocity at the jet exit, used in Equation 2.4, dimensionless
mx	number of grid points in X-direction, dimensionless
N	mass flux, kg/(s·m^2)
Nu	Nusselt number, dimensionless
n	fringe order, dimensionless
n_p	refractive index of glass prism, dimensionless
n_s	refractive index of swollen polymer coating, dimensionless
ny	number of grid points in Y-direction, dimensionless
P	total pressure, Pa
P_e, P_n, P_s, P_w	Peclet numbers defined in Equation 5.54, dimensionless
Pr	Prandtl number, dimensionless
P^0	vapour pressure of swelling agent, Pa
p_j	partial vapour pressure of swelling agent at jet nozzle, Pa
p_s	partial vapour pressure of swelling agent at polymer surface, Pa
q	a constant used in the holo-diagram shown in Figure 3.6, dimensionless
R	residual used to monitor the convergence of numerical iterations, defined in Equation 5.86, dimensionless
R_{tol}	residual tolerance used to terminate numerical iterations, dimensionless
Re	Reynolds number, dimensionless
r	radius distance measured from the jet centre, m
r_q	radius of the circle with constant q defined in Equation 3.2, m
r′	recession of polymer coating, m
S	jet-to-jet spacing defined as s/b, dimensionless
Sc	Schmidt number defined in Equation 5.6, dimensionless
Sh_b	Sherwood number defined in Equation 4.1, dimensionless
Sh_d	Sherwood number defined in Equation 2.16, dimensionless
St	Stanton number, St = Nu/(Re·Pr), dimensionless

s	jet-to-jet spacing, m
t	duration of mass transfer experiment, s
T	temperature, K
U	velocity in the X-direction defined in Equation 5.6, dimensionless
U_e, U_w	velocities in the X-direction evaluated at the east and west boundaries of the control volume, defined in Equations 5.6 to 5.8, dimensionless
u	velocity in the X-direction, m/s
u_{fd}	local fully developed velocity in the X-direction, m/s
$\bar{u}_{fd}$	average fully developed velocity in the X-direction, m/s
V	velocity in the Y-direction defined in Equation 5.6, dimensionless
V_n, V_s	velocities in the Y-direction evaluated at the north and south boundaries of the control volume, defined in Equations 5.59 and 5.60, respectively, dimensionless
v	velocity in the Y-direction, m/s
$\bar{v}_j$	mean velocity of jet at nozzle exit, m/s
X	streamwise coordinate defined in Equation 5.6, dimensionless
x	streamwise distance measured from the jet centre, m
Y	axial coordinate defined in Equation 5.6, dimensionless
y	axial distance measured from the impingement plate, m
y_c	the y-coordinate of the centre of the circle with constant q defined in Equation 3.1, m
Z	span-wise coordinate on the viewing surface used in the figures of digitized contours

Greek Symbols

α_Ω	underrelaxation factor for vorticity iterations used in Equation 5.88, dimensionless
β_1	incident angle of light path travelling from glass prism to polymer coating as shown in Figure 3.7, rad

β_2	refractive angle of light path travelling from glass prism to polymer coating as shown in Figure 3.7, rad
ΔX	grid increment in the X-direction measured between adjacent boundaries of control volume, dimensionless
ΔY	grid increment in the Y-direction measured between adjacent boundaries of control volume , dimensionless
δ	viscous boundary layer thickness in wall jet region, m
δ_0	viscous boundary layer thickness in stagnation flow region, m
δX	grid increment in the X-direction measured between adjacent nodes, dimensionless
δY	grid increment in the Y-direction measured between adjacent nodes, dimensionless
θ	angle of impact, rad
λ	wavelength of the light (laser beam), m
μ	viscosity of air at the experimental condition, kg/(s·m)
ν	kinematic viscosity of air at the experimental condition, kg/(s·m)
ρ	density of air at the experimental condition, kg/m^3
ρ_j	partial vapour density of the coating material at the jet exit as defined in Equation 2.15, kg/m^3
ρ_s	density of swollen polymer coating, kg/m^3
ρ_w	partial vapour density of the coating material on plate surface defined in Equation 2.15, kg/m^3
ρ^0	molar density of gas mixture, $kmol/m^3$
τ_s	shear stress at impingement plate, N/m^2
ϕ	general variable used in Equation 5.47, dimensionless
Ψ	stream-function defined in Equation 5.6, dimensionless
ψ	stream-function, m^2/s
Ω	vorticity defined in Equation 5.6, dimensionless
ω	vorticity, s^{-1}

Subscripts

b	slot width as the characteristic length
d	jet diameter as the characteristic length
E, W, N, S	east, west, north and south neighbouring nodes
e, w, n, s	east, west, north and south side boundaries of the control volume
fd	fully developed flow
i	element number in the X-direction used in discretized equations
j	element number in the Y-direction used in discretized equations; at the jet exit used in other cases
s	at the coating surface of the impingement plate

Chapter 1

Introduction

1.1 Background

Impinging jets are widely employed in industrial processes for their high heat and mass transfer rates and relative ease of control. Some industrial applications include drying of paper, veneer and textiles, cooling of electronic components and gas turbine blades, tempering of glass, annealing of metal and plastic sheets.

Heat and mass transfer characteristics of various types of impinging jets have been studied. However, most of the studies dealt with turbulent flow. The case of heat and mass transfer due to laminar impinging jets has received much less attention. For the limited number of studies involving laminar impinging jets, most dealt with circular jets. For the case of impinging laminar slot jets, only a few investigations, mostly theoretical or numerical, are available in the literature. The lack of systematic experimental data in laminar impinging jets, especially for slot jets, is remarkable.

In general, the lack of experimental studies dealing with laminar impinging jet flows may be attributed to the following reasons:

1. Most experimental studies dealing with impinging jets make use of some type of heat-flow transducer to determine local heat transfer coefficients, giving rise to high uncertainties when the heat flux was low due to laminar flow;
2 Theoretical and numerical predictions to the heat and mass transfer characteristics due to laminar impinging jets normally have better agreement with experimental results than those due to turbulent impinging jets, giving rise to the illusion that experimental studies may be replaced by theoretical work.

However, experimental studies dealing with laminar impinging jet flows are by no means unimportant. Besides its obvious significance in understanding the transfer mechanisms, heat and mass transfer due to laminar impinging jets also have important industrial applications (Adcock, 1962; Kohring, 1985). Because of the complexity of impinging jet flows, even for the cases of initially laminar jet flow, the heat and mass transfer characteristics may not be predicted accurately by theoretical or numerical models. Since experimental data on the confined single impinging laminar slot jet are lacking and there is no any study on the mass transfer due to two confined impinging laminar slot jets, more experimental data for these cases are needed.

1.2 Objectives of this work

Based on the above analysis, the current work has been initiated to achieve the following objectives (see Figure 1.1 for the three cases):

1. Experimentally examine the effects of the jet Reynolds number and jet-to-plate spacing on the local mass transfer due to the impingement of a single confined laminar slot jet;
2. Experimentally study the effects of the jet Reynolds number, jet-to-jet spacing, jet-to-plate spacing and jet flow ratio on the local mass transfer due to the impingement of two confined laminar slot jets;

3. Numerically predict the flow field and mass transfer rate due to one confined laminar impinging slot jet and two confined laminar impinging slot jets under symmetrical flow conditions.

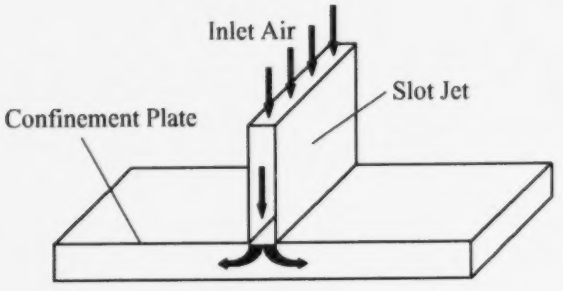

(a) Single Slot Jet

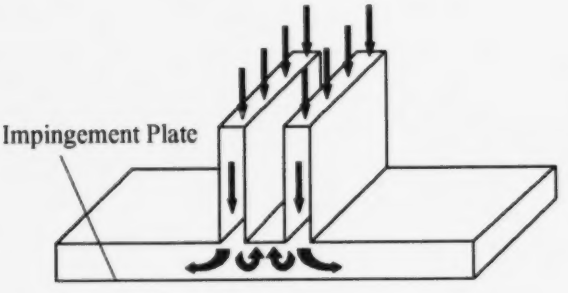

(b) Two Slot Jets: Symmetrical Flow

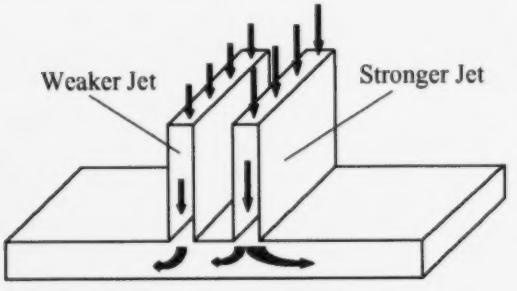

(c) Two Slot Jets: Asymmetrical Flow

Figure 1.1 The three flow configurations studied

Chapter 2

Literature Review

2.1 General Review

For the pass few decades, jet impingement heat and mass transfer has attracted much research attention (Button and Wilcox, 1978). Several state-of-the-art review publications on various aspects of the general topic of impinging jets can be found in Martin (1977), Button and Wilcock (1978), Downs and James (1987), Polat et al. (1989), Jambunathan et al. (1992) and Viskanta (1993).

Heat and mass transfer under impinging jets is characterized by large number of design options and parameters. To provide a comprehensive and updated knowledge of the whole research area, a general review covering most of the important aspects of impinging jets is conducted in sections 2.1 through 2.2. To lay the foundation for this work, a more detailed review on the relevant references dealing with single and multiple laminar impinging slot jets is provided in section 2.3.

2.1.1 Flow Characteristics of Impinging Jets

The flow pattern of slot or circular impinging jets can be divided into three characteristic regions as shown in Figure 2.1: (1) free jet, (2) stagnation flow, and (3) wall jet (Polat et al., 1989; Law, 1982).

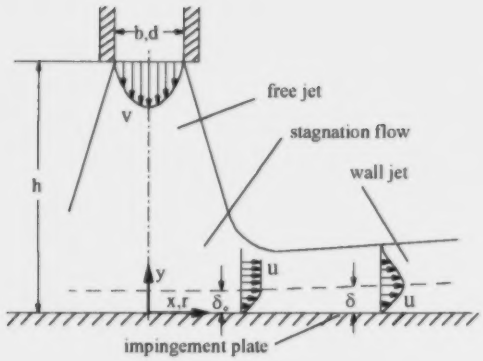

Figure 2.1 Flow field of an unconfined laminar impinging jet

The free jet region is defined as the region not influenced by the impingement plate. In general, near the nozzle exit, the jet is decelerated by the tangential shear stress caused by the surrounding still fluid. At the same time, the surrounding still fluid is accelerated, producing a "mixing region". The width of the mixing region increases continuously, and at some distance downstream it is wide enough to penetrate the centerline of the jet stream. Up to this point the centerline velocity is practically unaffected by mixing and is substantially equal to the centerline velocity at the nozzle exit. The region between the nozzle exit and the point where the centerline velocity starts to decrease is referred as "potential core".

The stagnation region is characterized by an increased static pressure as a result of the sharp decrease in the mean axial velocity. Upon impingement the flow deflects and starts to accelerate along the impingement plate. The end of the stagnation region is the location where the pressure gradient parallel to the impingement plate becomes zero.

Beyond the stagnation region is the wall jet region. The wall jet is the boundary layer flow formed by deflection of the jet through the stagnation region.

2.1.2 Effect of Flow Media

From the criterion of the jet flow medium and the ambient fluid, the impinging jet can be generally classified as (Law, 1982):

1. Liquid jet (or free jet): liquid to gas. The most common type is water to air, often referred to as "water jet".
2. Submerged jet: liquid to liquid or gas to gas, with the most popular one being "air jet".

The two types of jets differ substantially from each other. For a liquid jet, because of the large density difference between the liquid from the jet and its surrounding gas, the entrainment is negligible and the jet forms a free surface at the ambient pressure imposed by the surrounding gas. For the submerged jet, however, the density difference between the jet and its surrounding fluid is negligible and hence the entrainment is important and there is a substantial amount of mixing between the jet and the surrounding fluid.

There are many studies on liquid impinging jets, see Adcock (1962), Chaudhury (1964), Watson (1964), McMurray et al. (1966), Miyazaki and Silberman (1972), Ishigai et al. (1978), Miyasaka and Inada (1980), Zunbrunnen (1989a,b, 1990), Vader et al. (1991), among others. Detailed reviews can be found in Vader et al. (1992) and Viskanta and Incropera (1992).

There are numerous studies on impinging gas jets. More recent reviews can be found in Polat (1988), Polat et al. (1989), Jambunathan (1992) and Viskanta (1993).

2.1.3 Effect of Jet Shape

Theoretically, an impinging jet can assume any shape: circular (axisymmetric), slotted (also called planar or two-dimensional), and squared, etc. However, the circular and slot shapes are the most popular ones, since they are relatively easy to manufacture and install and possess favourable heat and mass transfer features.

In a review quoted by Viskanta (1993), Livingood and Hrycak (1973) concluded that for the same flow rate, nozzle exit area, and target area, the heat transfer rate due to a circular jet can be 8% higher than that due to a slot jet. However, the shape of the area to be cooled should be considered as well when determining which type of jet to use. For spot cooling, such as turbine vane cooling, circular jets are preferred for their larger heat transfer rate and easier construction. A drawback to the circular jet is that nonuniform cooling often occurs between the array of jets, due to their radial symmetry. Nonuniform cooling is especially undesirable for some applications, such as steel strip cooling, as regions of reduced strength due to recrystallization and grain growth can arise where cooling is deficient (Zumbrunnen, 1989b). Slot jets can span the entire surface and thereby provide more uniform cooling. Moreover, in some cases, slot jets may be more efficient than circular jets (Kohring, 1985). Therefore, for strip cooling such as used in steel and paper industries, slot jets may be preferred.

2.1.4 Effect of Confinement

Confinement in the impinging jet flow is an important design factor for industrial applications. A confinement plate at the nozzle exit level, parallel to the impingement surface, is normally required for reasons of thermal efficiency or environmental concerns (Polat, p4-5, 1988). For unconfined impinging jet flows, the jets entrain ambient air which affects heat transfer to an indeterminate extent depending on the relative temperatures at the nozzle exit, the ambient and the impinging surface. As heat transfer for unconfined jet systems inherently includes some equipment-specific effect, such data may not provide a reliable general basis for designing industrial confined jet systems.

Obot et al. (1982) studied the effect of confinement on the heat transfer of a circular impinging jet. They showed that confinement reduces heat transfer outside the stagnation region and the reduction increases as the jet-to-plate spacing decreases. At h/d = 2 (refer to Figure 2.1), for Re_d = 18128 and 29901, a reduction of 50% was

observed outside the stagnation region. With a small h/d, e.g., h/d = 2, the reduction of heat transfer by the confinement decreased with increasing Reynolds number. On the other hand, when h/d was large, the trend seemed to be reversed.

A few other studies (van Heiningen et al., 1976; Law and Masliyah, 1984a; Al-Sanea, 1992) also concluded that the confining plate has very little effect on the heat or mass transfer coefficient at and near the impingement region. Law and Masliyah (1984a) found that the local Sherwood number along the impingement plate for a confined slot jet behaved quite differently from that for an unconfined jet in the region far away from the stagnation point. In this region, the local Sherwood number exhibited a local minimum and a local maximum. The locations of these extrema are functions of jet Reynolds number and jet-to-plate spacing.

2.1.5 Effect of Reynolds Numbers

Classification of Flow Regimes

The flow regime remains one of the most important factors influencing the transfer rate of the impinging jets. McNaughton and Sinclair (1966) reported four flow patterns for a circular jet (Polat et al., 1989):

1. dissipated laminar jet: $Re_d < 300$
2. fully laminar jet: $300 < Re_d < 1000$
3. transition jet: $1000 < Re_d < 3000$
4. fully turbulent jet: $Re_d > 3000$

where Re_d is the Reynolds number based on the diameter of the jet. Gardon and Akfirat (1966) regarded slot jets with $Re_b > 2000$ as being turbulent. In general, whether an initially laminar free jet is still laminar before impact depends on many factors, e.g., jet Reynolds number, the velocity profile at the jet exit, the jet-to-plate spacing, jet confinement, etc. All these factors affect the level of mixing at the outer jet boundaries which determines how fast an initially laminar jet changes to a turbulent one.

For an unconfined jet, when the jet is laminar at impact, the flow remains laminar due to acceleration under the pressure gradient existing in the impingement region. Beyond this region, transition to turbulent flow takes place under the influence of free stream turbulence created by outer mixing layers of the free jet region. This transition occurs at larger distances away from the stagnation point when the Reynolds number and the jet-to-plate spacing are decreased.

Turbulent impinging jets are used more often than laminar jets due to their higher transfer rates. For the more recent and extensive reviews on turbulent jets, one is referred to Polat (1988), Jambunathan et al. (1992) and Viskanta (1993).

Laminar impinging jets may be encountered in practice especially when the jet dimensions and the nozzle-to-target distance are small (van Heiningen et al., 1976). In steel mills, laminar water jets are often used in cooling hot steel strips since they can provide more effective contact between water and the surface due to less entrainment compared to turbulent jets (Adcock, 1962; Kohring, 1985).

Laminar Impinging Jets

For laminar impinging jets, the effect of the Reynolds number on heat transfer coefficients is often expressed in the following form:

$$Nu = CRe_j^n \tag{2.1}$$

where Nu is the local Nusselt number and C is a constant. Boundary layer theory has shown that n = 0.5 for the stagnation region and n = 0.75 for the wall jet region for both circular jets (Scholtz and Trass, 1970) and slot jets (Schwarz and Caswell, 1961; Sparrow and Lee, 1975; Masliyah and Nguyen, 1979). However, numerical and experimental results show large discrepancies in the heat and mass transfer rates among different investigators (Polat et al., 1989).

Turbulent Impinging Jets

The effect of the Reynolds number on stagnation mass transfer for turbulent impinging jets is given by the following empirical equation (Popiel and Boguslawski, 1988; Jambunathan et al., 1992) for h/d ≥ 7:

$$Sh_0 = 0.461\, Re_d^{0.75} \left(\frac{h}{d}\right)^{-0.87} Sc^{0.4} \qquad (2.2)$$

where Sh_0 is the Sherwood number on the stagnation region, Re_d is the Reynolds number based on the diameter of the circular jet, h is the jet-to-plate spacing, d is the diameter of the jet and Sc is the Schmidt number. In the wall jet region (x/d ≥ 4.5), Jambunathan et al. (1992) correlated a large number of data from different sources using the form of Equation 2.1 and found that n is a function of x/d, h/d, nozzle geometry and varies from 0.5 to 0.85.

2.1.6 Effect of Jet-to-Plate Spacing

The jet-to-plate spacing affects the local transfer coefficient in a rather complex fashion. The effect on laminar impinging jets is very different from that on turbulent impinging jets.

Turbulent Impinging Jets For turbulent impinging jets, much experimental work has been conducted and well interpreted (Gardon and Cobonpue, 1961; Gardon and Akfirat, 1965, 1966; Akfirat, 1966; Korger and Krizek, 1966; Saad et al., 1992).

For small jet-to-plate spacings, the transfer coefficient at the stagnation point increases with increasing jet-to-plate spacing until h/b is about 8, where the local transfer coefficient at the stagnation point reaches a maximum value. This is due to the combined effect of the two opposing factors: the declining centerline mean velocity, U_0, and the increasing turbulence intensity, u'/U_0, when approaching the stagnation point (Saad et al., 1992). After the end of the potential core region, which is about 3 to 4 jet widths or diameters, U_0 decreases with the square root of the distance from the

nozzle exit. In the meantime, the turbulence intensity (u'/U_0) increases with the distance from the nozzle exit. The increase is sharp at first, but it levels out after 8b from the nozzle exit. For a jet-to-plate spacing up to about h/b = 8, the effect of the rapidly increasing turbulence intensity is more important than the opposing effect of the decreasing U_0. Beyond h/b = 8, the relative influences of these two opposing factors are reversed. This phenomenon is also seen in a multiple impinging jet system (Saad et al., 1992).

The shape of the lateral distribution of the local transfer coefficients depends on both the jet-to-plate spacing and the Reynolds number. When $h/b < 1$, and the Reynolds number is in the turbulent range, two peaks were observed on each side of the stagnation point, with the transfer rate at the stagnation point being a local minimum (Gardon and Akfirat, 1965, 1966; Akfirat, 1966; Korger and Krizek, 1966; Ichimiya and Hosaka, 1991). When $1 \leq h/b \leq 8$, there is a primary peak at the stagnation point and a secondary peak located between x/b = 5 and x/b = 8. The secondary peak was attributed to the transition from laminar boundary layer to turbulent boundary layer resulting from the mixing effect.

Laminar Impinging Jets There are much less experimental studies on laminar impinging jets compared to the case of turbulent jets. Although the work of Gardon and Akfirat (1966) and Akfirat (1966) covered the laminar flow range, their main attention was on the cases of higher Reynolds numbers. Scholtz and Trass (1970), Sparrow and Wong (1975), Law and Masliyah (1984a, 1984c), and Ichimiya and Hosaka (1991) studied the laminar impinging jets in more detail.

Scholtz and Trass (1970) studied a circular impinging air jet with a parabolic exit velocity profile both theoretically and experimentally. They found that when the jet-to-plate spacing, h/d, was less than 0.125, the lateral distribution of the Sherwood number had a maximum outside the stagnation point. For any larger jet-to-plate spacing, the maximum transfer rate was located at the stagnation point. For unconfined impinging

laminar slot jets, Gardon and Akfirat (1966) and Sparrow and Wong (1975) found that the local heat or mass transfer rates were not sensitive to the jet-to-plate spacing up to h/b = 5. For larger jet-to-plate spacings, the local Sherwood number decreased with increasing jet-to-plate spacings. Law and Masliyah (1984a, 1984c) investigated the mass transfer due to a confined impinging laminar slot jet and a semiconfined impinging circular jet both numerically and experimentally. Because of the limitation of their experimental set-up, they could not obtain the mass transfer coefficients at the stagnation region. However, their numerical results confirmed that the mass transfer rates were not sensitive to the jet-to-plate spacing when the dimensionless jet-to-plate spacings were less than 4. In addition, for the case of a confined laminar slot jet, they reported that the lateral distribution of the local Sherwood number exhibited a local minimum and local maximum. The locations and magnitudes of these extrema depended on both the Reynolds number and the jet-to-plate spacing.

2.1.7 Effect of Jet Exit Flow Conditions

For laminar impinging jets, the velocity profiles at the jet exit have significant influence on the transfer rate at the impinging surface (Sparrow and Wong, 1975). The most studied velocity profiles are those of parabolic and flat profiles. For a parabolic profile, the momentum of the jet is concentrated at the axis of symmetry, therefore penetrating farthest onto the impingement plate, resulting in a maximum heat or mass transfer rate at the stagnation point. In the case of a flat axial velocity profile, the large relative velocity at the outside boundary of the jet causes severe mixing and a rapid outward momentum transfer. Van Heiningen et al. (1976), Huang et al. (1978), Saad et al (1977), Deshpande and Vaishnav (1982), and Law (1982) all concluded that a parabolic jet exit velocity profile results in higher heat and mass transfer rates. For circular jets, Saad et al. (1977) reported a 50% increase at the stagnation point and a 15% increase at r/d = 2.5. They also noticed that for a flat jet exit velocity profile, the heat transfer rate was significantly lower over the entire impinging plate. For slot jets, both Law (1982) and van Heiningen et al. (1976) noticed that a parabolic velocity

profile doubled the transfer rate at the stagnation point as compared to a flat profile.

For a turbulent impinging jet flow, the turbulence intensity at the jet exit has significant effect on the transfer rate at the impinging surface. Gardon and Akfirat (1965) and Saad (1981) observed that at h/b < 8, the heat transfer profiles in the impingement region were quite sensitive to jet exit turbulence level. Gardon and Akfirat reported that for a jet Reynolds number of 11000, depending on the dimensionless nozzle-to-plate spacing, with an increase in the turbulent intensity at the nozzle exit from 2.5% to 18%, the stagnation point heat-transfer coefficient increased up to 50%. Because of the sensitivity to this boundary condition, local heat and mass transfer profiles for nozzle-to-surface spacings less than 8 from different researchers differ substantially.

The nozzle design has an significant influence on the exit turbulence level, which in turn affects the transfer coefficients on the impinging surface. A sharp-edged orifice can result in a 25% increase to the area mean transfer coefficient compared to a contoured ASME nozzle for h/d = 4, Re_d = 20000 and x/d = 1 (Popiel and Boguslawski, 1988; Jambunathan, 1992).

2.1.8 Effect of Nozzle Size

Some investigators have concluded that the nozzle size is not a significant variable for large jet-to-plate distances (h/d > 20) (Gardon and Conbonpue, 1961; Hollworth and Berry, 1978). However, the nozzle size (diameter for circular jets and width for slot jets) does have an effect on the stagnation transfer coefficient in the transition region for which h/d or h/b < 12. Obot et al. (1979) studied the effect of jet exit geometry on impinging heat transfer coefficients in the stagnation region for h/d < 6. Stevens and Webb (1991b) studied the influence of the nozzle diameter on the stagnation transfer coefficient for a circular turbulent impinging liquid jet. They reported that the Nusselt numbers rose consistently with the nozzle diameter. The use of dimensionless

parameters based on the nozzle diameter does not eliminate the dependence on the diameter. They argued that the nozzle size had a pronounced effect on the stagnation velocity gradient which in turn is an important parameter influencing the transfer coefficients. Saad et al. (1992) made a similar conclusion for the impinging slot jet flow. Their measurements showed that as the slot width increased, so did the turbulence intensity, which was mainly responsible for the increase in the transfer coefficients. They also found that with an increasing jet-to-plate spacing, the effect of the nozzle size was significantly reduced.

2.1.9 Effect of Angle of Impact

Perry (1954) was the first to study the influence of the angle of impact for an impinging jet (Martin, 1977). However, as Sparrow and Lovell (1980) pointed out, there was a basic misconception as well as several experimental inadequacies in his work which rendered his results unreliable. Martin (1977) reviewed Korger and Krizek's work (1972) for a slot jet. Korger and Krizek found that the stagnation point (or the point of maximum heat and mass transfer) did not coincide with the point of intersection between the jet axis and the impinging surface. The stagnation point shifted by a length of Δx upstream from the jet flow (see Figure 2.2). This length was given by

$$\Delta x = 1.4(b + 0.11h)\cot\theta \tag{2.3}$$

Korger and Krizek also found that the integral mean mass transfer coefficients were practically independent of the angle of impact, θ, for constant h within the range of $30° \leq \theta \leq 90°$. Only the position of the maximum is shifted by Δx and the local values downstream from the maximum are higher than those upstream.

Sparrow and Lovell (1980) and Goldstein and Franchett (1988) studied the effect of the angle of impact for impinging circular air jets. They had drawn similar conclusions as those of Korger and Krizek for the slot jets. Sparrow and Lovell noticed that the

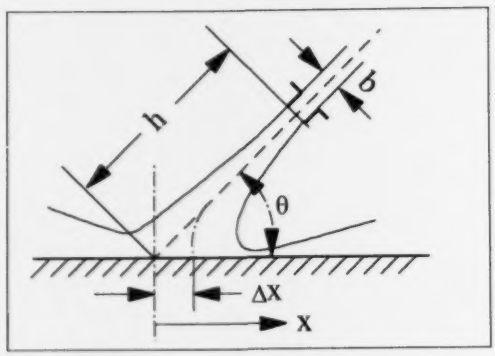

Figure 2.2 Inclined Impinging Jet

the local coefficients on the upstream side of the maximum point drop off more rapidly than do those on the downstream side. Thus, there were significant imbalances of the cooling or heating capability on the two sides of the maximum. The values of the maximum coefficient decreased with decreasing impact angle, with the greatest decrease being in the range of 15 to 20 percent. The surface average transfer coefficients were not very sensitive to inclination, with a maximum decrease of 15 to 20 percent compared to those for a normal incidence.

Stevens and Webb (1991a) examined the effect of inclination under circular liquid jets. They concluded that for the liquid jets, although the point of maximum heat transfer shifted upstream as reported for air jets, the magnitude of the shift was much smaller for a similar arrangement. Also differing from the submerged jet results, the magnitude of the peak heat transfer was observed to increase slightly with decreasing angle of impact. Both of the differences were attributed to the decrease in the entrainment and pre-impingement jet spreading in the case of liquid jets.

2.1.10 Effect of Surface Movement, Crossflow and Throughflow

Surface Movement Manufacturing processes frequently employ impinging jets to

cool or dry materials. Materials are often in motion since many manufacturing processes are designed to produce large quantities of products continuously (Zumbrunnen, 1990).

Polat (p22-24, 1988) reviewed some of the earlier investigations of the surface movement effect on the average transfer coefficients (Fechner, 1971; Subba Raju and Schlunder, 1977; Haslar and Krizek, 1984; Baines and Keffer, 1979), indicating that contradictions existed among them, with the majority showing a decrease in the average transfer coefficient with an increasing surface movement speed.

Van Heiningen (1982) studied the effect of surface motion on the local and the average heat transfer for a confined impinging slot jet. He found that the average heat transfer decreased with an increasing surface speed. For Re_b = 10,000 and h/b = 2.6, the average heat transfer at a relative surface moving speed (i.e., the surface moving speed with respect to the average flow speed at the nozzle exit) of 0.86 is 17% lower than that for a stationary impingement surface. Polat (1988) and Polat et al. (1990) studied heat transfer under multiple slot air jets impinging on a permeable moving surface. They based their arrangement for the multiple jet system on Saad's (1981) correlation for an optimal effect, i.e., h/b = 5 and s/h = 0.5, where s is the separation distance between the adjacent jets. Their experimental results gave the following correlation for the average Nusselt number incorporating both effects of the surface motion and the throughflow:

$$\overline{Nu} = 0.094 Re_b^{0.68} (1 + M_{vs})^{-0.69} + 0.16 Re_b Pr M_{us} \qquad (2.4)$$

where M_{vs} and M_{us} are the relative mass velocity of the surface and the throughflow with respect to the average mass velocity at the jet nozzle exit, respectively. The correlation is valid for $8000 < Re_b < 25800$, $0 < M_{vs} < 0.38$ and $0 < M_{us} < 0.0235$.

Zumbrunnen (1990) studied heat and mass transfer in the stagnation region of a single slot jet impinging on a moving surface. A similarity solution to the Navier-Stokes

equations was formulated to determine the flow velocity in the stagnation region. Heat and mass transfer distributions were determined from numerical solutions to the conservation equations for energy and species, using the velocity components calculated from the similarity solution. He concluded that convective heat and mass transfer was not affected by surface motion only when the surface temperature and the surface mass fraction of the mass transferring agent were constant along the impingement surface. Otherwise, the transfer rates were decreased.

Chen et al. (1991) conducted a numerical analysis to the heat transfer from a moving plate cooled by an array of submerged slot jets. They concluded that an increase in the plate speed had the following effects: (i) Flow separation near the flow merging plane between adjoining nozzles no longer occurred. (ii) The magnitude of the maximum Nusselt number decreased in the vicinity of the nozzle opening on the impingement plate. (iii) Heat transfer distributions became more uniform but the total heat transfer was reduced.

Contrary to all the above findings, if boiling occurs during cooling, the effect of the surface movement is quite different. Zumbrunnen et al. (1989a) investigated this effect theoretically. They found that when the plate moved opposite to the liquid, vapour travelling with the plate increased the vapour layer thickness and the Nusselt number decreased with an increasing surface moving speed. However, heat transfer was enhanced when the plate and liquid moved in the same direction, since vapour flow was aided and the vapour layer was thinned. On the runout table of a steel mill, when the relative speed of the plate was ten times that of the impinging jet, the Nusselt number could be 250% higher than that for a stationary plate.

Crossflow Crossflow is known to reduce the transfer rate for impinging jets. Sparrow et al. (1975) investigated experimentally the effect of jet-to-plate spacing on impinging heat transfer for a circular jet with a crossflow. They found that when the crossflow was weak ($M_{jc} \geq 8$, where M_{jc} is the mass velocity ratio of jet to crossflow),

the stagnation point heat transfer coefficient achieved a maximum value at jet-to-plate spacings of 5 to 6. But when the cross flow was stronger (M_{jc} = 4), the maximum was attained at smaller separation distances. Andrews and Hussain (1986) examined experimentally the effect of crossflow for square arrays of circular jets. They reported that crossflow produced a reduction to impingement heat transfer at large h/d values but an enhancement of heat transfer with small h/d values. It was shown that the latter effect was mainly due to flow maldistribution caused by pressure gradients within the gap. Chong et al. (1986) conducted an experimental study of heat and mass transfer due to an impinging slot air jet with crossflow. They obtained the following correlation to account for the effect of the cross flow:

$$\frac{Nu_m}{Nu_c} = 1 + 0.8M^{2/3} \tag{2.5}$$

where Nu_m is the peak Nusselt number and Nu_c is its counterpart immediately upstream from jet impingement ($x/b \approx -5$) and M is the momentum flow ratio defined as:

$$M = \left(\frac{U_j}{U_c}\right)^2 \frac{b}{h} \tag{2.6}$$

and U_j and U_c represent the jet and crossflow velocity, respectively.

Jaussaud et al. (1984) and Al-Sanea (1992) studied the crossflow effect for slot jets numerically. Jaussaud et al. investigated the combined effect of inclination and crossflow on the transfer coefficients. They noted that for a given h/b, Re and crossflow-to-jet-flow ratio, there exists an optimum inclination angle against the crossflow for which the heat transfer is maximum. Al-Sanea found that the average Nusselt number exhibited a maximum value when there was no crossflow and a minimum where the crossflow speed was about half of that of the jet flow. The minimum average Nusselt number is about 60% of its maximum nominal value obtained without a crossflow.

Throughflow If the impingement surface is permeable, there is one more option to enhance the transfer rate: applying suction or throughflow on the impingement surface. There are only a few studies on this effect, all from the researchers at McGill University. Van Heiningen et al. (1976) investigated numerically the effect of throughflow for a laminar slot jet, concluding that suction can enhance the local heat transfer rate by a constant amount for a given relative throughflow velocity based on the jet velocity. Saad et al. (1977) drew the same conclusion from a numerical study of a circular laminar impinging jet. Another numerical work by Huang et al. (1978) offered similar results for a laminar swirling impinging jet. They pointed out that suction created larger convective flow towards the plate and reduced the thermal boundary layer on the plate, hence enhancing the heat transfer rate. With a specially designed heat flux sensor described by Polat et al. (1991d), which was capable of measuring the heat flux with throughflow effect, Polat (1988) and Polat and Douglas (1990) experimentally investigated the effect of throughflow on the heat transfer coefficients for a system of multiple slot jets. They expressed the effect of throughflow as an enhancement of the average Stanton number given by:

$$\Delta \overline{St} = 0.17 M_{us} \tag{2.7}$$

where M_{us} is the relative velocity of suction with respect to the flow speed at the jet exit. The correlation was applicable for all confined impinging slot jets, from single jets to closely spaced multiple jets, with h/b spacings ranging from 2.5 to 8 and Re_b ranging from 8,000 to 58,000, and with either a stationary or a moving surface, up to a relative speed of 0.38 based on the jet velocity. More recently, Polat et al. (1991c) offered a numerical solution for turbulent jets impinging on a surface with throughflow. The flow and heat transfer under confined turbulent impinging slot jets were predicted by solving the two-dimensional Navier-Stokes, energy and turbulence model equations. The turbulence model was a high-Reynolds number version of the k-ε model. They concluded that the prediction of the enhancement of heat transfer by throughflow at the impinging surface was about 10% higher than the measured values for $M_{us} < 0.002$ and for higher throughflow rates, the model substantially

overpredicted the enhancement.

2.1.11 Multiple Impinging Jets

Heating or cooling of large areas with impinging jets requires a multiple jet system. Extensive reviews on this subject can be found in Martin (1977), Polat (1988) and Viskanta (1993). To design an efficient multiple jet system, a large number of factors needs to be considered: slot or circular jets, jet arrangement, jet-to-jet spacing, jet-to-surface spacing, exhaust port location, etc. Martin conducted a comprehensive review of some of the earlier studies on both arrays of circular jets and arrays of slot jets. He derived equations for the optimal spatial arrangement for the two types of jets. For arrays of circular jets, the optimal arrangement is:

$$f_{opt} = 0.0152 \tag{2.8}$$

$$\left(\frac{h}{d}\right)_{opt} = 5.43 \tag{2.9}$$

where f is the relative nozzle area defined as the cross-sectional area of the jet divided by the area directly influenced by the jet. If the nozzles are arranged in line, with each covering a squared area, the optimal jet-to-jet spacing from the above equations is $s/d \approx 7.2$. For arrays of slot jets, the optimal spatial arrangement is given by:

$$f_{opt} = 0.0718 \tag{2.10}$$

$$\left(\frac{h}{b}\right)_{opt} = 10.074 \tag{2.11}$$

giving a jet-to-jet spacing of $s/b \approx 14$. As Polat (p19, 1988) pointed out, Martin's optimal arrangement equations for the slot jets is based on the correlation derived for a case where the exhaust flow is in the lengthwise direction of the slot nozzles, causing vigorous crossflow and reduction of the transfer coefficients. Saad (1981) investigated the heat transfer distribution under confined multiple slot jets for a wide range of parameters. He exhausted the spent air flow symmetrically between the jets, avoiding detrimental crossflow effects, and achieving uniform transfer rates in the lengthwise direction of the slot nozzles. He used the correlation of his results to predict that the

highest average Nusselt number would occur at about h/b = 5 and s/h = 0.5. Polat (1988) and Polat and Douglas (1990) used Saad's predicted optimal arrangement to study heat transfer under multiple slot jets impinging on a permeable moving surface. Viskanta (1993) reviewed some of the experimental investigations for multiple circular impinging jet systems. Some of the more important findings include:

1. A single row of circular jets was more efficient than a slot jet for maximizing the heat and mass transfer rate for the same air mass flow rate.
2. The maximum average Nusselt number occurred when the jet-to-plate spacing, h/d, was from 1.5 to 2.0 as the Reynolds number was from 3,000 to 40,000.
3. In-line hole patterns provide better heat transfer than staggered ones.

Having tested about 40 kinds of different nozzles, Inoue et al. (1992) developed a high-performance impinging jet dryer with a heat transfer coefficient 1.5 times higher than that of a slot jet system. Their system consisted of staggered orifices on a punched plate with h/d = 4/3 or 8/5 and a fixed relative nozzle area of 0.015. The exhaust ports were provided with much larger holes and arranged one row for every four rows of orifices. Compared to the slot nozzle systems used in industries, the punched plate nozzle system proved to have the best energy efficiency because its fan power increased only slightly but the average heat transfer coefficient rose by more than 50%. This system was capable of cutting the total energy cost by 36%.

2.2 Impinging Jet Studies

In general, the studies on impinging jet flows may be classified as experimental, theoretical and numerical according to the means of investigation.

2.2.1 Experimental Heat and Mass Transfer Studies

Most of the experimental studies on impinging jets dealt with heat transfer measurements. Data are normally presented by dimensionless Nusselt numbers in the form of correlations or plots. Some investigators conducted mass transfer

measurements and present nondimensional Sherwood numbers in various forms. This is not much of a problem since the two sets of data can be easily converted with the well established heat and mass transfer analogy, or sometimes referred as Chilton and Colburn (1934) analogy in the form of:

$$\frac{Sh}{Sc^{n}} = \frac{Nu}{Pr^{n}} \tag{2.12}$$

where Sh, Nu, Sc, and Pr are the dimensionless Sherwood, Nusselt, Schmidt and Prandtl numbers, respectively. n is a parameter which does not have a unified value, taken as 0.33 (Chilton and Colburn, 1934; Huang, 1963; Rao and Trass, 1964; Hrycak, 1978), or 0.40 (van Heiningen et al., 1976; Law, 1982; Popiel and Boguslawski, 1986) or even 0.42 (Martin, 1977; Viskanta, 1993).

Heat Transfer Studies In general, the heat transfer coefficient and Nusselt number are defined by the following equations (Goldstein and Seol, 1991; Goldstein and Timmers, 1982):

$$h = \frac{q_w}{T_w - T_{ref}} \tag{2.13}$$

$$Nu = \frac{h D_h}{k} \tag{2.14}$$

where h is the heat transfer coefficient, q_w is the convective wall heat flux, T_w is the wall temperature, T_{ref} is the reference temperature, Nu is the Nusselt number, D_h is the hydraulic diameter, and k is the thermal conductivity of the fluid. The following temperatures have been taken as the reference temperature by different researchers: the jet recovery temperature (Sparrow et al., 1975; Goldstein and Timmers, 1982), the adiabatic wall temperature (Goldstein et al., 1986; Goldstein and Franchett, 1988; Goldstein and Seol, 1991), some kind of average temperature (Hollworth and Berry, 1978; Obot and Trabold, 1987), the nozzle exit temperature (Saad et al., 1992). Obot and Trabold (1987) and Sparrow et al. (1975) have demonstrated the importance of the selection of the reference temperature in the definition.

Having selected the reference temperature, a researcher's main task is to measure the heat flux or the impinging surface temperature at all locations of interest. There are mainly two ways of carrying out the measurements. First, the temperature of the whole impinging surface is kept constant and the heat flux at various locations are measured (Gardon and Cobonpue, 1961; Akfirat, 1966; Gardon and Akfirat, 1966; Hollworth and Berry, 1978; Saad et al., 1992). Second, the heat flux is kept constant on the entire surface and the temperature profiles are measured (Sparrow et al., 1975; Goldstein and Seol, 1991).

The conventional means of measuring the temperature is by thermocouples of various types. However, other techniques have also been used in recent years, such as liquid crystal (Goldstein and Timmers, 1982; Goldstein and Franchett, 1988) and infrared radiometry (Pan et al., 1992).

Measuring heat fluxes is much more involved than measuring the surface temperature. In one of the earlier studies on impinging jets, Perry (1954) used a calorimeter of 16.5 mm diameter to measure the "local" heat fluxes. A heat-flow meter of this size was certainly not adequate to provide a real local heat flux. What it did was to provide an average value over the area covered by the meter itself. In creating what later became the most quoted papers, Gardon and Cobonpue (1961), Gardon and Akfirat (1966) and Akfirat (1966) used a heat-flow transducer of 0.9 mm diameter. Van Heiningen et al. (1985) developed a heat flux sensor of the thin-film surface thermometry type which is capable of measuring the rapidly and widely fluctuating transient heat flux. Based on the same principles, Polat et al. (1991d) developed another heat flux sensor, with the added feature of working on permeable surfaces. With this special sensor, Polat et al. conducted a series of experiments examining the throughflow effect (Polat, 1988; Polat and Douglas, 1990; Polat et al., 1991a,b,c,d).

In general, the sources of errors for various heat transfer measurements may be attributed to the following:

1. Calibration of thermocouples and heat flux sensors or transducers. A typical example of this is that one of the most widely quoted papers (Gardon and Cobonpue, 1961) presented heat transfer results 40% too high due to a calibration error (Gardon and Akfirat, 1966).
2. The heat losses due to conduction and radiation. This problem is intrinsic with essentially all kinds of heat transfer measurements. It seems that the uncertainties in heat transfer measurements become larger when the heat transfer rate is low and vice versa (Saad et al., 1992). This is expected since erroneous heat losses take a larger portion when the total heat transfer rate is relatively low.
3. The finite size of the heat flux sensors. It is not possible to build a strict point heat flux sensor. Hence, almost all the local heat flux measurements with sensors of finite size are in fact measuring the average flux on the area covered by the size of the sensor.
4. Other sources, such as the non-uniformity of the surface temperature when it is supposed to be uniform. This problem is more severe where the heat flux changes sharply on the surface, such as in the stagnation region.

It is hardly surprising that there exist large discrepancies in the experimental data on heat transfer due to impinging jets in the literature. In addition to the experimental errors that each individual researcher may introduce, there are added sources of discrepancies, such as the selection of different reference temperatures in the definition of heat flux (Equation 2.13), different levels of turbulence at the nozzle exit, different geometric designs of the nozzles, different sizes of nozzles, all known to affect the experimental results (Martin, p11,41, 1977; Popiel and Boguslawski, 1986; Stevens and Webb, 1991b; Vader et al., p613, 1991; Jambunathan et al., p108, 1992; Saad et al. p10, 1992; Viskanta, 1993).

Mass Transfer Studies Similar to heat transfer studies, experimental mass transfer studies are based on the following definitions for the mass transfer coefficient and the Sherwood number (Koopman and Sparrow, 1976; Sparrow and Lovell, 1980):

$$k = \frac{N}{\rho_w - \rho_j} \tag{2.15}$$

$$Sh_d = \frac{kd}{D} \tag{2.16}$$

where k is the local mass transfer coefficient, N is the local mass transfer rate per unit area, ρ_w is the partial vapour density of the mass transfer agent on plate surface, ρ_j is the partial vapour density of the mass transfer agent at the jet exit, Sh is the Sherwood number, d is the hydraulic diameter and D is the mass diffusion coefficient of the system. To the knowledge of the author, all the mass transfer experiments on impinging jet flows are based on the same principle: coating or wetting the plate surface with a volatile material, keeping the partial vapour density or concentration at the surface constant, and measuring the mass flux at various locations of interest on the surface. This method is analogous to the heat transfer experiments with a constant surface temperature and measuring the heat flux on the surface.

Martin (1977) described the experimental setup used by Schlunder and Gnielinski to study mass transfer due to impinging air jets. In their setup, water was used as the mass transfer agent and was supplied to each of the separate cells on the surface by flasks. During the experimental runs, uniform water vapour pressure on the surface was maintained by putting each flask connected to each cell at a certain level above the plate according to the local pressure head. Mass transfer rates were determined by measuring the rate of water consumption of each cell. To study the mass transfer of water jets, researchers have used acetanilide and benzoic acid (Scholtz and Trass, 1963), and cinnamic acid (Rao and Trass, 1964; Dawson and Trass, 1966) as the coating materials. These materials give very high Schmidt numbers. In these systems, the local mass transfer rates were obtained by measuring the rate of decrease of the thickness of the coating. For air jets, the naphthalene sublimation technique has been widely used (Dawson and Trass, 1966; Korger and Krizek, 1966; Scholtz and Trass, 1970; Sparrow and Wong, 1975; Koopman and Sparrow, 1976; Sparrow and Lovell, 1980; Chong et al., 1986). An air-naphthalene system provides low Schmidt numbers.

The contours of the naphthalene surface was normally measured both before and after an experimental run by a precision dial gauge. A detailed description of the naphthalene sublimation technique can be found in Sparrow and Wong (1975). For various mass transfer experiments with surface coating techniques, the sources of errors may be attributed to:

1. Inaccuracy of the partial vapour pressure of the coating material on the surface, since this pressure is highly sensitive to the temperature, about 10% variation per degree C at the room temperature (Sparrow and Wong, 1975; Downs and James, 1987);
2. Roughness of the coating surface, especially for high Schmidt numbers; Large roughness may cause up to 100% higher mass transfer rate (Dawson and Trass, 1966);
3. Mechanical erosion, especially in the stagnation region for high Reynolds numbers;
4. Thickness change of the coating due to natural convection (Sparrow and Wong, 1975);
5. Coating thickness measurement, since the change in thickness before and after an experimental run is extremely small, normally in the micron level (Sparrow and Wong, 1975).

Kapur and Macleod (1972) and Macleod and Todd (1973) developed an innovative approach to coating the surface and measuring the mass transfer coefficients — swollen polymer combined with holographic interferometry. The method involves the coating of a surface with a polymer film and the swelling of the film with a suitable swelling agent. Under certain operating conditions, the rate of transfer of the swelling agent from the polymer surface to the experimental fluid stream can be directly deduced from measurements of the shrinkage rate of the coating. The shrinkage can be measured by holographic interferometry. Interference fringes formed between holograms of the coated plate made before and after exposure to the air jet for a given time period can be recorded as "frozen fringes" by double exposure photography. The

fringes can be interpreted as contours of equal mass transfer rate. Masliyah and Nguyen (1974,1976,1977,1979) employed the above technique to study mass transfer due to unconfined impinging circular, square, rectangular and slot jets. Law (1982) and Law and Masliyah (1984a,b,c) used the same technique to study confined laminar impinging circular and slot jets. The swollen polymer combined with the double exposure holographic interferometry technique has the following advantages compared to the traditional naphthalene sublimation and dial gauge technique:

1. The polymer coating is easier to make and can be used repeatedly.
2. The measurement of the mass transfer profile is faster, more accurate and can provide the entire pattern of change in configuration of the surface.

On the other hand, the technique also has some limitations:

1. It is often very difficult to identify the reference fringe, the so called "zero order" fringe.
2. It is often difficult to interpret the fringes when the mass transfer pattern is non-monotonic and complex, since the fringe pattern does not distinguish an increasing mass transfer pattern from a decreasing one.
3. For impinging jet study, this method is often incapable of measuring the mass transfer coefficient of the most important area — the stagnation region, since the fringes there are normally too crowded to be counted.

Most of the disadvantages listed above may be overcome if real-time holographic interferometry combined with high resolution video recording is employed. This is the technique employed in this study. Detailed information regarding real-time holographic interferometry will be given in Chapter 3.

2.2.2 Theoretical and Numerical Studies

Theoretical Studies

Glauert (1956) was the first to introduce the term "wall jet" and to perform a complete

theoretical analysis for the radial and plane wall jets for both laminar and turbulent cases. He utilized the concept of self-preservation of the shape of the velocity profiles with downstream position to obtain similarity solutions of the flow field. He also predicted the flow field for turbulent wall jets by using eddy viscosity and a combination of Blasius' law and Prandtl's hypothesis for the inner and outer part of the wall jet. For laminar radial wall jet, the similarity solution gives (refer to Figure 2.1 for the notation):

$$u \propto r^{-3/2} \tag{2.17}$$

$$\delta \propto r^{5/4} \tag{2.18}$$

where u, δ and r are the velocity components parallel to the wall, the jet thickness and the radial distance along the wall, respectively. For a laminar slot wall jet, the following results were obtained:

$$u \propto x^{-1/2} \tag{2.19}$$

$$\delta \propto x^{3/4} \tag{2.20}$$

where x is the distance along the wall measured from the centre plane of the jet. It has been noted that Glauert's solutions for the turbulent wall jet are good only as a first approximation (Schwarz and Caswell, 1961).

Schwarz and Caswell (1961) extended Glauert's exact solution for the slot wall jet case to heat transfer with constant physical properties, neglecting viscous dissipation. Scholtz and Trass (1963) extended Glauert's momentum analysis of the laminar radial wall jet to mass transfer and compared the theory with their own experimental data. Dawson and Trass (1966) conducted both theoretical and experimental work on a turbulent radial wall jet. The hydrodynamic solution was obtained by the momentum integral technique, and the mass transfer was predicted by analogy. In their experimental work, the effect of Schmidt number was systematically examined.

Scholtz and Trass (1970) studied both the flow field and mass transfer of a laminar impinging circular jet theoretically and experimentally. Their work extended the previous studies from the wall jet region to both stagnation and wall jet regions, hence has much more practical significance. Other studies on laminar impinging jet systems can be found in Wang et al. (1989a,b), Martynenko et al. (1989) and Liu et al. (1992).

Heat and mass transfer due to a laminar impinging slot jet has also been theoretically investigated by several researchers (Miyazaki and Silberman, 1972; Sparrow and Lee, 1975; Inada et al., 1981).

Zumbrunnen et al. (1989a) theoretically studied the effect of surface motion on film boiling heat transfer due to a water jet.

Numerical Studies

Unlike theoretical studies which typically use the concept of self-preservation of the velocity profiles with the downstream position in order to convert the laminar boundary layer equations into an ordinary, non-linear differential equation and then solve the equation analytically, numerical methods solve the complete nonlinear governing equations by discretizing them into a set of algebraic equations which may be solved iteratively. Polat et al. (1989) gave a rather extensive and state-of-the-art review on this topic, covering both laminar and turbulent impinging jets for various arrangements. Therefore, only a brief review and a few new references will be given here.

Numerical solution of laminar impinging jets is relatively straightforward and has been investigated with a large degree of success (Polat et al., 1989). However, because of the much added complexity, the governing equations describing turbulent impinging jets are not easy to solve numerically and still attract much research attention. For laminar impinging jets, the number of governing equations is equal to the number of variables to be solved and hence the problems are well defined. After discretization,

the variables, either in their primary forms or having been transformed into stream function-vorticity format, are solved by an iterative method. For turbulent impinging jets, there are added variables representing the turbulent effects and hence the number of governing equations are less than the number of variables. Extra equations have to be found and solved along with the regular governing equations. This is done using the so-called turbulent models. Most of these models fall into one of the three categories (Polat et al., 1989): one-equation models, two-equation models and algebraic stress models, with the two-equations models being the most popular.

Van Heiningen et al. (1976), Jaussaud et al. (1984), Law and Masliyah (1984d) and Al-Sanea (1992) numerically studied single laminar impinging slot jets. Van Heiningen et al. investigated the effect of suction and variable properties. Jaussaud et al. examined the combined effect of angle of impact and crossflow. Law and Masliyah evaluated the effect of the confinement length and the outflow boundary conditions. Al-Sanea studied the influence of the flow confinement and crossflow.

Unconfined arrays of laminar impinging slot jets were studied numerically by Mikhail et al. (1982) and Chen et al. (1991). The latter examined the influence of a moving plate along with other parameters.

Unconfined single laminar impinging circular jets are investigated numerically by Deshpande and Vaishnav (1982), Fairweather et al. (1984) and Wang et al. (1993). The confined cases are examined by Saad et al. (1977), Huang et al. (1978), Mujumdar et al. (1980) and Law and Masliyah (1984b).

The more challenging cases of turbulent impinging slot jets were studied by Chuang (1989), Polat et al. (1991c), Chuang and Wei (1991) and Yuan and Liburdy (1992). Knowles and Bray (1991) numerically investigated unconfined turbulent impinging circular jets. All the above studies used the k-ε two-equation turbulent model. Chuang studied the effect of confinement plate on the length of the potential core and found

that the present of the confinement plate reduces the length of the potential core. Polat et al. examined the case of multiple slot jets with or without the effect of throughflow. Chuang et al. studied the effect of angle of impact. Yuan and Liburdy used a zonal approach to solve the turbulent impinging jet problem. This approach identifies an outer flow and an impingement region. The outer region flow is determined by using the standard k-ε model while the impingement region is modeled using the surface renewal concept. Their results gave very good agreement with the experimental data and they concluded that the surface renewal model in the impingement region provides an attractive alternative in the prediction of the surface interactions.

2.3 Heat and Mass Transfer due to Submerged Laminar Impinging Slot Jets

The flow characteristics of confined and unconfined impinging laminar slot jets have been reviewed rather extensively by Law (1982) and will not be repeated here. The heat and mass transfer due to laminar impinging submerged slot jets is reviewed in detail in this section.

2.3.1 Unconfined Impinging Slot Jets

Schwarz and Caswell (1961) studied heat transfer due to a slot wall jet by solving the boundary layer flow and energy equations analytically. Their analysis was based on the method developed by Glauert (1956). They found the local Nusselt number correlation for the case of a constant temperature to be:

$$Nu_b = C Re_b^{0.75} \left(\frac{x}{b}\right)^{-0.75} \frac{\Gamma\left(Pr+\frac{1}{3}\right)}{\Gamma(Pr)\Gamma\left(\frac{1}{3}\right)} \tag{2.21}$$

where Γ is the Gamma function, Pr is the Prandtl number and C is a constant depending on the value of the exterior flux of the momentum flux, a concept introduced by Glauert (1956). After evaluating the exterior flux of the momentum flux

for both parabolic and flat velocity profiles, it was found that C = 0.374 for both cases. This is reasonable since the above equation is for the wall jet region only and the initial velocity profiles mainly affect the stagnation region.

Gardon and Akfirat (1966) studied experimentally heat transfer of unconfined impinging slot air jets for both laminar and turbulent cases. For the laminar case, they worked on three Reynolds numbers: 450, 650 and 950. They found that for low Reynolds numbers (Re < 2000) with the jet-to-plate spacings within the potential core of the jet (0.5 < h/b < 5), the stagnation Nusselt numbers depend on Reynolds number only and $Nu \propto Re_b^{0.32}$. For larger jet-to-plate spacings and Re = 450, stagnation point Nusselt numbers are proportional to $(h/b)^{-0.5}$. However, for the cases of Re = 650 and 950, Nusselt numbers do not decrease with h/b monotonically. This fact was attributed to the penetration of the mixing-induced turbulence to the centre line of the initially laminar jets.

Akfirat (1966) carried out extensive measurements of heat transfer coefficients along the continuous length of a wall jet produced by air discharging through a slot formed by the plate on one side and the nozzle exit on the other (see Figure 2.3).

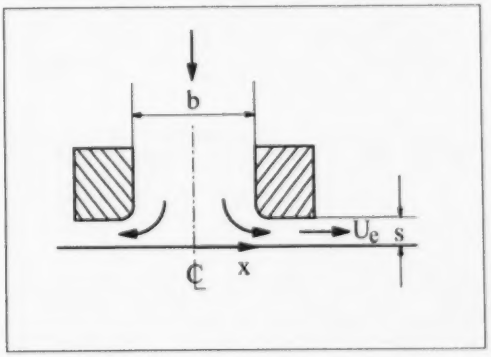

Figure 2.3 Wall Jet Definition

The characteristic length and velocity are s and U_e, respectively. Corresponding to the

notation of impinging jet (Figure 2.1), they tested the cases of h/b = 0.1 and 0.2. Their data show that, typically, the heat transfer rate, starting from the stagnation point, increases rapidly until the inner wall of the nozzle. Beyond this point, the heat transfer rate decreases sharply for about four slot widths downstream from the nozzle exit. With further increase in distance, except for the case of Re = 190, the heat transfer coefficients start rising again, reaching a maximum at about x/s = 14, and then decreasing gradually and monotonically. The first peak has been shown to be the result of the thinning of the boundary layer under the influence of flow acceleration. The second peak has been explained to be due to the effect of mixing-induced turbulence. Unless the Reynolds number is very small, as is the case for Re = 190, the second peak exists for both laminar and turbulent jets.

Miyazaki and Silberman (1972) theoretically investigated unconfined impinging slot jets with an initially flat velocity profile. Contrary to Gardon and Akfirat's findings (1966), they concluded that jet-to-plate spacings have a strong influence on the Nusselt number even when the spacings are within the potential core. For $1.0 < h/b < 2.0$, they found that the maximum Nusselt number was at $x/b \approx 1$, not at the stagnation point.

Sparrow and Wong (1975) experimentally investigated mass transfer due to an unconfined impinging laminar slot jet. Their study covered a wide range of jet-to-plate spacings (from 2 to 20) and jet Reynolds numbers (from 150 to 950). Their results showed that when h/b = 2, for almost all the Reynolds numbers investigated, the Sherwood numbers showed local maxima when plotted against lateral distance. For h/b = 5 and 10, local maxima still existed for jet Reynolds number above 450. When h/b > 15, all local maxima disappeared. Their data were found to be 30% higher than those of Gardon and Akfirat (1966), with the reason being attributed to the difference in the initial velocity profile. For the stagnation region, the Sherwood number can be related to the Reynolds number by $Sh_b \propto Re_b^{0.6}$.

Sparrow and Lee (1975) conducted a theoretical study on the flow field and heat and

mass transfer due to a fully developed laminar slot jet. They solved the velocity field within the impinging jet using an inviscid model. The results for the flow field were used as the input for the analysis of the heat boundary layer. The transfer coefficients were found to be insensitive to the jet-to-plate spacing within the range investigated ($0.375 \leq h/b \leq 1.5$). The correlation between the Sherwood number and the Reynolds number at the stagnation point was given as

$$Sh_b = 0.99 Re_b^{0.5} \tag{2.22}$$

which predicted the transfer coefficients as 10% higher than the data of Sparrow and Wong (1975).

Masliyah and Nguyen (1979) studied experimentally an unconfined laminar impinging slot air jet with an initially parabolic velocity profile. Their data were correlated as

$$Sh_b = 0.51 Re_b^{0.55} \left(\frac{x}{b} \right)^{-0.73} \tag{2.23}$$

for $Sc = 2.85$, $90 \leq Re_b \leq 300$, $1 \leq x/b \leq 30$, and $h/b = 4$.

Mikhail et al. (1982) performed a numerical study of the flow field and heat transfer from both single and a row of unconfined impinging laminar slot jets. They employed Patankar and Spalding's (1972) SIMPLE type of numerical procedure to solve for the primitive variables. The effects of the Reynolds number and the shape of the velocity profile at the nozzle exit for various nozzle spacings were investigated. They found that the Nusselt number at the stagnation point for a parabolic profile was almost twice as much as that for a uniform profile. Their results also showed that the maximum Nusselt number occurred at the stagnation point for both single and multiple jet systems. For multiple jet systems, the Nusselt number decreased to a minimum value located at a distance very close to the separation point and then increased to a secondary peak at the line of symmetry. The minimum and secondary peaks varied slightly as the jet-to-jet spacing was decreased.

Chen et al. (1991) conducted a numerical analysis of heat transfer for an array of unconfined submerged slot jets with a moving surface. The effects of the surface speed, the jet-to-jet spacing, the jet-to-plate spacing, and the Reynolds number on the flow and heat transfer coefficient were investigated. Patankar's SIMPLE algorithm (1980) was adopted in the computation. They found that an increase in the plate speed had the following effects: i) The flow separation near the symmetrical plane between jets no longer occurred; ii) The magnitude of the maximum Nusselt number decreased in the vicinity of the nozzle opening; iii) The heat transfer distribution became more uniform but the total heat transfer rate was reduced.

2.3.2 Confined Impinging Slot Jets

Van Heiningen et al. (1976) predicted the flow field and the impinging heat transfer characteristics due to a confined laminar slot jet by a numerical method. They studied both flat and parabolic initial velocity profiles. Interestingly, they found that the jet contracted slightly below the nozzle for a parabolic profile while for a flat profile the jet expanded continuously. Their results showed that the Nusselt number and the Reynolds number were related by $Nu_b \propto Re_b^{0.5}$.

Jaussaud et al. (1984) provided a numerical model to evaluate the combined effects of the crossflow and the angle of impact for a confined laminar impinging slot jet with $h/b = 3$ and $Re_b = 1000$. Their results showed the influence of the speed ratio of crossflow with respect to the jet flow, M_{cj}, on the local Nusselt number for an impact angle of $\theta = 30°$. As M_{cj} increased from 0.10 to 2.0, the influence of the impinging jet progressively diminished. Up to $M_{cj} = 0.4$, the jet impact was noticeable; at $M_{cj} = 1.0$, the influence of the jet was overshadowed by the crossflow and the heat transfer distribution approached that for a single channel. They also concluded that both the maximum and the average Nusselt numbers decreased markedly with increasing negative angles of inclination (against the crossflow).

Law (1982) and Law and Masliyah (1984a,d) conducted both numerical and experimental studies on the mass transfer due to a confined laminar impinging slot jet. They employed the swollen polymer method coupled with the double-exposure laser holographic interferometry technique to perform the mass transfer measurements. The experimental work covered four Reynolds numbers (100, 200, 300, 400) and two jet-to-plate spacings (2 and 4). Because of the limitation of their experimental setup, no stagnation point mass transfer results were obtained. Both their experimental data and numerical results showed that there was a local maximum and a local minimum in the wall jet region with the location being dependent on both the Reynolds number and the jet-to-plate spacing. From their mass transfer results, the following correlation for the Sherwood number in the wall jet region was obtained:

$$Sh_b = 0.34 Re_b^{0.66} \left(\frac{x}{b} \right)^{-0.78} \tag{2.24}$$

for $2 \le h/b \le 4$, $100 \le Re_b \le 400$ and $x/b \ge 1$.

Ichimiya and Hosaka (1991) experimentally and numerically investigated heat transfer due to a single and three confined slot air jets. In the laminar flow range, they studied only one Reynolds number, Re = 500. For a single jet, they covered three jet-to-plate spacings, h/b = 0.25, 0.5, and 1.0. For the case of three laminar jets, they fixed the Reynolds number (Re = 500) and jet-to-plate spacing (h/b = 0.25) and studied three different jet-to-jet spacings, s/b = 3, 5 and 8. For the case of a single jet, the following conclusions were drawn from their results:

1) The Nusselt number decreased with increasing jet-to-plate spacing, with the peak being at the stagnation point.
2) The numerical computations always overpredicted the Nusselt number in the stagnation region and underpredict those in the wall jet region.

For the case of three jets, symmetrically arranged, the following results were observed:

1) There exist one primary and two secondary peaks, with the primary one being located under the central jet and the secondary ones being lower in value and

shifted downstream due to the induced crossflow from the central jet.

2) The values of the secondary peaks became progressively smaller when jet-to-jet spacing was increased.

3) The numerical computations overpredicted the Nusselt number for the primary peak and predict the location and value of the secondary peaks closely and underpredicted the Nusselt numbers elsewhere.

From flow visualization, two small vortices were noticed in the stagnation region, and these were believed to be responsible for the discrepancies between the predicted and measured Nusselt numbers at the stagnation point.

2.4 Conclusions

1. Although there are a few numerical studies on confined laminar slot jets (van Heiningen et al., 1976; Law and Masliyah, 1984a,d; Ichimiya and Hosaka, 1991; Al-Sanea, 1992), there are only two experimental studies (Law and Masliyah, 1984a; Ichimiya and Hosaka). In Law and Masliyah's work, no stagnation region mass transfer coefficients were obtained because of the limitation of their experimental setup. In Ichimiya and Hosaka's work, only one Reynolds number was investigated in the laminar regime and only three very small jet-to-plate spacings were studied. Hence, more experimental work on the single confined impinging laminar slot jet is needed to provide the transfer coefficients on both the stagnation region and the wall jet region with the effects of both Reynolds number and jet-to-plate spacing.

2. From the literature survey, it can be concluded that there is no study for the case of two confined symmetrical slot jets which may arise in practice when multiple slot jets arrangement is employed. Since the symmetry can create a dead zone between the two jets and result in dramatic decease in heat and mass transfer rates, this effect of symmetry needs to be investigated systematically.

Chapter 3

Experimental Techniques

Experimental techniques employed in this study dealt with the swollen polymer coating and the real-time holographic interferometry with video camera recording. The swollen polymer technique was first used by Kapur and Macleod (1972) and described in detail by Macleod and Todd (1973). The swollen polymer and holographic interferometry techniques can provide fast, accurate and comprehensive profilometric measurement of mass transfer rates at solid-fluid interfaces and hence have been widely used (Kapur and Macleod, 1974, 1975, 1976a,b; Masliyah and Nguyen, 1974, 1976, 1977, 1979; Law, 1982; Law and Masliyah, 1984a,b,c; Hay et al., 1982, 1985a,b, 1986; Saluja et al., 1984; Paterson et al., 1987; Ammari et al., 1989a,b).

3.1 Swollen Polymer

The swollen polymer technique involves the coating of a flat surface under study with a thin layer of a non-volatile silicon polymer and the swelling of this coating with a volatile swelling agent (SA). A variety of SA has been tested (Macleod and Todd, 1973; Kapur and Macleod, 1975, 1976a; Paterson et al., 1987), with ethyl salicylate being the most preferred, since its vapour pressure does not depend on the age of the sample. Transfer of the SA from the swollen polymer coating to the flow stream results in local changes in the degree of swelling. These changes cause the polymer coating to shrink. The rates of shrinking at different points on the surface are

proportional to the different mass transfer coefficients at these points if, and only if, the following conditions hold over the period of measurement:

1. The decrease of thickness is essentially proportional to the transferred mass of the SA.
2. The effective vapour pressure of the SA over the surface is everywhere the same initially, and remains essentially constant as the mass transfer proceeds. Since the vapour pressure of the SA over the mass transfer surface depends on both the temperature and the composition of the coating, it must change as volatilization proceeds at a constant temperature. However, a change in the partial vapour pressure of up to 5% at the polymer coating during an experiment has a negligible effect on the determination of mass transfer coefficients compared to other sources of error. Therefore, the "constant rate period" is defined as the time period when the vapour pressure remains 95% of its initial value during an experimental run. Within this period, the partial vapour pressure of the SA at the surface may be assumed to be the vapour pressure of the pure SA, provided that the polymer is swollen to equilibrium with pure SA at the beginning of an experimental run.
3. The overall resistance to mass transfer is predominantly in the fluid phase.
4. The effect of diffusion of the SA parallel to the surface from regions of low mass transfer to regions of high mass transfer is negligible.
5. The relationship between mass transfer and the shrinkage rate is independent of the coating thickness.

The "constant rate period" depends on, among other variables, the mass flux of the SA, the initial degree of swelling, the initial thickness of the swollen polymer, and can be determined by the graphic method proposed by Macleod and Todd (1973). However, it has been pointed out that when the above method was applied to ethyl salicylate/water system, the predicted "constant rate period" was three times as great as that found experimentally. In any experiment having a duration more than half the predicted period, the mass transfer rate will decline significantly as the mass transfer

proceeds, and the time-averaged value of this rate will appear low (Kapur and Macleod, 1975).

The practical advantages of the swollen polymer technique are summarized as follows:

1. The coating itself can be used repeatedly; for each new experiment it can be re-activated by re-immersion in the SA bath.
2. The Schmidt number of the system can be varied; this can be accomplished by changing the swelling agent alone, without changing the experimental fluid or the polymer coating.
3. Because the mass transfer rate is independent of the coating thickness, no uniformity of thickness other than that implied by the need of hydraulic smoothness at the polymer surface of the coating is required.
4. Unlike the surface of a sublimating solid, the surface of the shrinking polymer maintains a nearly constant optical quality. It is therefore possible to record its shrinkage by the established techniques of holographic interferometry.

3.2 Holographic Interferometry

Holographic interferometry is a well-established technique to measure minute changes of optical path resulting from surface displacement, change of refractive indices, etc. The technique is a combination of holography and interferometry.

3.2.1 Principles of Holography and Holographic Interferometry

To help understand the concept of holographic interferometry, a brief introduction to the principles of holography is covered below.

Holography is a means by which one may record the wavefront reflected from an object and, later, reconstruct this wavefront in such a way that the effect on an observer is to produce the sensation of actually seeing the object (Wenyon, 1985). When two plane light waves of the same wavelength are projected towards a screen

from two slightly different directions, at some points on the screen, the waves are in phase and combine to produce bright illumination there, while at others the waves are in antiphase, cancel each other out and produce a dark region (see Figure 3.1).

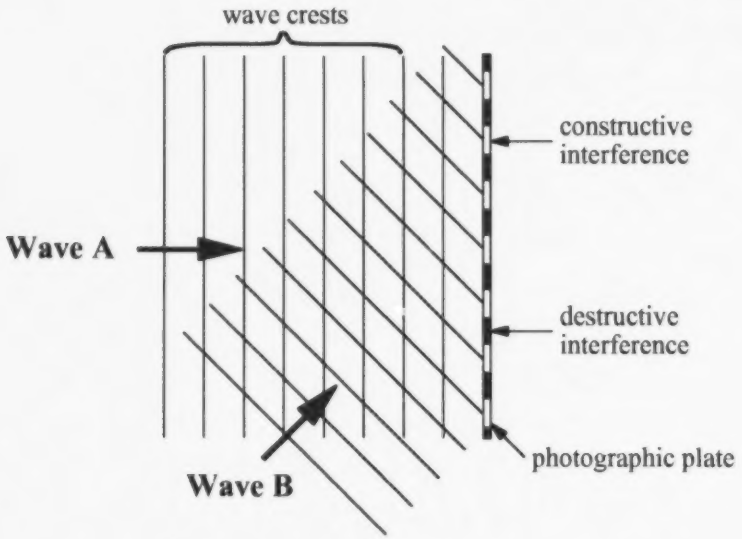

Figure 3.1 Interference of Two Plane Waves

The pattern of dark and bright lines produced on the screen is an interference pattern as shown in Figure 3.2. The bright and dark lines making up the interference pattern are known as interference fringes. The interference pattern can be recorded by placing a photographic plate at the position of the screen, exposing it to the pattern of light and then developing it. The record will be a photographic negative of the original pattern and is termed as a hologram. To produce the hologram, the light waves have to be coherent. The laser is such a device which produces light that has a high coherence and is an ideal source of light to produce the interference patterns. In holography, the stage to produce the hologram is known as the recording stage of the process. One of the plane waves, say wave A in Figure 3.1, is called the reference wavefront and the other, wave B, the objective wavefront (this is the one to be recorded and later

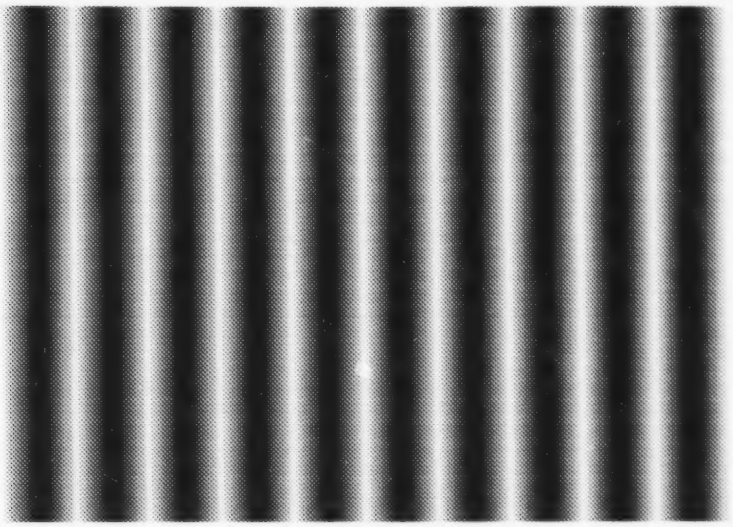

Figure 3.2 The Hologram of Two Plane Wavefronts

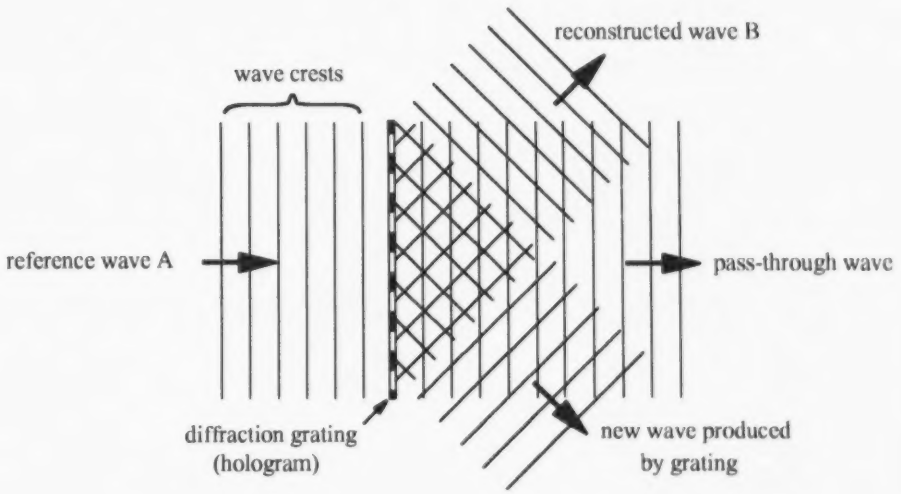

Figure 3.3 Reconstruction of Wave B

reconstructed). When the hologram is placed in the path of the original reference beam, two new wavefronts accompany the beam when it emerges from the other side of the plate due to the effect known as diffraction (see Figure 3.3). One of the new wavefronts is an identical replica of the original object wavefront, i.e., it consists of a plane wavefront travelling in the same direction as Wave B in Figure 3.1, and the other is responsible for the real image of the object which usually appears unsharp and highly distorted. This stage is termed as reconstruction.

Interferometry is a laboratory technique by which extremely small movements of objects are detected and measured by exploiting the interference properties of light. Conventional interferometry has a number of limitations, restricting its use to rather specialised applications. An accidental discovery by the first holographers at the University of Michigan led to the invention of a powerful new technique, the combination of holography and interferometry termed naturally as holographic interferometry. It is possible to make two or more exposures on the same photographic plate. After processing, when the multiple exposed hologram is illuminated with the reference wave, the object waves due to different exposures will all be reconstructed. If they differ only slightly from one another, they can interfere with each other to form fringes which are superimposed on the surface of the reconstructed image of the object. The fringes can be used to determine the degree of deformation or movements of the object. This is the basic principle of holographic interferometry.

3.2.2 Double-Exposure Holographic Interferometry

In double-exposure holographic interferometry (DEHI), as used by Law (1982), a hologram of the object, the polymer coating, is made before subjecting the polymer coating to the air jet. After the polymer coating is subjected to the air jet, a second exposure is made onto the same photographic plate. After processing the photographic plate, the double-exposed hologram is repositioned and illuminated by the reference wave. The interference from the two object waves before and after the coating

shrinkage indicates the thickness change of the polymer coating between the two exposures. These interference fringes, so called "frozen fringes", are contours of equal coating shrinkage or equal mass transfer and can be photographed and analyzed. The main drawback with DEHI in determining mass transfer coefficients is the identification of the order of the frozen fringe. Therefore, this technique is not employed in the current work.

3.2.3 Real-Time Holographic Interferometry

Real-time holographic interferometry (RTHI) can be performed by using a precise and adjustable hologram mount. After the first exposure of the mass transfer surface, the photographic plate is processed and replaced in its original position. The "reference image", which is the image of the object prior to the mass transfer experiment, is then reconstructed continuously by illuminating the hologram with the reference wave. Then the mass transfer experiment is started, and the reconstructed wavefront is superimposed onto the changing object wave. The changes of the interference pattern can then be continuously observed and the order of any particular fringe at any given time can be easily determined by counting the number of fringes generated or passed by at a given location. When a high resolution video camera is utilized to record the process of fringe development in RTHI, this powerful technique of RTHI is further enhanced and it has the following advantages when compared to DEHI and the conventional RTHI with naked-eyed observation.

1. The burden and uncertainties due to determination of the order of the fringe at various locations have been eliminated completely.
2. The recording can be replayed as many times as needed so that the data from one run of a recorded RTHI experiment may be equivalent to those obtained from a large number of runs of DEHI experiments covering different time periods.
3. In DEHI, because of the limitation of operating time and resolutions of the reconstructed frozen fringes, it is extremely difficult to determine the mass

transfer coefficients in the high mass transfer rate regions such as the stagnation region of the impinging jet flow. While in the RTHI, this region can be processed easily by using as short a time period as needed.

4. The accuracy of data obtained from recorded RTHI can be improved by observing the "constant rate period" individually for each point of interest according to its local mass transfer rate. Another factor contributing to the higher accuracy of the recorded RTHI is that the size of a 20 inch high resolution monitor on which the digitization of the recorded RTHI is conducted is much larger than a 4 by 6 inch black-and-white photograph where the digitization of the DEHI is conducted.

Compared with the DEHI, the technique of RTHI requires more practice to master.

From the above analysis, it can be concluded that the RTHI in conjunction with video camera recording remains the optimal technique among the holographic interferometry techniques and hence is used in the current work.

3.3 Experimental Set-up

The experimental set-up used in this study can be seen in Figure 3.4 which includes both the optical set-up for recording the hologram and the reconstructed fringes and the apparatus for mass transfer due to two impinging parallel slot jets. This set-up is similar to that of Law (1982). A non-invasive method of mass transfer measurement as reported by Harper and Macleod (1978) has been used since it allows real-time observation and recording.

3.3.1 Optical Set-up

A concrete table with a concrete slab of size 2.74 by 1.37 by 0.13m is used as the working surface for the optical set-up. The function of the heavy slab is to prevent floor vibration from being transmitted to the optical components. The optical

components include:

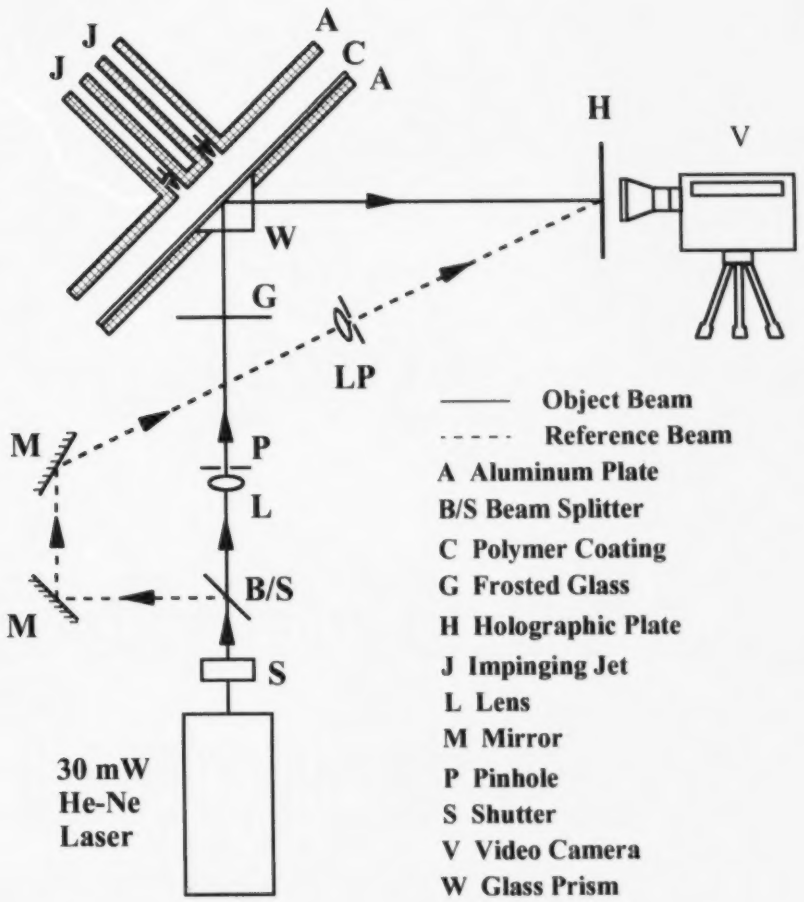

Figure 3.4 Experimental Set-up

1. a Spectra Physics model 124B 35mW He-Ne laser to provide coherent light of wavelength 6.328×10^{-7}m;
2. a Prontor-Press shutter to set the exposure time for making holograms;
3. an Elomag beam splitter-attenuator, model VBA-200, which is a variable reflectivity aluminum mirror for splitting the laser beam and adjusting the ratio of the beam intensities;

4. a Spectra Physics model 332 spatial filter and expanding lens assembly (expanding lens L3, aperture A3) mounted on a Spectra Physics model 306A precision optical mount with base and vertical post used to eliminate spatial noise and produce a smooth intensity profile across the expanded object beam;
5. two Spectra Physics model 386-11 utility mirror mounts (includes model 564 mirrors) which are used to reflect the reference beam;
6. a Spectra Physics model 332 spatial filter and expanding lens assembly (expanding lens L4, aperture A4) mounted on a Spectra Physics model 306A precision optical mount with base and vertical post used to eliminate spatial noise and produce a smooth intensity profile across the expanded reference beam;
7. a piece of 0.3 by 0.2m frosted glass mounted on a heavy metal base to provide the white background for the interference fringes;
8. an Elomag immersion-type X-Y micropositionable photographic plate holder, model MPH-45W, including a PC-45 plate carriage which is used to hold reposition a full size Agfa-Gevaert 10E75 (0.1016 by 0.127m) photographic plate for real-time holographic interferometry.

The positions of the optical components and the polymer coating surface are determined according to the holodiagram developed by Abramson (1969, 1970a,b). Holodiagram is a concept and device which provides a simple geometrical approach to fringe interpretation. For the basic hologram recording system shown in Figure 3.5, the holodiagram consists, as shown in Figure 3.6, of a set of ellipses with their foci at O and Q (Abramson, 1969; Hariharan, 1984). Each of these ellipses is the locus of points for which the distance OPQ is a constant, and this distance changes in steps of λ, the wavelength of the laser beam, from one ellipse to the next. The displacement of P is a minimum when its motion is normal to the ellipse, i.e., along the sensitivity vector **I**. The holodiagram also shows that while a displacement of P of $\lambda/2$ along the x axis results in a shift of one fringe, at any other location a larger displacement, $q\lambda/2$, where

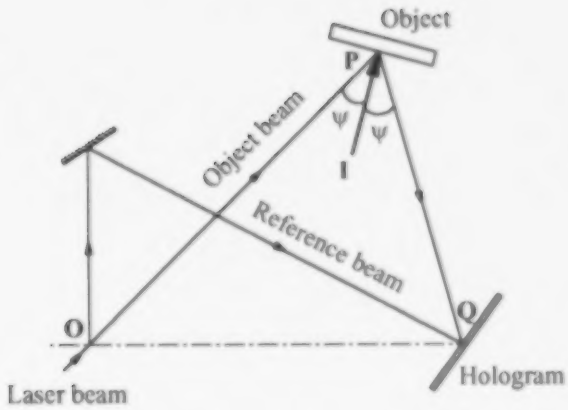

Figure 3.5 Schematic of a Holographic System

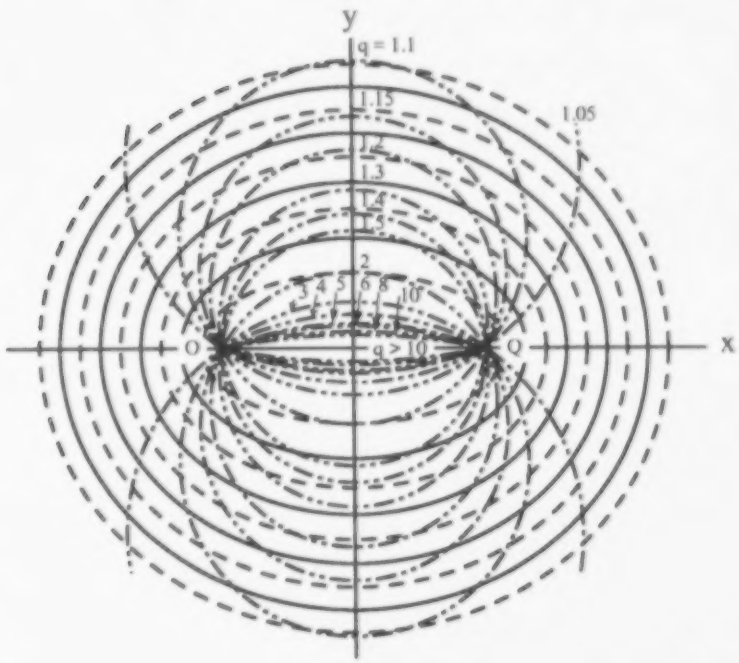

Figure 3.6 The Holodiagram

$q = 1/\cos\psi$, normal to the ellipse is required for the same fringe shift. The q values are presented in the holodiagram. These are the loci of points for which the angle $OPQ = 2\psi$ is a constant, and are, therefore, circles passing through O and Q. The centres of these circles are located on the y axis at points given by the relation (Abramson, 1970b):

$$y_c = \left(\frac{L}{2}\right)\frac{2-q^2}{\sqrt{q^2-1}} \tag{3.1}$$

where L is half of the distance OQ. It can be shown that the radii of these q circles, r_q, can be obtained from the following relation:

$$r_q = \left(\frac{L}{2}\right)\frac{q^2}{\sqrt{q^2-1}} \tag{3.2}$$

The value of q obtained from the holodiagram permits direct interpretation of the fringe pattern. If the fringe order at a point P on the object is n, the component of the displacement normal to the ellipse passing through P is merely $qn\lambda/2$.

In this study, the polymer coating is placed along the ellipse whose foci are the beam splitter and the centre of the photographic plate. The distance between the two foci is 1.2m. The length of the object surface to be studied, the hypotenuse of a right-angled glass prism, is 0.125m. Because of the geometry of the optical set-up, the angle of illumination and observation of the object surface is restricted to 45° by use of the right-angled prism. According to the holodiagram, the q value of this set-up is $1/\cos(45°) = 1.414$. The object surface is located corresponding to the y axis in the holodiagram, giving equal distances to both foci. The positions of the two mirrors are adjusted so that the path lengths of the object and the reference beams are equal (refer to Figure 3.4). In this way, the maximum coherent length of the laser is utilized so as to give maximum object field depth. The reference beam is directed by two mirrors and expanded by the spatial filter and expanding lens assembly, falling on the

photographic plate. The object beam is expanded by the spatial filter and expanding lens assembly so that it is wide enough to cover the whole object. The object beam travels through the prism and polymer coating, where it experiences a total internal reflection at the surface of the coating, and reaches the photographic plate. The interference patterns of the object beam and the reference beam are recorded by the photographic plate to form a hologram.

In real-time holographic interferometry, during the mass transfer process, the changing real object image interferes with the reconstructed object prior to the mass transfer process to form fringes. The absolute magnitude of the change in coating thickness is given by

$$r' = nB\lambda \tag{3.3}$$

where r' is the displacement of a given point on the object surface, n is the order of the fringe at the point under consideration, B is a constant related to the set-up, and λ is the wavelength of the laser beam. It is appropriate to clarify that there are two ways of defining the order of fringes in the literature. Some investigators counted both dark and bright lines as fringes (Kapur and Macleod, 1976a; Law, 1982; Law and Masliyah, 1984a,c) while others counted only dark lines (Abramson, 1969, 1970a,b; Vest, 1979; Hariharan, 1984). The former corresponds to the change of half a wavelength in the light path while the latter corresponds to the change of a whole wavelength. In this study, both dark and bright lines are counted as fringes. The B values used in the above equation can be evaluated from the optical set-up by calculating the difference in the path lengths of a light ray before and after a change of the coating thickness (see Figure 3.7). The change in the light path length between a-a and b-b before and after the mass transfer process may be derived from the geometric relations shown in Figure 3.7 and related to the nth order of the fringe by the following equation (both dark and bright lines are counted as fringes):

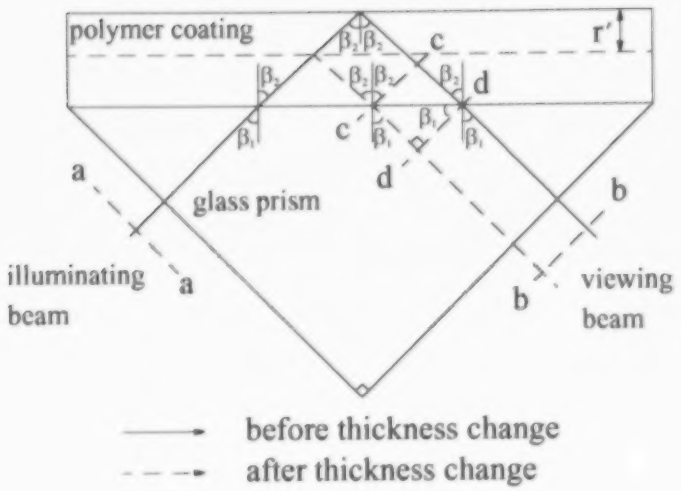

Figure 3.7 Light Path Before and After a Thickness Change

$$\frac{2\,r'(n_s - n_p \sin\beta_1 \sin\beta_2)}{\cos\beta_2} = n\frac{\lambda}{2} \tag{3.4}$$

where n_s and n_p are refractive indices of the swollen polymer and the glass prism, respectively (n_s = 1.428 and n_p = 1.5). The angle β_1, as shown in Figure 3.7, is 45°. The angle $\beta_2 = \sin^{-1}(n_p \sin\beta_1 / n_s)$ is calculated as 47°58′. From the above equation, the change in the coating thickness can be expressed by

$$r' = \frac{1}{4}\frac{n\lambda\cos\beta_2}{n_s - n_p \sin\beta_1 \sin\beta_2} \tag{3.5}$$

Comparing Equations 3.3 and 3.5 the constant B in Equation 3.3 can be expressed as

$$B = \frac{1}{4}\frac{\cos\beta_2}{n_s - n_p \sin\beta_1 \sin\beta_2} \tag{3.6}$$

Having known the fringe order and the value of B, one can calculate the absolute magnitude of the polymer coating shrinkage at a given point by using Equation 3.3.

3.3.2 Mass Transfer Experimental Set-up

The mass transfer experimental set-up is composed of an aluminium impingement plate on which the right-angled prism is mounted, a confinement plate on which the slot jets are mounted, a top spacer and a bottom spacer. The details of each of the components are described as follows:

1. The mass transferring surface is the hypotenuse surface of a right-angled glass prism (0.089 by 0.125m) which is fitted into a window cutting of an aluminum plate. The aluminum plate has dimensions of 0.158 × 0.625 × 0.012m. The surface of the prism forms a smooth surface with the aluminum plate. This surface is then coated with a thin layer of silicone rubber to form the impingement plate surface. The front and top views of this impingement plate are shown in Figure 3.8.

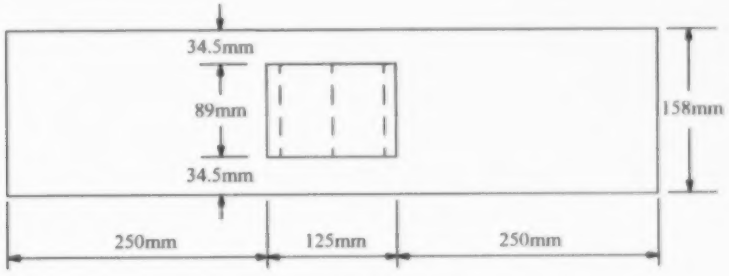

(a) Front View

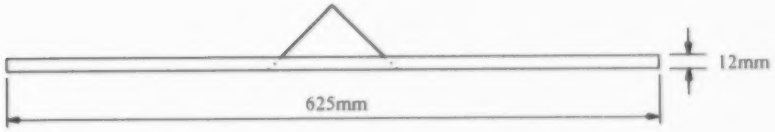

(b) Top View

Figure 3.8 Front and Top Views of Impingement Plate

2. A set of three aluminum confinement plates along with a pair of parallel aluminum slot jets are shown in Figure 3.9. The jets have a nozzle width of

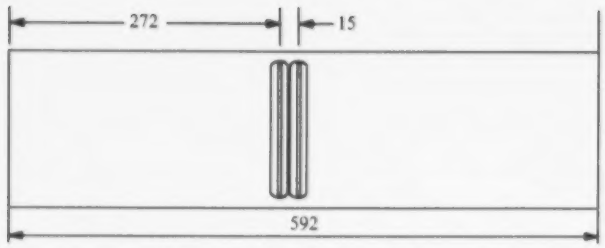

(a) Front view for s = 10b

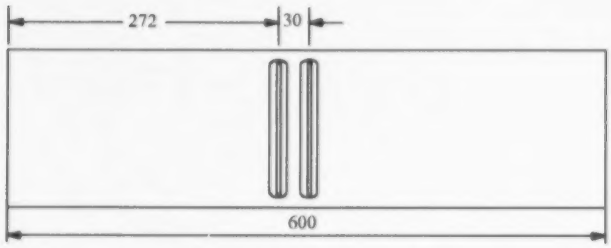

(b) Front view for s = 20b

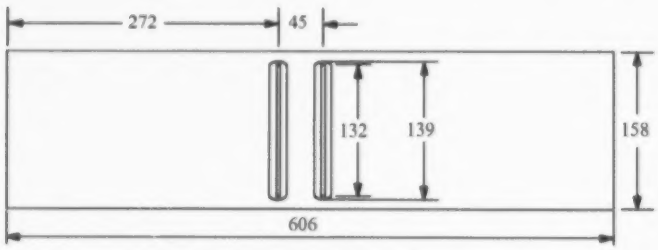

(c) Front view for s = 30b

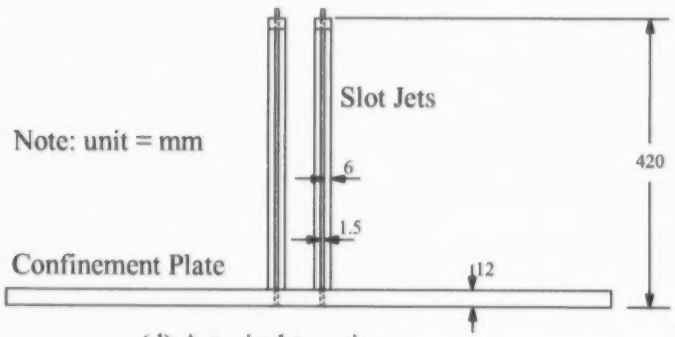

(d) A typical top view

Figure 3.9 Front and Top Views of the Confinement Plate with Slot Jets

0.0015m and a height of 0.132m, giving an aspect ratio of 88, large enough to ensure a nearly two-dimensional flow in the centre region of the jets. The length of the jets is 0.42m, long enough to provide a fully developed parabolic velocity profile at the jet exit at the highest Reynolds number used in this study. As for the end effect of the slot jet, a boundary layer analysis (Schlichting, p26, 1979) shows that when the Reynolds number changes from 150 to 450, the boundary layer thickness on each side of the slot at the jet exit varies from 0.01 to 0.006 m, much less than the spanwise dimension of the slot jet (0.132 m). The confinement plates, having slightly different lengths, are machined to accommodate jet-to-jet spacings of 10, 20 and 30 slot widths, respectively.

3. The jet-to-plate spacings are adjusted by changing the top and bottom spacers. For the single jet case, the jet-to-plate spacings used are 2b, 4b and 12b, where b is the slot width. For the case of two parallel jets, the jet-to-plate spacings used are 2b, 4b and 8b.

The mass transfer experimental set-up is mounted on a heavy metal base. Spacers are used to fit between the impingement and confinement plates so as to form a rectangular channel in which the jet flow is confined. The air impinges normally on the impingement surface, which is arranged such that both the central region between the two jets and downstream from one jet can be viewed and recorded.

3.3.3 Recording and Other Equipment

During the experimental process, the developing fringe patterns are monitored and recorded by the video camera for later analysis. The monitor is a high resolution 20-inch colour TV, Sony Trinitron, model KV-20TS30. The recording is accomplished by a Sony Hi-8 video camera recorder, model CCD-V101.

The laboratory room is equipped with a safelight consisting of a 15-Watt soft white light bulb and a Kodak 3 dark green safelight filter as recommended by Unterseher

et al. (1982). The intensities of the object and reference beams are measured by a Science and Mechanics darkroom photo meter, model A-3.

The fluid used in the experiments is industrial dry air supplied by compressed air cylinders. The Reynolds numbers are adjusted by changing the flow rate with two Brooks rotameters, model 1307EJ23CE1AA. The calibration of the rotameters is described in Appendix B.

3.4 Experimental Procedure

The experimental procedure consists of preparation of the polymer coating, the making and recording of the real-time holograms.

3.4.1 Preparation of the Polymer Coating

The polymer coating is prepared as follows:

1. Apply liquid silicone primer, SS-4120 from General Electric, by brushing it evenly on the mass transfer surface, and let it dry for one hour.
2. Follow the product instruction and mix thoroughly ten parts by weight of RTV-615A silicone rubber with one part of RTV-615B catalyst (both are from General Electric and supplied as one package) in a styrofoam cup to make about 0.1 kg mixture.
3. Pour the mixture evenly on the mass transfer surface which has been positioned perfectly level.
4. Allow the coated surface to spread out evenly at room temperature for about ten hours in a fumehood. During this period, the tiny bubbles generated during mixing will eventually disappear and the thickness of the coating becomes uniform.
5. Cure the coated surface in a clean oven at 65°C for three hours.

The complete swelling of a fresh polymer coating with ethyl salicylate takes at least

ten hours, while re-swelling a partially exhausted coating after an experimental run requires about three hours of immersion in the swelling agent bath.

The refractive index of the silicone rubber swollen to various degrees was found by Masliyah and Nguyen (1976). It is evident that the refractive index is a weak function of the degree of swelling when the swollen polymer is near its equilibrium.

3.4.2 Making and Recording of Real-Time Holograms

To prepare for real-time holography, the optical set-up has to be adjusted properly. The spatial filter and expanding lens assemblies for both the object beam and the reference beam need to be adjusted and fine-tuned extremely carefully to ensure proper focusing. The light ratio of the reference beam versus the object beam reaching the location of photographic plate needs to be adjusted to about 40 to 50 by turning the beam splitter dial to about 95. The light intensities are measured by the photo meter described in section 3.3.3. It should be noted that when the dial of the beam splitter is turned, it may be necessary to readjust the spatial filter and expanding lens assemblies. The shutter speed is set to 1/15 second. The valves of the two rotameters are adjusted so that the desired flow rates and hence the Reynolds numbers are ensured. For each run, the water in the photographic plate holder must be replaced by fresh tap water mixed from hot and cold water to the room temperature. All bubbles have to be removed from the water cell of the plate holder.

To make and record the real-time holograms, the following procedure is followed:

1. Turn on the laser at least 30 minutes prior to the experimental run.
2. Mount the impingement plate, the surface of which has been soaked with ethyl salicylate to equilibrium, to the heavy metal base.
3. Set the shutter speed to 1/15 second.
4. Switch on the safelight and switch off the regular light.
5. Take a full size Agfa-Gevaert 10E75 NAH photographic plate and place it to the

PC-45 plate carriage such that the emulsion side (the sticky side) of the plate faces the mass transfer surface when placed on the holder. Place the carriage with the plate back to the water cell in the plate holder. Allow about 15 minutes for the emulsion on the plate to pre-sensitize.

6. Activate the shutter with an exposure time of 1/15 s.
7. Remove the plate carriage with the exposed photographic plate from the water cell and process the plate. First, develop it under safelight in Kodak D-19 developer solution until the surface is about 30% dark by eye. This process takes about 1.5 minutes. Then, put the plate in Kodak indicator stop bath for about one minute. Finally, immerse the plate into Kodak rapid fixer solution for about 2 to 3 minutes. At this stage, the regular room light may be switched on to make the following steps easier to perform.
8. Replace the carriage and the plate back to the water cell of the plate holder.
9. Set the shutter to B position to allow the laser beam through continuously.
10. Set up the video camera recorder and connect it to the monitor. In order to obtain clear images, the settings of the video camera should be the following: iris = 3.4; shutter speed = 1/60 s; gain = 12 to 15.
11. Switch off the regular room light.
12. Adjust the precision X-Y controls on the plate holder to eliminate all the fringes superimposed on the mass transfer surface displayed on the monitor.
13. Open the valve of the compressed air cylinder and start recording the development of the fringes. The recording lasts about ten minutes, giving enough number of fringes for analysis.
14. Remove the aluminum impingement plate and re-immerse it in the swelling agent bath. The plate will be ready for another run in three hours.

Chapter 4
Validity of the Experimental Procedure

Mass transfer characteristics due to confined one and two laminar impinging slot jets can be studied by measuring the local Sherwood number along the centre line of the impingement plate surface. The local Sherwood number is defined as

$$Sh_b = \frac{kb}{D} \tag{4.1}$$

where k is the local mass transfer coefficient and D is the diffusion coefficient of the air-ethyl salicylate system. The local mass transfer coefficient k is defined in the following equation:

$$N = \frac{k(p_s - p_j)\rho^0 M_m}{P} \tag{4.2}$$

where N is the mass flux, ρ^0 is the molar density of the gas mixture, M_m is the molar mass of the swelling agent, p_s and p_j are the partial pressures of the swelling agent at the coating surface and the jet nozzle, respectively, and P is the total pressure. In this study, since the supply to the jet nozzle is pure air, $p_j = 0$. The partial pressure of the swelling agent at the coating surface, p_s, can be approximated by its equilibrium vapour pressure, P^0, during the "constant rate" period. Therefore, Equation 4.2

becomes

$$N = \frac{kP^0\rho^0 M_m}{P} \tag{4.3}$$

On the other hand, the mass flux can be measured and calculated from the following equation:

$$N = \frac{r'\rho_s}{t} \tag{4.4}$$

where r′ is the change of the coating thickness given by Equation 3.3, ρ_s is the density of the swollen polymer and t is the time period during which the change in the thickness has occurred. It is now appropriate to mention that in the above equation, the density used is equal to the partial density of the swelling agent in the swollen polymer. If the volume of the swollen polymer were the sum of the volume of the dry polymer and that of the pure swelling agent, the density of the pure swelling agent would be used in the above equation. However, it has been shown (Kapur and Macleod, 1976a) that the partial density of the swelling agent in the swollen polymer is equal to the density of the swollen polymer for small recessions within the "constant rate" period. Therefore, the product $r'\rho_s$ is the mass of swelling agent transferred per unit area. Substituting Equation 3.3 into Equation 4.4 gives,

$$N = \frac{nB\lambda\rho_s}{t} \tag{4.5}$$

From Equations 4.3 and 4.5, one obtains

$$k = \frac{B\lambda\rho_s P}{P^0\rho^0 M_m}\frac{n}{t} \tag{4.6}$$

Substitution of Equation 4.6 into Equation 4.1 results in

$$Sh_b = \frac{B\lambda\rho_s Pb}{DP^0\rho^0 M_m}\frac{n}{t} \tag{4.7}$$

where B can be evaluated from Equation 3.6 as 0.2615 and the various physical properties are provided in Appendix A. Equation 4.7 can be used to calculate the local Sherwood numbers when the physical properties, fringe order and the duration of the run are known. The FORTRAN code for computing the experimental Sherwood number is listed in Appendix C.

The experimental set-up used in this study is similar to that used by Law (1982). To calibrate and validate his experimental set-up, Law conducted two sets of experimental runs for both unconfined circular jets and unconfined slot jets. Comparing the results for circular jets with the theoretical results of Scholtz and Trass (1963), Law obtained a calibration constant, $A = B \lambda \rho_s$, which was about 3% smaller than the calculated value. He then used this experimental calibration constant to calculate the Sherwood numbers for the case of unconfined slot jets and compared the results with those of Masliyah and Nguyen (1979). Law's data were within ±9% of those of Masliyah and Nguyen. Consequently Law concluded that the calibration constant was confirmed.

In this study, the calibration process used by Law (1982) was not repeated. Since the calibration constant determined by Law is very close to the calculated value, the latter is employed in this study. To validate the current experimental set-up and extend Law's experimental studies for a single slot jet, a series of experimental runs for single slot jets was conducted. The comparisons of the current experimental results with those of Law are given in Figures 4.1 and 4.2 for Re = 400 and jet-to-plate spacings of 2b and 4b, respectively. From the comparison, the following points may be observed:

1. Only the current work provided Sherwood numbers for the stagnation point.
2. The agreement between the current results with those of Law is very good up to

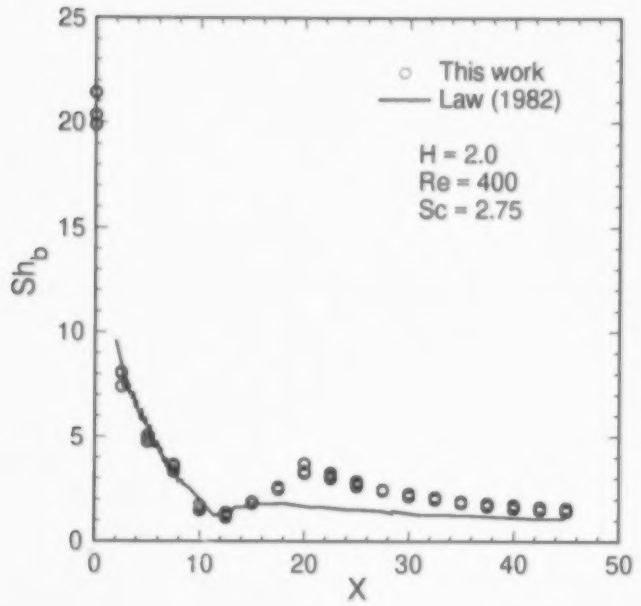

Figure 4.1 Comparison with Law's Experimental Data for a Single Slot Jet with Re = 400 and H = 2

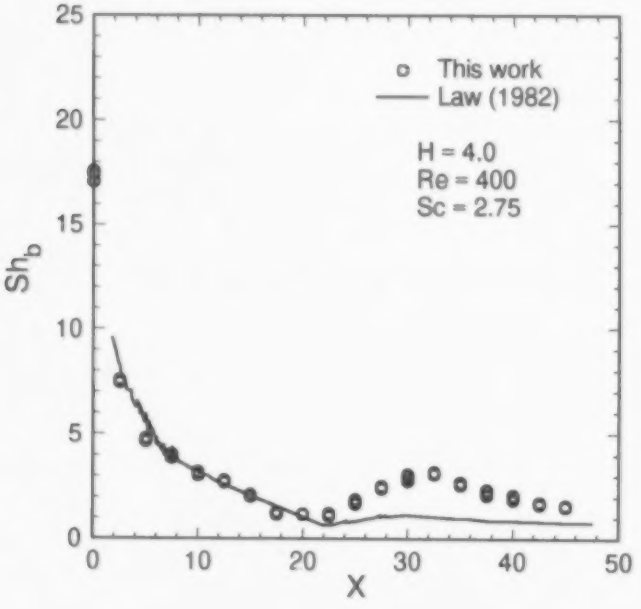

Figure 4.2 Comparison with Law's Experimental Data for a Single Slot Jet with Re = 400 and H = 4

the minimum point in the plot, indicating that the calibration constant used inthis work is valid.

3. There is some disagreement in the plots beyond the local minimum value of Sh_b. The disagreement could not have been caused by the experimental set-up since the two studies shared the same experimental set-up. The difference may be attributed to the difficulties of locating the fringe orders in the double-exposure holographic interferometry method employed by Law. The real-time holographic interferometry method employed in the current study gives the real surface recession rate at every point independent of any other point, eliminating the need to locate the so-called "zeroth order" fringe altogether. It should also be pointed out that the second peak after the minimum point can be seen very clearly by using the current real-time method.

Chapter 5

Numerical Study

A two-dimensional vorticity-stream function numerical model is used to simulate the experiments involving mass transfer due to one and two confined impinging laminar slot jets. Because of the limitation of the numerical model, no numerical simulation is conducted for the case of two slot jets with asymmetrical flow. Making use of the symmetrical nature of the cases for the single jet and two symmetrical jets, only half of the flow region is taken as the computational domain for both cases (see Figure 5.1). Air issues from a slot jet of width b with an average velocity of $\bar{v}_j$. The confinement plate is located parallel to and at a distance of h from the impingement plate. For the description of the flow and concentration fields, a two-dimensional rectangular coordinate system is used with the origin at the intersection of the axis of symmetry and the impingement plate (see Figure 5.1). The outflow region is chosen at a location sufficiently far away from the stagnation flow region to ensure that the velocity and the concentration profiles at this location are fully developed.

5.1 Governing Equations

In this study, since the relative change in density for the air, $\Delta\rho/\rho$, has a magnitude of 1×10^{-4} for the highest Reynolds number involved, the flow can be treated as an incompressible Newtonian flow (Schlichting, p9-10, 1979).

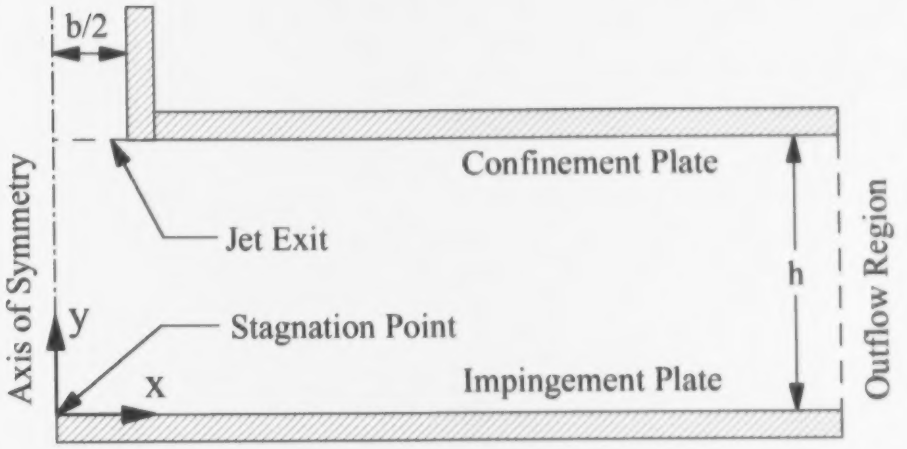

(a) One Slot Jet

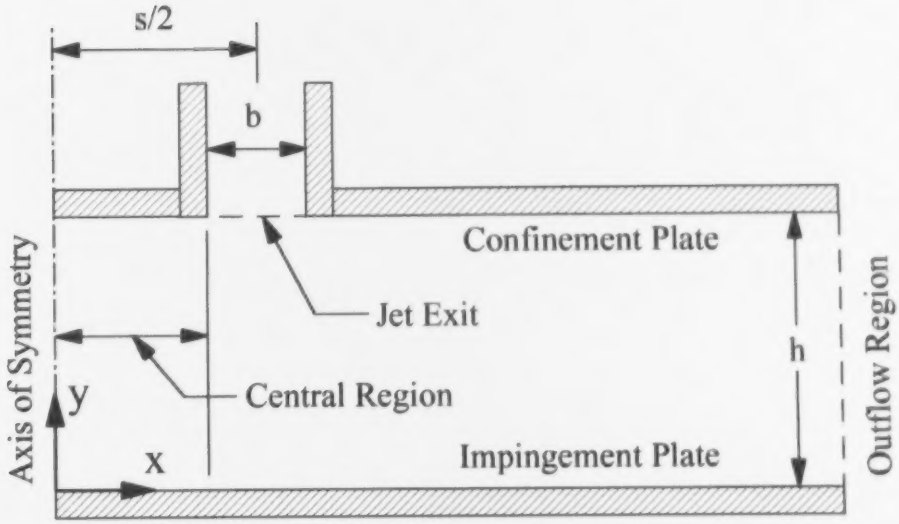

(b) Two Parallel Slot Jets

Figure 5.1 Computational Domain for the Impinging Jet Systems

The two-dimensional momentum and transport equations can be reduced to the corresponding vorticity-stream function form with the assumption of steady state, incompressible viscous Newtonian fluid flow with constant physical properties. The governing equations are (Bird et al., p554-559, 1960; Law, p84, 1982):

$$\frac{\partial(u\omega)}{\partial x} + \frac{\partial(v\omega)}{\partial y} = \nu\left(\frac{\partial^2\omega}{\partial x^2} + \frac{\partial^2\omega}{\partial y^2}\right) \tag{5.1}$$

$$\frac{\partial^2\psi}{\partial x^2} + \frac{\partial^2\psi}{\partial y^2} = \omega \tag{5.2}$$

$$\frac{\partial(uc)}{\partial x} + \frac{\partial(vc)}{\partial y} = D\left(\frac{\partial^2 c}{\partial x^2} + \frac{\partial^2 c}{\partial y^2}\right) \tag{5.3}$$

where ω is the vorticity defined by

$$\omega = \frac{\partial u}{\partial y} - \frac{\partial v}{\partial x} \tag{5.4}$$

ψ is the stream function defined by

$$\frac{\partial\psi}{\partial y} = u \quad and \quad \frac{\partial\psi}{\partial x} = -v \tag{5.5}$$

c is the molar concentration of the swelling agent, ν is the kinematic viscosity of the air and D is the diffusion coefficient of the air-ethyl salicylate system. When dimensionless variables are introduced as follows:

$$H = \frac{h}{b}$$

$$U = \frac{u}{\bar{v}_j}$$

$$
\begin{aligned}
V &= \frac{v}{\bar{v}_j} \\
X &= \frac{x}{b} \\
Y &= \frac{y}{b} \\
C &= \frac{c - c_j}{c_s - c_j} \\
\Omega &= \omega\left(\frac{b}{\bar{v}_j}\right) \\
\Psi &= \frac{\psi}{b\bar{v}_j} \\
Re_b &= \frac{b\bar{v}_j}{\nu} \\
Sc &= \frac{\nu}{D}
\end{aligned}
\tag{5.6}
$$

Equations 5.1-5.5 become:

$$\frac{\partial(U\Omega)}{\partial X} + \frac{\partial(V\Omega)}{\partial Y} = \frac{1}{Re_b}\left(\frac{\partial^2\Omega}{\partial X^2} + \frac{\partial^2\Omega}{\partial Y^2}\right) \tag{5.7}$$

$$\frac{\partial^2\Psi}{\partial X^2} + \frac{\partial^2\Psi}{\partial Y^2} = \Omega \tag{5.8}$$

$$\frac{\partial(UC)}{\partial X} + \frac{\partial(VC)}{\partial Y} = \frac{1}{Re_b Sc}\left(\frac{\partial^2 C}{\partial X^2} + \frac{\partial^2 C}{\partial Y^2}\right) \tag{5.9}$$

$$\frac{\partial\Psi}{\partial Y} = U \quad \text{and} \quad \frac{\partial\Psi}{\partial X} = -V \tag{5.10}$$

The objective of the numerical study is to solve Equations 5.7-5.9 for Ω, Ψ and C.

5.2 Boundary Conditions

The boundary conditions for the single impinging slot jet are different from those for the two parallel impinging slot jets. Therefore, the following two subsections are designed to specify the boundary conditions for the two cases.

5.2.1 Boundary Conditions for Single Slot Jet

Since the governing equations are elliptic in nature, boundary conditions must be specified at all the boundaries. The boundary conditions for the single confined impinging laminar slot jet flow are specified in the following five regions: jet exit, confinement plate, impingement plate, axis of symmetry and outflow region.

Jet Exit

Since the slot jet is long enough to provide fully developed parabolic velocity profiles at the jet exit, the following velocity components are specified:

$$V = -1.5(1-4X^2) \quad and \quad U = 0 \tag{5.11}$$

By setting the reference value of the stream function at the centre of the jet exit as 0, the following boundary conditions for the stream function and vorticity may be obtained from Equations 5.8 and 5.10:

$$\Psi = 1.5X - 2X^3 \tag{5.12}$$

$$\Omega = -12X \tag{5.13}$$

The boundary condition for the concentration at the jet exit is

$$C = 0 \tag{5.14}$$

Confinement Plate

Since the confinement plate is impermeable, the value of the stream function is a

constant along the plate. By substituting X = 0.5 into Equation 5.12 one obtains:

$$\Psi = 0.5 \tag{5.15}$$

The boundary condition for the vorticity at the confinement plate is evaluated by using the no-slip boundary condition. From Equation 5.8, one obtains:

$$\Omega = \frac{\partial^2 \Psi}{\partial Y^2} \tag{5.16}$$

The boundary condition for the concentration is

$$\frac{\partial C}{\partial Y} = 0 \tag{5.17}$$

due to the impermeability of the plate.

Impingement Plate

As mentioned before, the value of the stream function at the centre of the jet exit has been taken as zero. It follows that the values of stream function along the axis of symmetry and the impingement plate are both 0, i.e.,

$$\Psi = 0 \tag{5.18}$$

The boundary condition for the vorticity at the impingement plate is similar to that at the confinement plate, giving

$$\Omega = \frac{\partial^2 \Psi}{\partial Y^2} \tag{5.19}$$

The boundary condition for the concentration is given by

$$C = 1 \tag{5.20}$$

Axis of Symmetry

The stream function along this line has been set to be a constant of zero. From the symmetrical nature of this line, all the boundary conditions along this line can be determined as follows:

$$\Psi = 0 \tag{5.21}$$

$$\Omega = 0 \tag{5.22}$$

$$\frac{\partial C}{\partial X} = 0 \tag{5.23}$$

Outflow Region

When the outflow boundary is located far away from the slot jet, the following boundary conditions may be specified on this boundary (Roache, p155, 1982):

$$\frac{\partial \Omega}{\partial X} = 0 \tag{5.24}$$

$$\frac{\partial^2 \Psi}{\partial X^2} = 0 \tag{5.25}$$

$$\frac{\partial^2 C}{\partial X^2} = 0 \tag{5.26}$$

5.2.2 Boundary Conditions for Two Symmetrical Slot Jets

From Figure 5.1 (b), it can be seen that there are six regions where boundary conditions need to be specified for the two symmetrical slot jets system: axis of symmetry, central region of the confinement plate, jet exit, outer region of the confinement plate, outflow region, and impingement plate. With the stream function value being set to be zero along the axis of symmetry and the impingement plate, the

boundary conditions for various regions can be determined as follows, following similar arguments as in the case of a single slot jet.

Axis of Symmetry

Along this line, the boundary conditions are as follow:

$$\Psi = 0 \tag{5.27}$$

$$\Omega = 0 \tag{5.28}$$

$$\frac{\partial C}{\partial X} = 0 \tag{5.29}$$

Central Region of the Confinement Plate

For this region, because of the impermeability of the confinement plate, the following boundary conditions are specified:

$$\Psi = 0 \tag{5.30}$$

$$\Omega = \frac{\partial^2 \Psi}{\partial Y^2} \tag{5.31}$$

$$\frac{\partial C}{\partial Y} = 0 \tag{5.32}$$

Jet Exit

The parabolic velocity profile at the jet exit can be expressed as:

$$U = 0 \tag{5.33}$$

$$V = -1.5\left[1-4\left(X-\frac{S}{2}\right)^2\right] \tag{5.34}$$

where S is the nondimensional jet-to-jet distance defined by s/b. Substituting Equation 5.34 into Equation 5.10 and integrating, one obtains:

$$\Psi = 1.5\left(X-\frac{S}{2}\right) - 2\left(X-\frac{S}{2}\right)^3 + \frac{1}{2} \tag{5.35}$$

where $S/2 - 0.5 \leq X \leq S/2 + 0.5$. It follows that the vorticity can be expressed as

$$\Omega = -12\left(X-\frac{S}{2}\right) \tag{5.36}$$

The boundary condition for the concentration at the jet exit is

$$C = 0 \tag{5.37}$$

Outer Region of the Confinement Plate

This region is located on the confinement plate outside the slot jet. The stream function at this boundary is constant. When substituting $X = S/2 + 0.5$ into Equation 5.34 one obtains:

$$\Psi = 1 \tag{5.38}$$

The boundary conditions for vorticity and concentration may be specified as

$$\Omega = \frac{\partial^2 \Psi}{\partial Y^2} \tag{5.39}$$

$$\frac{\partial C}{\partial Y} = 0 \tag{5.40}$$

Outflow Region

Similar to the case of single slot jet, the boundary conditions for this region can be specified as:

$$\frac{\partial \Omega}{\partial X} = 0 \tag{5.41}$$

$$\frac{\partial^2 \Psi}{\partial X^2} = 0 \tag{5.42}$$

$$\frac{\partial^2 C}{\partial X^2} = 0 \tag{5.43}$$

Impingement Plate

The boundary conditions on this plate are as follows:

$$\Psi = 0 \tag{5.44}$$

$$\Omega = \frac{\partial^2 \Psi}{\partial Y^2} \tag{5.45}$$

$$C = 1 \tag{5.46}$$

5.3 Numerical Formulation

The numerical technique used in this study is the control-volume formulation in conjunction with the power-law scheme to discretize the convection-diffusion terms in the generalized partial differential equation (Patankar, 1980).

5.3.1 Finite-Difference Equations

The governing differential equations are:

$$\frac{\partial(U\phi)}{\partial X} + \frac{\partial(V\phi)}{\partial Y} = G\left(\frac{\partial^2\phi}{\partial X^2} + \frac{\partial^2\phi}{\partial Y^2}\right) \tag{5.47}$$

$$\frac{\partial^2\Psi}{\partial X^2} + \frac{\partial^2\Psi}{\partial Y^2} = \Omega \tag{5.48}$$

where

$$\frac{\partial\Psi}{\partial Y} = U \quad and \quad \frac{\partial\Psi}{\partial X} = -V \tag{5.49}$$

Equation 5.47 is the generalized equation where ϕ represents vorticity, Ω, in the momentum equation and C in the concentration equation. The coefficient G for these two cases becomes $1/Re_b$ and $1/(Re_bSc)$, respectively.

The computational domain is represented by a rectangular grid network shown in Figure 5.2 (for the case of a single slot jet) with grid lines parallel to the X- and Y-coordinates. Grid lines in X- and Y-directions are designated by i and j, respectively.

Figure 5.3 shows a typical computational node and its control volume in the two-dimensional domain. The point of interest is designated as P, where the variables Ω, Ψ, and C are to be evaluated. The surrounding points are marked as E, W, N and S, denoting east, west, north and south of the central point, respectively. The faces of the control volume are located at the midway between the neighbouring grid points, corresponding to the so-called Practice A in Patankar (p68-71, 1980). Using the power-law scheme, the generalized differential equation, Equation 5.47, can be discretized as follows (p99-100, Patankar, 1980):

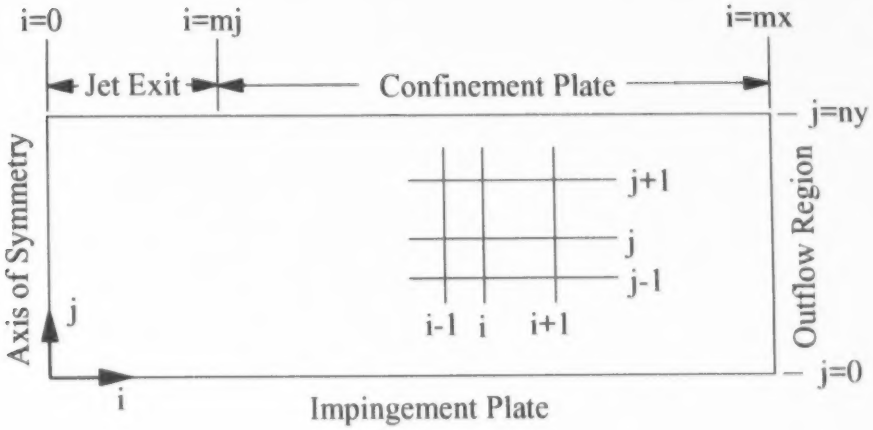

Figure 5.2 Grid Network for the Single Slot Jet System

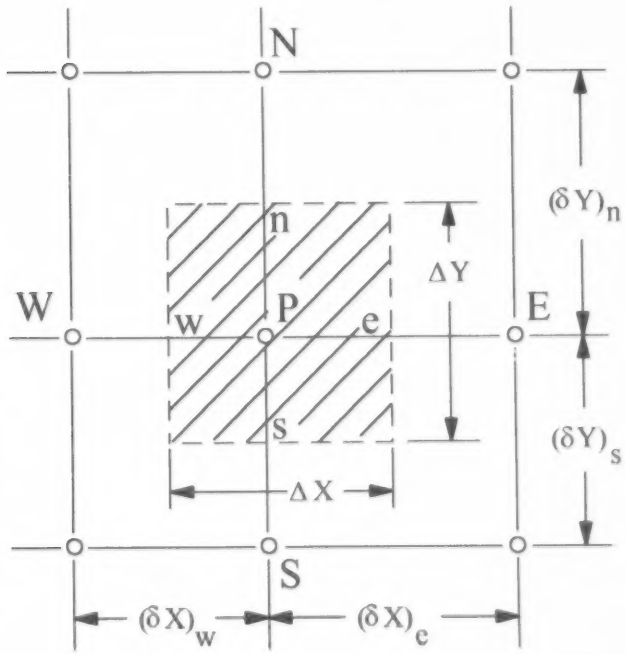

Figure 5.3 A Typical Node of Computation

$$a_P\phi_P = a_E\phi_E + a_W\phi_W + a_N\phi_N + a_S\phi_S \tag{5.50}$$

where

$$\begin{aligned} a_E &= D_e A(|P_e|) + [\![-F_e, 0]\!] \\ a_W &= D_w A(|P_w|) + [\![F_w, 0]\!] \\ a_N &= D_n A(|P_n|) + [\![-F_n, 0]\!] \\ a_S &= D_s A(|P_s|) + [\![F_s, 0]\!] \\ a_P &= a_E + a_W + a_N + a_S \end{aligned} \tag{5.51}$$

The F's are the mass flow rates defined as

$$\begin{aligned} F_e &= U_e \Delta Y \\ F_w &= U_w \Delta Y \\ F_n &= V_n \Delta X \\ F_s &= V_s \Delta X \end{aligned} \tag{5.52}$$

The D's are the conductances defined by

$$\begin{aligned} D_e &= \frac{G_e \Delta Y}{(\delta X)_e} \\ D_w &= \frac{G_w \Delta Y}{(\delta X)_w} \\ D_n &= \frac{G_n \Delta X}{(\delta Y)_n} \\ D_s &= \frac{G_s \Delta X}{(\delta Y)_s} \end{aligned} \tag{5.53}$$

The P's are the Peclet numbers defined by

$$P_e = \frac{F_e}{D_e} \qquad P_w = \frac{F_w}{D_w} \qquad P_n = \frac{F_n}{D_n} \qquad P_s = \frac{F_s}{D_s} \tag{5.54}$$

For the chosen power-law scheme, the function A(|P|) is given by

$$A(|P|) = [\![0, (1 - 0.1|P|)^5]\!] \tag{5.55}$$

The special operator, [ ], stands for the largest of the arguments within it.

It should be noted that in Equation 5.52, the U's and V's are evaluated at the faces of the control volume. To obtain the finite-difference expressions for Equations 5.48 and 5.49, it is more convenient to denote the grid nodes by the i-j notation. In doing so, nodes P, E, W, N, S become (i,j), (i+1,j), (i-1,j), (i,j+1), and (i,j-1), respectively. In the mean time, $(\delta X)_e$, $(\delta X)_w$, $(\delta Y)_n$, $(\delta Y)_s$ in Figure 5.3 are denoted as δX_i, δX_{i-1}, δY_j, δY_{j-1}, respectively. Therefore, from Equation 5.49, the U's and V's at the interfaces as used in Equation 5.52 can be derived to give:

$$U_e = \frac{1}{2}\left(\frac{\Psi_{i+1,j+1} - \Psi_{i+1,j-1}}{\delta Y_j + \delta Y_{j-1}} + \frac{\Psi_{i,j+1} - \Psi_{i,j-1}}{\delta Y_j + \delta Y_{j-1}} \right) \tag{5.56}$$

which can be reduced to

$$U_e = \frac{\Psi_{i,j+1} - \Psi_{i,j-1} + \Psi_{i+1,j+1} - \Psi_{i+1,j-1}}{4\Delta Y} \tag{5.57}$$

when $\Delta Y = (\delta Y_j + \delta Y_{j-1}) / 2$ is introduced. Similarly, the other velocity components can be obtained as:

$$U_w = \frac{\Psi_{i-1,j+1} - \Psi_{i-1,j-1} + \Psi_{i,j+1} - \Psi_{i,j-1}}{4\Delta Y} \tag{5.58}$$

$$V_n = -\frac{\Psi_{i+1,j+1} - \Psi_{i-1,j+1} + \Psi_{i+1,j} - \Psi_{i-1,j}}{4\Delta X} \tag{5.59}$$

$$V_s = -\frac{\Psi_{i+1,j} - \Psi_{i-1,j} + \Psi_{i+1,j-1} - \Psi_{i-1,j-1}}{4\Delta X} \tag{5.60}$$

The discretization of Equation 5.48 can now be carried out as follows. Taking the Taylor expansion at (i,j) leads to

$$\Psi_{i+1,j} = \Psi_{i,j} + \left(\frac{\partial \Psi}{\partial X}\right)_{i,j} \delta X_i + \frac{1}{2}\left(\frac{\partial^2 \Psi}{\partial X^2}\right)_{i,j} \delta X_i^2 + O[(\delta X_i)^3]$$
$$\Psi_{i-1,j} = \Psi_{i,j} - \left(\frac{\partial \Psi}{\partial X}\right)_{i,j} \delta X_{i-1} + \frac{1}{2}\left(\frac{\partial^2 \Psi}{\partial X^2}\right)_{i,j} \delta X_{i-1}^2 + O[(\delta X_{i-1})^3] \quad (5.61)$$

Solving for $(\partial^2\Psi/\partial X^2)_{i,j}$, one obtains

$$\left(\frac{\partial^2 \Psi}{\partial X^2}\right)_{i,j} = 2\frac{\delta X_i(\Psi_{i-1,j} - \Psi_{i,j}) + \delta X_{i-1}(\Psi_{i+1,j} - \Psi_{i,j})}{\delta X_i \delta X_{i-1}(\delta X_i + \delta X_{i-1})} \quad (5.62)$$

Similarly,

$$\left(\frac{\partial^2 \Psi}{\partial Y^2}\right)_{i,j} = 2\frac{\delta Y_j(\Psi_{i,j-1} - \Psi_{i,j}) + \delta Y_{j-1}(\Psi_{i,j+1} - \Psi_{i,j})}{\delta Y_j \delta Y_{j-1}(\delta Y_j + \delta Y_{j-1})} \quad (5.63)$$

Substitution of Equations 5.61 and 5.62 into Equation 5.48 gives

$$2\frac{\delta X_i(\Psi_{i-1,j} - \Psi_{i,j}) + \delta X_{i-1}(\Psi_{i+1,j} - \Psi_{i,j})}{\delta X_i \delta X_{i-1}(\delta X_i + \delta X_{i-1})} + 2\frac{\delta Y_j(\Psi_{i,j-1} - \Psi_{i,j}) + \delta Y_{j-1}(\Psi_{i,j+1} - \Psi_{i,j})}{\delta Y_j \delta Y_{j-1}(\delta Y_j + \delta Y_{j-1})} = \Omega_{i,j} \quad (5.64)$$

Rearrangement of the above equation results in

$$b_{i,j}\Psi_{i,j} = b_{i-1,j}\Psi_{i-1,j} + b_{i+1,j}\Psi_{i+1,j} + b_{i,j-1}\Psi_{i,j-1} + b_{i,j+1}\Psi_{i,j+1} - \Omega_{i,j} \quad (5.65)$$

where

$$b_{i,j} = 2\left(\frac{1}{\delta X_i \delta X_{i-1}} + \frac{1}{\delta Y_j \delta Y_{j-1}}\right)$$
$$b_{i-1,j} = \frac{2}{\delta X_{i-1}(\delta X_i + \delta X_{i-1})} \quad (5.66)$$
$$b_{i+1,j} = \frac{2}{\delta X_i(\delta X_i + \delta X_{i-1})}$$

$$b_{i,j-1} = \frac{2}{\delta Y_{j-1}(\delta Y_j + \delta Y_{j-1})}$$

$$b_{i,j+1} = \frac{2}{\delta Y_j(\delta Y_j + \delta Y_{j-1})}$$

The distribution of vorticity, stream function and concentration inside the region of interest can now be obtained by solving Equations 5.50 and 5.65 using an iterative method.

5.3.2 Boundary Conditions

The finite-difference expression of the boundary conditions for single and two slot jets systems are discussed separately for each region.

5.3.2.1 Single Slot Jet Systems

Jet Exit

This boundary, defined as $0 \leq i \leq mj$ and $j = ny$ in the computational domain, has the following discretized boundary conditions:

$$\Psi_{i,ny} = 1.5X_i - 2X_i^3 \tag{5.67}$$

$$\Omega_{i,ny} = -12X_i \tag{5.68}$$

$$C_{i,ny} = 0 \tag{5.69}$$

Confinement Plate

This boundary, defined as $mj < i \leq mx$ and $j = ny$, has the following constant stream function:

$$\Psi_{i,ny} = 0.5 \tag{5.70}$$

The boundary condition for the vorticity at the confinement plate, Equation 5.16, is approximated by the following finite-difference expression derived from a Taylor series expansion with a truncation error of $O(\delta Y)^2$:

$$\Omega_{i,ny} = 2\,\frac{(\Psi_{i,ny-1}-\Psi_{i,ny})(\delta Y_{ny-1}+\delta Y_{ny-2})^3 - (\Psi_{i,ny-2}-\Psi_{i,ny})\delta Y_{ny-1}^3}{\delta Y_{ny-1}^2\,\delta Y_{ny-2}(\delta Y_{ny-1}+\delta Y_{ny-2})^2} \qquad (5.71)$$

The boundary condition for the concentration at the confinement plate, Equation 5.17, is approximated by a finite-difference expression with a truncation error of $O(\delta Y)^2$, giving

$$C_{i,ny} = \frac{C_{i,ny-1}(\delta Y_{ny-1}+\delta Y_{ny-2})^2 - C_{i,ny-2}\delta Y_{ny-1}^2}{(\delta Y_{ny-1}+\delta Y_{ny-2})^2 - \delta Y_{ny-1}^2} \qquad (5.72)$$

Impingement Plate

This boundary is defined as $0 \le i \le mx$ and $j = 0$. The boundary condition for the stream function, Equation 5.18, now becomes

$$\Psi_{i,0} = 0 \qquad (5.73)$$

The boundary condition for the vorticity is similar to that at the confinement plate and it is given by

$$\Omega_{i,0} = 2\,\frac{(\Psi_{i,1}-\Psi_{i,0})(\delta Y_0+\delta Y_1)^3 - (\Psi_{i,2}-\Psi_{i,0})\delta Y_0^3}{\delta Y_0^2\,\delta Y_1(\delta Y_0+\delta Y_1)^2} \qquad (5.74)$$

The boundary condition for the concentration is

$$C_{i,0} = 1 \tag{5.75}$$

Axis of Symmetry

This boundary is defined as i = 0 and 0 < j < ny. The boundary conditions for the stream function and vorticity are given by

$$\Psi_{0,j} = 0 \tag{5.76}$$

$$\Omega_{0,j} = 0 \tag{5.77}$$

To implement the boundary condition of the concentration on the axis of symmetry, Equation 5.23, a boundary control volume surrounding a boundary node (0,j) is introduced. Because of the symmetry, the various quantities of this control volume outside the boundary line are identified as follows (refer to Figure 5.3):

$$\begin{aligned} \delta X_{-1} &= \delta X_0 \\ \Psi_{-1,j} &= -\Psi_{1,j} \\ (U_e)_{-1,j} &= (U_w)_{0,j} = -(U_e)_{0,j} \\ C_{-1,j} &= C_{1,j} \end{aligned} \tag{5.78}$$

where U_e and U_w are the velocity components in the X-direction located at the east and west interface of the control volume, respectively. It should be noted that the computation needs to start from i = 0 only for the concentration variable, since both the stream function and vorticity values are known at the axis of symmetry.

Outflow Region

This boundary is defined as i = mx and $1 \le j \le ny-1$. According to Roache (p154-161, 1980), the outflow boundary conditions for stream function and vorticity, Equations 5.24 and 5.25, can be implemented as

$$\Omega_{mx,j} = \Omega_{mx-1,j} \tag{5.79}$$

$$\Psi_{mx,j} = 2\Psi_{mx-1,j} - \Psi_{mx-2,j} \tag{5.80}$$

The boundary condition of the concentration, Equation 5.26, can be obtained following a similar way as in the case of stream function,

$$C_{mx,j} = 2C_{mx-1,j} - C_{mx-2,j} \tag{5.81}$$

It is appropriate to mention that for this outflow boundary, when the local Peclet number in the X-direction as defined in Equation 5.54 is sufficiently large, the X-coordinate becomes one-way and the outflow boundary values of the variables do not have influence on the computation of the variables at the interior nodes (Patankar, p102-105, 1980). Therefore, it is not too critical as to how the outflow boundary conditions are specified for sufficiently large Reynolds numbers.

5.3.2.2 Two Slot Jets Systems

Since the boundary conditions for the two slot jets systems are vary similar to those of the single slot jet system, only the differences are mentioned below.

Confinement Plate

There are two separate regions, inside and outside the jets. The implementation of the boundary conditions for vorticity and concentration is the same as in the case of single slot jet system, the only difference is with the constant value of the stream function which is 0 in the central region and 1 in the outer region.

Jet Exit

Comparing to the single jet case, the position of the jet is moved to the right a distance of S/2. Furthermore, a whole jet instead of half has to be dealt with. Therefore, the boundary conditions, Equations 5.35-5.37, for the jet exit are

implemented in the region of S/2 - 0.5 ≤ X ≤ S/2 + 0.5 at Y = H:

$$\Psi_{i,ny} = 1.5\left(X_i - \frac{S}{2}\right) - 2\left(X_i - \frac{S}{2}\right)^3 + \frac{1}{2} \tag{5.82}$$

$$\Omega_{i,ny} = -12\left(X_i - \frac{S}{2}\right) \tag{5.83}$$

$$C_{i,ny} = 0 \tag{5.84}$$

5.4 Computational Procedure

This section covers the following topics: grid design, convergence criterion, solution of the discretization equations, presentation of the computed results.

5.4.1 Grid Design

A non-uniform grid is used in the numerical computations. The grid size and its arrangement are very important factors to affect both the accuracy of the solution and the convergence characteristics. Because of relatively large gradients of velocity and concentration along the impingement plate, the grid lines parallel and adjacent to this plate must be very closely spaced. Similarly, the vertical grid lines covering the area underneath the jet are also closely spaced to accommodate large velocity gradients.

Grid Design in the X-Direction

There are three aspects to consider when designing the computational grid in the X-direction: the number of total grid points, the non-dimensional length to be covered and the distribution of the grid lines. The case of single slot jet flow is employed to test the various factors. To examine the influence of the total number of grid points in the X-direction, three different numbers of grid points, mx = 200, 250 and 300, are tested for computing the skin friction factor at the impingement plate (to be discussed in section 5.4.4), and the results are presented in Figure 5.4. It can be concluded that

for the cases tested, the effect of the total number of grid points in the X-direction on the numerical results is negligible. Therefore, the number of grid points in the X-direction is chosen as 200 for all the three jet-to-plate spacings. The dimensionless length covered by these grid lines is chosen such that no reversed flow should occur on the outflow region for all the cases to be computed. It was found that the length of 195.6 used for the case of mx = 200 meets this criterion. The grid lines are spaced such that the finest grid spacing is located on the area underneath the jet. For the half-jet width, 10 uniform grid points are used. The grid spacing is then increased in the format of a step function with a step ratio of 2. For the region between X = 10 and 20, a finer grid is used again in order to accommodate the changes of the flow field due to the local vertices. Similar arguments also apply to the case of the two slot jet flow systems and 250 grid points are used in the X-direction for all the three different jet-to-plate spacings studied. The detailed grid arrangements in X-direction for the single and two slot jets systems are presented schematically in Figure 5.5 (not proportional to the real scale).

Grid Design in the Y-Direction

Since finer grid spacings must be employed adjacent to the impingement plate, the following coordinate stretching method is used to specify the grid locations in Y-direction (Law, p119, 1982):

$$Y_j = \frac{\exp\left(b_1 H \frac{j}{ny}\right) - 1}{\exp(b_1 H) - 1} H \tag{5.85}$$

where b_1 is the stretching factor used to adjust the degree of stretching and ny is the total number of grid points in the Y-direction. Therefore, to design the grid in the Y-direction, two numbers need to be chosen: ny and b_1. Ideally, the number of total grid points in the Y-direction should be proportional to the jet-to-plate spacing, H. However, this may not be possible due to limitations in the computing resources or divergence. To examine the influence of the number of grid points in the Y-direction,

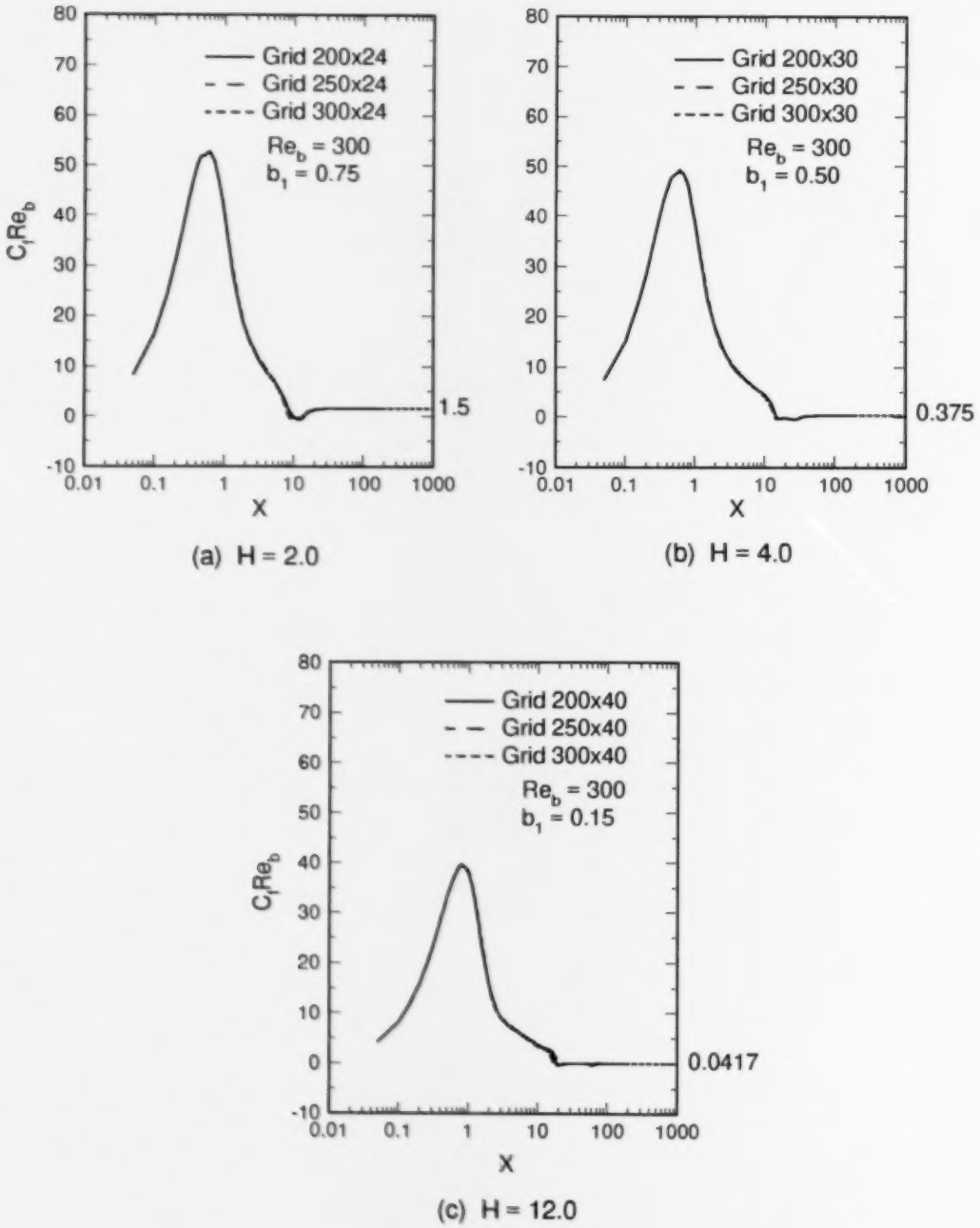

Figure 5.4 Effect of Number of Grid Points in X-Direction

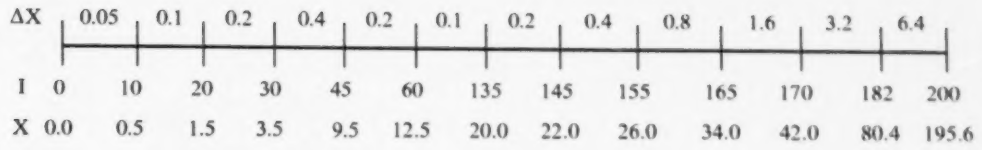

(a) X-Grid Distribution for a Single Slot Jet

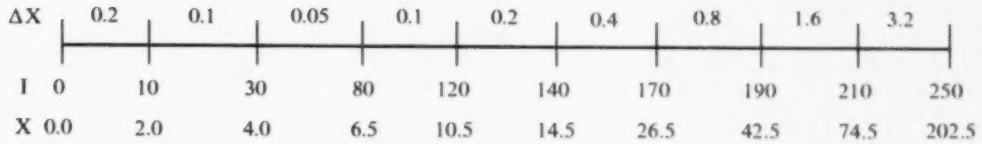

(b) X-Grid Distribution for Two Slot Jets With S = 10

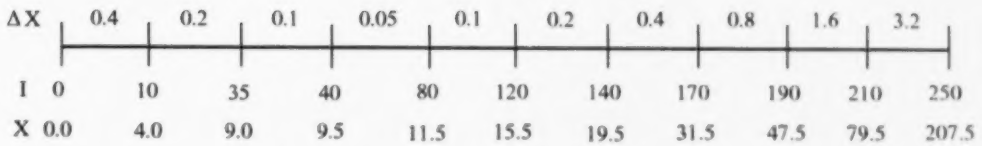

(c) X-Grid Distribution for Two Slot Jets With S = 20

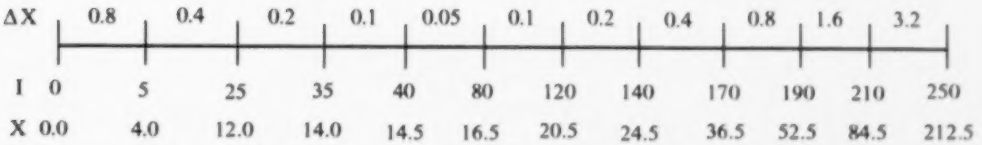

(d) X-Grid Distribution for Two Slot Jets With S = 30

Figure 5.5 X-Grid Distribution for One and Two Slot Jets

three different numbers of grid points, ny = 24, 30 and 40, are tested for all three jet-to-plate spacings with Re_b = 300 and the results are presented in Figure 5.6. For H = 2, it can be seen that when ny is increased from 24 to 40, no sensible change in the computed skin-friction factor has occurred. For the case of H = 4, more changes are observed on the area of the peak value, with the cases of ny = 30 and 40 giving very close results. When H = 12, it can be seen clearly that the number of grid points in the Y-direction has significant influence on the numerical solution. Similar results were also noticed by Law (1982). Therefore, out of a balance of accuracy and efficiency, the numbers of grid points in Y-direction for the case of a single slot jet are 24, 30 and 40 for H = 2, 4, and 12, respectively. For the case of two slot jets, the numbers of grid points in the Y-direction are 30, 40 and 50 for H = 2, 4 and 8, respectively.

The stretching factor, b_1, affects the grid distribution in the Y-direction such that the higher the value of b_1, the more unevenly distributed the grid will be. The influence of b_1 on the numerical solution is systematically examined and the results are presented in Figure 5.7. It can be seen from the plots that for all three jet-to-plate spacings, the effect of the stretching factor is mainly on a very small region nearby the peak value, with a maximum error about 10% for the cases tested. The stretching factors chosen for the case of a single slot jet are 0.75, 0.50 and 0.15 for H = 2, 4 and 12, respectively. For the case of two slot jets, the stretching factors used are 0.50, 0.25 and 0.15 for H = 2, 4 and 8, respectively.

The grid designs for both the single slot jet and the two slot jet systems are summarized in Tables 5.1 and 5.2, respectively.

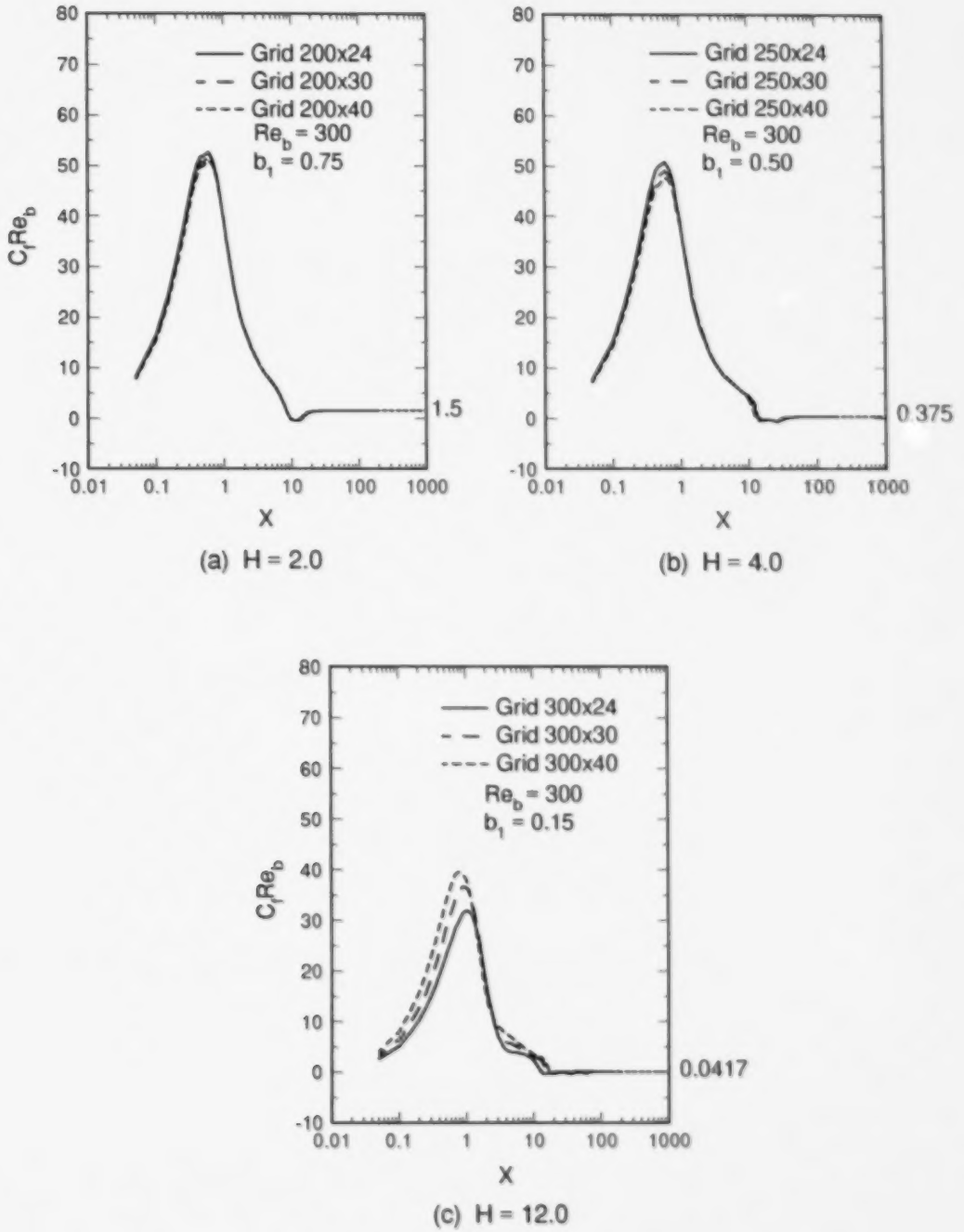

Figure 5.6 Effect of Number of Grid Points in Y-Direction: Single Slot Jet

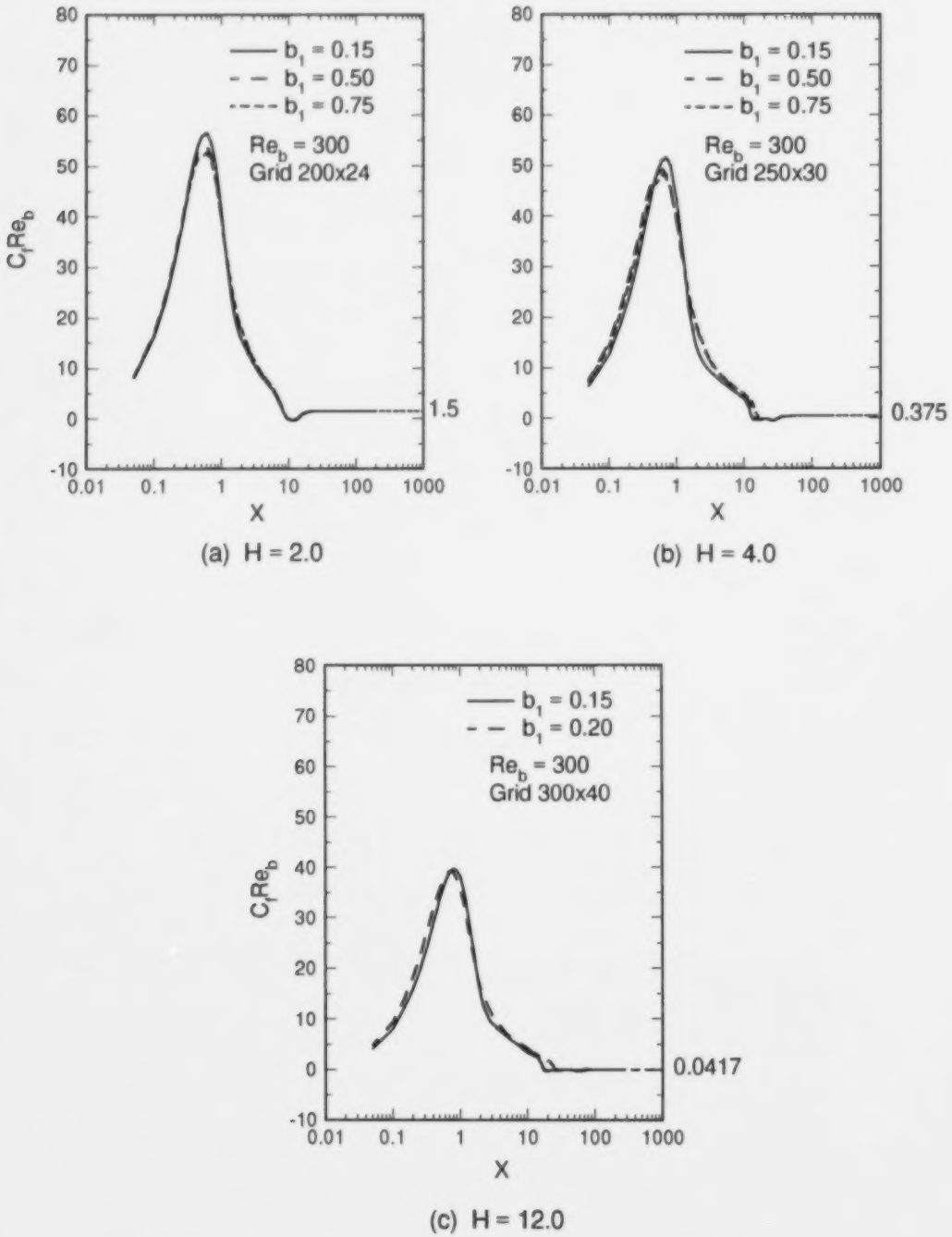

Figure 5.7 Effect of Stretching Factor in Y-Coordinate: Single Slot Jet

Table 5.1 Grid Design for Single Slot Jet Systems

H	L_x	mx	ny	b_1
2	195.6	200	24	0.75
4	195.6	200	30	0.50
12	195.6	200	40	0.15

Table 5.2 Grid Design for Two Slot Jets Systems

H	S	L_x	mx	ny	b_1
2	10	202.5	250	30	0.50
4	10	202.5	250	40	0.25
4	20	207.5	250	40	0.25
4	30	212.5	250	40	0.25
8	10	202.5	250	50	0.15

5.4.2 Convergence Criterion

In principle, an iterative process is considered as converged when further iterations will not produce any change in the values of the dependent variables. In practice, the iterative process is terminated when some arbitrary convergence criterion is satisfied. Often the relative change in the grid-point values of all the dependent variables is used to formulate the convergence criterion. However, when heavy under-relaxation is used, the change in the dependent variables between successive iterations is intentionally slowed down; this may create an illusion of convergence although the computed solution may be far from being converged (Patankar, p142, 1980). Therefore, a more reliable method of monitoring the convergence is to examine how perfectly the discretization equations are satisfied by the current values of the dependent variables. In the general discretization equation, Equation 5.50, for each grid point, a residual R can be calculated from

$$R = a_E\phi_E + a_W\phi_W + a_N\phi_N + a_S\phi_S - a_P\phi_P \tag{5.86}$$

It is seen that when the discretization equation is satisfied, R will be zero. To ensure an overall convergence for the whole computational domain, the following convergence criterion is used:

$$\sqrt{\frac{\Sigma(R_{i,j})^2}{n_{xy}}} \leq R_{tol} \tag{5.87}$$

where $R_{i,j}$ is the residual at point (i,j) which covers all the grid points where the variable of interest is unknown, n_{xy} is the corresponding total number of grid points for the summation and R_{tol} is an arbitrary tolerance. A similar criterion can also be obtained for the discretization equation for stream function, Equation 5.65. In this study, the residual tolerance is set to 10^{-5} for the stream function and vorticity and 10^{-8} for concentration.

5.4.3 Solution of the Discretization Equations

Of the discretized governing equations, Equations 5.50 and 5.65, the equations for the stream function and vorticity are coupled and highly non-linear. The concentration equation is linear and not coupled with any of the other equations. Therefore, it is appropriate to solve the stream function and vorticity equations simultaneously first with iterative methods. These processes need much computing effort since both the coefficients and the variables need to be updated with iteration. When the stream function and vorticity are known, the velocity field can then be evaluated and the coefficients for the discretized concentration equation become constant. It is much easier to solve for the concentration since only one variable needs to be updated. To solve the discretized stream function and vorticity equations, the following procedure is followed:

1. For a lower Reynolds number, make an initial guess for both the stream function and vorticity. This step is needed only once for one grid system, since converged

results can always be served as initial guesses for computations with higher Reynolds numbers.

2. Evaluate the velocity fields from Equations 5.57 and 5.59.
3. Compute the a's from Equations 5.51-5.55.
4. Solve Equation 5.50 for the vorticity by the tridiagonal matrix algorism (TDMA).
5. Apply under-relaxation to update the vorticity in the following manner:

$$\Omega_n = \Omega_o + \alpha_\Omega(\Omega' - \Omega_o) \tag{5.88}$$

where Ω_n and Ω_o denote the new and old values of vorticity, respectively, and Ω' is the vorticity value computed from the TDMA. α_Ω is the under-relaxation factor for the vorticity, ranging from 0.1 to 0.3.

6. Solve for the stream function from Equation 5.65 by the successive over relaxation (SOR) method. The over-relaxation factor takes a value between 1.0 and 1.7.
7. Update the boundary conditions for the vorticity at the confinement plate and impingement plate from Equations 5.71 and 5.74. An under-relaxation method similar to that used in the case of vorticity is applied to these boundary conditions, the relaxation factor being around 0.5.
8. Check if the convergence criteria for both stream function and vorticity are met. If so, terminate the iteration procedure and print out the converged results for both the stream function and vorticity. If not, repeat steps 2 to 8 until convergence is reached or a preset maximum number of iterations is reached.

To solve for the concentration field after the stream function and vorticity field have been obtained, the following steps are taken:

1. Read in the converged stream function and vorticity fields.
2. Compute the velocity field from Equations 5.57 and 5.59.
3. Compute the a's of Equation 5.50 from Equations 5.51-5.55.
4. Solve Equation 5.50 for the concentration by TDMA.
5. Apply under-relaxation to update the concentration field, with the under-

relaxation factor being about 0.7.

6. Check if the convergence criterion is met. If so, go to the next step to compute the skin friction factors and the Sherwood numbers as described below. If not, repeat steps 2 to 6 until the convergence criterion is met or a preset maximum number of iterations is met.

All the computations in this study were conducted on IBM RISC/6000 375 work stations with 64 MB RAM.

5.4.4 Presentation of the Computed Results

To examine the impact of the flow on the impingement plate, it is often desirable to evaluate the local skin friction factors along the impingement plate. The local skin friction factor, C_f, is defined as

$$C_f = \frac{\tau_s}{0.5\rho\bar{v}_j^2} \tag{5.89}$$

where ρ is the density of air and τ_s is the shear stress exerted on the impingement plate by the fluid defined by:

$$\tau_s = \mu\left(\frac{\partial u}{\partial y} + \frac{\partial v}{\partial x}\right)\Bigg|_{y=0} \tag{5.90}$$

Since the impingement plate is impermeable, i.e., $v = 0$ and $\partial v/\partial x = 0$ at the impingement plate, the above equation reduces to

$$\tau_s = \mu\frac{\partial u}{\partial y}\Bigg|_{y=0} \tag{5.91}$$

Introducing the dimensionless variables of Equation 5.6 and combining Equations 5.89 and 5.91 yields

Combining the above equation with Equations 5.10 and 5.19, one obtains

$$C_f = \frac{2}{Re_b}\frac{\partial U}{\partial Y}\bigg|_{Y=0} \tag{5.92}$$

$$C_f = \frac{2}{Re_b}\Omega\bigg|_{Y=0} \tag{5.93}$$

or

$$C_f Re_b = 2\Omega\,|_{Y=0} \tag{5.94}$$

along the impingement plate.

It is constructive to note that if both the impingement and confinement plates are infinitively long, one obtains

$$u_{fd} = 6\bar{u}_{fd}\left(\frac{y}{h} - \frac{y^2}{h^2}\right) \tag{5.95}$$

where u_{fd} and $\bar{u}_{fd}$ are the fully developed local and average velocity, respectively, parallel to the impingement plate. Therefore, one obtains

$$\tau_{fd} = \frac{6\mu\bar{u}_{fd}}{h} \tag{5.96}$$

along the impingement plate. For the case of single jet systems, mass balance between the jet exit and the channel exit results in

$$\bar{u}_{fd} = \frac{1}{2}\frac{b}{h}\bar{v}_j \tag{5.97}$$

With some simple manipulations, one obtains

$$C_{f_{fd}} = \frac{6}{Re_b}\frac{1}{H^2} \tag{5.98}$$

or

$$C_{f_{fd}} Re_b = \frac{6}{H^2} \tag{5.99}$$

Therefore, for the case of a single slot jet system, if the computational domain is long enough to resemble the fully developed parallel flow, the numerically computed local skin friction factor given by Equation 5.93 should approach that of the theoretical, fully developed parallel flow given by Equation 5.98. For the case of the two parallel jets system, a similar derivation gives

$$C_{f_{fd}} Re_b = \frac{12}{H^2} \tag{5.100}$$

Equations 5.98 and 5.100 can be used to check the validity of the computer programs for the single and two parallel slot jets systems, respectively.

After the concentration distribution is obtained, the local Sherwood numbers along the impingement plate can be obtained as follows.

The definition of local mass transfer coefficient, k, in Equation 4.2 can also be written in terms of the molar concentration of the swelling agent,

$$N = k(c_s - c_j)Mw \tag{5.101}$$

According to Fick's law, the mass transfer of swelling agent from the impingement plate is given by

$$N = -DMw\left(\frac{\partial c}{\partial y}\right)\Big|_{y=0} \tag{5.102}$$

Combining the above two equations with Equation 4.1 and introducing the nondimensional variables of Equation 5.6 yields

$$Sh_b = -\left(\frac{\partial C}{\partial Y}\right)\Big|_{Y=0} \tag{5.103}$$

Therefore, the local Sherwood numbers along the impingement plate can be evaluated from the gradient of concentration at the impingement plate.

5.5 Validation of the Numerical Solution

To ensure that the computer programs developed in this study are free of errors, a comparison between the results computed by the current computer programs and those presented by Law (1982) using different numerical schemes was conducted.

It is known that the design of grid network influences the numerical solution (Law, p134, 1982). For the sake of comparison, the same grid network as used by Law (1982) has been adopted and the local skin friction factors and Sherwood numbers along the impingement plate have been computed. The results for H = 2, Re_b = 100 and a grid network of 54×24 are compared with those presented by Law in Figures 5.8 and 5.9. Excellent agreement has been observed for both the local skin friction factors and the Sherwood numbers along the impingement plate. In the case of local skin friction factors, both the current results and those of Law agree well with the theoretical values for the outflow region resembling the fully developed flow between two parallel plates. Therefore, the current computer programs are free of errors.

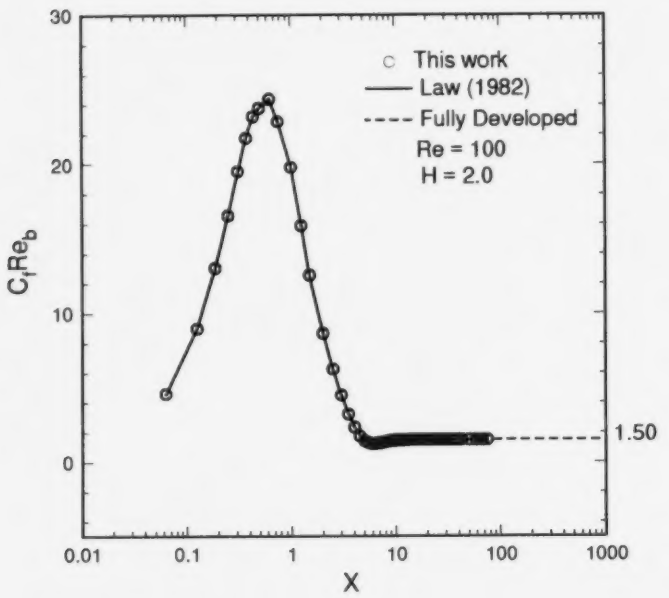

Figure 5.8 Comparison of Local Skin Friction Factors

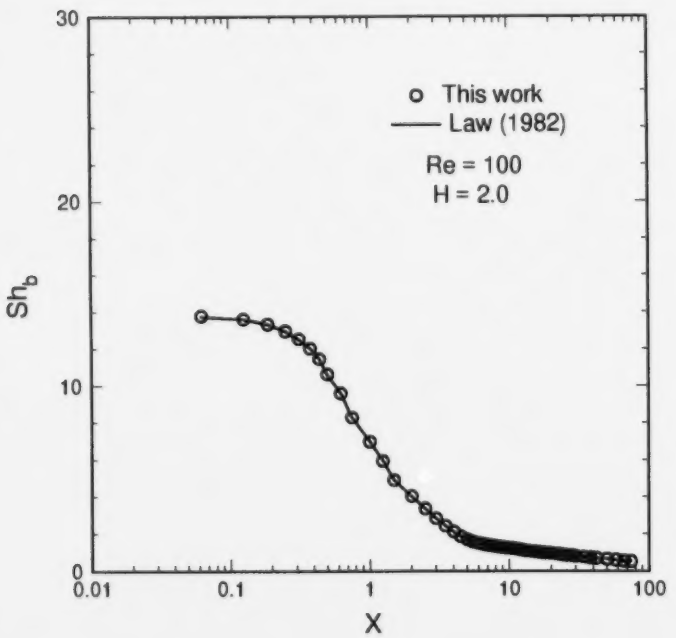

Figure 5.9 Comparison of Local Sherwood Numbers

Chapter 6
Mass Transfer Due to One Confined Impinging Laminar Slot Jet

As the first part of this work, the flow and mass transfer characteristics of a single confined impinging laminar slot jet have been studied. The flow characteristics are examined only numerically in this study, while the mass transfer characteristics are studied both numerically and experimentally. For the numerical work, compared with the previous work of Law (1982), the current work employed a different numerical scheme and much finer grid systems. For the experimental work, this study extended the work of Law by providing the local mass transfer coefficients for the stagnation region and much more detailed mass transfer results for the areas of local maximum and local minimum.

6.1 Flow Characteristics

The flow streamlines and the skin-friction factors along the impingement plate are investigated numerically.

6.1.1 Streamline Contours

The flow field is best represented by contours of the streamlines. The contours of the stream function for H = 2, 4 and 12 with an initial parabolic velocity profile are shown in Figures 6.1-6.3. In all these figures, the jet exit is at the upper left corner and the flow deflects upon approaching the impingement plate and travels to the right. The upper horizontal streamline represents the confinement plate and the lower horizontal streamline represents the impingement plate.

From the cases studied, in general, a primary vortex rotating counter-clockwise is found near the confinement plate with its size increasing with the jet Reynolds number. Except for the case of low Reynolds numbers for H = 2, a second vortex rotating clockwise is located near the impingement plate and to the right of the primary vortex. The secondary vortex is smaller in size and much weaker in rotational intensity than the primary one. It is interesting to note that for the case of H = 12, for Reynolds numbers of 100 and 200, there appears even a weaker third vortex near the confinement plate and to the left of the primary vortex. However, for the case of higher Reynolds numbers, both the primary and secondary vortices are far away downstream and no tertiary vortex appeared. A similar phenomenon can also be found in Law's (1982) plots, but it was not discussed.

For both the primary and the secondary vortices, the locations of the centres of vortices move downstream with increasing Reynolds number and the jet-to-plate spacing, as shown in Figure 6.4. These results confirmed the findings of Law (1982), with a slight exception that for H = 2, a secondary vortex started to appear for a Reynolds number of 300 rather than 400 as found by Law.

To examine the detailed flow development in the vicinity of the jet exit and stagnation point, the enlarged plots of streamline contours for all the cases studied for a single slot jet are presented in Figures 6.5-6.7. To avoid confusion, all the streamlines are

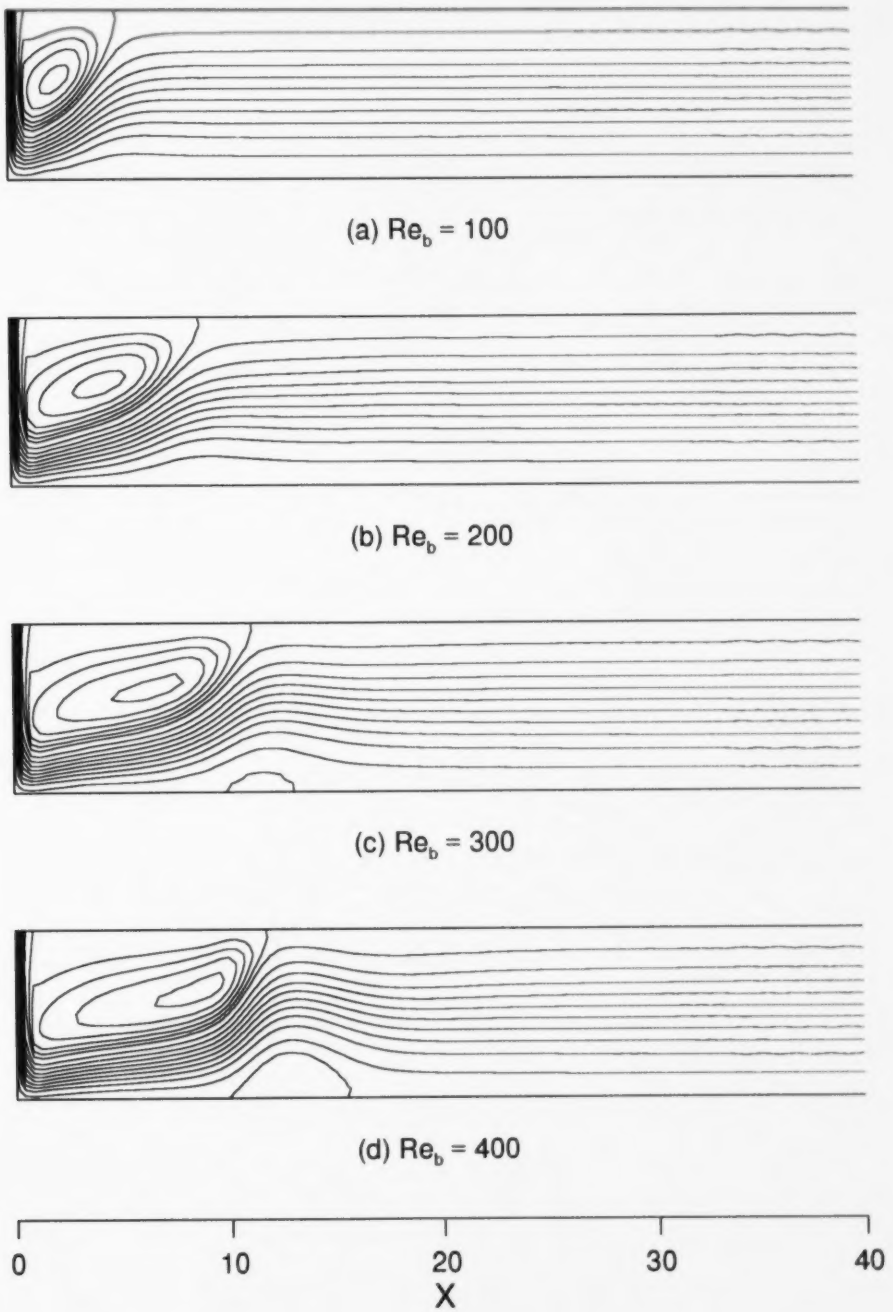

Figure 6.1 Streamline Contours for H = 2: Single Jet

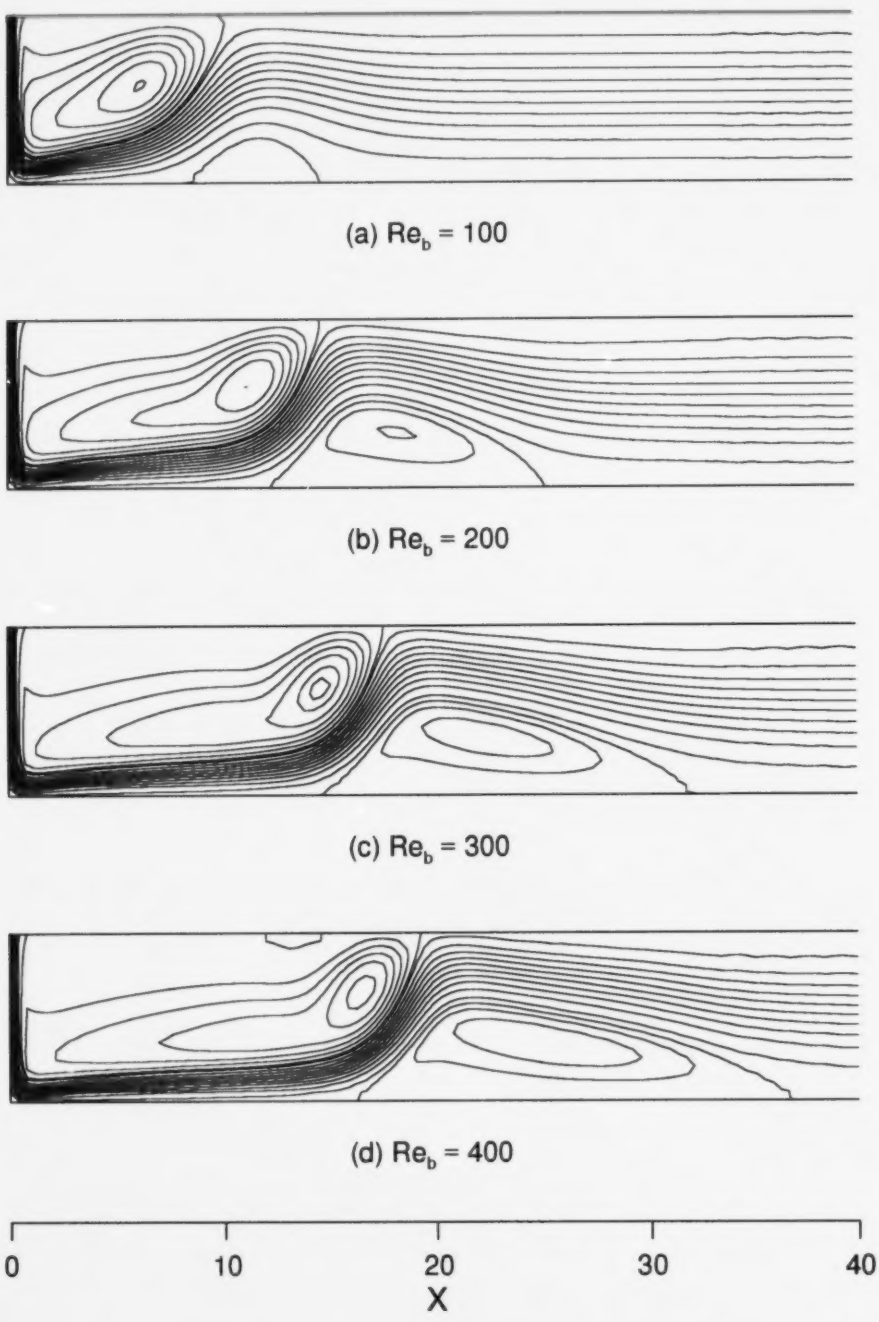

Figure 6.2 Streamline Contours for H = 4: Single Jet

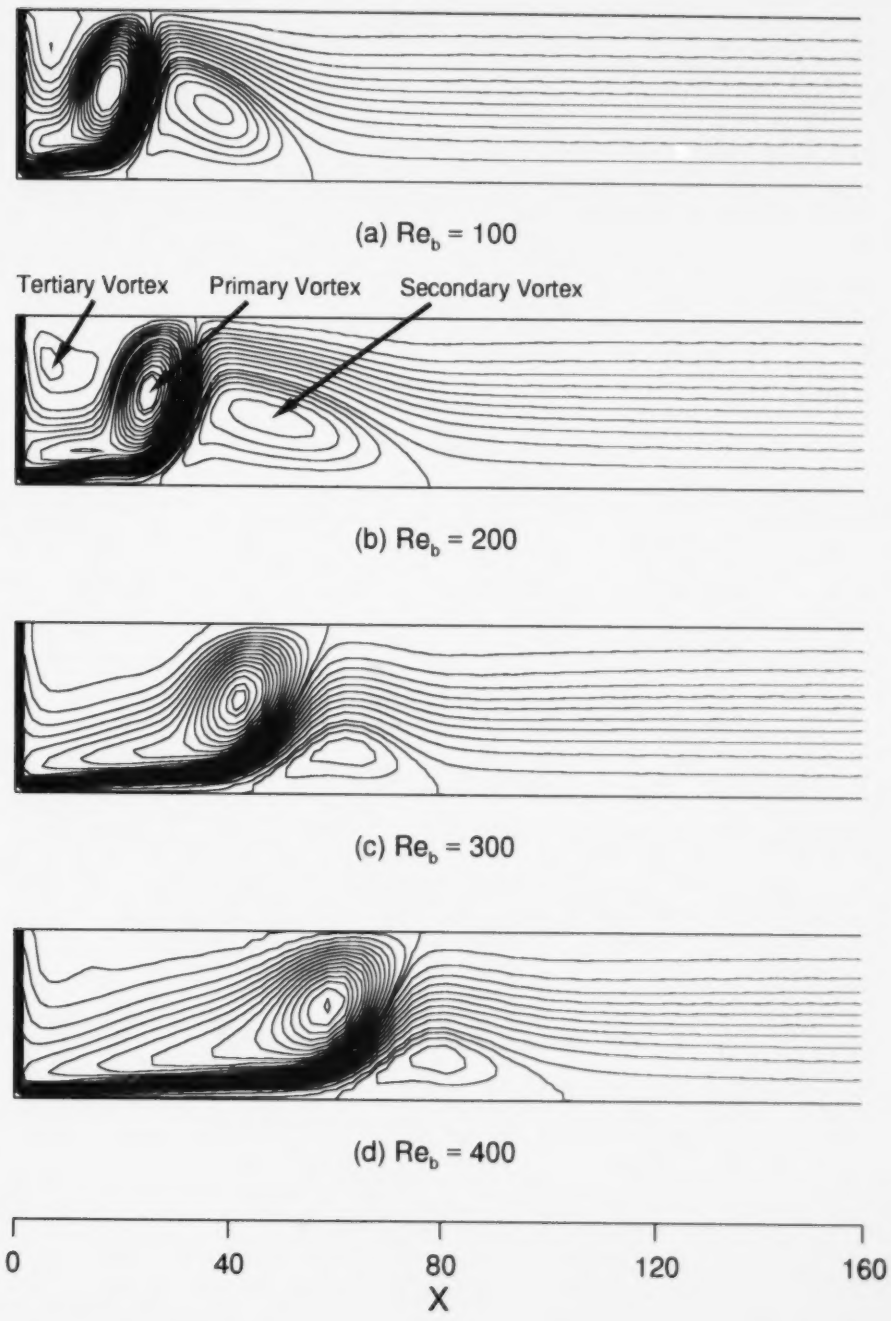

Figure 6.3 Streamline Contours for H = 12: Single Jet

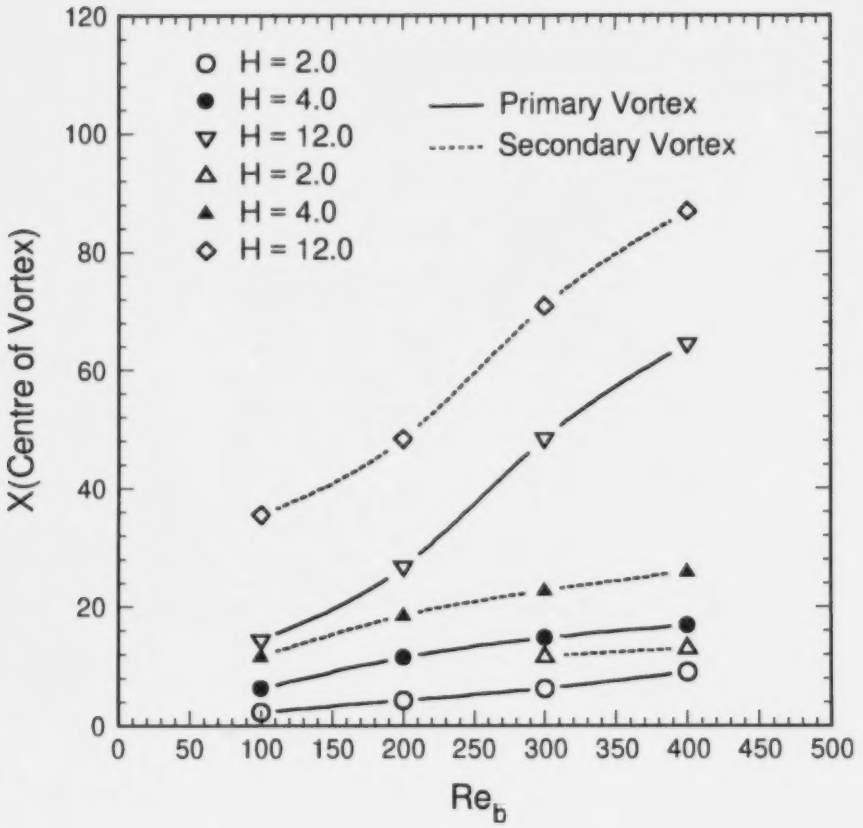

Figure 6.4 Locations of the Centres of Vortices for Single Jet

numbered with No.1 denoting $\Psi = 0$. The interval is 0.1 for streamlines 1 to 6 and 0.025 afterwards. Therefore, streamline No.1 represents the axis of symmetry and impingement plate and No.6 represents the confinement plate and the outermost free streamline of the submerged jet.

The spreading effect of the jet under the influence of the confinement plate can be examined from the outermost free streamline, No. 6, in Figures 6.5-6.7. It can be concluded that for all the cases, the jet contracts below the nozzle exit for an initially parabolic profile, with the contraction increasing as the jet-to-plate spacing increases.

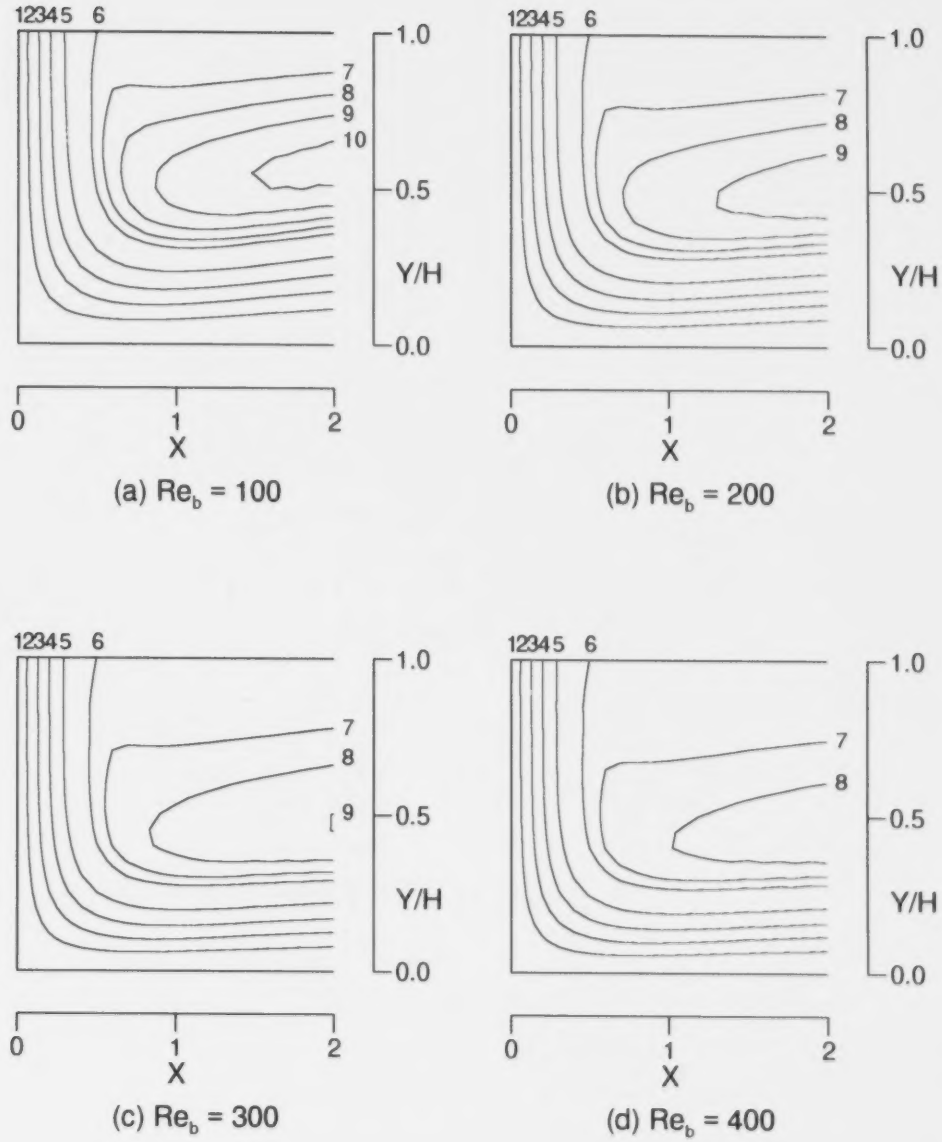

Figure 6.5 Streamline Contours Near the Stagnation Point for H = 2: Single Jet

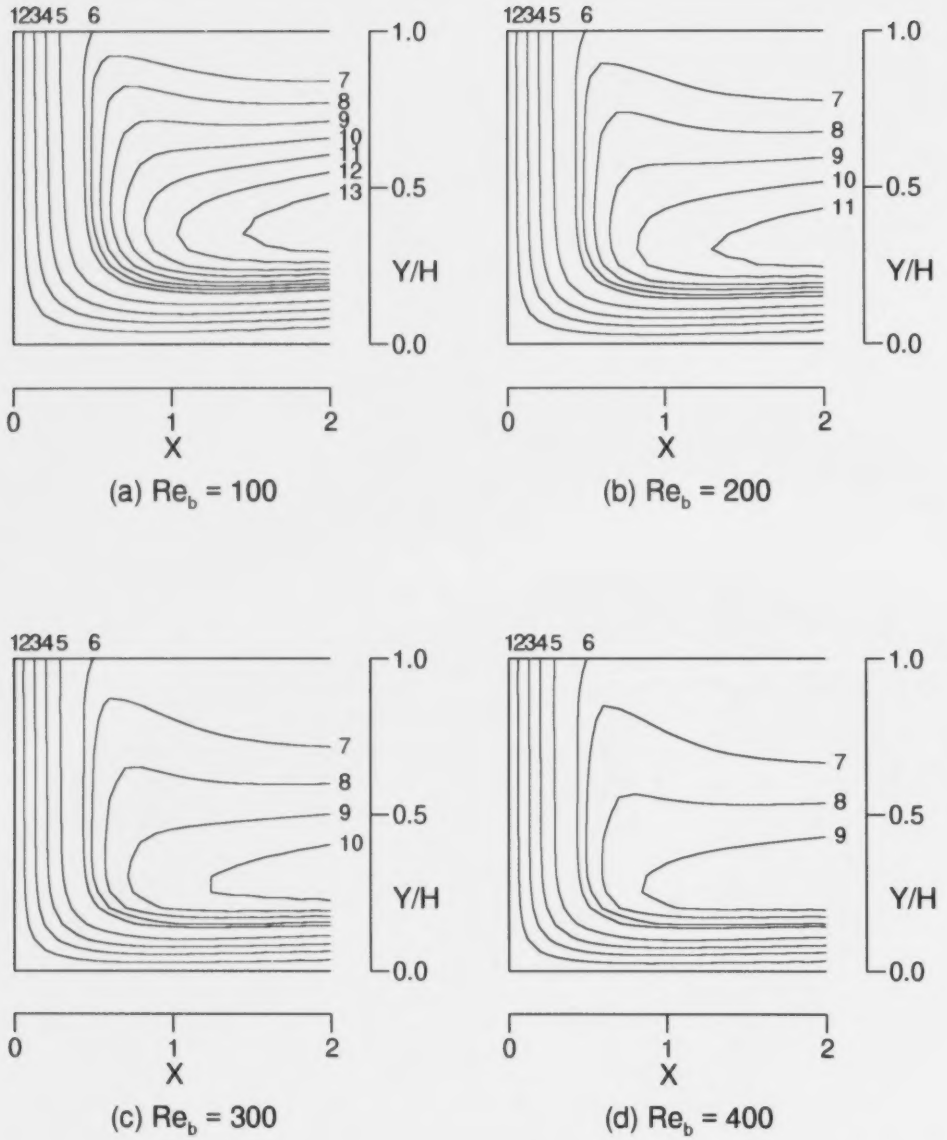

Figure 6.6 Streamline Contours Near the Stagnation Point for H = 4: Single Jet

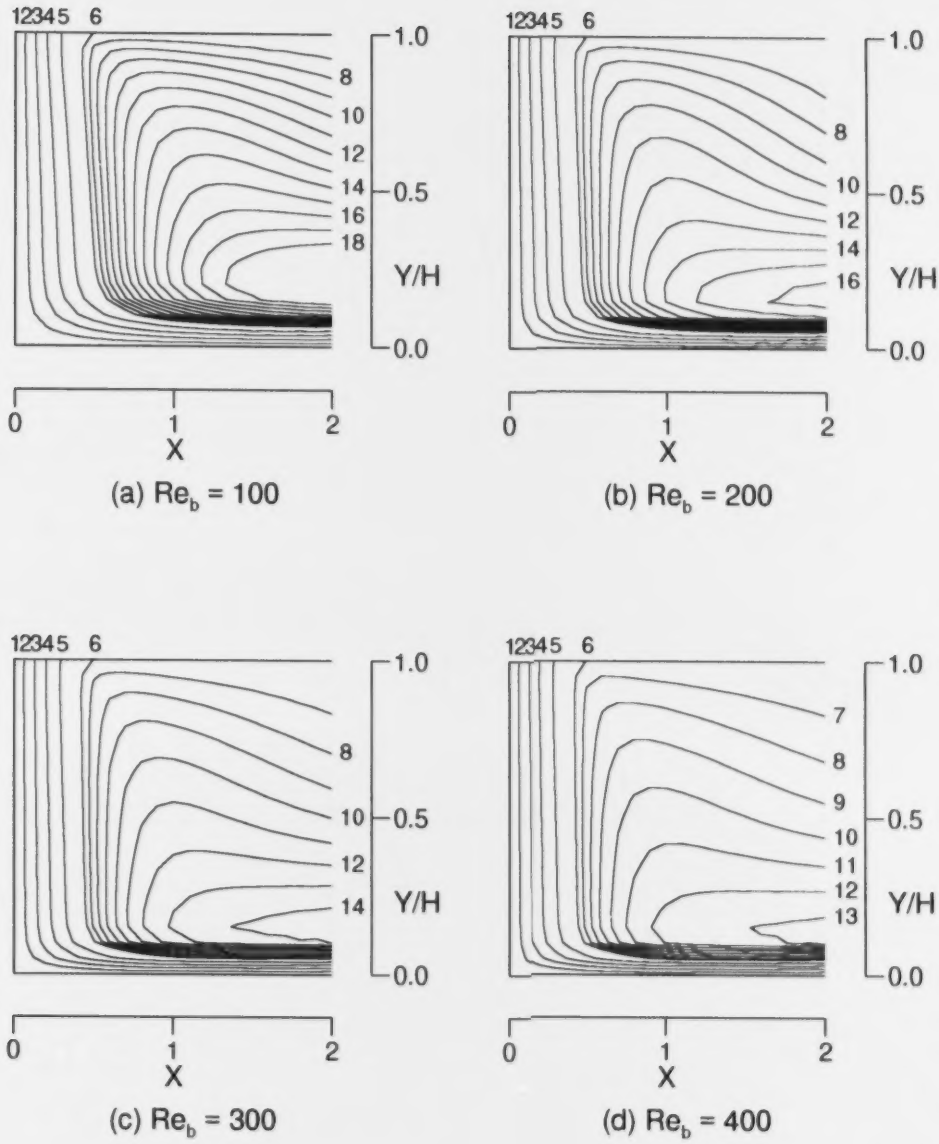

Figure 6.7 Streamline Contours Near the Stagnation Point for H = 12: Single Jet

A similar contracting effect due to the presence of a confinement plate was also found by Law (1982) for confined single slot jets and by van Heiningen et al. (1976) for semi-confined single slot jets.

6.1.2 Skin-Friction Factor along Impingement Plate

The study of local skin-friction factor along the impingement plate provides information for the local shear stress on the plate. The local skin-friction factor is defined by Equation 5.89. For fully developed flow between two parallel plates, the local skin-friction factor is given by Equation 5.98 for the case of a single impinging jet flow. If $C_f Re_b$ is plotted versus X for a given jet-to-plate spacing, all the curves for different Reynolds numbers should converge to the single constant value resulting from a fully developed flow in the region far away from the stagnation point. The constant depends only on the jet-to-plate spacing, being 1.5, 0.375 and 0.0417 for H = 2, 4 and 12, respectively. The plots of $C_f Re_b$ versus X are presented in Figures 6.8-6.10 for H = 2, 4 and 12, respectively.

From Figures 6.8-6.10, it can been seen that the local friction-factor along the impingement plate increases sharply near the stagnation point and reaches a maximum value in a short distance, and then decreases with the streamwise distance, X. The location of the maximum value is at about X = 0.6 for both H = 2 and 4, and at about X = 0.8 for H = 12 except for Re_b = 100, for which the location of maximum value is at X = 1.1. The longer distance for the case of low Reynolds number may be attributed to the relatively stronger retardation effect of the ambient fluid for a flow with a low Reynolds number and high jet-to-plate spacing.

To examine the effect of grid network on the computational results, a comparison of the local friction-factors computed by the current work and by Law (1982) for the highest Reynolds number used, Re_b = 400 and all the three jet-to-plate spacings is presented in Figure 6.11. For H = 2, the current work employed a grid network of

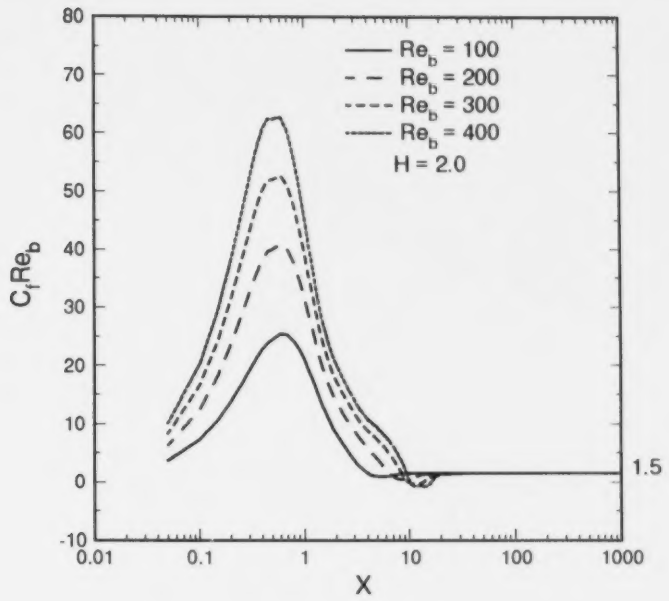

Figure 6.8 Skin-Friction Factor for H = 2.0: Single Jet

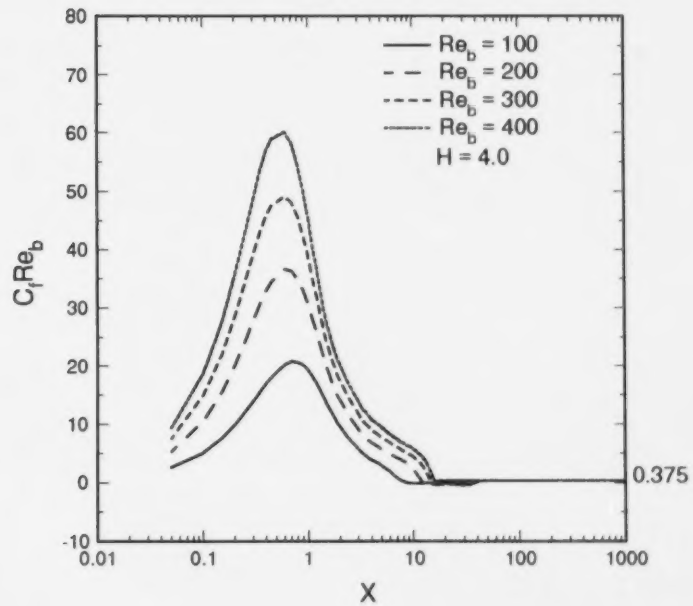

Figure 6.9 Skin-Friction Factor for H = 4.0: Single Jet

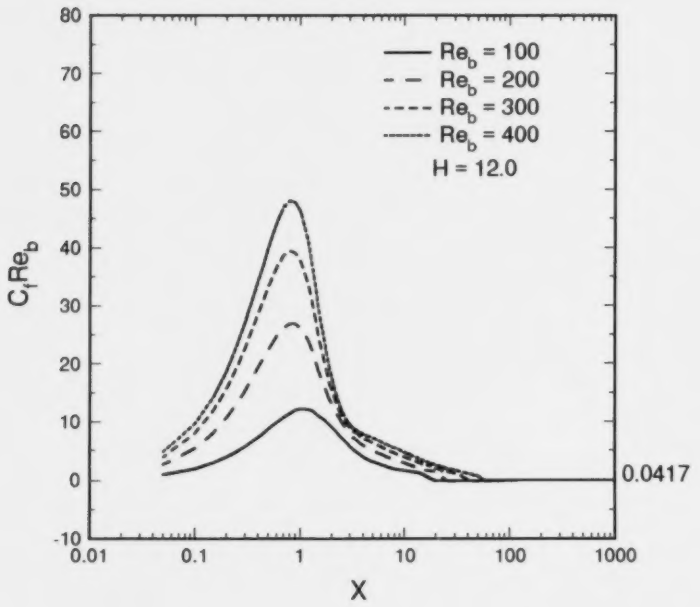

Figure 6.10 Skin-Friction Factor for H = 12.0: Single Jet

200×24 while Law used a grid network of 54×24. The comparison shows very good agreement for the results obtained by the two networks. For H = 4, the current work used a grid network of 200x30 and Law still used the same grid network as for H = 2. For this case, there is about 20% discrepancy in the region up to the peak, and there is little difference afterwards. The largest discrepancy occurred for the case of H = 12 where the maximum value from the current work is about 2.5 times as large as that given by Law. The grid network of the current work is 200×40 while that used by Law is 68×24. As is already shown by Law (Figure 9.3, 1982), for this large jet-to-plate spacing, more grid lines in the Y-direction should have been used. However, because of the limitation of Law's computing scheme and the computing resources, he failed to obtain a converged solution even for the grid network of 68×33 for Re_b = 400. Therefore, Law had to use the same coarse grid for all the three different jet-to-plate spacings, sacrificing accuracy. Similar convergence difficulties have also

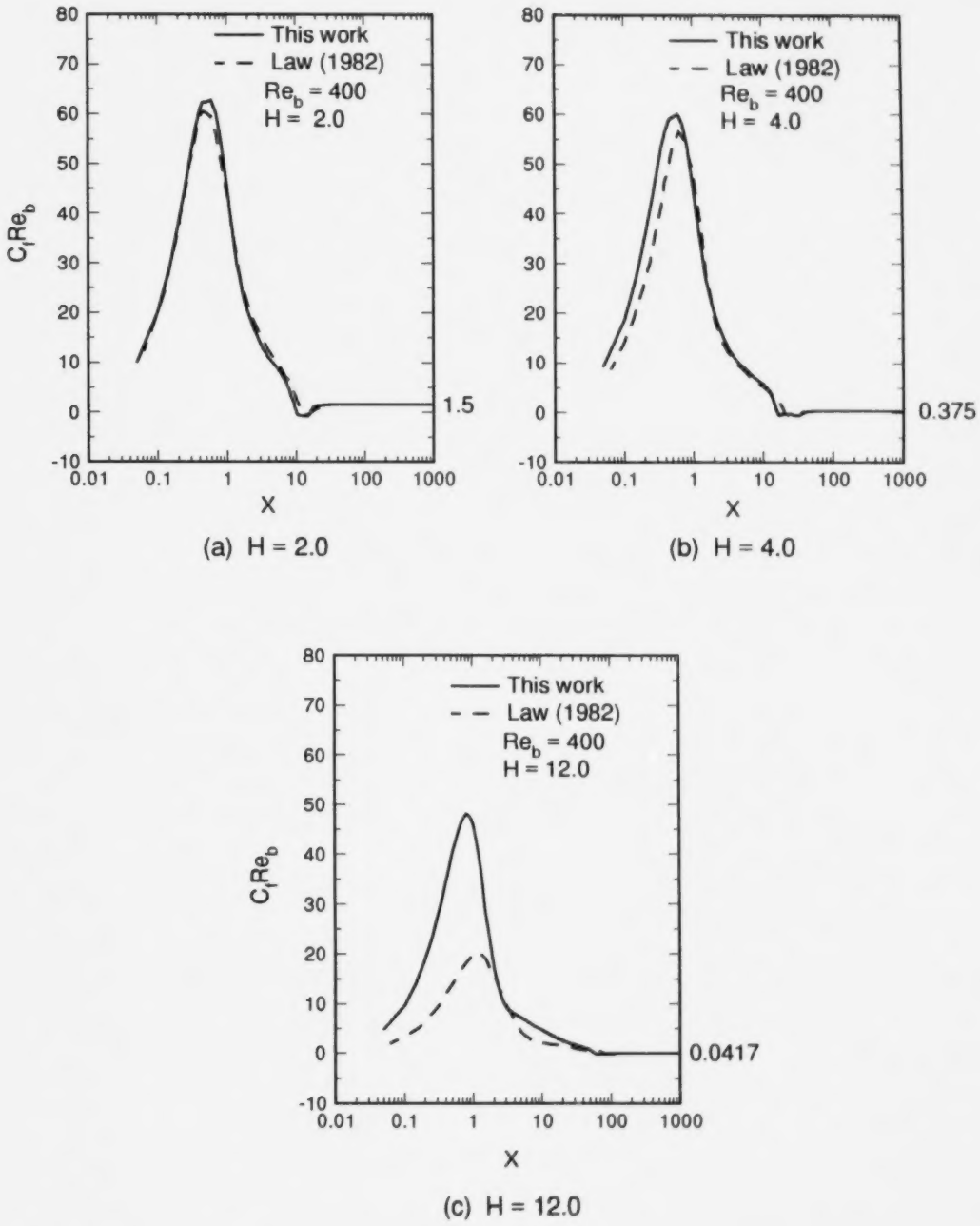

Figure 6.11 Comparison of Skin-Friction Factor with the Results of Law: Single Jet

been experienced by van Heiningen et al. (1976) for the case of large Reynolds number and jet-to-plate spacing. In the current work, it was found that for the case of H = 12, the convergence rate is extremely slow for large Reynolds numbers. It normally takes 20,000 to 30,000 iterations to converge since small relaxation factors have to be employed. All these difficulties are the result of the greatly elongated grid cells and near singular coefficient matrix for the discretized system of the algebraic equations.

6.2 Mass Transfer Characteristics

The local mass transfer is represented by the local Sherwood number along the impingement plate. In this section, the numerical prediction on the local Sherwood number along the impingement plate will be presented first, followed by the experimental results, comparison with the experimental data in the literature, and a detailed examination of the mass transfer at the stagnation point.

6.2.1 Numerical Results

The effect of Reynolds numbers on the numerically computed Sherwood numbers along the impingement plate is presented in Figure 6.12 for the three jet-to-plate spacings. The experimental data are also included in this figure for overall comparison. From the plots, it can be seen that there exists a local minimum in the Sherwood number for all cases except for H = 2 and Re_b = 100. The location of the local minimum is a function of both the Reynolds number and the jet-to-plate spacing. The magnitude and location of the local minimum are directly related to the secondary vortex as seen in Figures 6.1-6.4. For the cases of H = 2 and 4, an increase in Reynolds number gives a higher Sherwood number for the whole computational domain, except near the local minimum area, where the pattern becomes complex. For the case of H = 12, the curves for Re_b = 200, 300 and 400 all collapse into one curve near the stagnation point up to X = 1. This is an indication that the potential core has ended before it reaches the impingement plate, rendering the Reynolds number less

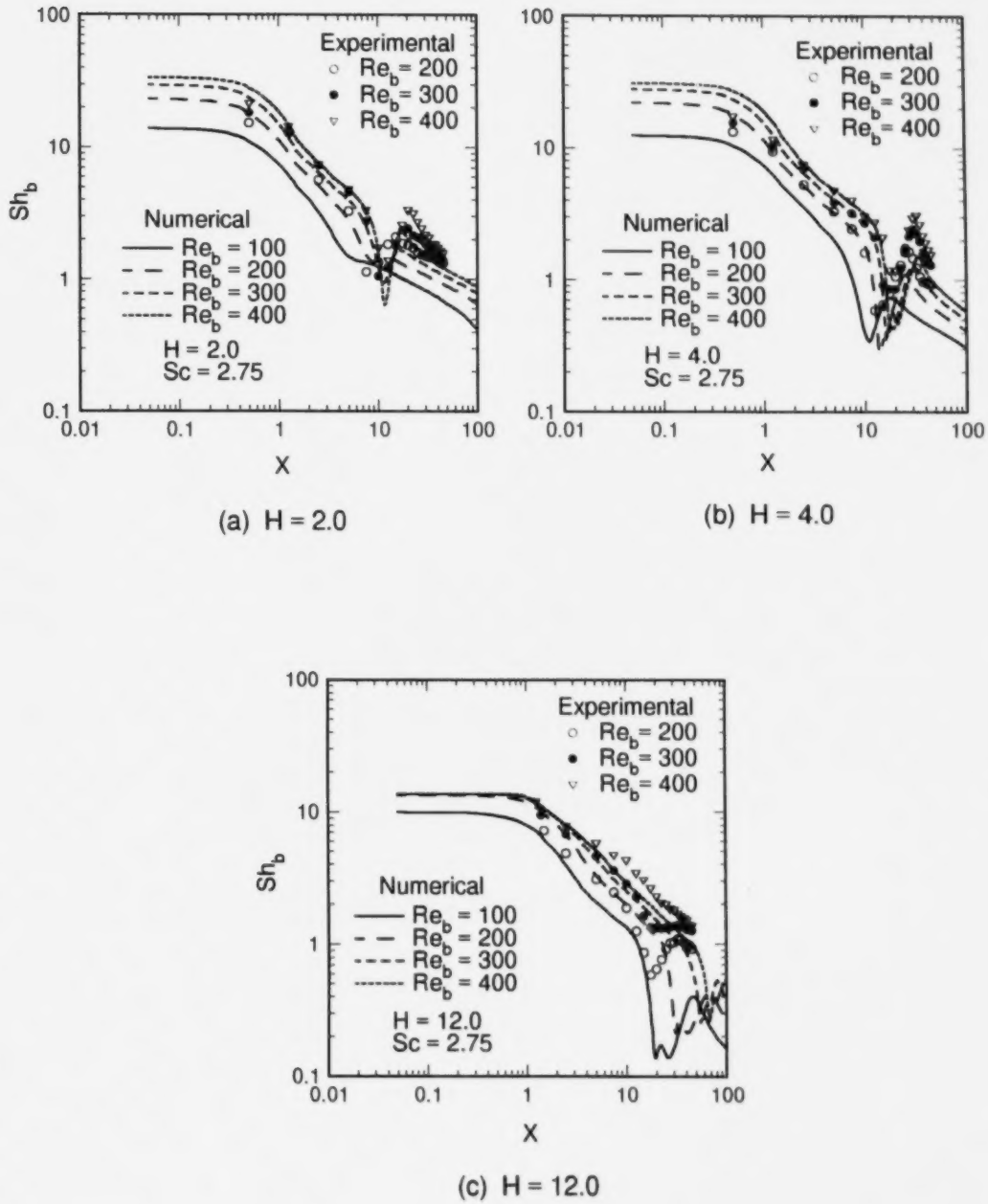

Figure 6.12 Effect of Reynolds Number on Mass Transfer Rate: Single Jet

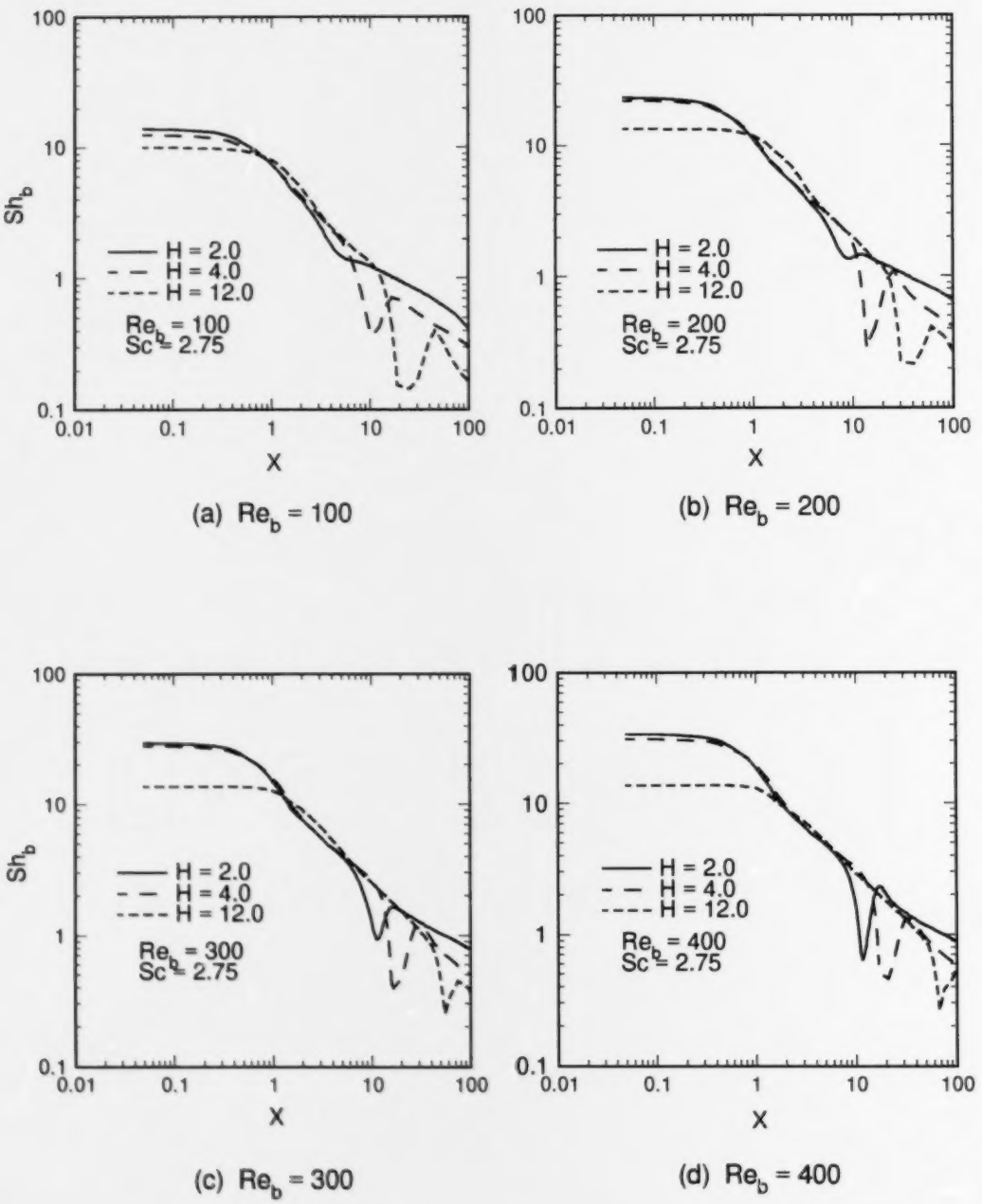

Figure 6.13 Effect of Jet-to-Plate Spacing on Mass Transfer Rate: Single Jet

influential. However, for the very low Reynolds number, Re_b = 100, the momentum is too low to overcome the retardation by the surrounding fluid and generate a Sherwood number matching the cases for the higher Reynolds numbers. The effect of jet-to-plate spacing on the local Sherwood numbers for the cases of different Reynolds numbers can be examined from Figure 6.13. For Re_b = 100, which is too low to overcome the retardation effect by the surrounding fluid, the Sherwood numbers for the different jet-to-plate spacings are close to each other, except for the region of local minimum. For higher Reynolds numbers, the Sherwood numbers for the cases of H = 2 and 4 are close to each other, indicating that the potential core underneath the jet exit is longer than 4. However, when H = 12, the Sherwood numbers for the case of higher Reynolds numbers are significantly lower than those for H = 2 and 4, indicating that the potential core has been engulfed by the surrounding fluid before reaching the impingement plate.

6.2.2 Experimental Results

For the case of a single confined impinging slot jet, experimental runs for various Reynolds numbers and jet-to-plate spacings were conducted by the method of real-time holographic interferometry, each lasting for about 10 minutes. The Reynolds numbers based on the jet width examined are 200, 300 and 400. Because of the limitation of the rotameters used in the experiments, no runs could be conducted for Re_b = 100. The jet-to-plate spacings investigated in this work are 2, 4 and 12.

6.2.2.1 Mass Transfer Pattern

Typical "frozen fringe" patterns extracted from the video recording for the three jet-to-plate spacings are presented in Figures 6.14-6.16. These figures represent the real images seen on the viewing surface as shown in Figure 3.8a. In addition, typical mass transfer patterns are digitized and presented in Figures 6.17-6.19.

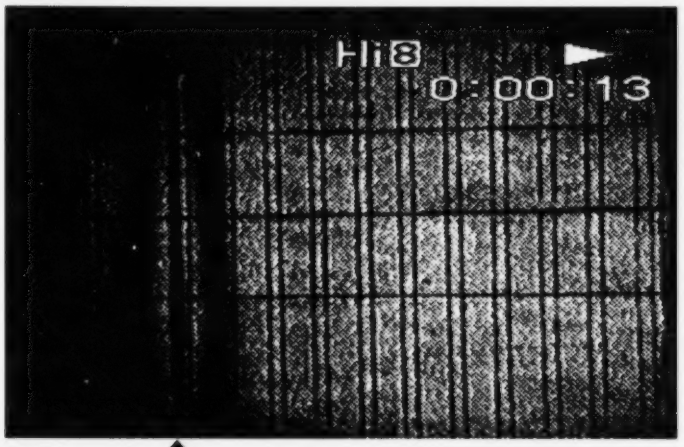

(a) t = 13 s

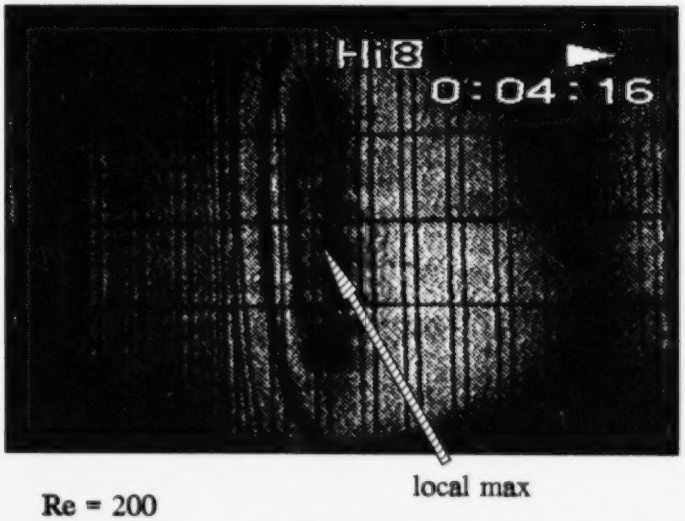

(b) t = 256 s

Figure 6.14 Contours of Equal Mass Transfer Rate for H = 2: Single Jet

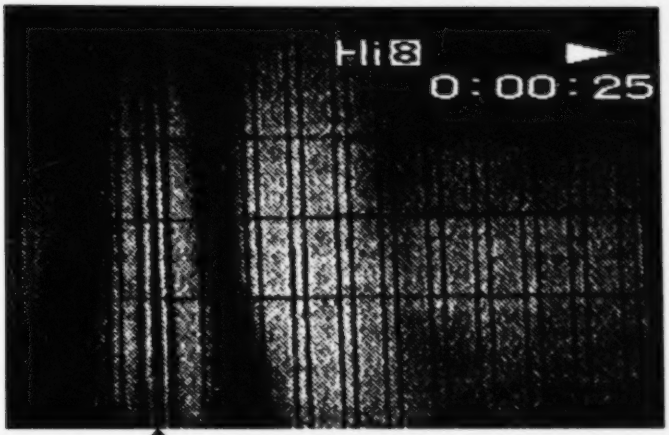

(a) t = 25 s

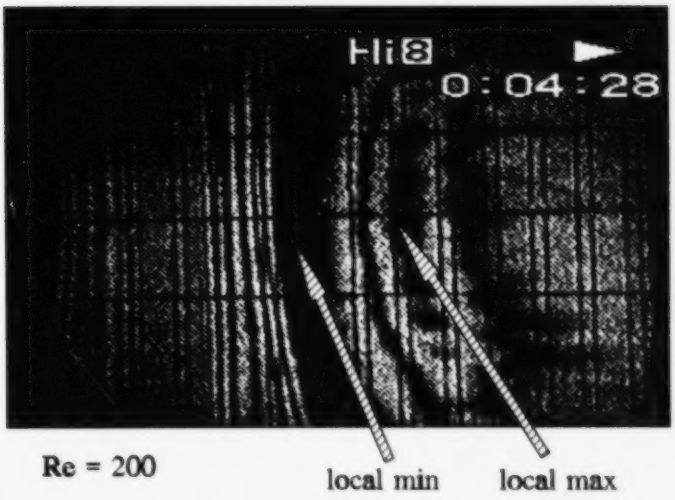

(b) t = 268 s

Figure 6.15 Contours of Equal Mass Transfer Rate for H = 4: Single Jet

(a) t = 21 s

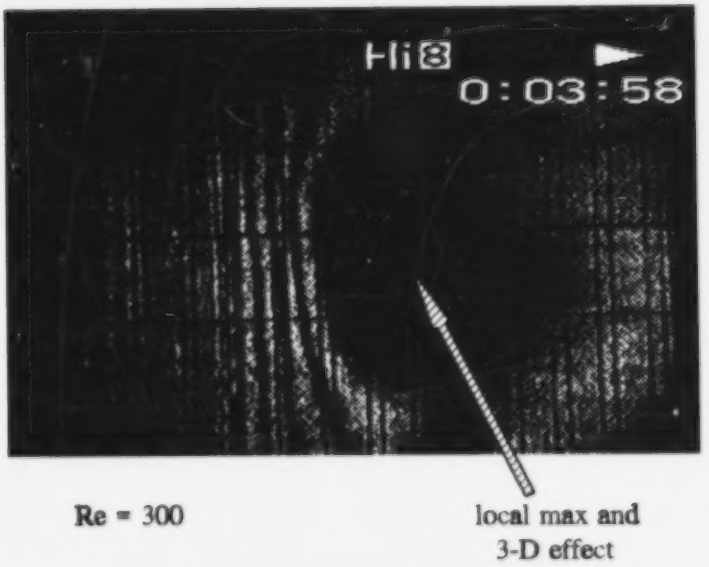

(b) t = 238 s

Figure 6.16 Contours of Equal Mass Transfer Rate for H = 12: Single Jet

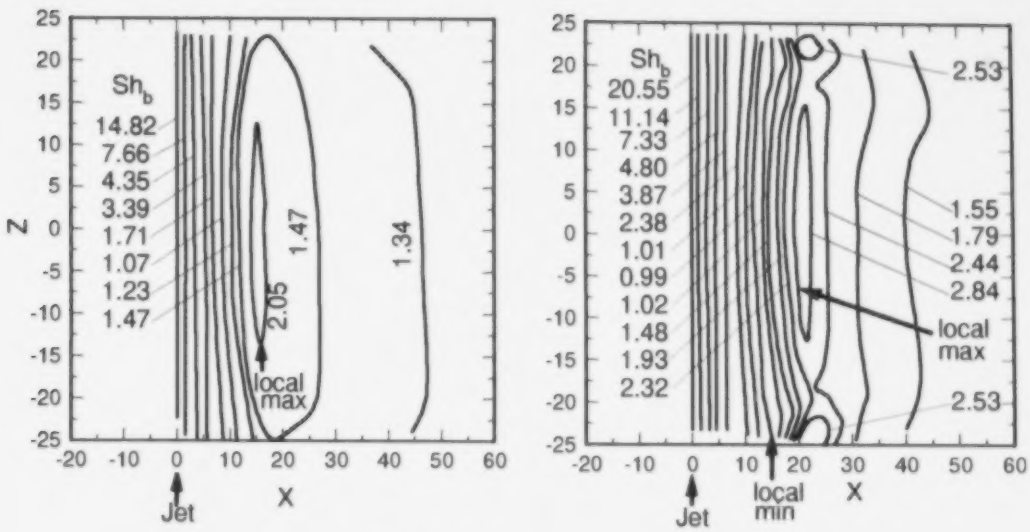

Figure 6.17 Digitized Contours of Sherwood Numbers for H = 2: Single Jet

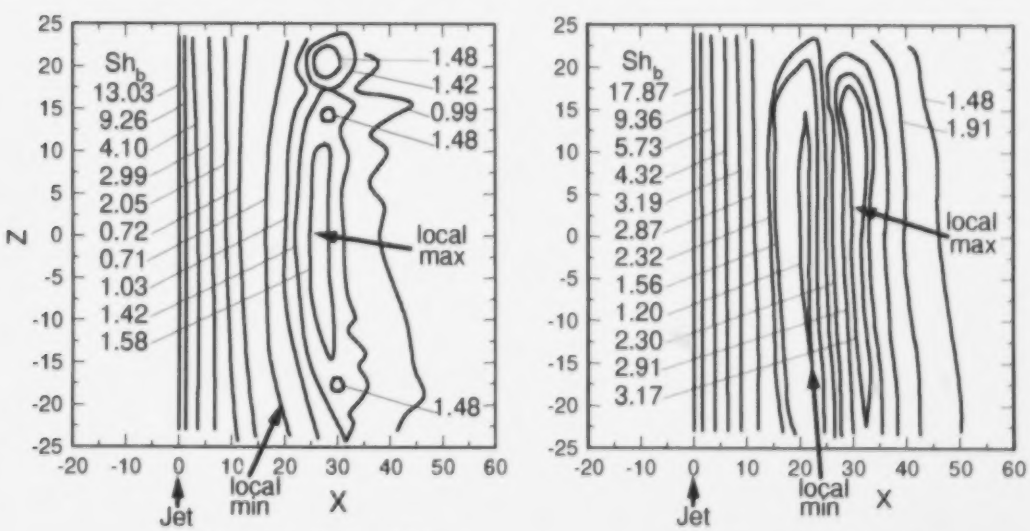

Figure 6.18 Digitized Contours of Sherwood Numbers for H = 4: Single Jet

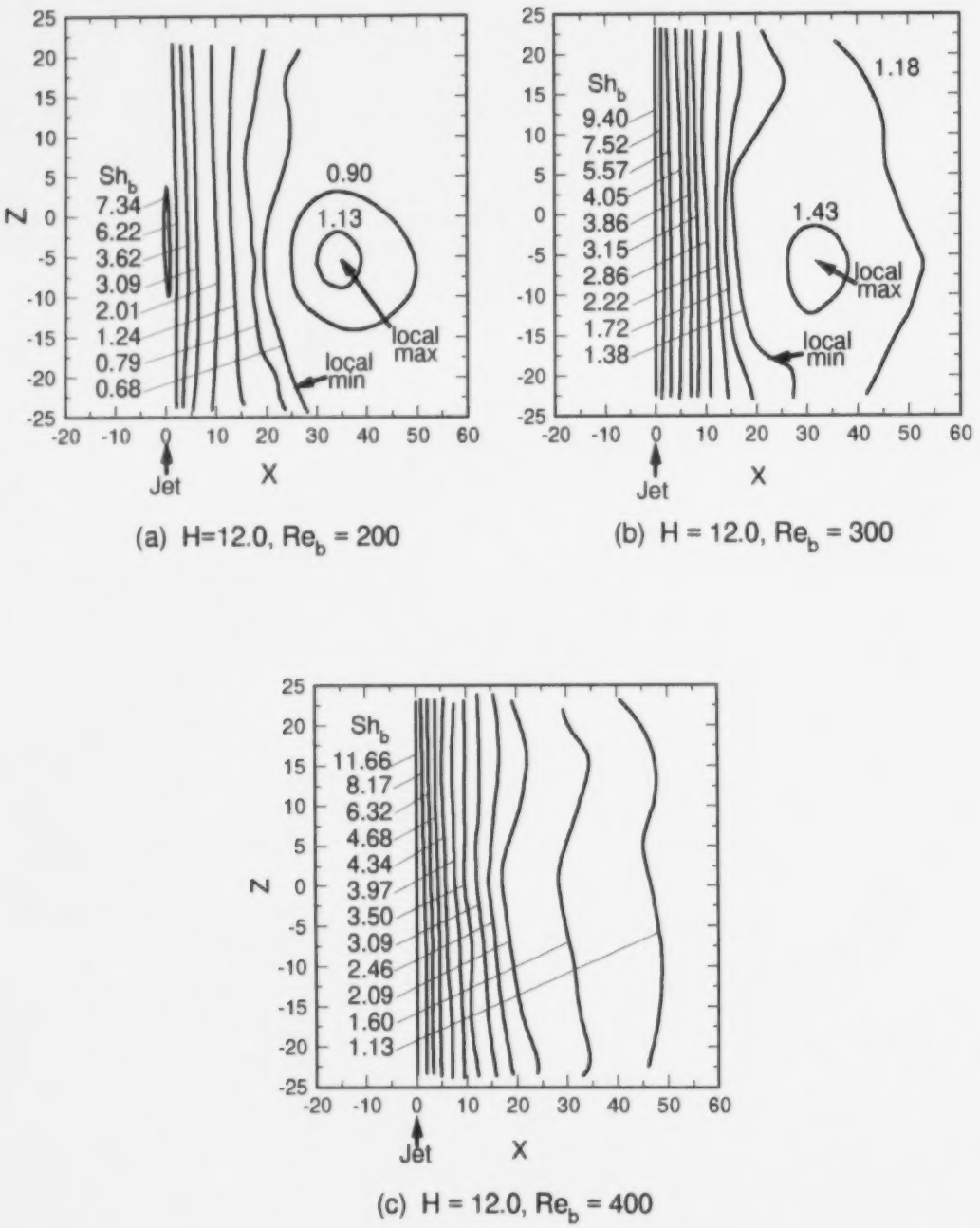

(a) H=12.0, Re_b = 200

(b) H = 12.0, Re_b = 300

(c) H = 12.0, Re_b = 400

Figure 6.19 Digitized Contours of Sherwood Numbers for H = 12: Single Jet

The "frozen fringe" patterns for a typical run with H = 2 and Re_b = 200 are presented in Figure 6.14. The fringes are contours of equal mass transfer rate. Figure 6.14a shows a short time into the run when a dark fringe has just appeared underneath the jet. It should be mentioned that the initial thickness of each fringe when first generated underneath the jet is about 1 slot width, indicating that the width of the stagnation region is about 0.5 to each side of the stagnation line. Within the stagnation region, the mass transfer rate is essentially constant. Figure 6.14b shows the mass transfer pattern after the run has lasted for 256 seconds. At this moment, on the one hand, the fringes in the vicinity of the stagnation line have become indistinguishable; on the other hand, the fringes further downstream can be clearly identified. As marked in Figure 6.14b, a local maximum, acting as a secondary fringe generating centre, can be clearly identified. Figure 6.17 shows the typical digitized mass transfer patterns for H = 2 and Re_b = 200 and 400. Figure 6.17 not only combines various time scales for different regions of the test section, giving an overall picture of the whole region of interest, but also provides Sherwood numbers for all the fringes included, and hence the local maximum and local minimum may be easily identified. Again, a local maximum is seen for both Reynolds numbers.

The "frozen fringe" patterns for a typical run with H = 4 and Re_b = 200 are presented in Figure 6.15. Figure 6.15a shows that the initial thickness of each fringe when first generated underneath the jet for H = 4 is also about 1 slot width, similar to the case of H = 2. Figure 6.15b depicts both a local maximum and local minimum in the mass transfer pattern. The local minimum occurs in such a region where two fringes meet, one from the stagnation line and the other from the region of local maximum.

The digitized mass transfer patterns for H = 4 and Re_b = 200 and 400 are shown in Figure 6.18. From Figure 6.18a, it is noted that for Re_b = 200, besides the local maximum and local minimum as seen from Figure 6.17 for H = 2, some 3-D effect starts to appear. This effect is less obvious for higher Reynolds numbers, as can be seen from Figure 6.18b.

The typical fringe patterns for H = 12 and Re_b = 300 are presented in Figure 6.16 and the digitized version for three Reynolds numbers are shown in Figure 6.19. From Figure 6.16a, one can observe that the initial thickness of the fringe when first generated by the flow underneath the jet is about 2 to 3 times that of the slot width. This is a clear indication that the potential core from the exit of the slot jet has been engulfed by the surrounding fluid before the stream reaches the impingement plate. This phenomenon has the following effect on the impinging jet mass transfer: dramatically decreasing the local mass transfer rate in the stagnation region and the average mass transfer rate, widening the stagnation region and reducing the difference between the mass transfer rates resulting from different Reynolds numbers. Figures 6.16b, 6.19a and 6.19b show obvious 3-D effects on the mass transfer pattern. The 3-D effect decreases with increasing Reynolds numbers. This is understandable since for this large jet-to-plate spacing, a small Reynolds number flow is not strong enough to counteract the retardation effect by the surrounding fluid on both ends of the flow channel, and the flow is concentrated in the centre region of the flow channel. When the Reynolds number is high, there is more momentum to counteract the end effect, and the 3-D effect will be reduced. From Figure 6.19a, for Re_b = 200, it can be seen that if the mass transfer rate on the centerline of the flow channel (Z = 0) is taken to represent the streamwise mass transfer rate, this mass transfer rate will be overestimated.

6.2.2.2 Effect of Reynolds Numbers

The experimental mass transfer rates due to a single laminar slot jet are reported as Sherwood numbers along the impingement plate along the centerline of the flow channel. The effect of the Reynolds number on the mass transfer rate can be examined from Figure 6.20. From these plots, one can observe that for all the three different jet-to-plate spacings, both the stagnation and the average Sherwood numbers increase as the Reynolds number is increased. For all cases investigated, the maximum Sherwood numbers are at the stagnation point. For H = 2 and 4 and all the three Reynolds

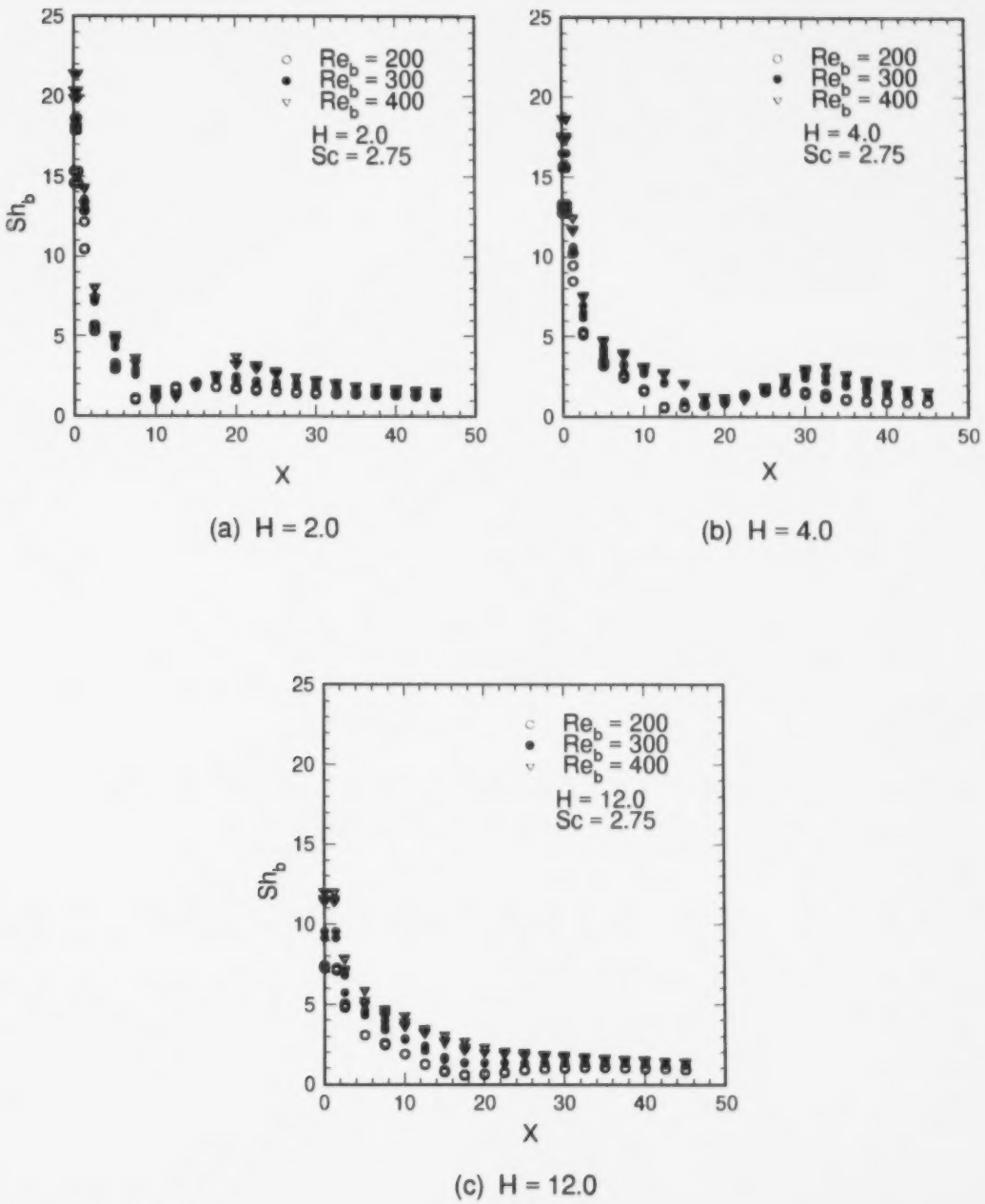

Figure 6.20 Effect of Reynolds Number on Experimental Mass Transfer Rate: Single Jet

numbers, the Sherwood number decreases with X, the dimensionless streamwise distance from the stagnation point, until the local minimum, which is a function of both H and Re_b, and then increases to a local maximum, and eventually decreases thereafter. For H = 12, one can notice a weak local minimum only for the low Reynolds number, Re_b = 200. For higher Reynolds numbers, the plots of Sh_b versus X are essentially monotonous. This may be explained by examining the numerical streamline contours of Figure 6.3. The secondary vortices, which are responsible for the local minimum for H = 12 and Re_b = 300 and 400, are outside the section of the impingement plate where the optical prism is located and hence this outer region cannot be studied in this work.

6.2.2.3 Effect of Jet-to-Plate Spacing

To examine the effect of jet-to-plate spacing, H, on the local mass transfer rate, the same experimental data are plotted in Figure 6.21. For all the three Reynolds numbers investigated, the stagnation Sherwood number decreases with increasing jet-to-plate spacing. However, the difference of the Sherwood numbers between H = 2 and 4 is much less than that between H = 4 and 12. The locations of the local maximum and minimum are located further downstream when the jet-to-plate spacing is increased. The observations conform with the numerical predictions as presented earlier.

6.2.3 Comparison Between Numerical and Experimental Results

Detailed comparison between the numerical and experimental results for the mass transfer rate due to a single laminar slot jet is given in Figures 6.22-6.24 for H = 2, 4 and 12.

From Figures 6.22-6.24, three distinct regions may be identified. They are discussed in detail as follows.

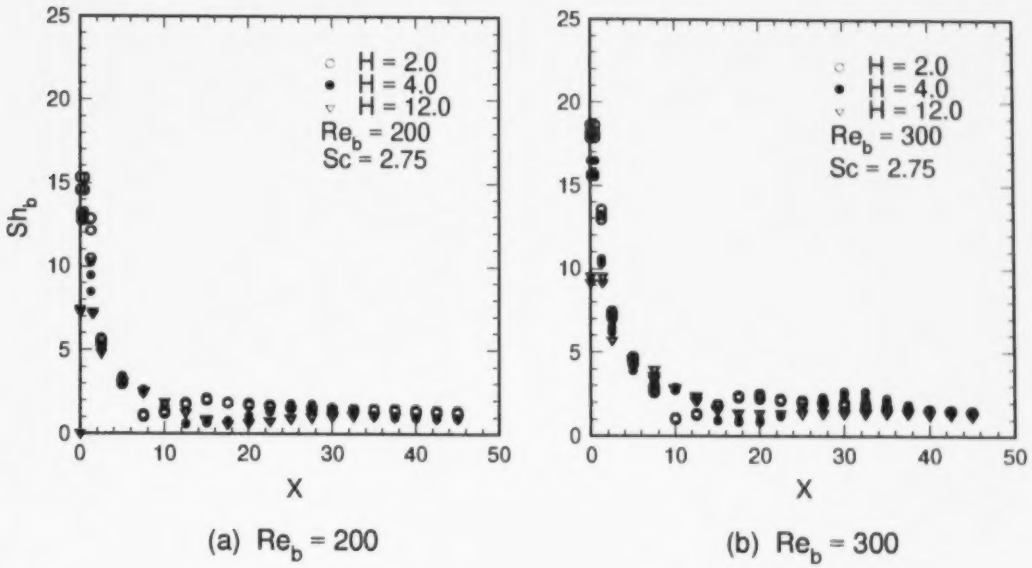

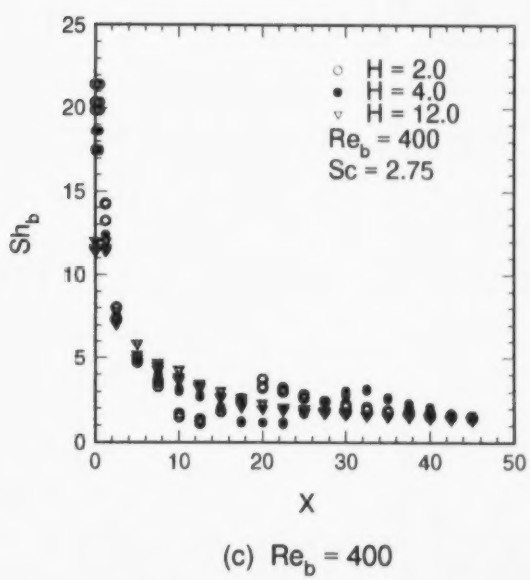

Figure 6.21 Effect of Jet-to-Plate Spacing on Experimental Mass Transfer Rate: Single Jet

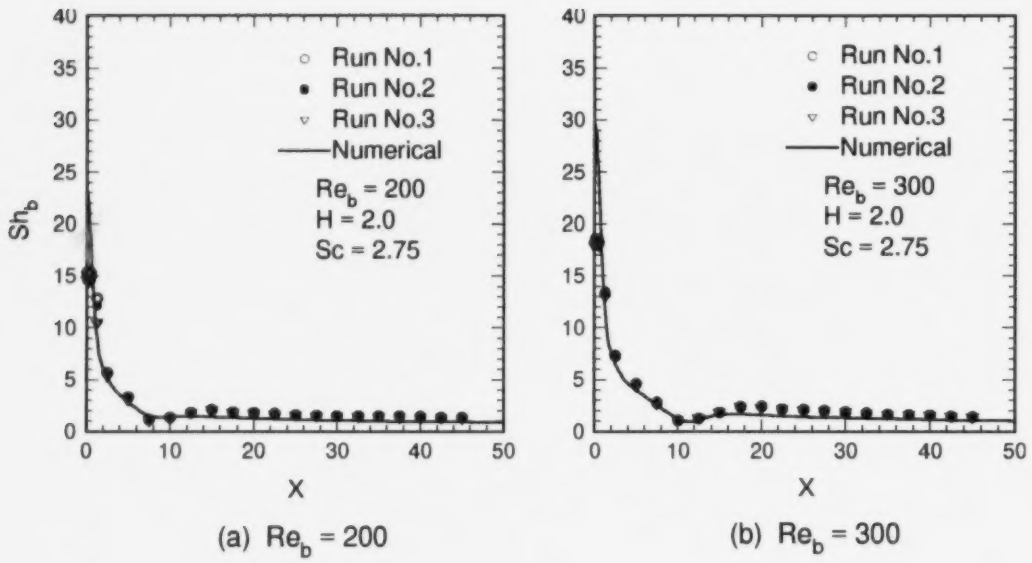

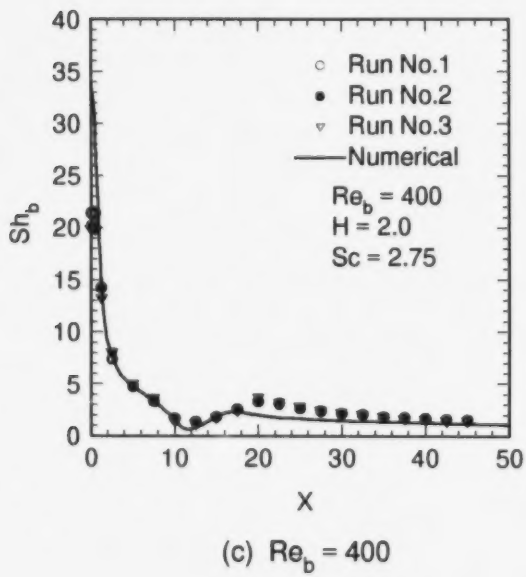

Figure 6.22 Comparison Between Numerical and Experimental Mass Transfer Rates for H = 2: Single Jet

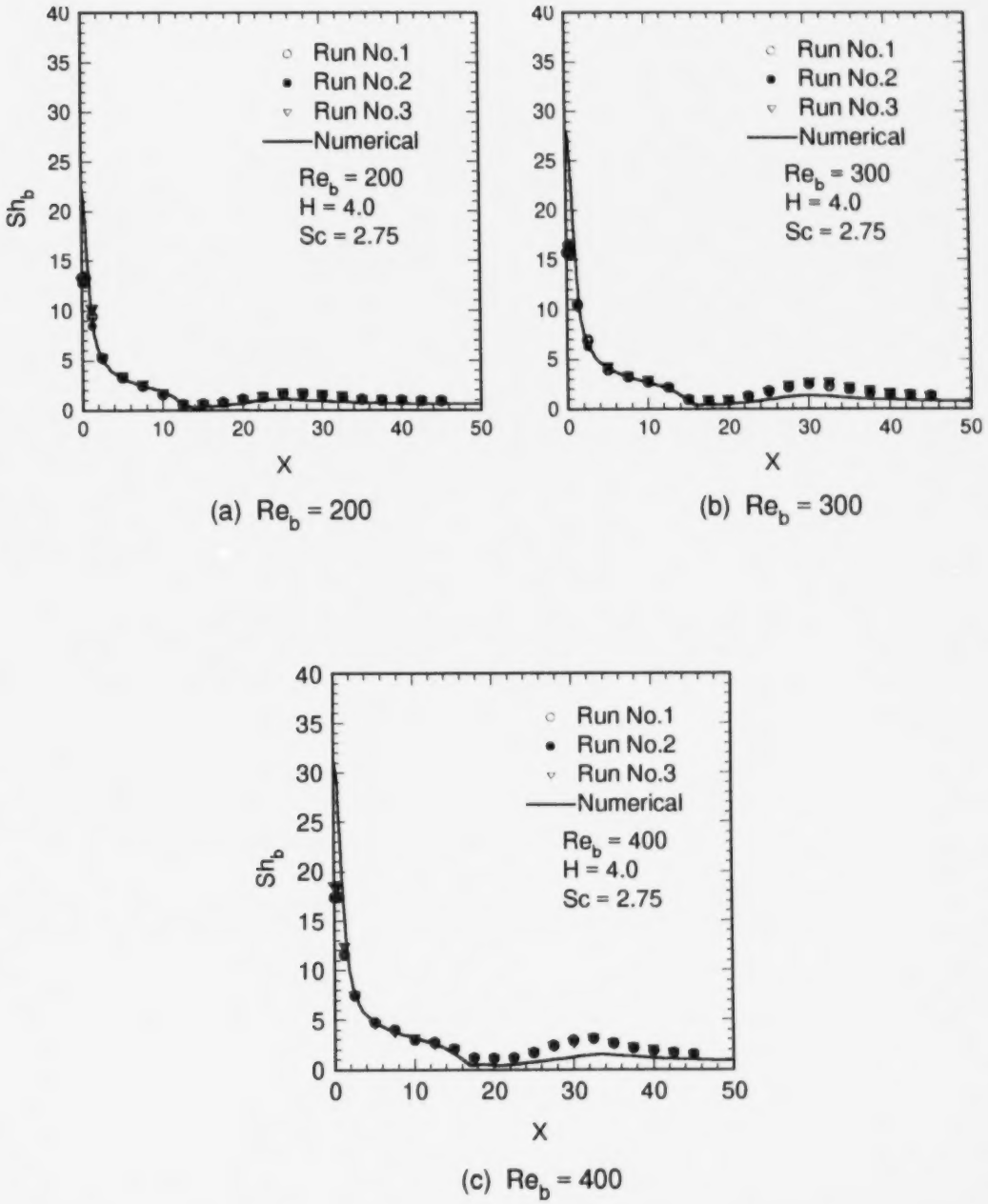

Figure 6.23 Comparison Between Numerical and Experimental Mass Transfer Rates for H = 4: Single Jet

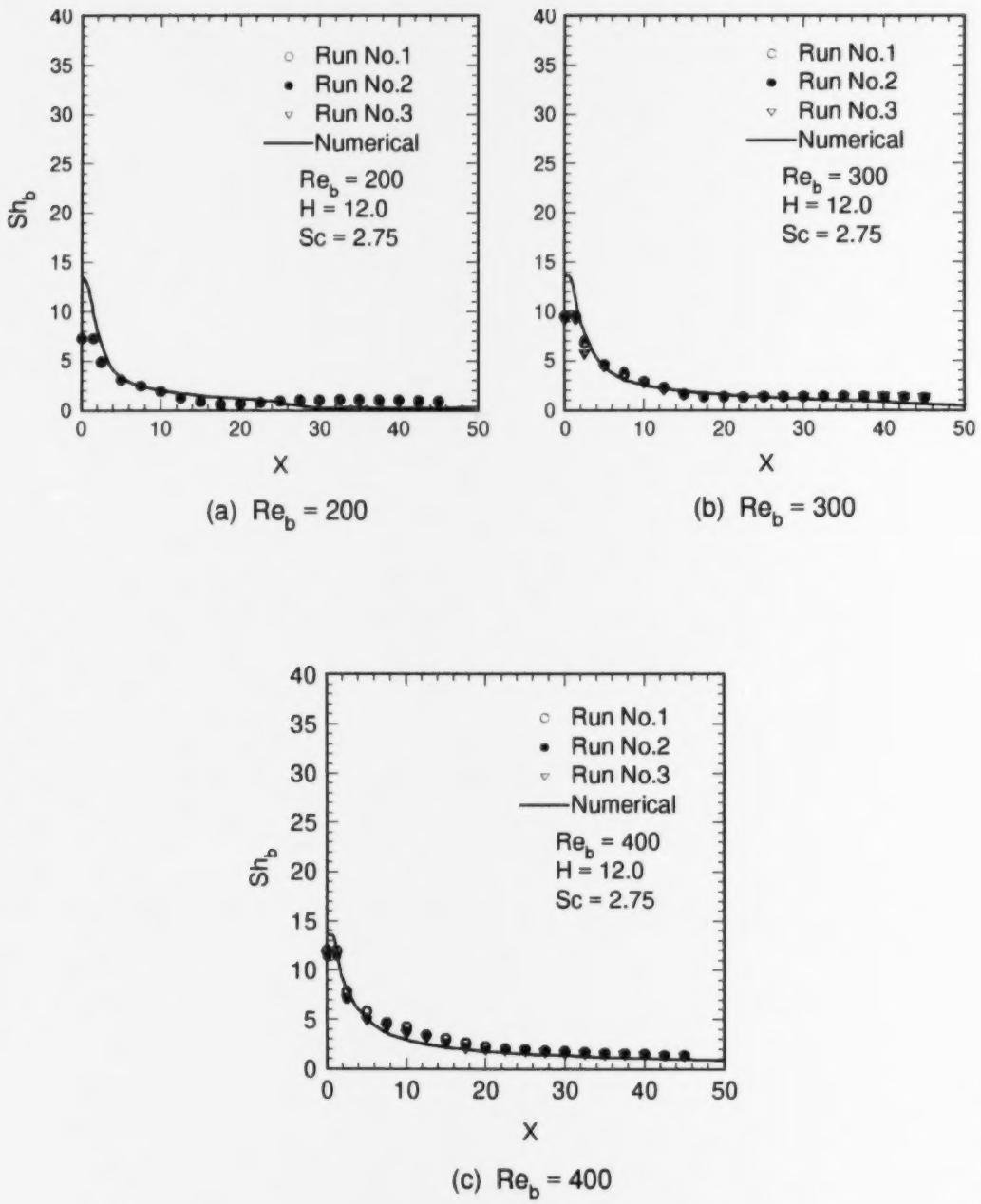

Figure 6.24 Comparison Between Numerical and Experimental Mass Transfer Rates for H = 12: Single Jet

The first region is the stagnation region where the numerical prediction is always higher than the experimental results, with the least discrepancy occurring for H = 12 and Re_b = 400. Similar problems have also been encountered by van Heiningen et al. (1976), Ichimiya and Hosaka (1991) and Al-Sanea (1992). Except for Ichimiya and Hosaka, no other investigators have given any explanations to the over-prediction of transfer rate at the stagnation region by numerical methods. With an oil-film method of visualization, Ichimiya and Hosaka noticed a pair of small vortices at the stagnation region which are believed to have the effect of reducing the mass transfer rate and hence are responsible for the discrepancy.

The second region is outside the stagnation region and before the local minimum. In this region, the average difference between the experimental results and the numerical prediction is within ±10%. It should be mentioned that the numerical work of van Heiningen et al. (1976) and Al-Sanea (1992) only covered the stagnation region and this region.

The third region is downstream from the local minimum. In this region, the local transfer rate first recovers from the local minimum due to the secondary vortex and reaches a local maximum in a short distance and decreases monotonously afterwards. For H = 2 and 4, the numerical prediction is generally good for Re_b = 200, and the discrepancy increases with the Reynolds number. For Re_b = 300 and 400 and H = 2 and 4, it can be seen that the numerical prediction has the appropriate trend in recovering from the local minimum, but the numerically predicted Sherwood numbers are not as high as the experimental results. After the maximum value in Sherwood number, the agreement is improved. Figure 6.24 shows that for H = 12, Re_b = 300 and 400, except for the stagnation region, the agreement between the numerical prediction and the experimental results is excellent. For Re_b = 200, the prediction falls short of the experimental values for $X \geq 28$.

In general, the discrepancy for the third region may be attributed to two important factors: mixing-induced disturbances and three-dimensional effects. Mixing-induced disturbance has been discussed by various authors (Gardon and Akfirat, 1965; Akfirat, 1966; Gardon and Akfirat, 1966; Sparrow and Wong, 1975; Vader et al., 1991). Mixing-induced disturbance enhances transfer rate and its effect increases with the Reynolds number. Figures 6.22-6.23 for H = 2 and 4 provided evidence to support this argument. Similar phenomena have also been reported by Sparrow and Wong (1975).

The three-dimensional effects are caused by the end effect of the flow channel. Therefore, the 3-D effect becomes more influential when the jet-to-plate spacing is large and the Reynolds number is small. The former reduces the aspect ratio of the cross-section of the flow channel and the latter reduces the flow momentum to counteract the end effect. The 3-D effect causes the flow to concentrate on the centerline region and thus increases the transfer rate in that region but decreases the transfer rate elsewhere. As a result, if the transfer rate on the centerline of the impingement plate is taken (as is the case in the current work) to represent the average in the span-wise direction, the transfer rate will be over-estimated. This point is evident when Figures 6.19a and 6.24a are examined.

6.2.4 Comparison with the Experimental Data in the Literature

In this section, the experimental data from this work are compared with the experimental data available in the literature for similar cases. Since the current work extends the experimental work of Law (1982) for the case of single two-dimensional laminar jet, the comparison with Law's data is conducted first. For other experimental work in the literature, since the experimental conditions are normally different, the comparison will only be approximate. Nevertheless, some insight into the whole subject can still be gained through the comparison.

6.2.4.1 Comparison with the Data of Law

The comparison of the current experimental data for the case of a single confined slot laminar jet with those of Law (1982) is presented in Figures 6.25-6.27 for H = 2, 4 and 12, respectively. Since Law used the technique of double-exposure holographic interferometry, he could not obtain the mass transfer rate in the stagnation region. Furthermore, with the double-exposure technique, it is very difficult to determine accurately the order of the fringes for the areas of local maximum and minimum. However, with the current technique of real-time holographic interferometry, the mass transfer rate of any point of interest can be determined independent of any other point. From comparison, it can be concluded that the current data agree well with Law's data for H = 2 and 4 upstream from the local minimum. For the local maximum, the current study shows a much higher mass transfer rate than reported by Law for higher Reynolds numbers. The strong local maximum is evident from Figures 6.14-18. For H = 12, Law failed to obtain any data close to the local maximum and minimum, and for the limited data available, they are much lower than the current data which agree well with the numerical prediction.

6.2.4.2 Comparison with the Data of Sparrow and Wong

The work of Sparrow and Wong (1975) dealt with unconfined laminar slot jets. They studied five jet-to-plate spacings (H = 2, 5, 10, 15, and 20) for five Reynolds numbers (Re_b =150, 300, 450, 650, 950). The cases of Re_b = 300 for H = 2, 5 and 10 are chosen to compare with the current work for Re_b = 300 and H = 2, 4 and 12, as seen in Figure 6.28. Figures 6.28a and 6.28b show that for small jet-to-plate spacings, the current data agree well with those of Sparrow and Wong, with the largest difference being less than 20% and located at the stagnation point. As for the larger jet-to-plate spacings shown in Figure 6.28c, the stagnation point mass transfer rate given by Sparrow and Wong is significantly higher than the current experimental results. An examination of Figures 6.28a to 6.28c reveals that Sparrow and Wong's data at the stagnation point do not have much change when the jet-to-plate spacing is increased

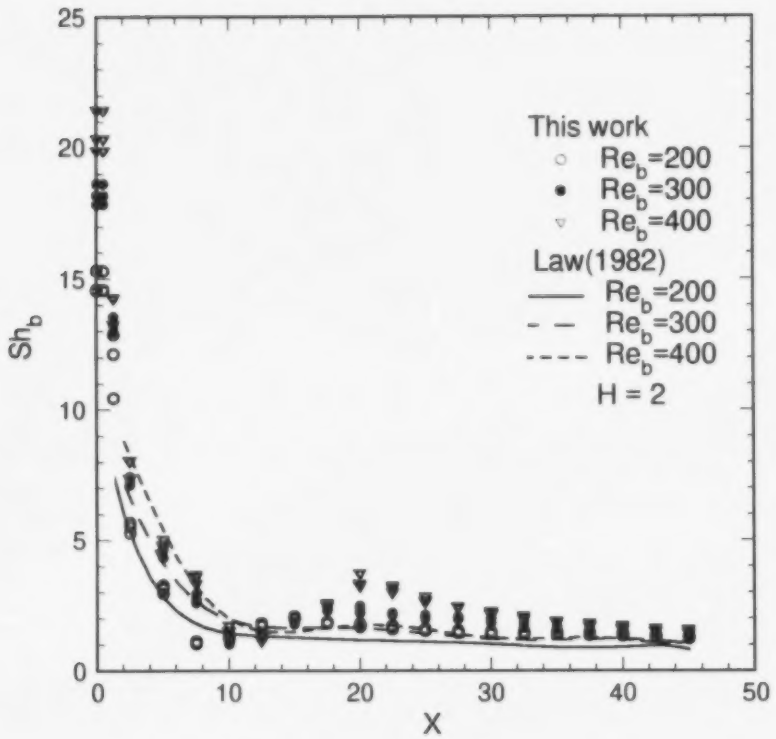

Figure 6.25 Comparison with the Data of Law for H = 2: Single Jet

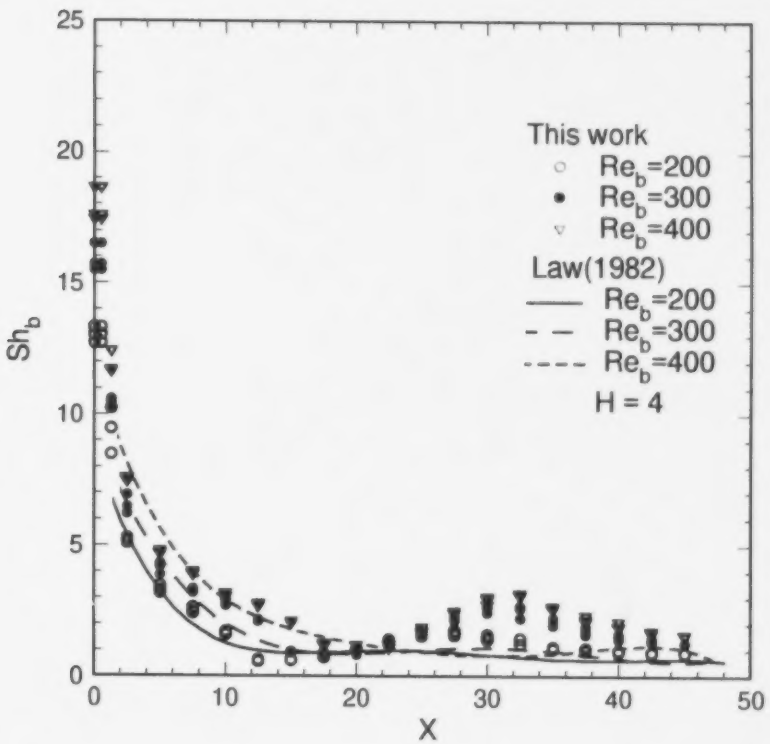

Figure 6.26 Comparison with the Data of Law for H = 4: Single Jet

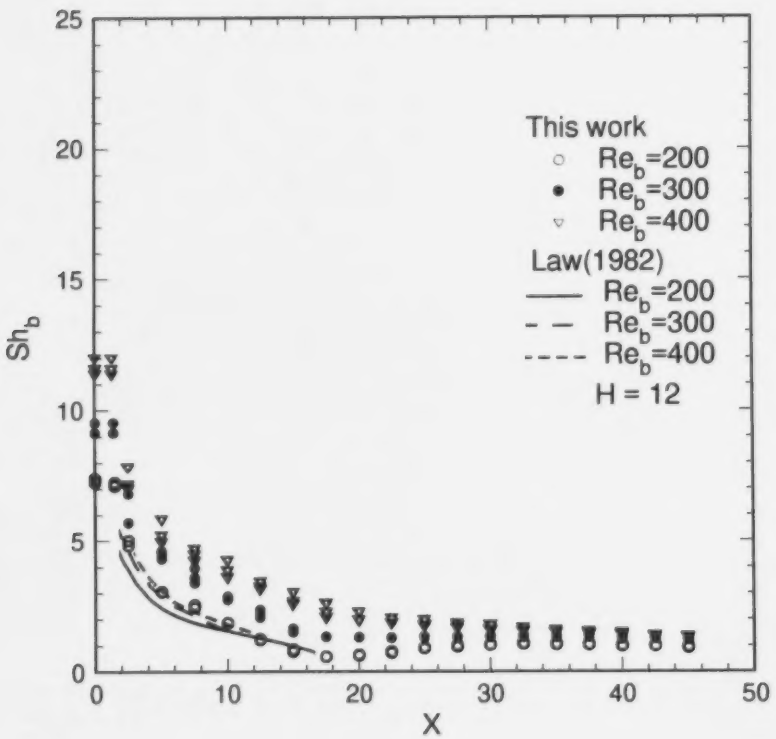

Figure 6.27 Comparison with the Data of Law for H = 12: Single Jet

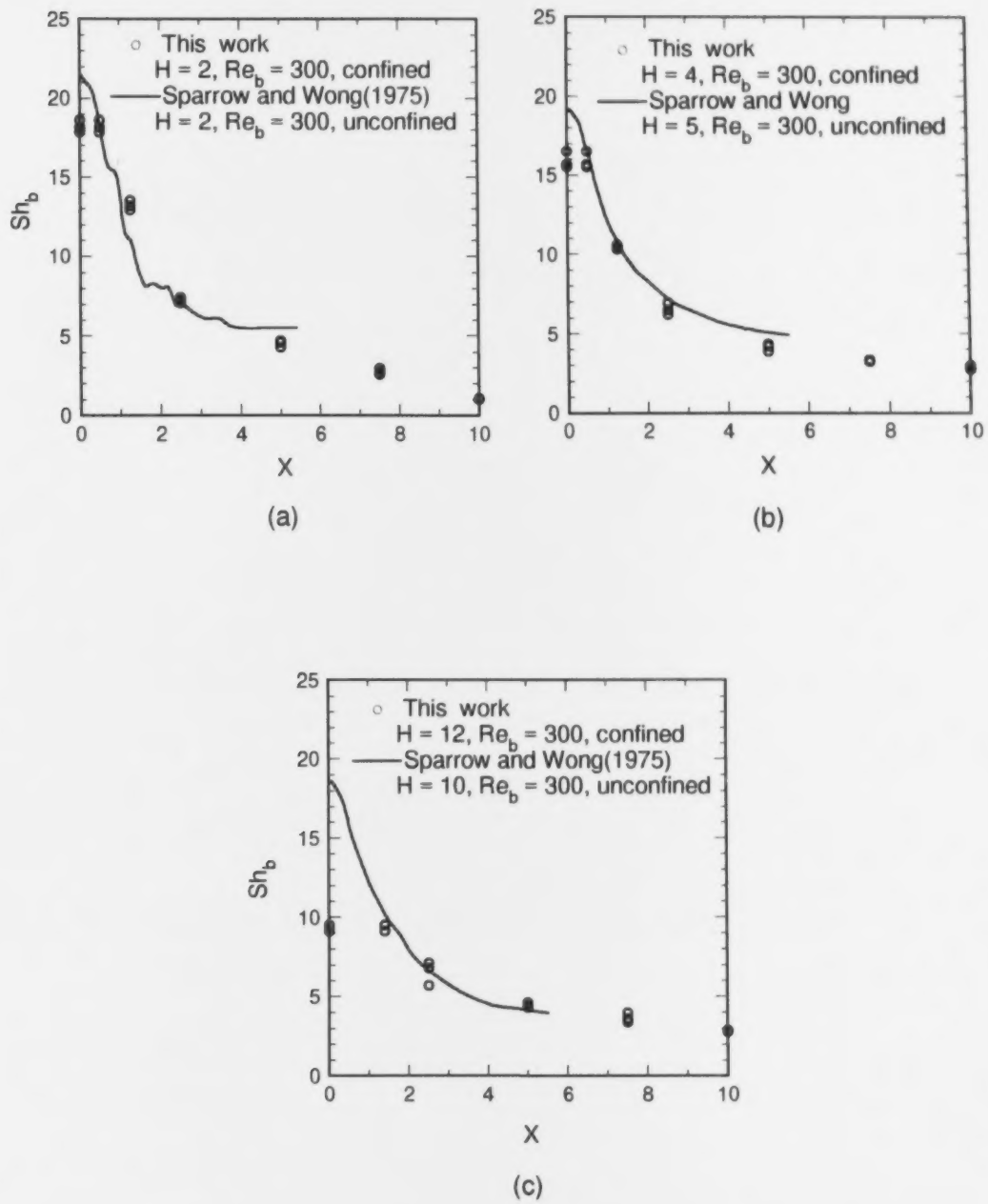

Figure 6.28 Comparison with the Data of Sparrow and Wong: Single Jet

from 2 to 10. This phenomenon disagrees with both the current data and the data of Gardon and Akfirat (1966).

6.2.4.3 Comparison with the Data of Gardon and Akfirat

Gardon and Akfirat (1966) experimentally studied the heat transfer characteristics due to unconfined two-dimensional air jets. Their main interest was for turbulent flow and only two runs dealt with laminar flow, i.e., Re_b = 450 and 950, for H = 4. The comparison of the current data for Re_b = 300 and 400 and H = 4 with those of Gardon and Akfirat for Re_b = 450 and H = 4.0 is given in Figure 6.29. It can be observed that the data of Gardon and Akfirat, which have been converted to Sherwood numbers by the heat and mass transfer analogy with n = 0.4, fit well into the figure except for the stagnation region and the region of local minimum and maximum. The discrepancy near the region of local minimum and maximum is mainly due to the confinement plate used in this work.

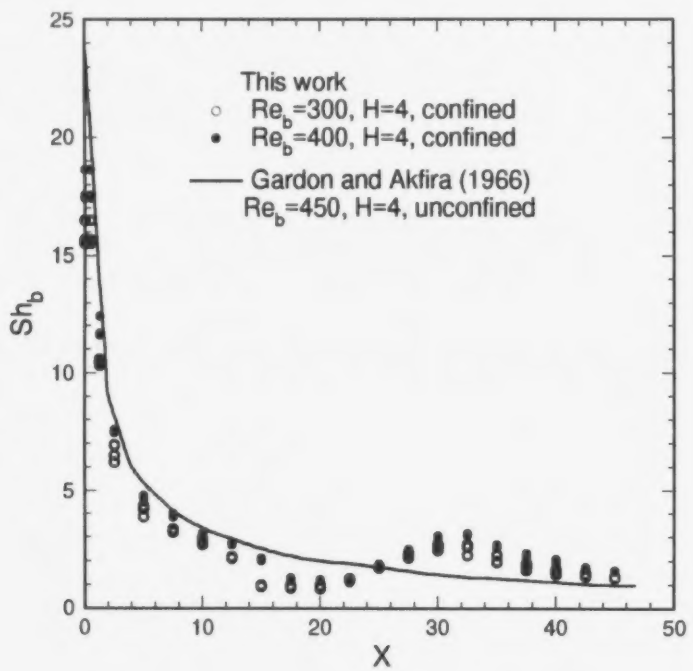

Figure 6.29 Comparison with the Work of Gardon and Akfirat: Single Jet

6.2.5 Mass Transfer at the Stagnation Point

In Figure 6.30, the experimental stagnation mass transfer rates due to a single slot jet obtained in this study are compared with the experimental data of Gardon and Akfirat (1966) and Sparrow and Wong (1975). From the comparison, it may be concluded that the data on the stagnation transfer rates vary greatly among the different investigations. The contributing factors to the large discrepancy may be the following:

1) The transfer rate at the stagnation point is normally the maximum and very sensitive to the experimental conditions.
2) The dimension of the jets and the shape of the velocity profile at the jet exit used by different investigators have some influence on the transfer rate at the stagnation point.
3) The size of the sensors used by different investigators studying heat transfer may have different averaging effects.

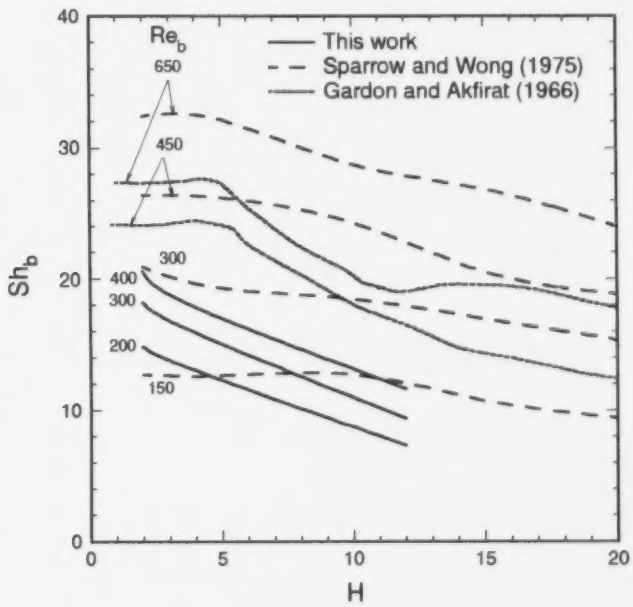

Figure 6.30 Comparison of the Stagnation Mass Transfer Rate with the Experimental Data in the Literature

Chapter 7
Mass Transfer Due to Two Confined Impinging Laminar Slot Jets: Symmetrical Flow

As the second the major part of this work, the flow and mass transfer characteristics of two confined impinging laminar slot jets with symmetrical flow are studied. The flow characteristics are examined numerically while the mass transfer characteristics are studied both numerically and experimentally. The case studied here resembles the two jets symmetrically located at the centre of a multiple confined impinging slot jet system. It may be anticipated that the mass transfer rate in the area between the two jets (the central region) will be low since the flow streams from the two jets counteract each other to form a stagnation flow region. This study examined the magnitude of the mass transfer rates inside and outside the stagnation region and the factors influencing the mass transfer rate. The parameters investigated are: Reynolds numbers: Re_b = 150, 300 and 450; jet-to-plate spacings: H = 2, 4, and 8; jet-to-jet spacings: S = 10, 20, and 30 for the case of H = 4. For every set of parameters, three experimental runs were conducted.

7.1 Flow Characteristics

The streamlines and the skin-friction factors along the impingement plate are investigated numerically and are presented in this section.

7.1.1 Streamline Contours

The effect of Reynolds number on the streamline contours for various cases is shown in Figures 7.1-7.5. It should be noted that the jet Reynolds number is defined for either of the two jets. This means that for the same Reynolds number, the actual flow rate out of the two jet system is twice as high as that of a single jet system.

For H = 2 and S = 10 shown in Figure 7.1, there is a primary vortex on the side downstream from the jet near the confinement plate. For the central region the fluid is essentially in a state of standstill except for the area immediately upstream from the jet, where a small and weak vortex (centre vortex) induced by the jet exists. An increase of Reynolds number has the effect of elongating the primary vortex.

For H = 4 and S = 10, 20 and 30, shown in Figures 7.2-7.4, a secondary vortex is formed downstream from the primary vortex near the impingement plate. With increasing Reynolds numbers, both the primary and the secondary vortices become stronger and larger. Except for shifting the locations of the vortices, the effect of jet-to-jet spacing on the flow streamlines is not obvious.

For H = 8 and S = 10 shown in Figure 7.5, the primary and secondary vortices are located further downstream when compared to the cases of H = 2 and 4 for S = 10. The centre vortex has completely filled the space between the two jets. For the case of the highest Reynolds number, Re_b = 450, another much weaker vortex appears near the confinement plate downstream from the secondary vortex.

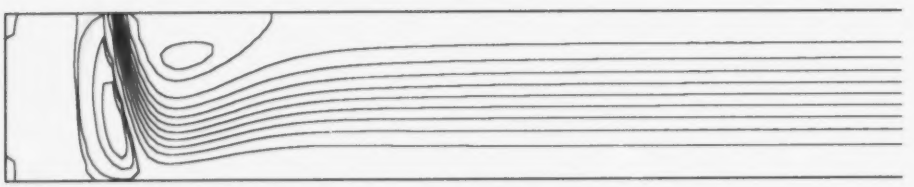

(a) $Re_b = 150$

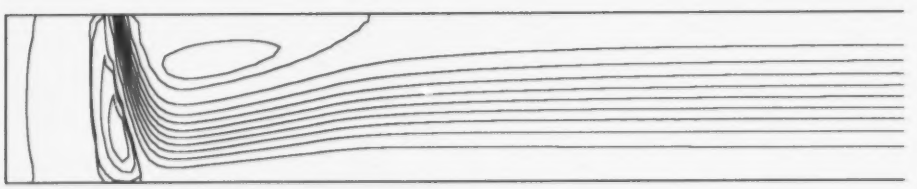

(b) $Re_b = 300$

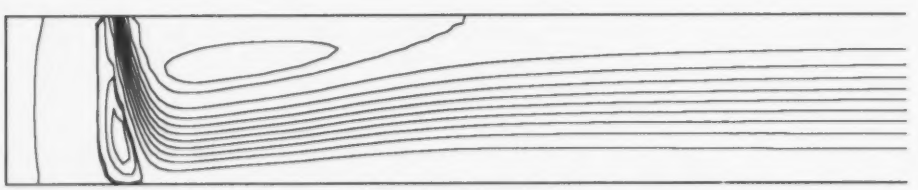

(c) $Re_b = 450$

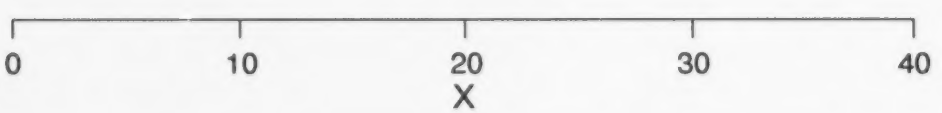

Figure 7.1 Streamline Contours for H = 2, S = 10: Symmetrical Flow

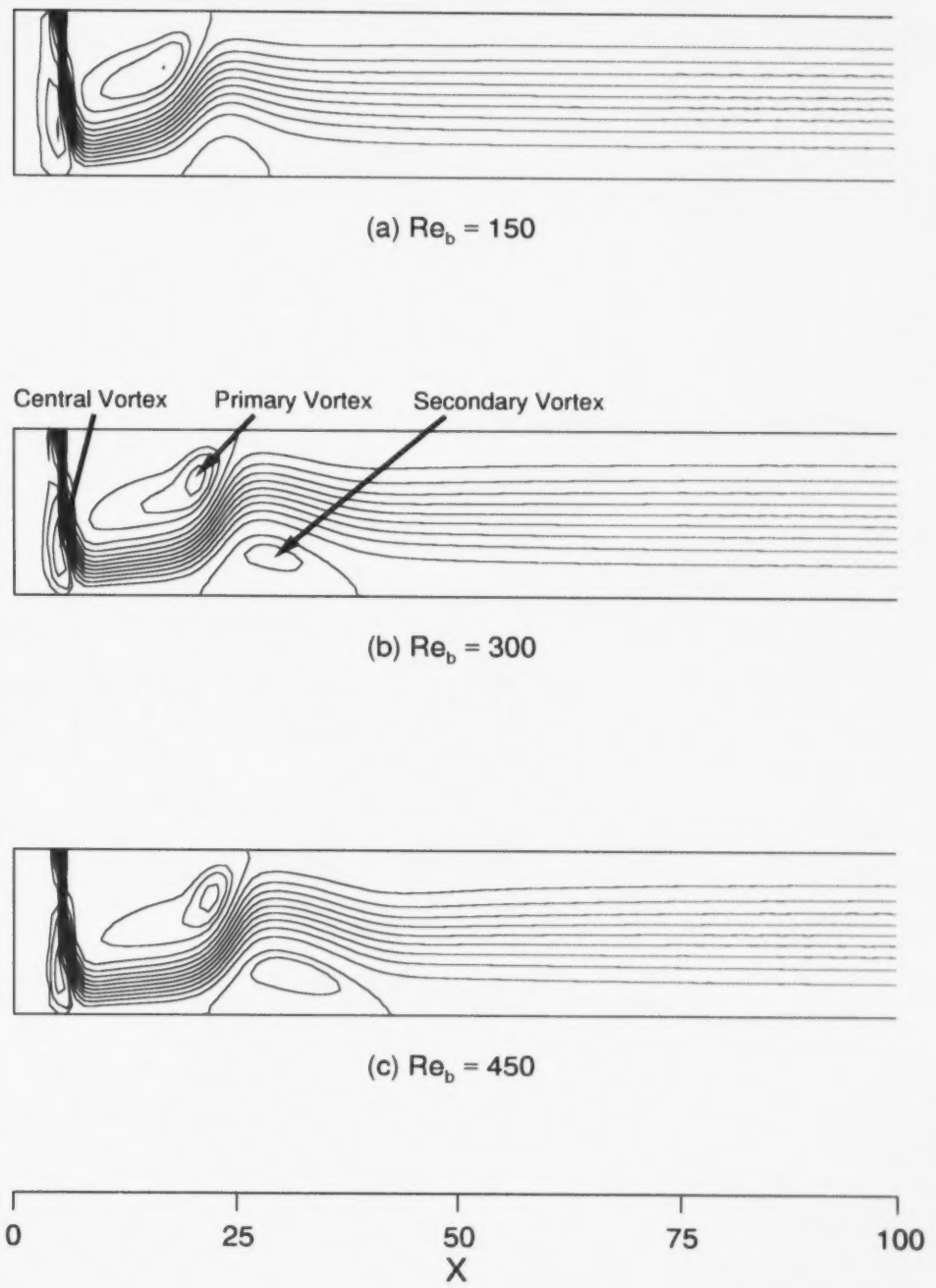

Figure 7.2 Streamline Contours for H = 4, S = 10: Symmetrical Flow

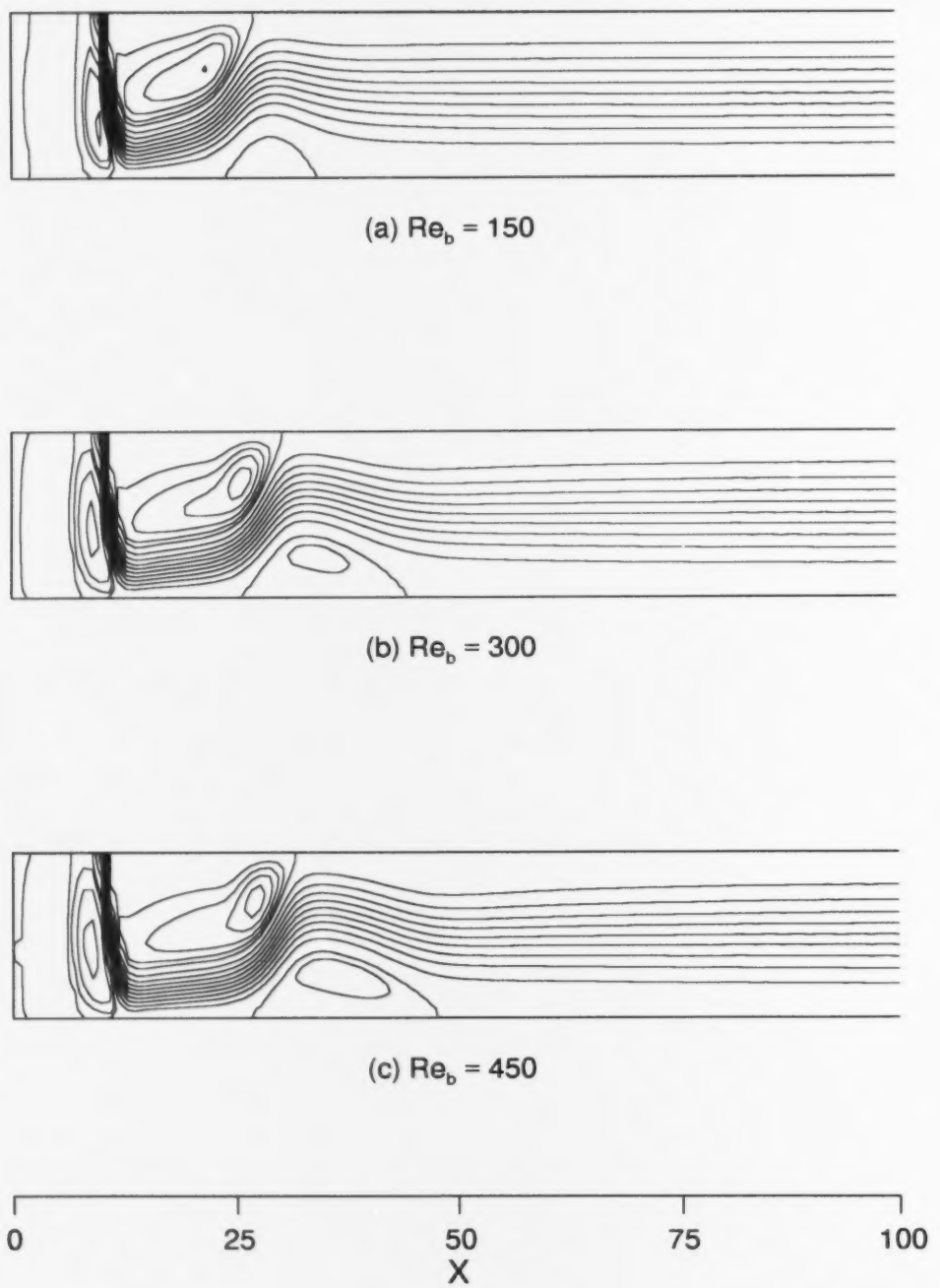

Figure 7.3 Streamline Contours for H = 4, S = 20: Symmetrical Flow

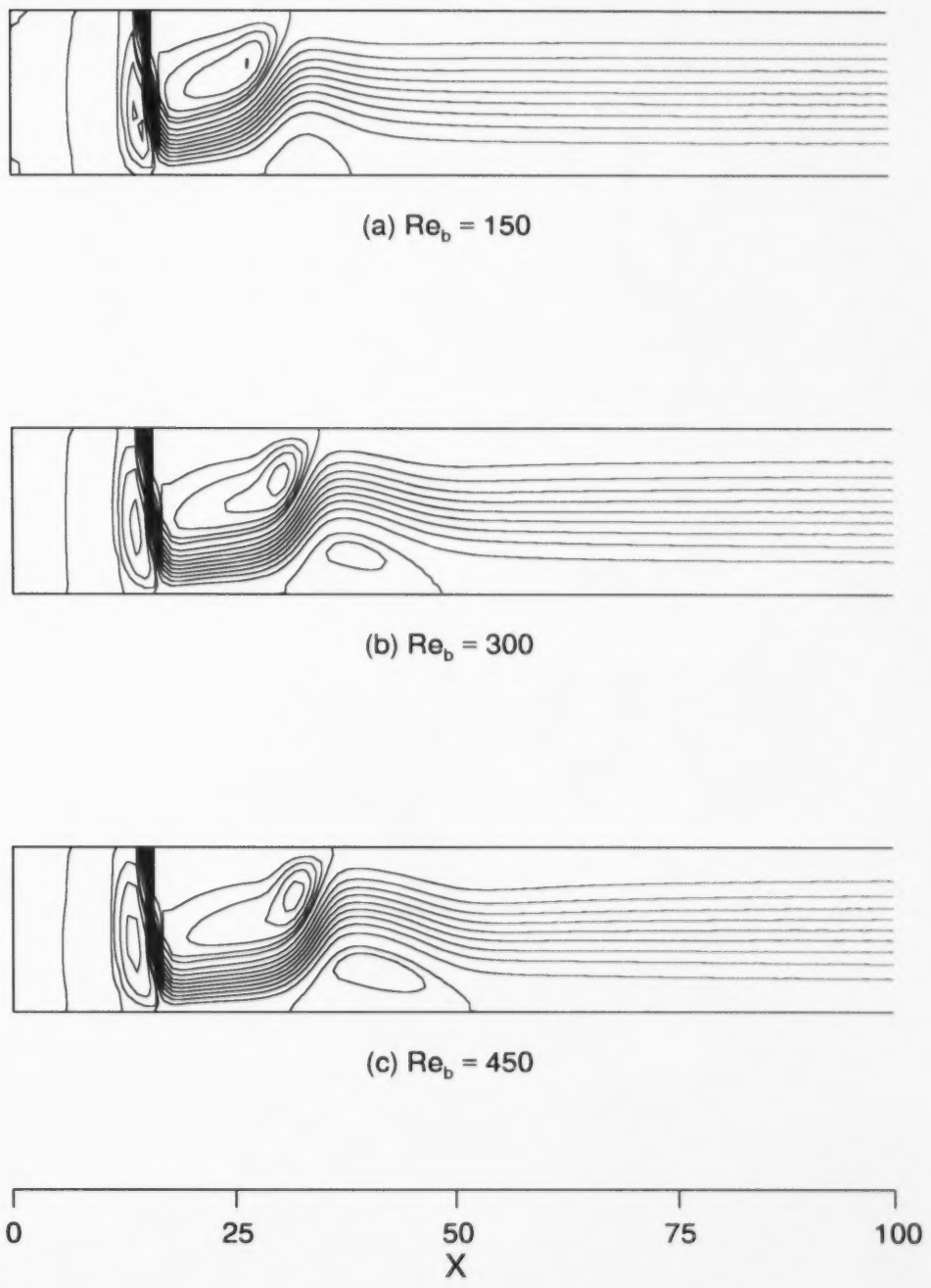

Figure 7.4 Streamline Contours for H = 4, S = 30: Symmetrical Flow

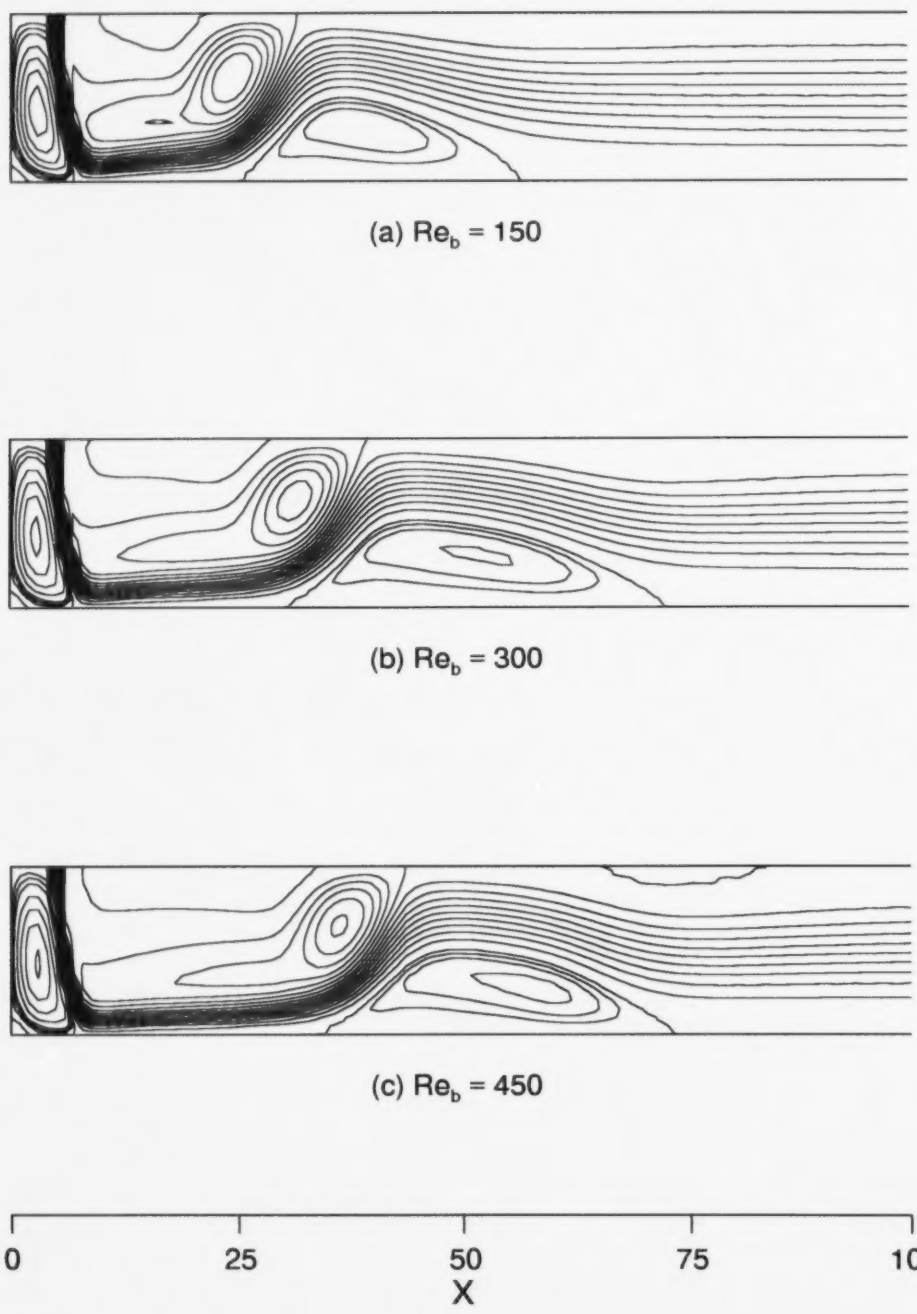

Figure 7.5 Streamline Contours for H = 8, S = 10: Symmetrical Flow

7.1.2 Skin-Friction Factor Along Impingement Plate

The local skin-friction factors along the impingement plate for various cases have been obtained from the numerically computed flow field and presented as C_fRe_b versus X in Figures 7.6-7.7. For fully developed flow between two parallel plates, the value of C_fRe_b is a constant given by Equation 5.100. For H = 2, 4, and 8, the constants are 3.0, 0.75 and 0.1875, respectively. When X is sufficiently large, the plot of C_fRe_b versus X for a given jet-to-plate spacing should approach its corresponding constant asymptotically.

Figure 7.6 shows the effect of Reynolds number on the friction-factor for a fixed jet-to-jet spacing, S = 10, and various jet-to-plate spacings. In all these cases, it is found that the maximum values of the friction-factor are located downstream from the jet. Higher Reynolds numbers result in larger positive or negative peaks. For H = 2 and 4, the friction-factor for almost the whole region between the two jets along the impingement plate remains zero. For the case of H = 8, non-zero values of friction-factor dominated the region between the two jets. For large X values, all the curves converge to the single constant value corresponding to that obtained for the fully developed flow between two parallel plates.

Figure 7.7 shows the effect of Reynolds number on the friction-factor for a fixed jet-to-plate spacing, H = 4, and various jet-to-jet spacings. From the plots, one can observe that a larger Reynolds number results in higher positive and negative peak values in C_fRe_b. Furthermore, with increasing jet-to-jet spacing, the peaks shift downstream, while the values of the peaks and shape of the curves remain essentially unchanged.

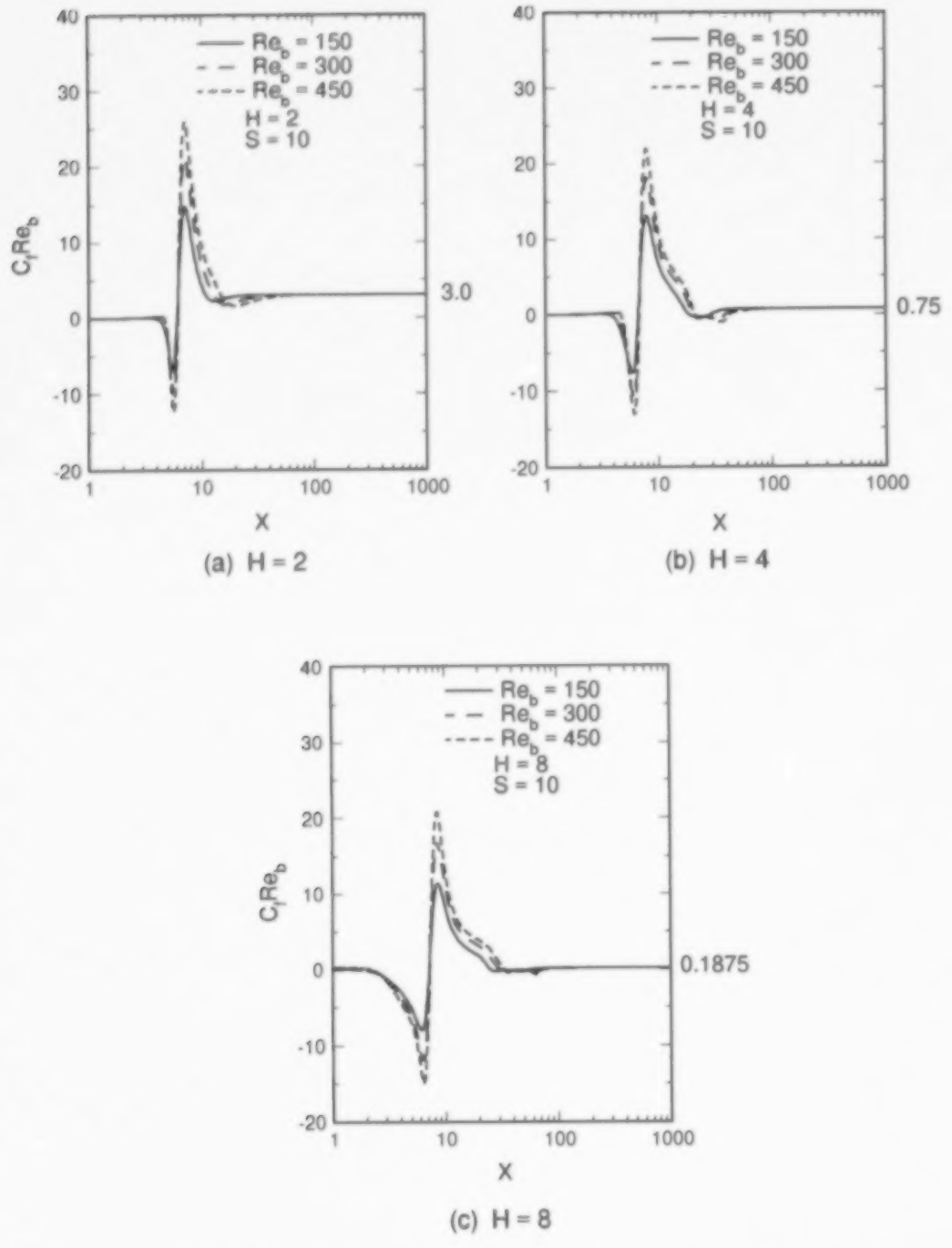

Figure 7.6 Skin-Friction Factor for S = 10: Symmetrical Flow

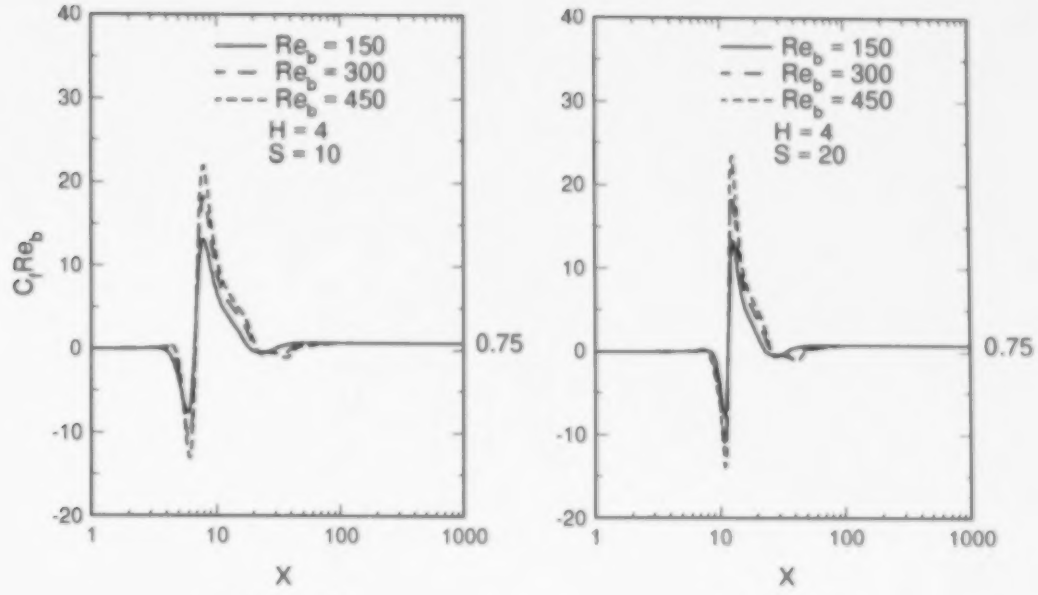

(a) S = 10

(b) S = 20

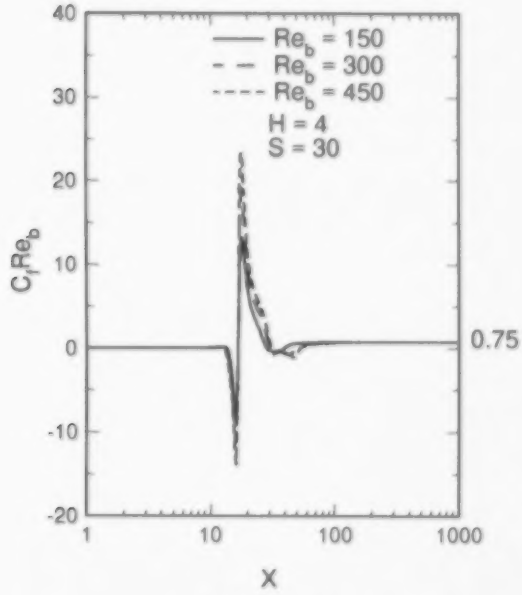

(c) S = 30

Figure 7.7 Skin-Friction Factor for H = 4: Symmetrical Flow

7.2 Mass Transfer Characteristics

The local mass transfer due to two confined impinging laminar slot jets is studied both numerically and experimentally. The effects of Reynolds number, jet-to-plate spacing, jet-to-jet spacing on the mass transfer rate along the impingement plate are investigated. The mass transfer rate is presented as Sherwood numbers defined in Equation 4.1. The experimental Sherwood number is calculated from Equation 4.7 while the numerical counterpart is evaluated from Equation 5.103.

7.2.1 Numerical Results

The effects of Reynolds number, jet-to-plate spacing and jet-to-jet spacing on the mass transfer rate along the impingement plate for various cases are presented in Figures 7.8-7.11. Figure 7.8 also contains some experimental data for general comparison.

Figure 7.8 shows the effect of Reynolds number on the mass transfer rate for a fixed jet-to-jet spacing, S = 10, and various jet-to-plate spacings. In all the cases shown, the increase in Reynolds number results in a higher mass transfer rate. However, the increase in the mass transfer rate from Re_b = 150 to 300 is much higher than that from Re_b = 300 to 450. An examination of the variation of Sh_b with X shows the following:

1) For H = 2 and 4, from the point of symmetry, X = 0, to the left side of the right jet, X = 4.5, the mass transfer rate is very low. For the same region with H = 8, the mass transfer rate first decreases up to X = 1 to 2, depending on the Reynolds numbers, and then increases monotonously until reaching the maximum.
2) For H = 2 and X > 4.5, the Sherwood number increases monotonously until a maximum value located downstream from the jet, then decreases monotonously. The monotonous decrease in Sherwood number is the result of lack of secondary vortex as was indicated by Figure 7.1. For both H = 4 and 8, the plot of Sh_b versus X shows a secondary peak and trough downstream from the jet.

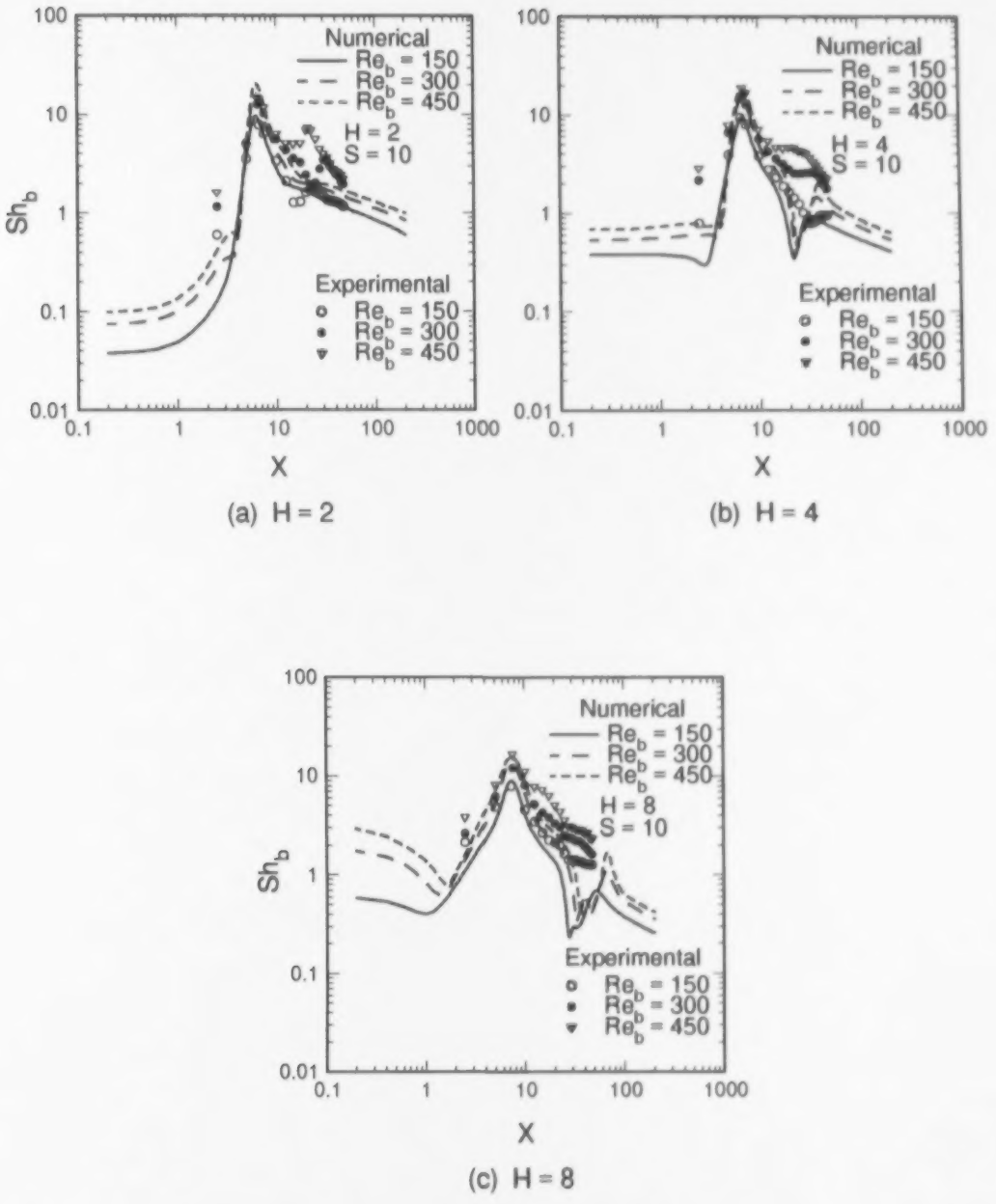

Figure 7.8 Effect of Reynolds Number on Numerical Mass Transfer Rate for S = 10: Symmetrical Flow

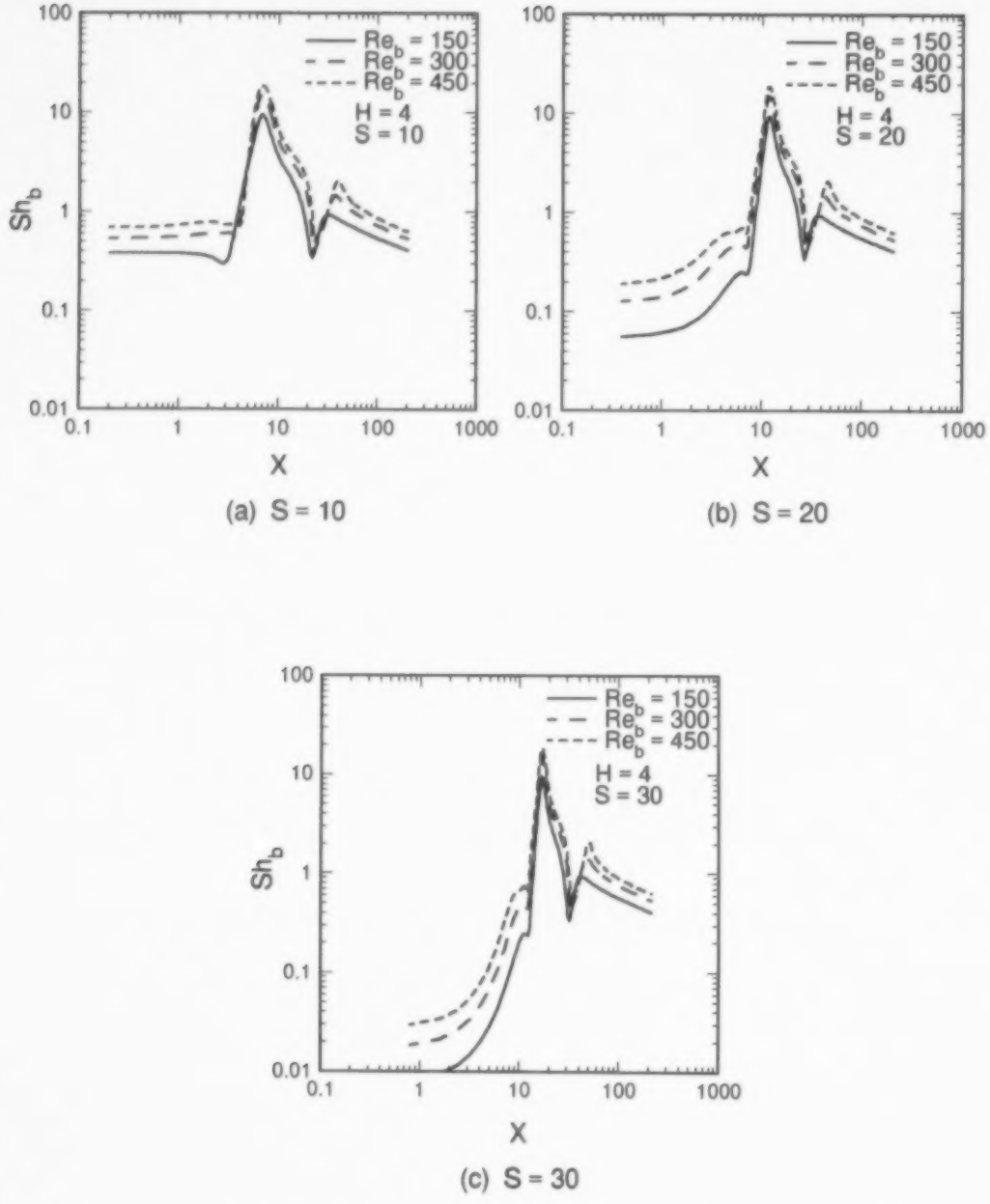

Figure 7.9 Effect of Reynolds Number on Numerical Mass Transfer Rate for H = 4: Symmetrical Flow

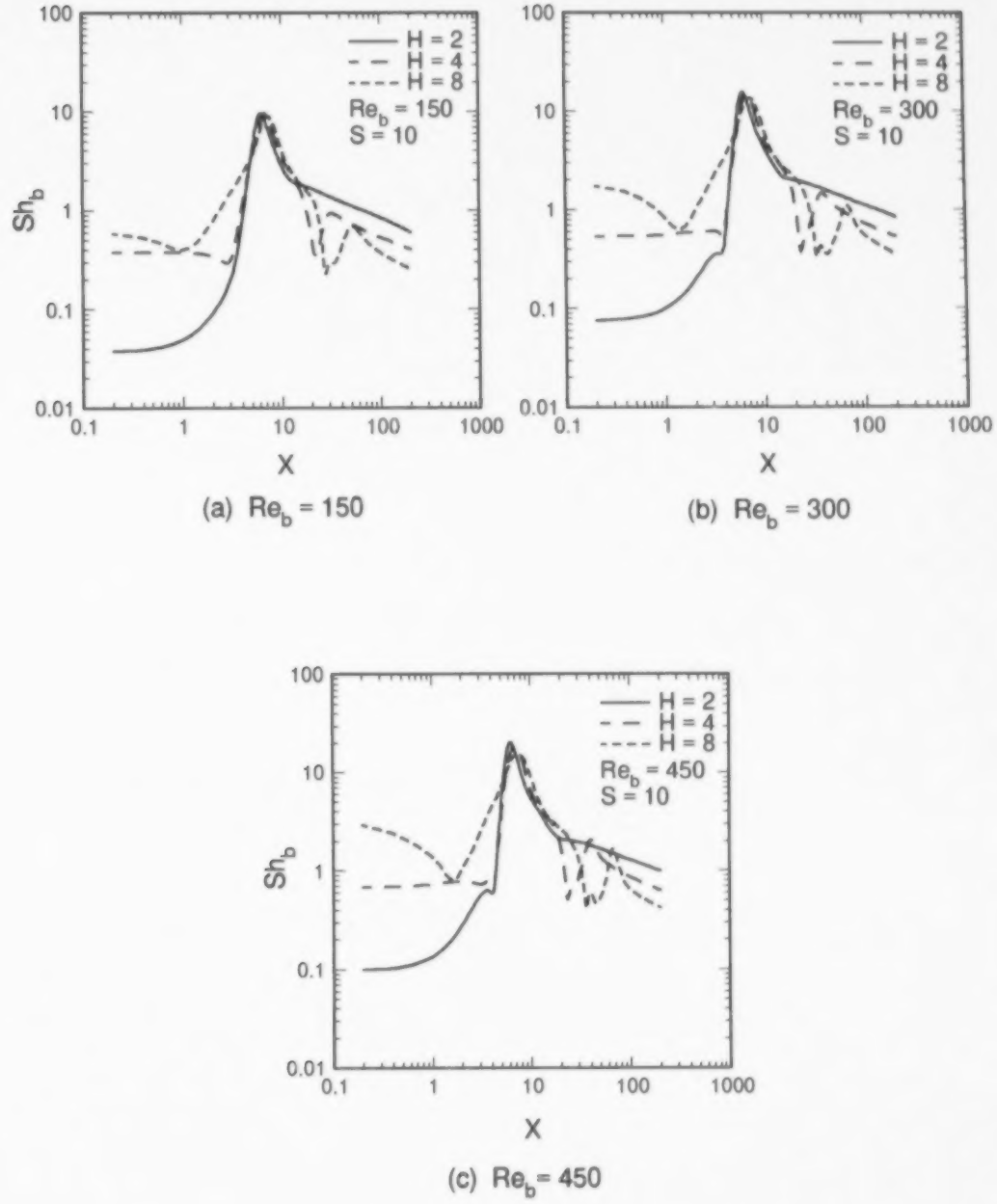

Figure 7.10 Effect of Jet-to-Plate Spacing on Numerical Mass Transfer Rate for S = 10: Symmetrical Flow

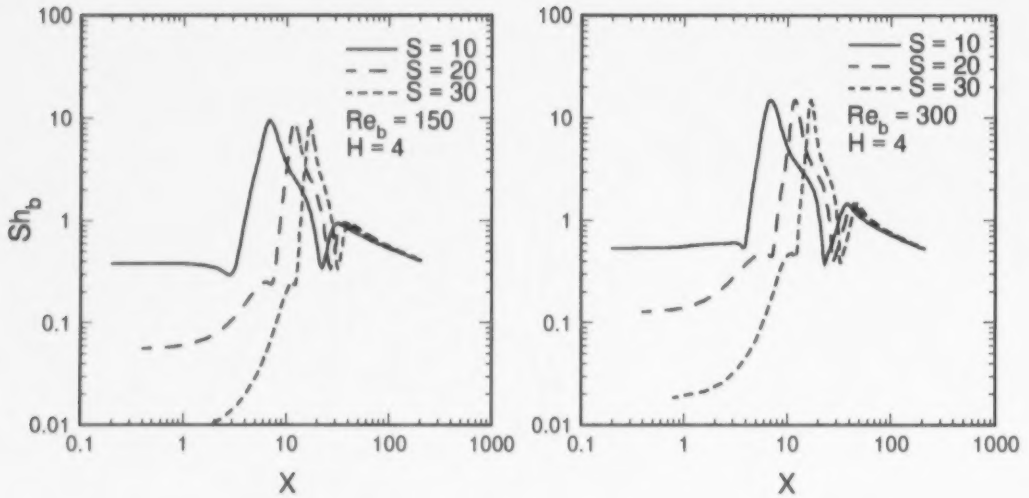

(a) $Re_b = 150$ (b) $Re_b = 300$

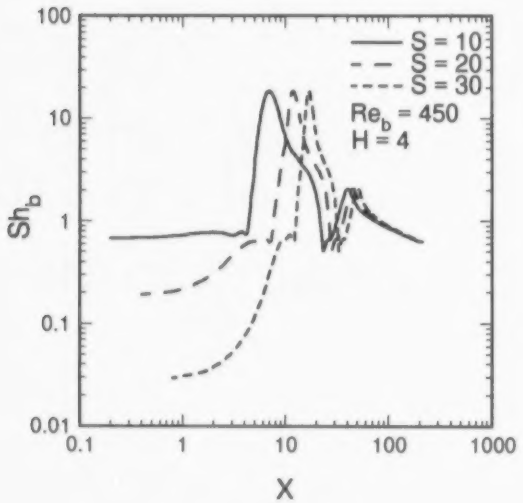

(c) $Re_b = 450$

Figure 7.11 Effect of Jet-to-Jet Spacing on Numerical Mass Transfer Rate for H = 4: Symmetrical Flow

The secondary peak and trough can be attributed to the secondary vortex as shown in Figures 7.2 and 7.5.

3) For all the cases shown in Figure 7.8, the maximum Sherwood number does not occur at the centre of the jet, rather it appears at a location downstream. This is different from the case of a single impinging jet. The difference can be explained by examining the streamlines for the two different systems. For the single impinging jet system, as shown in Figures 6.1-6.3, the streamline at the centre of the jet travels along the axis of symmetry to the impingement plate, forming a stagnation point. The streamlines near the stagnation point change their directions sharply near this point. Therefore, the maximum transfer rate occurs right at the stagnation point, and the whole stagnation region is characterised as a high transfer rate region. On the other hand, for the two-jet system, all the flow from one jet travels to one side of the channel confined by the impingement plate and the confinement plate. Therefore, as shown in Figures 7.1-7.5, the streamline connecting to the impingement plate is not the central streamline of the jet which has the highest momentum, but the streamline from the inner wall of the jet which has a momentum of zero. Since all the streamlines from one jet are forced to travel to one side of the channel, the maximum mass transfer rate also occurs downstream from the jet.

Figure 7.9 shows the effect of the Reynolds number on the local mass transfer rates for H = 4 and three different jet-to-jet spacings. Again, a higher Reynolds number results in a higher mass transfer rate.

Figure 7.10 depicts the effect of jet-to-plate spacing on the mass transfer rate for S = 10 and various Reynolds numbers. The following four points can be drawn from the plots:

1) For the region between the two jets, the mass transfer rate increases with increasing jet-to-plate spacing.
2) The maximum value of the mass transfer rate is not significantly influenced by

the jet-to-plate spacing in the range investigated.

3) The location of the maximum mass transfer rate moves slightly downstream with an increasing jet-to-plate spacing.

4) Except for H = 2, there exist a local maximum and a local minimum for the mass transfer rate downstream from the jet, and the location of the local extrema moves downstream when the jet-to-plate spacing is increased.

The effect of jet-to-jet spacing on the mass transfer rate can be examined in Figure 7.11. From these plots, the following conclusions can be drawn:

1) For the region between the two jets, an increase in the jet-to-jet spacing decreases the mass transfer rate up to the vicinity of the jet.

2) The magnitudes of the primary and secondary peaks and the secondary trough are not influenced by the increase of the jet-to-jet spacing, but their locations are shifted downstream.

3) Far away from the jet, the plots of Sh_b versus X for all the three jet-to-jet spacings converge to a single curve.

7.2.2 Experimental Results

For the case of two confined impinging laminar slot jets with symmetrical flow, the experimental results are presented in this section in the form of plots showing the influences of various factors. The operating conditions and the complete compilation of the experimental results are presented in Appendix E.

7.2.2.1 Mass Transfer Pattern

Typical "frozen fringe" patterns for H = 2, 4 and 8 with S = 10 and Re_b = 300 are presented in Figures 7.12-7.14. In each of the figures, two image photographs from the video recording are presented, one was taken a short time after the experiment has started, mainly showing the mass transfer patterns around the jets; the other was taken at a much longer time, mainly showing the mass transfer patterns downstream.

Figure 7.12a shows that for H = 2, S = 10 and Re_b = 300, the equal mass transfer rate lines (the dark fringes) near the jets are mainly straight, signifying a typical laminar and two dimensional behaviour. This photograph also shows that while the first couple of fringes just started to appear on the region nearby of the impinging jets, another much wider dark fringe was also formed far downstream. This shows that the secondary peak downstream is also quite strong. Figure 7.12b shows the mass transfer patterns at t = 255 seconds. At this time, although the fringes near the jets are already unrecognizable, those downstream from the jet are very clear. It is noted from this figure that there exists a local maximum in the mass transfer rate region and that the fringe lines are quite irregular in shape.

Figure 7.13a shows the mass transfer patterns around the impinging jets for t = 30 seconds for H = 4, S = 10 and Re_b = 300. Again, the mass transfer pattern in this region may be regarded as laminar and two-dimensional. Unlike the case shown in Figure 7.12a, no secondary peak downstream appeared even though the time elapsed is longer. However, the next photograph, Figure 7.13b, shows a very complex mass transfer pattern for the region downstream from the jet. This is a clear and strong indication that the flow in the region where the complex mass transfer pattern appear is no longer two-dimensional. The complex mass transfer pattern may be the result of flow-induced disturbances in combination with three-dimensional effect.

When the jet-to-plate spacing is further increased to H = 8, as shown in Figure 7.14, the mass transfer pattern seems to have changed back such that it is similar to the case of H = 2 as shown in Figure 7.12. However, a comparison between Figure 7.14a and Figure 7.12a reveals that the dark fringes around the jets for H = 8 are not as straight as those for H = 2, signifying three-dimensional effects for the case of H = 8. In addition, a comparison of Figure 7.14b with Figure 7.12b also shows some dramatic differences: for H = 8, the local maximum for the mass transfer rate is nonexistent and the fringe lines are much smoother.

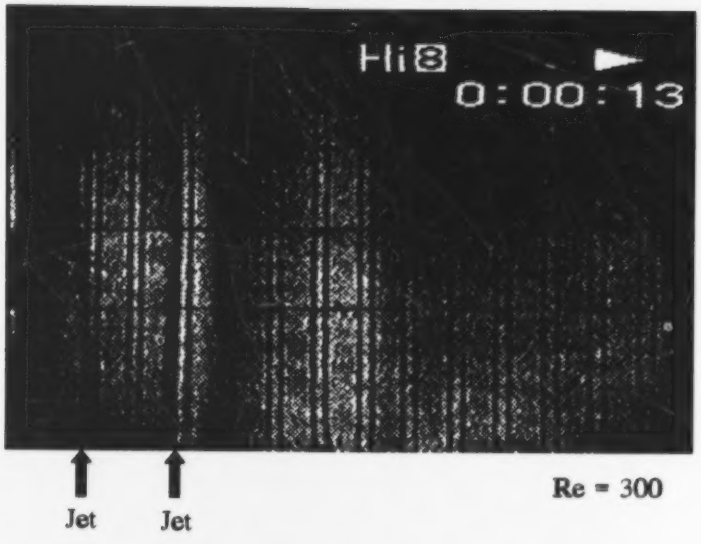

(a) t = 13s

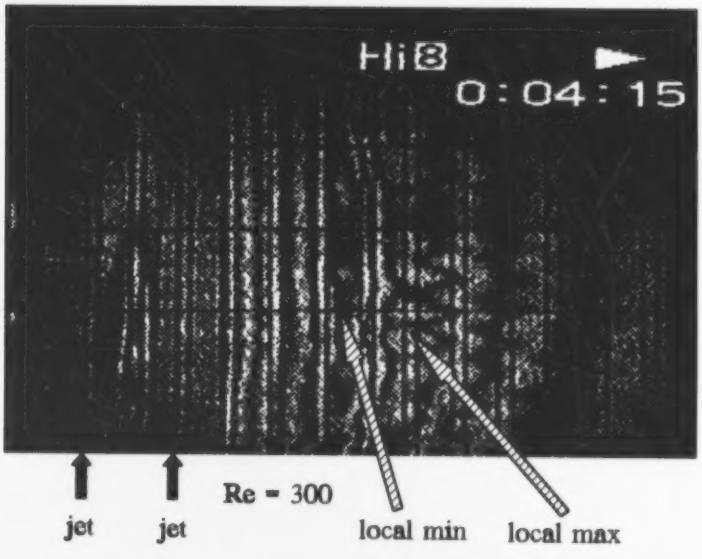

(b) t = 255s

Figure 7.12 Contours of Equal Mass Transfer Rate for H = 2, S = 10: Symmetrical Flow

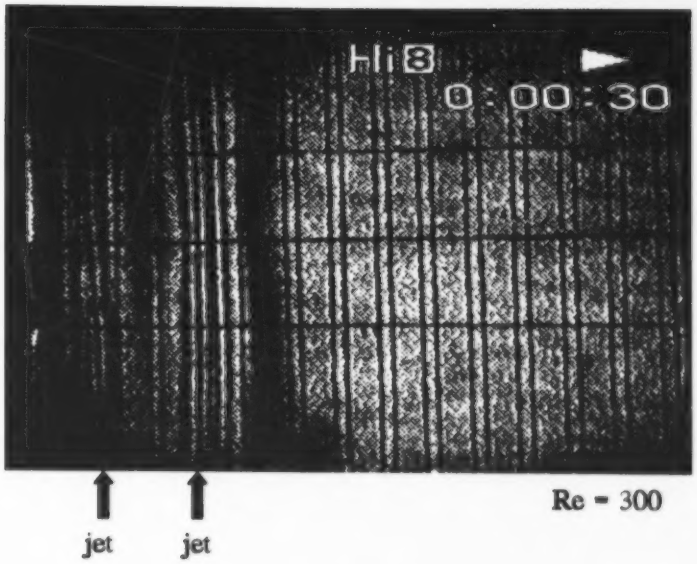

(a) t = 30 s

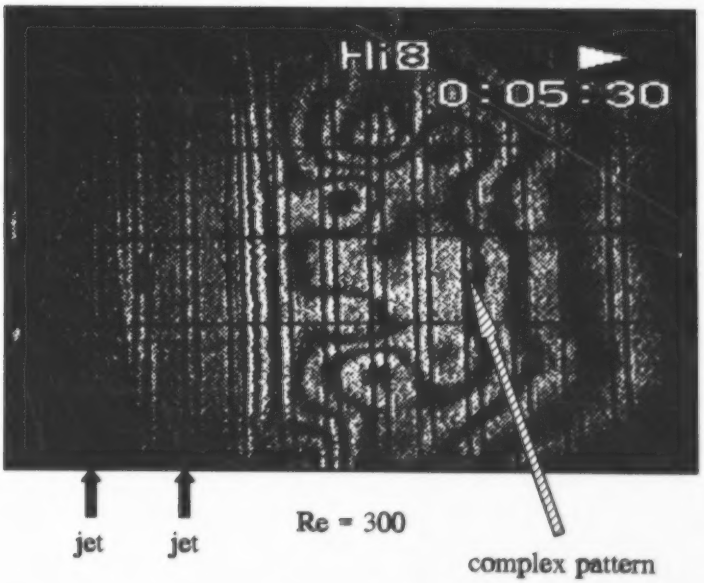

(b) t = 330 s

Figure 7.13 Contours of Equal Mass Transfer Rate for H = 4, S = 10: Symmetrical Flow

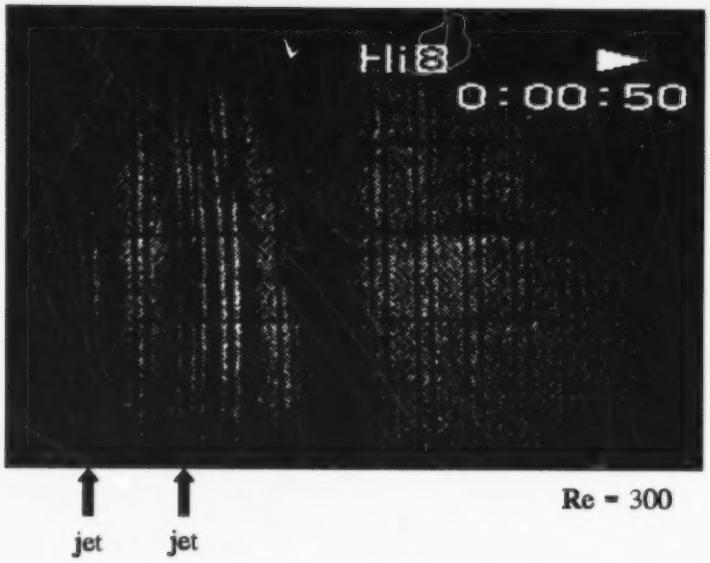

(a) t = 50 s

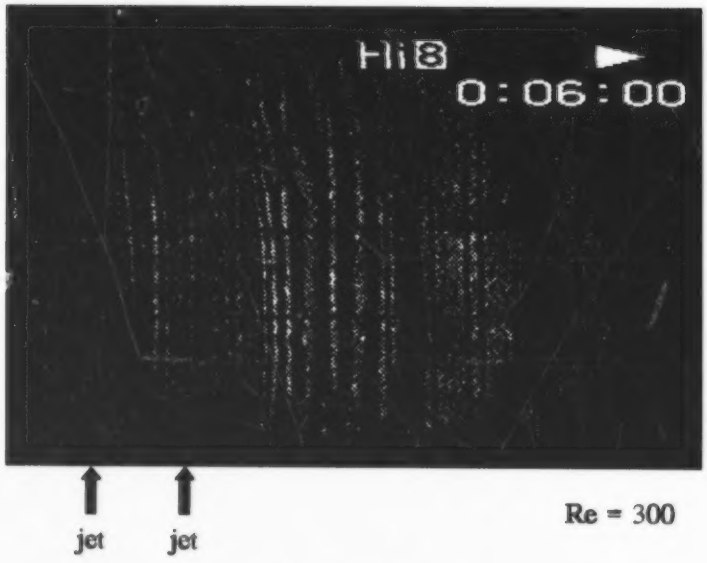

(b) t = 300 s

Figure 7.14 Contours of Equal Mass Transfer Rate for H = 8, S = 10: Symmetrical Flow

To have a better view of the overall mass transfer patterns for the typical cases, digitized contours of Sherwood numbers for various cases are presented in Figures 7.15-7.17. By examining these figures, one may clearly identify two influencing factors to the mass transfer pattern: three-dimensional (3-D) effect and disturbances. The former depicts itself as higher mass transfer rate in the central region of the cross-section and the latter is responsible for the irregularity of the mass transfer pattern as seen in Figures 7.15b and 7.16b. When Reynolds number is small, as shown in Figures 7.15a, 7.16a, and 7.17a, the 3-D effect is more obvious, especially for the region far downstream from the impinging jet. The 3-D effect increases with increasing jet-to-plate spacing. The effect of disturbances increases with increasing Reynolds numbers. Similar to the argument for the case of a single impinging jet, the "potential core" theory seems to be still applicable to the two-jet case. For H = 2 and 4, when the jet flow stream reaches the impingement plate, the centre of the stream is still in the "potential core" with high momentum, resulting in high mass transfer rate in the region of impact. However, since the flow from one jet is directed to one side due to counteracting effect of the two jets, the impact is weaker compared to the case of a single jet. To some extent, the effect of the two symmetrical impinging jet flow is similar to that of a one impinging jet flow combined with a cross-flow, a factor known to reduce the mass transfer rate. In this case, the location where the maximum mass transfer rate occurs is shifted downstream from directly underneath the jet. The distance of the shift depends on the jet-to-plate spacing and the Reynolds number. When the Reynolds number is high, the flow stream may induce some disturbances, resulting in a secondary peak in the transfer rate, as shown in Figures 7.15b and 7.16b.

For H = 8 shown in Figure 7.17, since the flow stream has been engulfed before reaching the impingement plate, the impact is weakened, resulting in a much lower mass transfer rate in the region of impact when compared with the case of same Reynolds number but a smaller jet-to-plate spacing. In addition, since this weakened flow stream is not capable of inducing disturbances, no secondary peak in mass transfer rate exists downstream from the impinging jet. However, the 3-D effect can

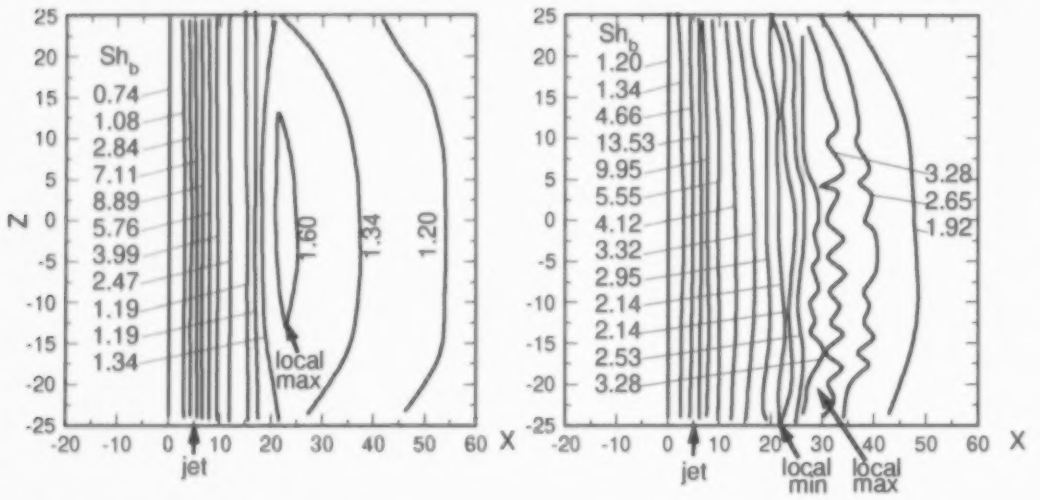

(a) H = 2, S = 10, Re_b = 150 (b) H = 2, S = 10, Re_b = 300

Figure 7.15 Digitized Contours of Sherwood Numbers for H = 2, S = 10: Symmetrical Flow

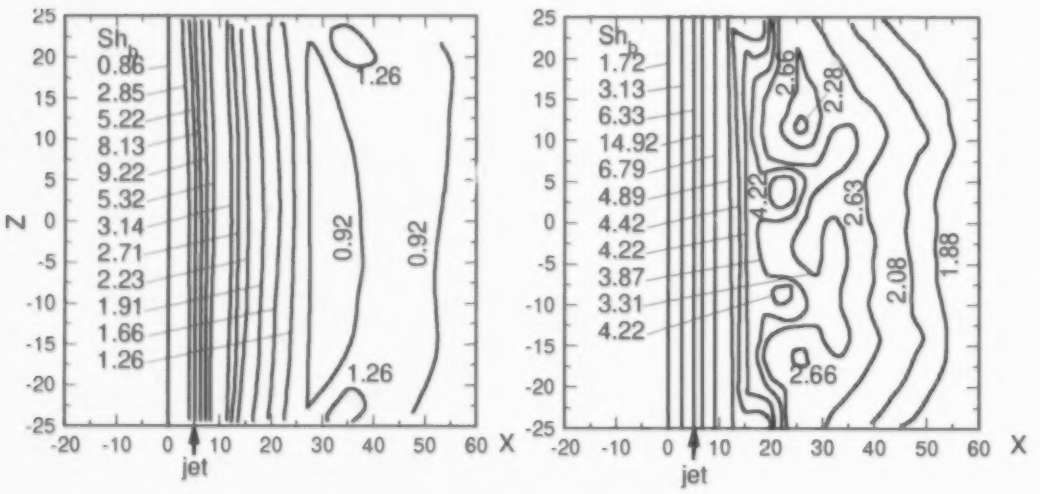

(a) H = 4, S = 10, Re_b = 150 (b) H = 4, S = 10, Re_b = 300

Figure 7.16 Digitized Contours of Sherwood Numbers for H = 4, S = 10: Symmetrical Flow

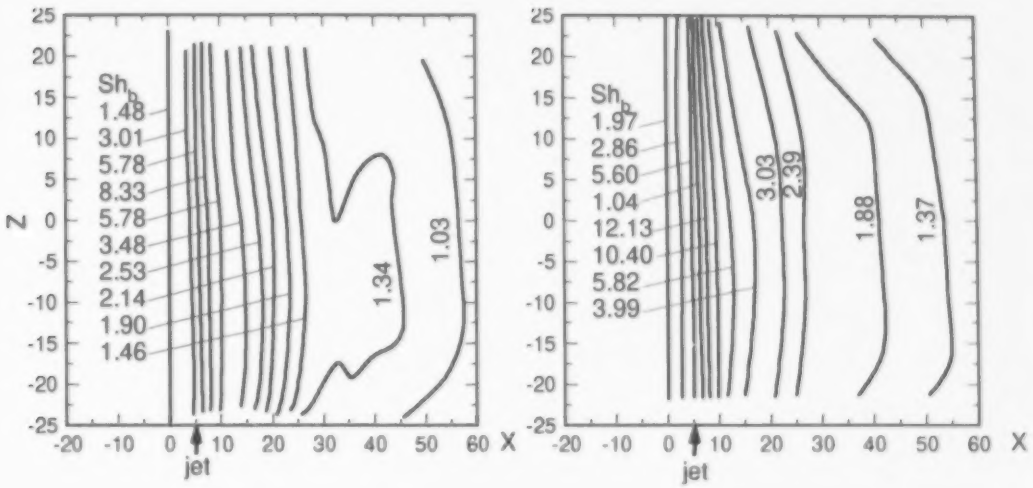

(a) H = 8, S = 10, Re_b = 150 (b) H = 8, S = 10, Re_b = 300

Figure 7.17 Digitized Contours of Sherwood Numbers for H = 8, S = 10: Symmetrical Flow

be clearly identified, especially for the low Reynolds number shown in Figure 7.17a.

7.2.2.2 Effect of Reynolds Number

The effect of the Reynolds number on the mass transfer rate for S = 10 and various jet-to-plate spacings is shown in Figure 7.18. For H = 2, as shown in Figure 7.18a, the following points may be observed:

1) In general, higher Reynolds numbers result in higher local Sherwood numbers.
2) For all the three different Reynolds numbers studied, the Sherwood numbers on the central region are about ten times smaller than the maximum values located close but downstream from the jet.
3) Starting from X = 5, half of the distance between the two jets, the Sherwood numbers increase sharply and reach the maximum values at about X = 6.5.
4) Downstream from the peak values, the Sherwood numbers decrease sharply. For all three Reynolds numbers, there exists a local maximum Sherwood number

and a local minimum Sherwood number. The secondary peaks become more obvious with increasing Reynolds numbers.

Figure 7.18b shows the plots of Sherwood number versus X for H = 4. The following points may be observed from the plots.

1) The Sherwood numbers on the central region are about ten times smaller than their corresponding peak values.
2) The peak values are located at about X = 6.75.
3) For Re_b = 150, no secondary peak is observed. For Re_b = 300 and 450, there exists a secondary peak, but the fluctuations are much smaller compared with the case of H = 2.

Figure 7.18c shows the plots of Sherwood number versus X for H = 8. The following points may be observed from the plots.

1) The Sherwood numbers on the central region are about five times smaller than their corresponding peak values.
2) The peak values are located at about X = 7.5.
3) The plots of Sherwood number versus X are monotonic after the peak values.

The effect of the Reynolds number on the mass transfer rate for H = 4 and various jet-to-jet spacings is shown in Figure 7.19. The case of H = 4 and S = 10 has been discussed earlier as in Figure 7.18b. It is included in this set of plots only for the sake of comparison. From Figure 7.19b for S = 20, the following conclusions can be drawn:

1) The average Sherwood numbers on the central region are still about ten times smaller than the corresponding peak values for the three Reynolds numbers investigated. For Re_b = 150, the Sherwood number on the central region does not change significantly. For both Re_b = 300 and 450, the Sherwood numbers show a local maximum at the point of symmetry, X = 0. The Sherwood numbers then decrease to a local minimum at about X = 5 before increasing to a peak value at about X = 11.5.

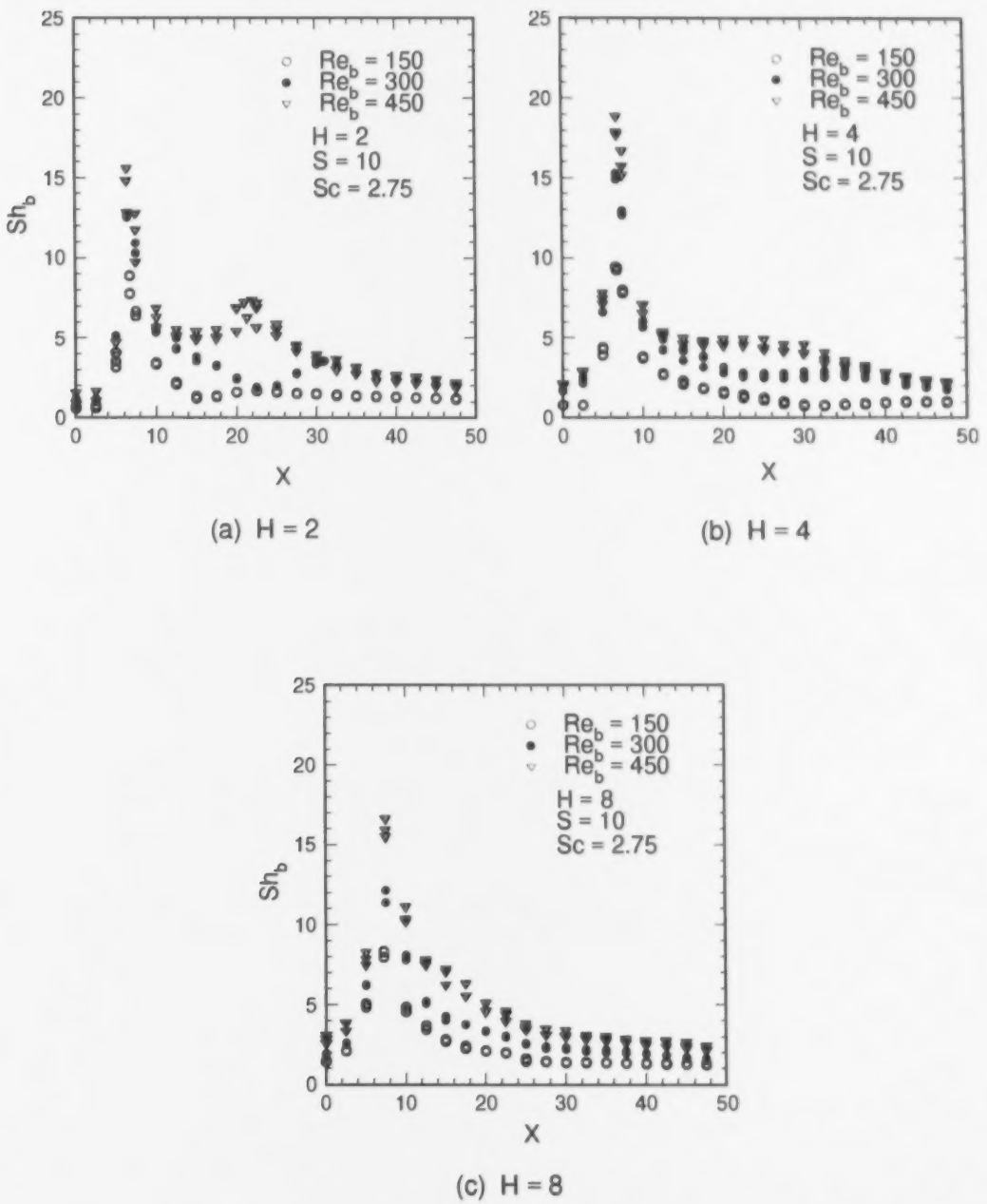

Figure 7.18 Effect of Reynolds Number on the Experimental Mass Transfer Rate for S = 10: Symmetrical Flow

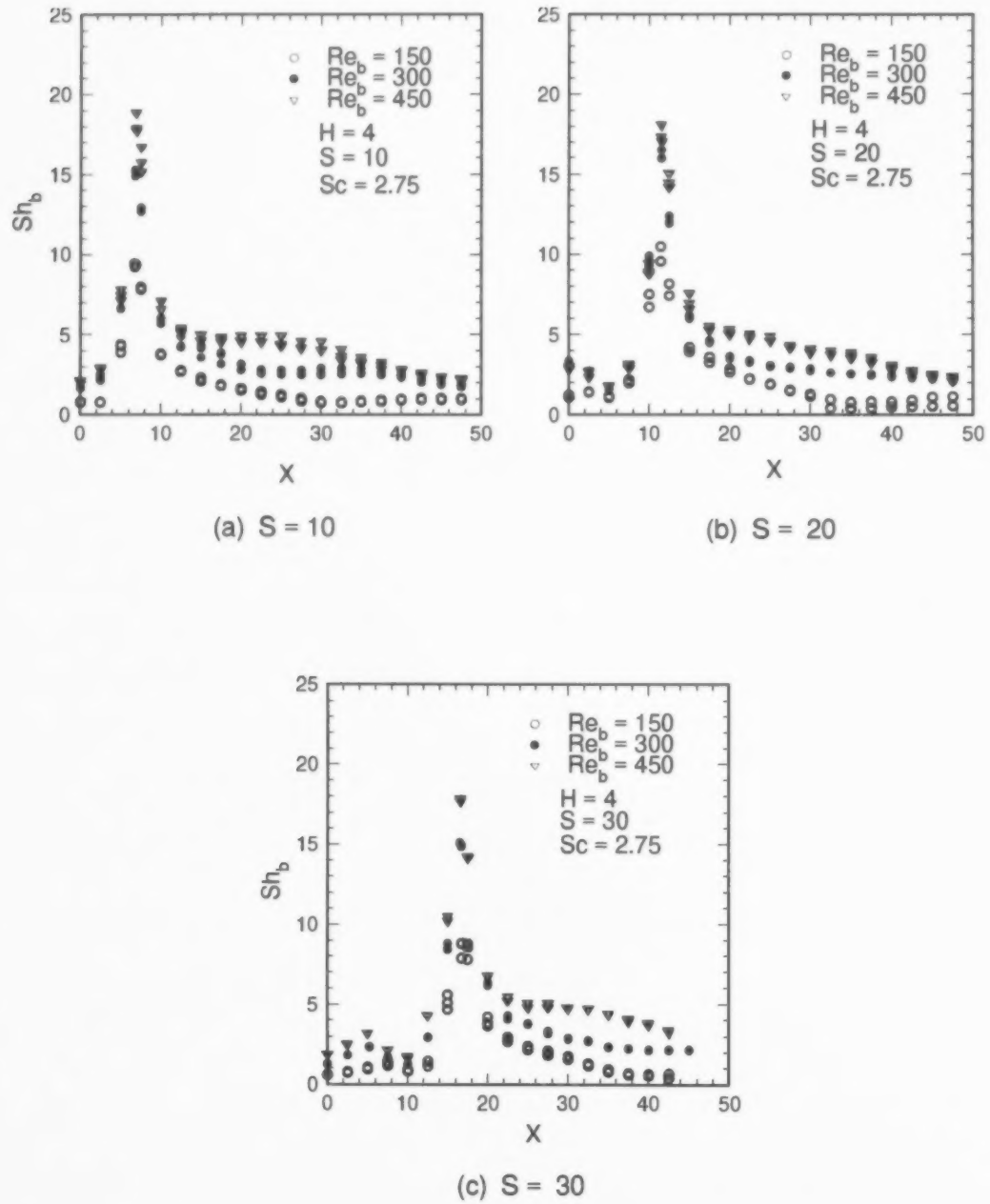

Figure 7.19 Effect of Sherwood Number on the Experimental Mass Transfer Rate for H = 4: Symmetrical Flow

2) The plots of Sherwood numbers versus X are nearly monotonous downstream from the peak values.

Figure 7.19c shows the effect of Reynolds number on the mass transfer rate for the case of H = 4 and S = 30. It can be observed that the increase in the jet-to-jet spacing make the local Sherwood numbers on the central region more complicated. For all the three Reynolds numbers, the local Sherwood number first increases from X = 0 until X is about 5, and then decreases until X is about 10. The average Sherwood number in the central region is about nine times smaller than the corresponding peak values which are located at about X = 16.6.

7.2.2.3 Effect of Jet-to-Plate Spacing

The effect of jet-to-plate spacing on the mass transfer rate can be examined in Figure 7.20. From all the plots shown in Figure 7.20, one can draw the following conclusions:

1) In the central region, the Sherwood number increases as the jet-to-plate spacing increases.
2) The case of H = 4 produces the highest peak Sherwood numbers for all the three Reynolds numbers investigated.
3) Higher jet-to-plate spacings result in less fluctuation in the Sherwood number downstream from the peak values for all the three Reynolds numbers studied.

7.2.2.4 Effect of Jet-to-Jet Spacing

Figure 7.21 shows the effect of jet-to-jet spacing on the mass transfer rate for H = 4 and various Reynolds numbers. With the same Reynolds number, the shape of the curves for the three different jet-to-jet spacings is very similar, with the peak moving downstream for higher jet-to-jet spacings. Although the average Sherwood number in the central region remains nearly constant for a given Reynolds number, the fluctuation increases with a higher jet-to-jet spacing. For Re_b = 150 and 300, the case with S = 20 gives the highest peak in the Sherwood number, while for Re_b = 450 the

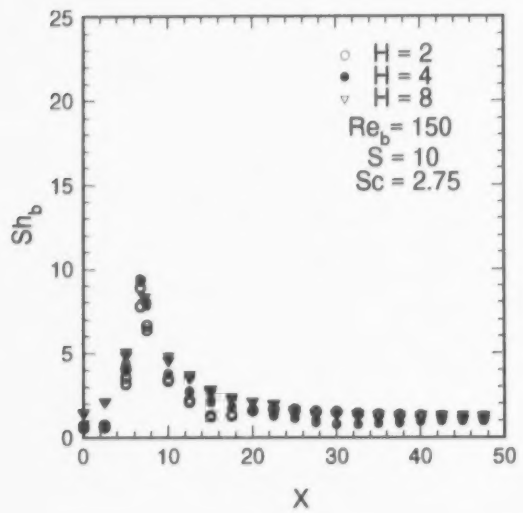

(a) $Re_b = 150$

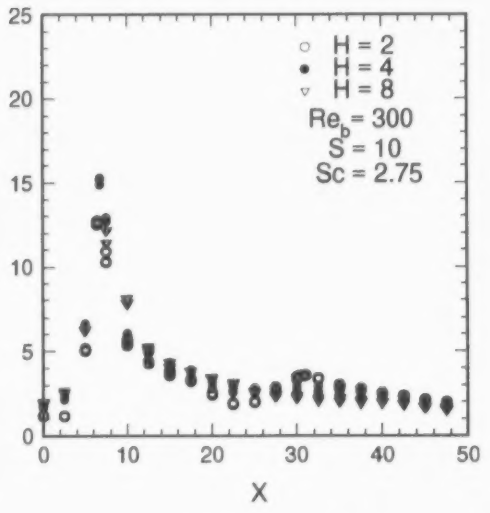

(b) $Re_b = 300$

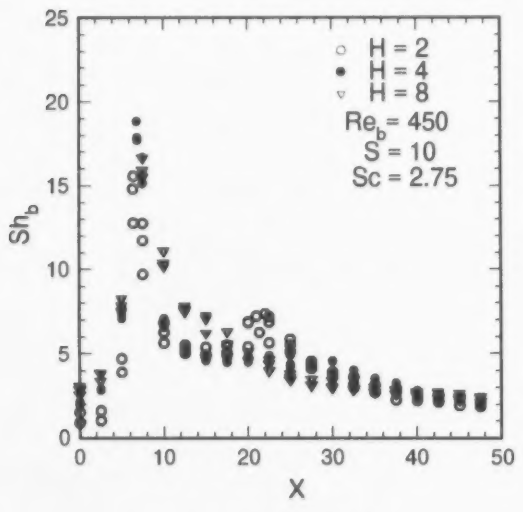

(c) $Re_b = 450$

Figure 7.20 Effect of Jet-to-Plate Spacing on the Experimental Mass Transfer Rate for S = 10: Symmetrical Flow

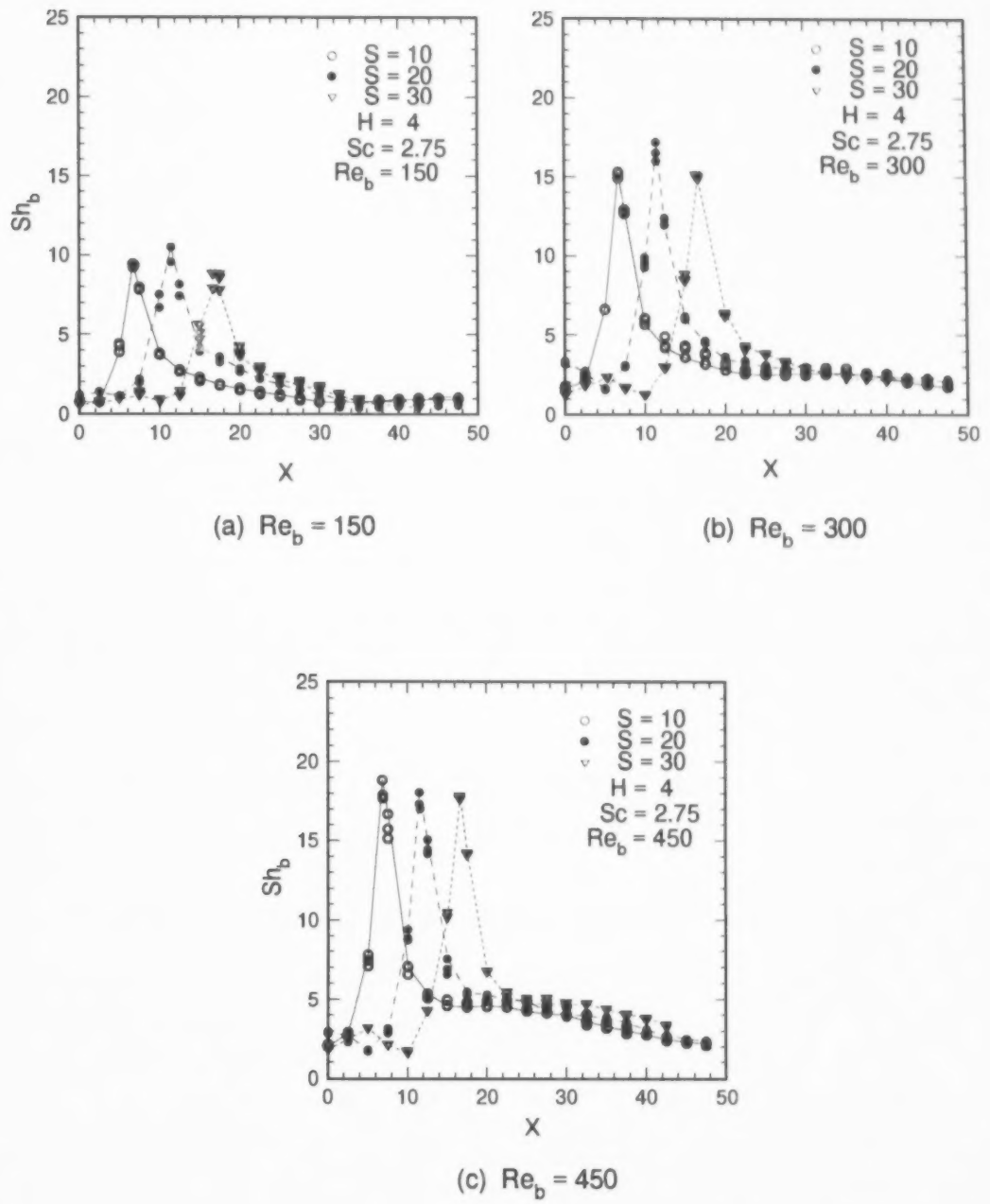

Figure 7.21 Effect of Jet-to-Jet Spacing on the Experimental Mass Transfer Rate for H = 4: Symmetrical Flow

peak value decreases monotonically with a higher jet-to-jet spacing. The difference in the peak values for various jet-to-jet spacings for a given Reynolds number is not significant.

7.2.3 Comparison Between Numerical and Experimental Results

Comparison between the numerical and experimental mass transfer results due to two impinging laminar slot jets with symmetrical flow is discussed in this section.

For H = 2 and S = 10, the results for the three Reynolds numbers, i.e., Re_b = 150, 300 and 450 are presented in Figure 7.22. For Re_b = 150, the agreement between the numerical and experimental results is very good. When Reynolds number is increased to 300 and 450, the following points can be observed:

1) The location of the maximum Sherwood number predicted by the numerical computation coincides with the experimental results. The predicted peak values, on the other hand, are about 23% and 36% higher than the experimental values for Re_b = 300 and 450, respectively.
2) For the region downstream from the peak, the numerical computation fails to predict the local maximum Sherwood number. As discussed earlier, the secondary peak becomes more and more evident when the Reynolds is increased. From Figure 7.15b, it may be postulated that the secondary peak is caused by flow induced disturbances. And the intensity of the disturbances increases with Reynolds numbers. However, in the numerical prediction, no disturbance effect is taken into consideration.
3) For the central region, the numerical prediction is lower than the experimental results. This may be attributed to the fact that the region is in a state of very delicate balance due to the competing flow streams from the two jets. Any small disturbances or asymmetry in the flow of the two jets will disturb the balance, resulting in a slightly higher mass transfer rate than the predicted value which is based on perfect symmetry and balance.

Figure 7.23 shows the comparison for H = 4 and S = 10 with different Reynolds numbers. Similar to the observation above, the numerical prediction is better for lower Reynolds numbers. However, the numerical prediction for both the location and value of the Sherwood numbers at and around the peak is almost perfect for all the three Reynolds numbers. There is significant disagreement between the numerical and experimental results downstream from the peak for both Re_b = 300 and 450. And the disagreement becomes more severe with higher Reynolds numbers. An examination of the flow pattern shown in Figure 7.13b reveals that the rather complex flow pattern may have been caused by the flow-induced disturbances and 3-D effect.

Figures 7.24 and 7.25 present a comparison for the cases of increased jet-to-jet spacing. Again, good agreement for the peak area can be noticed for all the cases in the figures. Similar disagreement also appears in the regions downstream from the peak for higher Reynolds numbers. It is worth noting that although the increased jet-to-jet spacing brings more fluctuation in the Sherwood number in the central region between the two jets, the average value remains relatively small and constant.

Figure 7.26 shows a comparison for the largest jet-to-plate spacing in this study, H = 8. Comparing to the cases of H = 2 and 4, the numerical prediction of the Sherwood numbers for H = 8 is much better for the central region. Very good agreement can be observed for the region around the peak. Downstream from the peak, the numerically predicted Sherwood numbers are less than the experimental results. The discrepancy becomes larger with higher Reynolds numbers.

7.2.4 Conclusions for the case of Two Symmetrical Slot Jets

Summarizing all the discussions for the case of two confined impinging laminar slot jets with symmetrical flow, the following conclusions can be drawn:

1) For jet-to-plate spacings of 2 and 4, the mass transfer rates in the central region between the two jets are about ten times smaller than the peak values

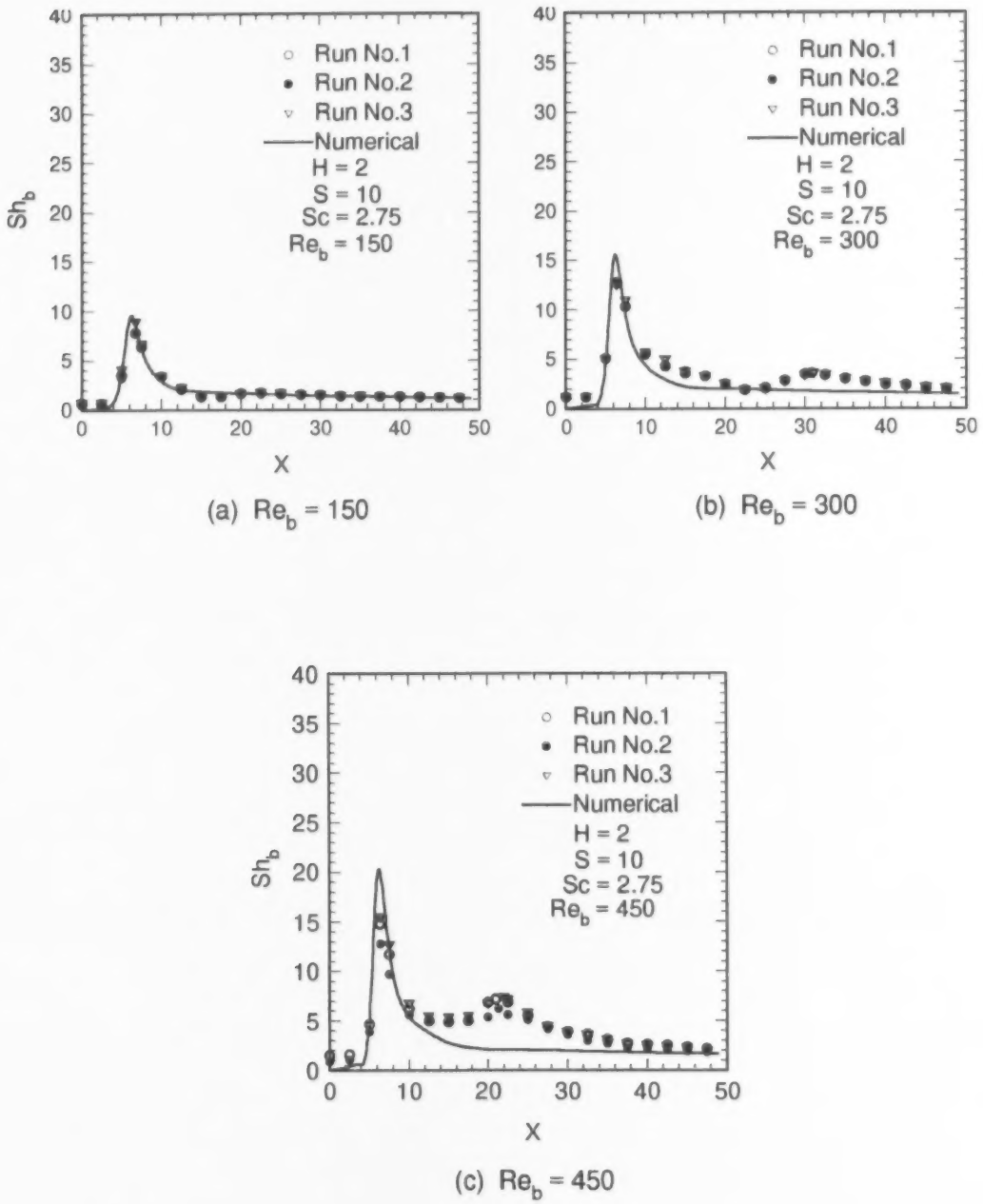

Figure 7.22 Comparison Between Numerical and Experimental Mass Transfer Rates for H = 2 and S = 10: Symmetrical Flow

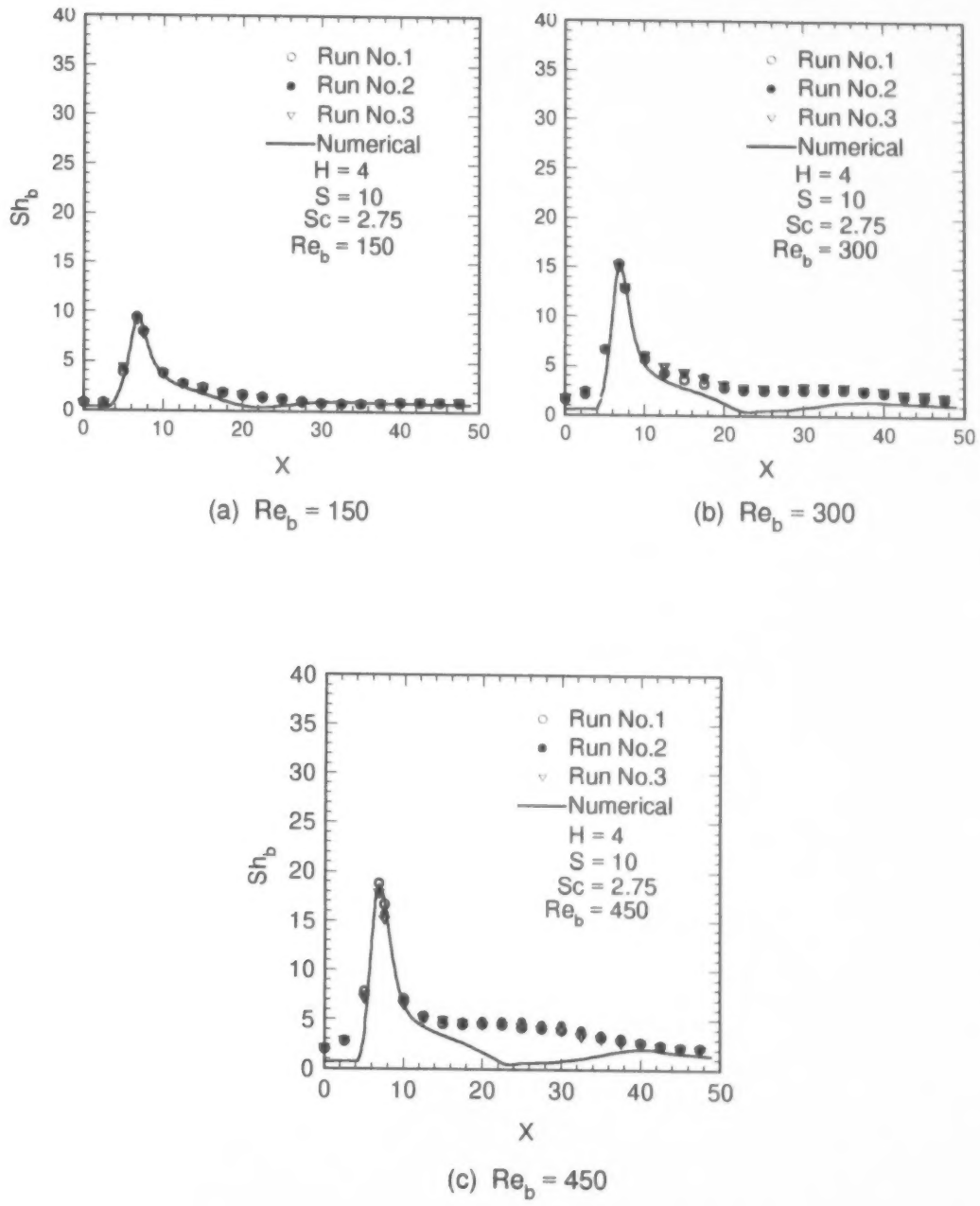

Figure 7.23 Comparison Between Numerical and Experimental Mass Transfer Rates for H = 4 and S = 10: Symmetrical Flow

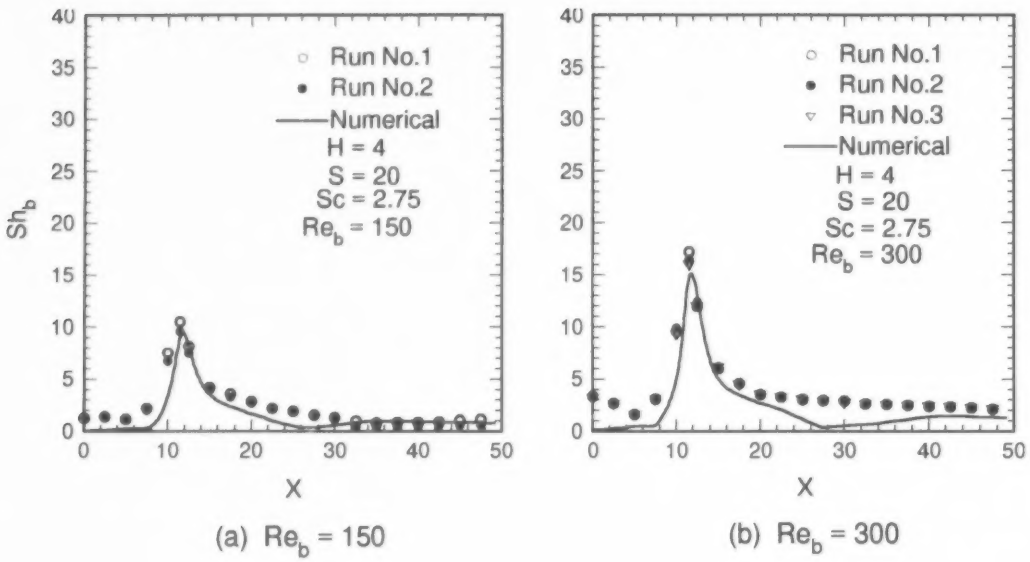

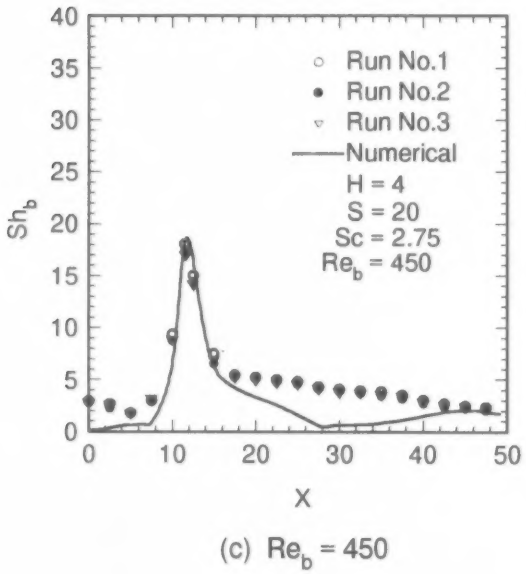

Figure 7.24 Comparison Between Numerical and Experimental Mass Transfer Rates for H = 4 and S = 20: Symmetrical Flow

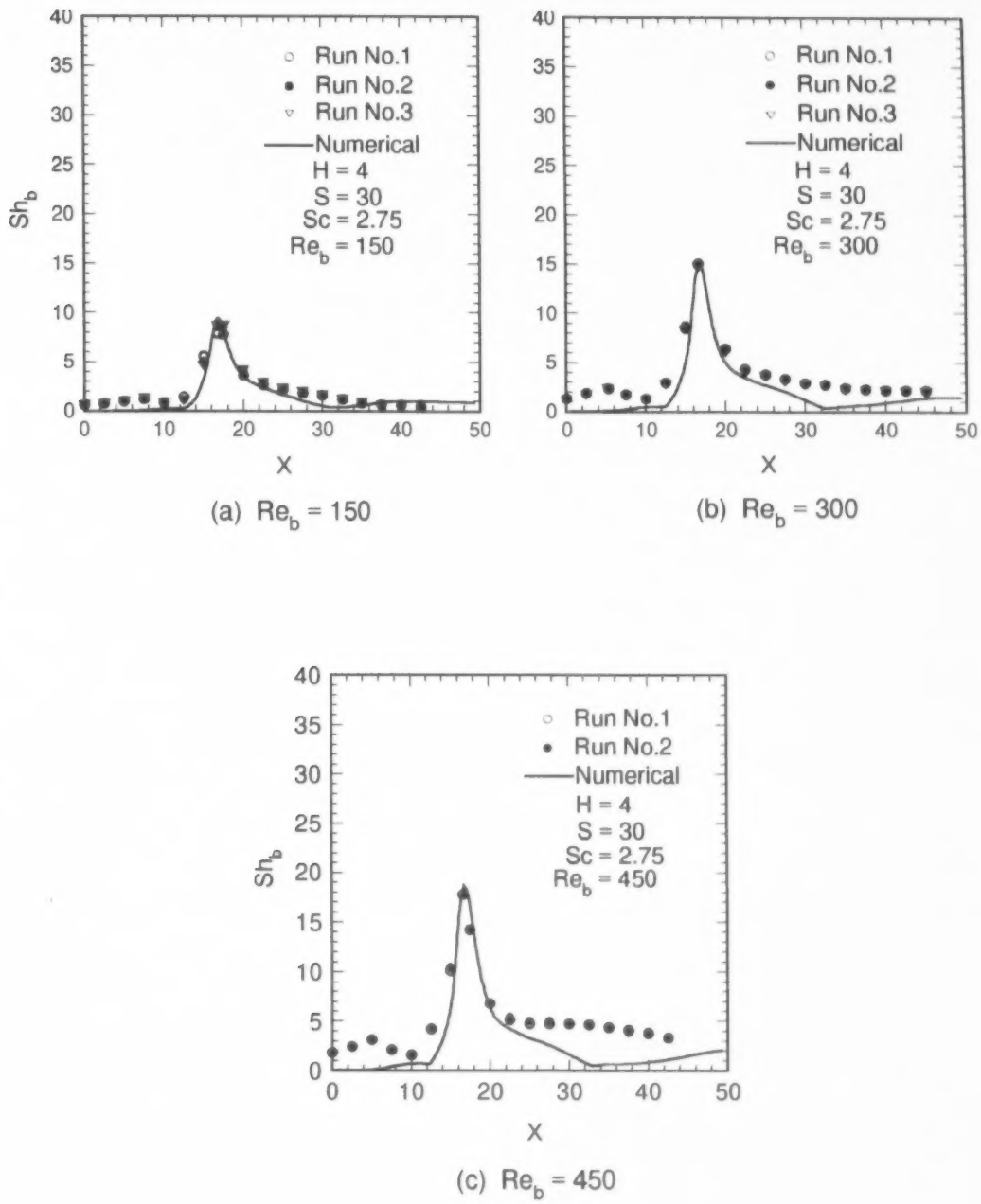

Figure 7.25 Comparison Between Numerical and Experimental Mass Transfer Rates for H = 4 and S = 30: Symmetrical Flow

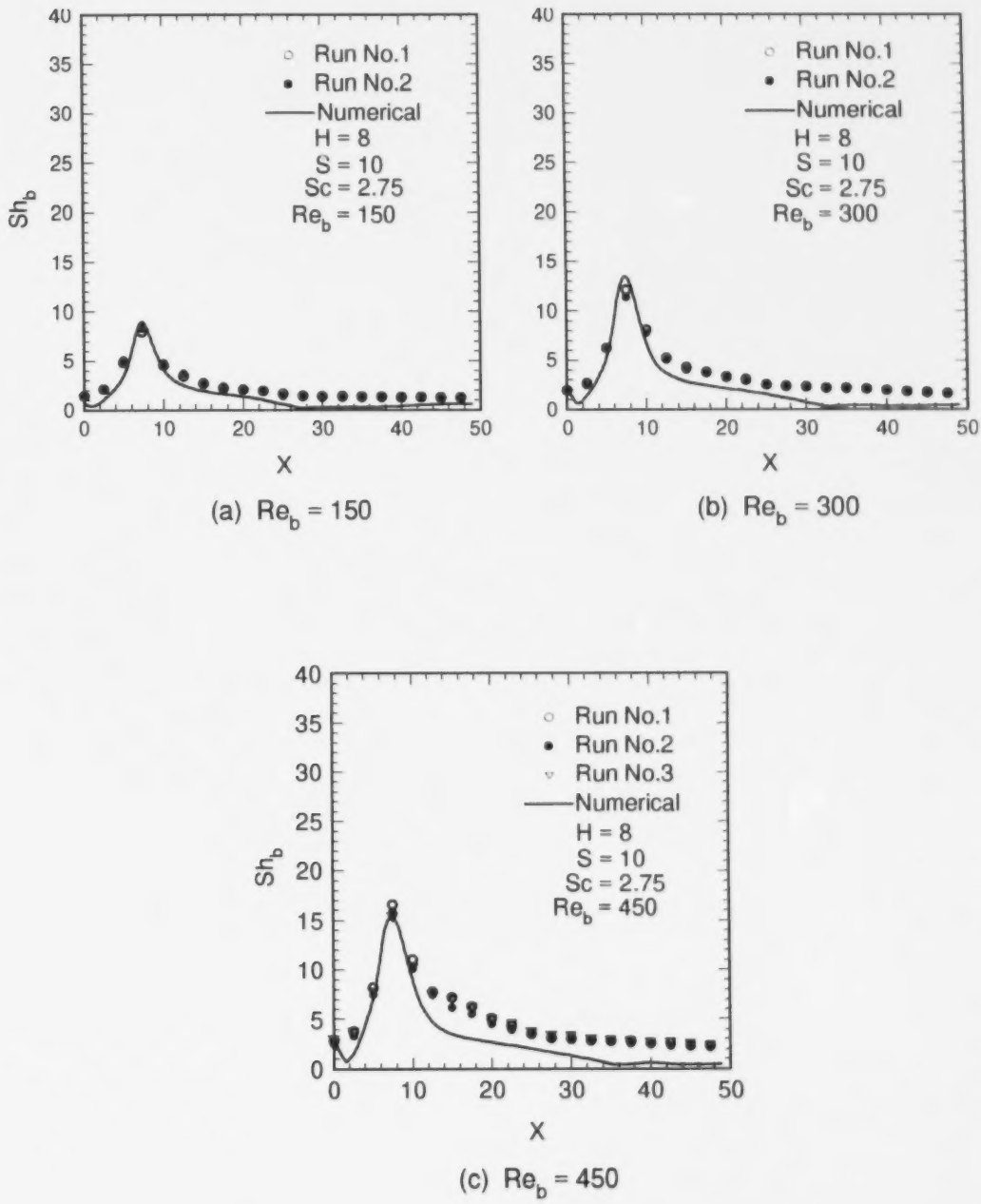

Figure 7.26 Comparison Between Numerical and Experimental Mass Transfer Rates for H = 8 and S = 10: Symmetrical Flow

located downstream from the jets. For a jet-to-plate spacing of 8, the average mass transfer rate in the central region is about five times smaller than their corresponding peak values.

2) In general, there is very good agreement between the numerical and experimental Sherwood numbers near the peak value. However, for both the central region and downstream from the peak, the numerically predicted mass transfer rates are less than the experimental results. For the central region, the discrepancy may be attributed to the disturbances and the imperfect balance between the two flow streams from the two jets. For the region downstream from the peak, the discrepancy may be due to the combined effect of flow-induced disturbances and 3-D effect. This argument is supported by the rather complex mass flow patterns for higher Reynolds numbers shown in the image photographs extracted from the video tapes.

Chapter 8

Mass Transfer Due To Two Confined Impinging Laminar Slot Jets: Asymmetrical Flow

As the last part of this work, the mass transfer characteristics of two confined impinging laminar slot jets with asymmetrical flow are studied experimentally. Because of the difficulty in specifying the boundary conditions for stream function on the impingement plate, the vorticity-stream function numerical formulation as used in the cases of one slot jet and two symmetrical slot jets is not suitable for the asymmetrical case, and hence the numerical analysis was not conducted for this set of experiments. The mass transfer patterns and the Sherwood numbers along the centerline of the impingement plate are obtained experimentally. The cases studied here resemble any two neighbouring jets located off-centre of a multiple confined slot jets system where the exhaust ports are located at both ends of the confined flow channel. When the flow rate of one jet is higher than the other, there is cross flow towards the jet with the lower flow rate. The cross flow has an effect of lowering the peak value in mass transfer rate produced by the weaker jet. The location of the peak of the weaker jet is also shifted downstream by the cross-flow. The effect of the cross-flow depends on the flow rate ratio of the two jets. Two flow ratios were examined for

the cases of H = 2 and 4 with S = 10 while one flow ratio was tested for the case of H = 4 and S = 20. The operating conditions and the results for these runs are compiled in Appendix F.

8.1 Mass Transfer Pattern

Typical "frozen fringe" patterns for the cases of H = 2 and 4, S = 10 with two flow ratios are presented in Figures 8.1-8.4. In each of the figures, two image photographs extracted from the video recordings are presented. Figure (a) presents the case when the stronger jet is on the left while Figure (b) presents the opposite. This is necessary since the jets are located near one end of the prism for a larger distance downstream to be viewed and recorded.

Figure 8.1 shows the mass transfer patterns for H = 2, S = 10 with a flow ratio of 2. From Figure 8.1a, it can be observed that the peak mass transfer rate on the side of the weaker jet has been shifted downstream as compared to the case of symmetrical jets. There is also a weak local maximum region further downstream from the weaker jet. It can also be noted that the shape of the fringe lines is quite irregular. Figure 8.1b shows the mass transfer pattern on the side of the stronger jet. Again, a region of irregular local maximum Sherwood number can be clearly identified.

With the same jet-to-plate spacing, H = 2, when the flow ratio is increased to 3, as shown in Figure 8.2, the mass transfer pattern behaves differently. Downstream from the weaker jet, shown in Figure 8.2a, the peak due to the weaker jet is further diminished. On the other hand, downstream from the stronger jet, a very complex mass transfer pattern emerges. This pattern may be due to the effect of flow induced disturbances.

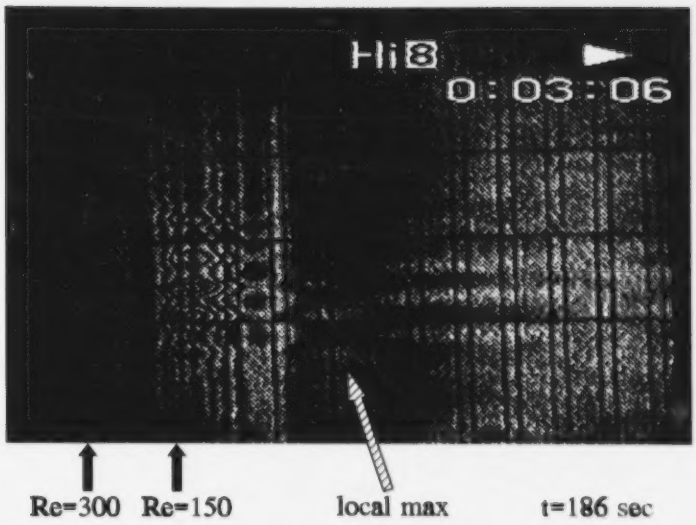

(a) flow rate ratio (left/right) = 2

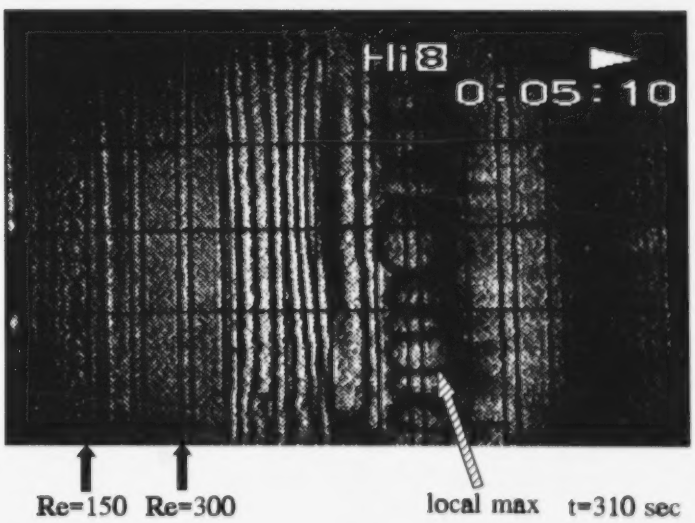

(b) flow rate ratio (right/left) = 2

Figure 8.1 Contours of Equal Mass Transfer Rate for H = 2, S = 10 and a Flow Ratio of 2

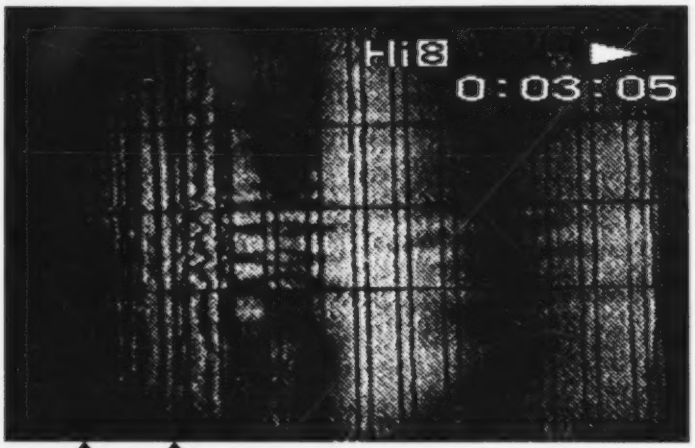

(a) flow rate ratio (left/right) = 3

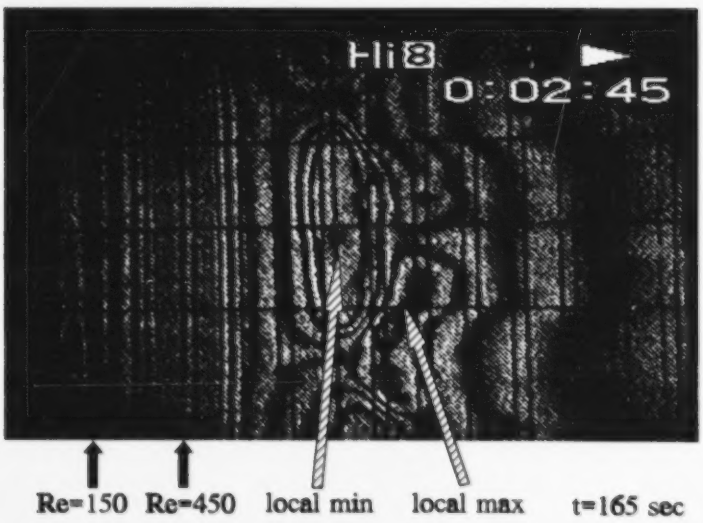

(b) flow rate ratio (right/left) = 3

Figure 8.2 Contours of Equal Mass Transfer Rate for H = 2, S = 10 and a Flow Ratio of 3

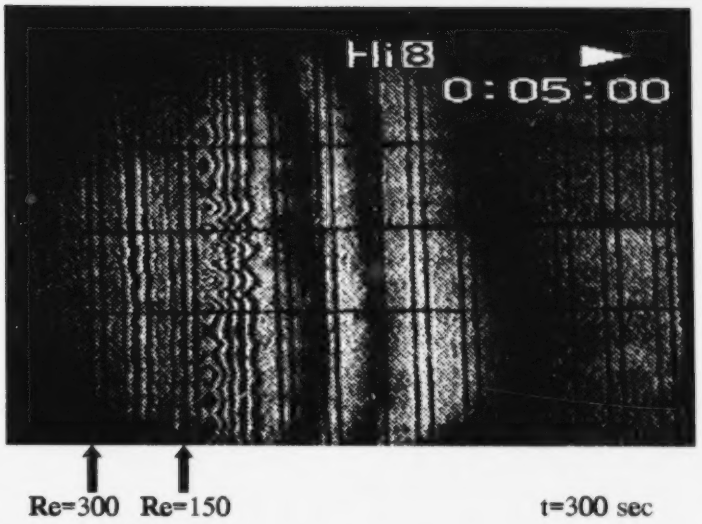

(a) flow rate ratio (left/right) = 2

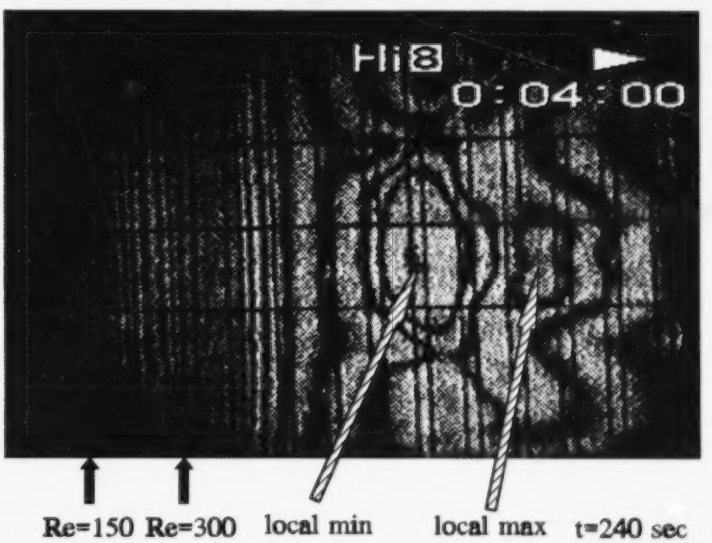

(b) flow rate ratio (right/left) = 2

Figure 8.3 Contours of Equal Mass Transfer Rate for H = 4, S = 10 and a Flow Ratio of 2

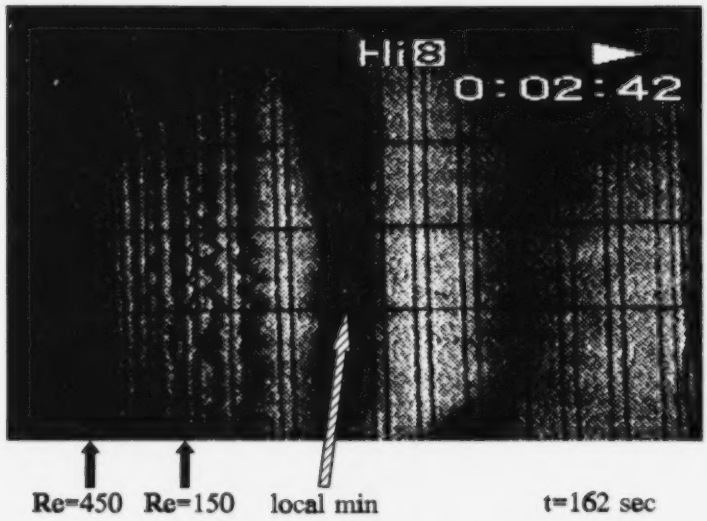

(a) flow rate ratio (left/right) = 3

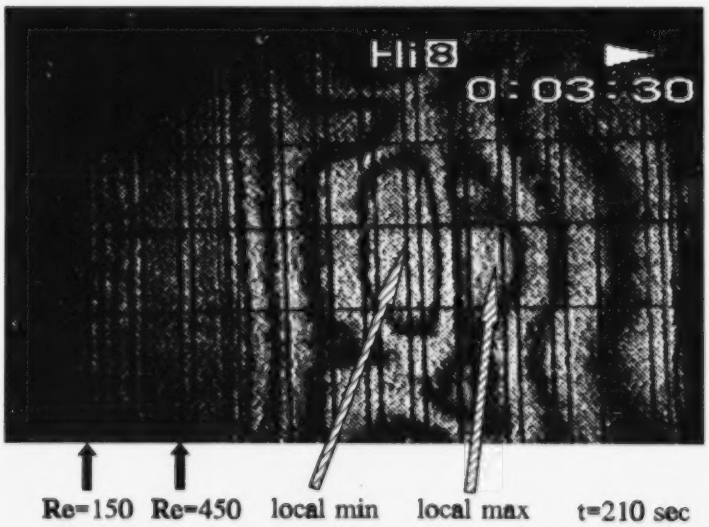

(b) flow rate ratio (right/left) = 3

Figure 8.4 Contours of Equal Mass Transfer Rate for H = 4, S = 10 and Flow Ratio of 3

Figure 8.3 shows the mass transfer pattern for H = 4, S = 10 and a flow ratio of 2. Comparing with Figure 8.1 for the case of H = 2, one can notice that the increase in the jet-to-plate spacing has the following effects:

1) Downstream from the weaker jet, while the primary peak due to the jet still exists, the secondary maximum (the local maximum) no longer appears. In addition, the fringe lines downstream from the weaker jet are also smoother.
2) Downstream from the stronger jet, the mass transfer pattern for H = 4 is much more complex than that for H = 2.

When the flow ratio is increased to 3, as shown in Figure 8.4, compared with the similar case for H = 2, Figure 8.2, the mass transfer pattern is relatively unaltered, except that the locations of the local maximum and minimum have shifted further downstream for both the weaker and stronger jets.

The digitized contours of equal Sherwood numbers for a few typical cases are presented in Figures 8.5 and 8.6. These figures further confirmed the above discussions.

8.2 Mass Transfer Rate

The mass transfer rates along the centerline of the impingement plate for all the asymmetrical flow cases are presented in Figures 8.7-8.9.

Figure 8.7 shows the local Sherwood numbers for the cases of H = 2, S = 10 and flow ratios of 2 and 3. By comparing Figure 8.7a with 8.7b, the following conclusions can be drawn:

1) For a flow ratio of 2, the peak mass transfer rate due to the weaker jet is about 4 times smaller than that due to the stronger jet. The location of the weaker peak is shifted downstream due to the cross flow produced by the stronger jet.

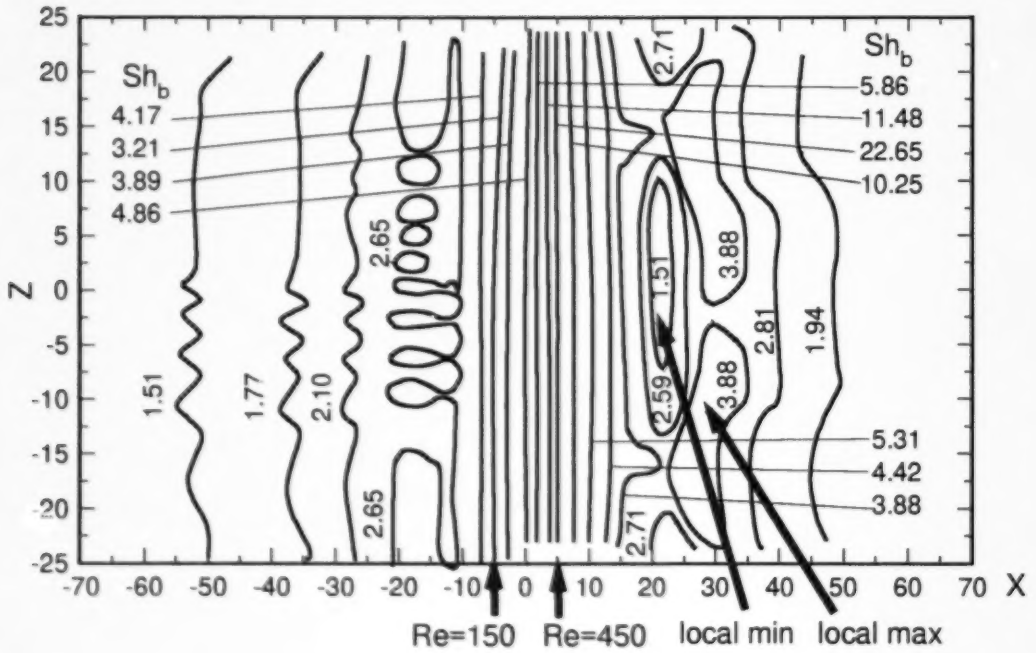

Figure 8.5 Digitized Contours of Sherwood Numbers for H = 2, S = 10 and a Flow Ratio of 3

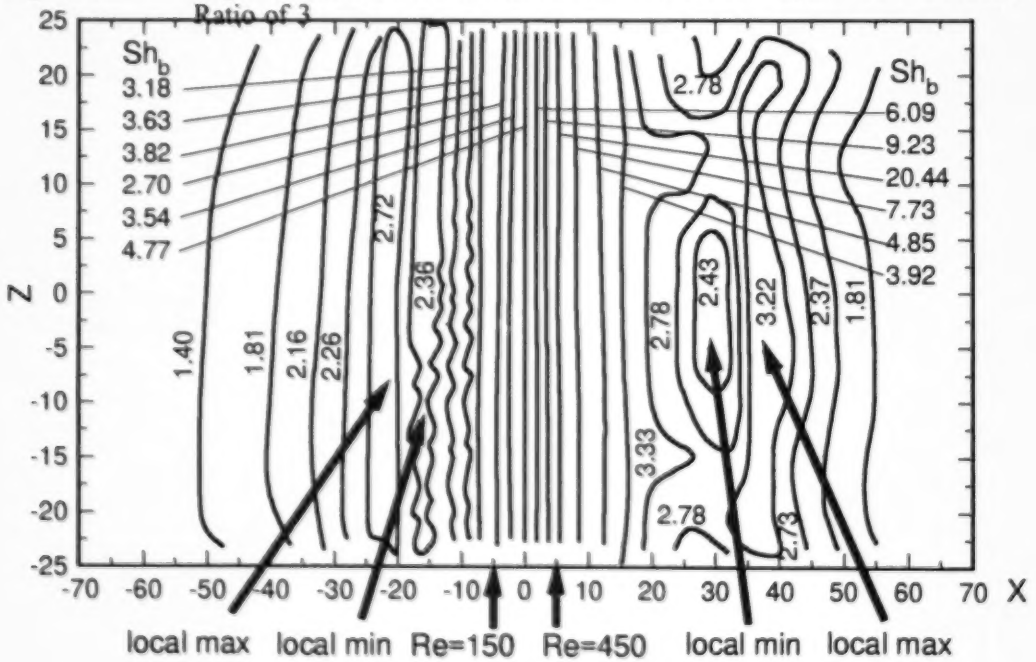

Figure 8.6 Digitized Contours of Sherwood Numbers for H = 4, S = 10 and a Flow Ratio of 3

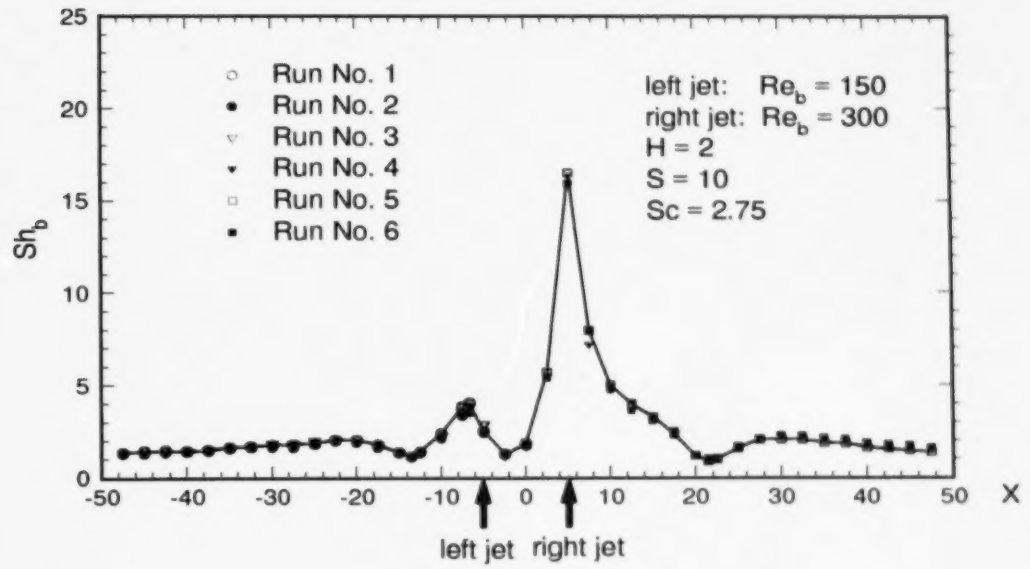

(a) flow rate ratio = 2

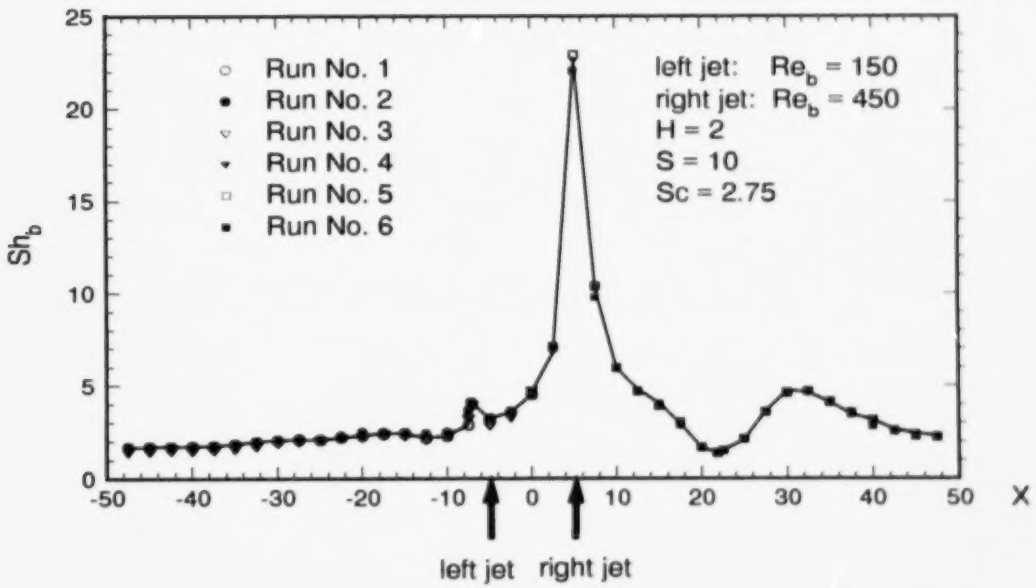

(b) flow rate ratio = 3

Figure 8.7 Mass Transfer Rate for H = 2, S = 10 and Flow Ratios of 2 and 3

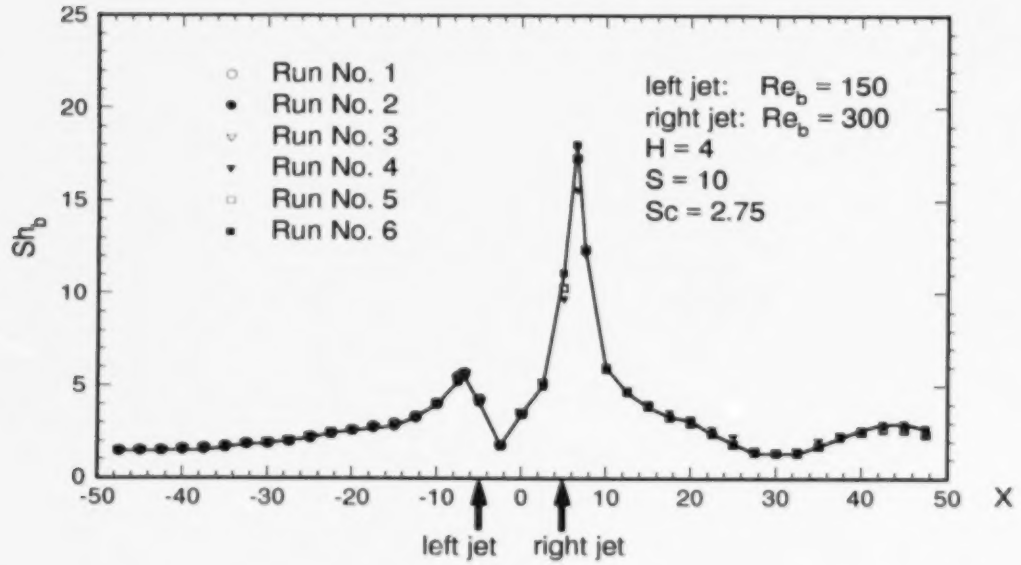

(a) flow rate ratio = 2

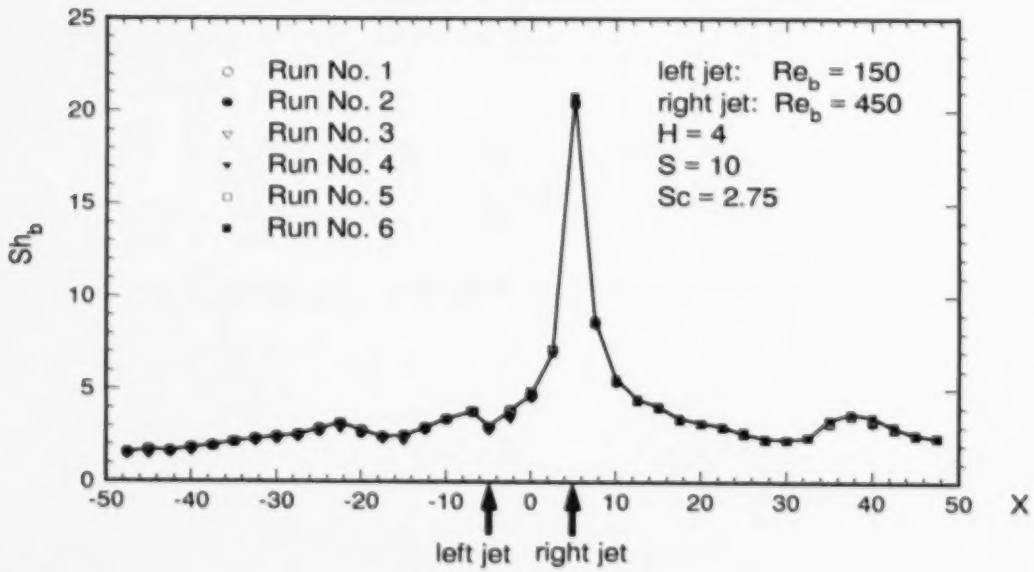

(b) flow rate ratio = 3

Figure 8.8 Mass Transfer Rate for H = 4, S = 10 and Flow Ratios of 2 and 3

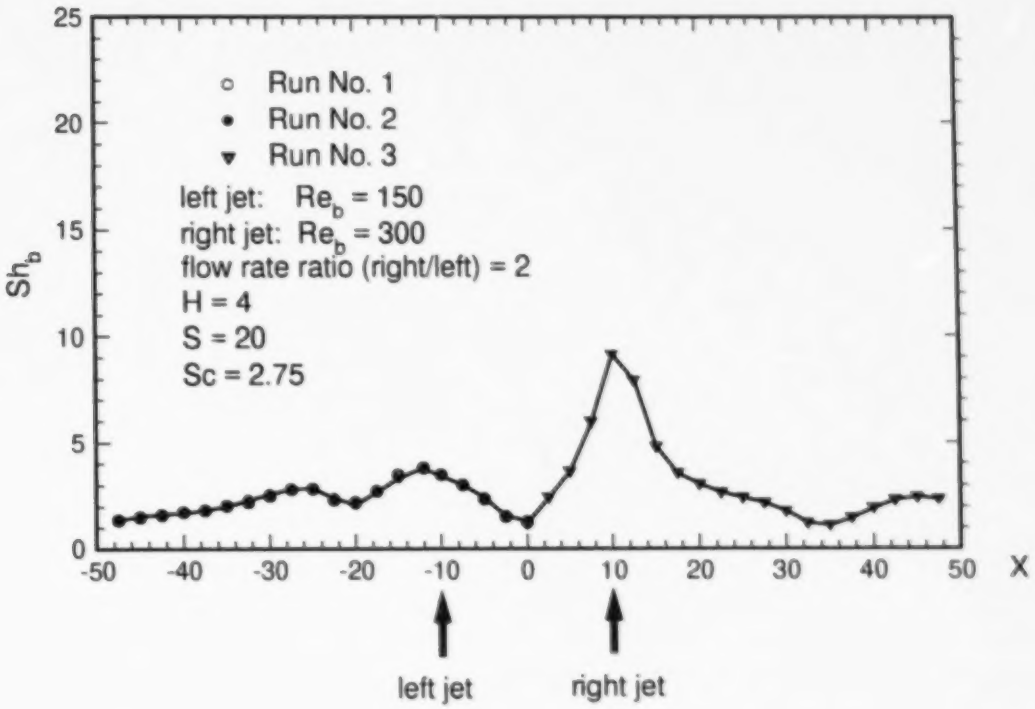

Figure 8.9 Mass Transfer Rate for H 4, S = 20 and a Flow Ratio of 2

2) For a flow ratio of 3, the peak mass transfer rate due to the weaker jet can hardly be recognized. This means that for the two neighbouring jets, when one jet is 3 times stronger than the other, the crossflow produced by the stronger jet can almost nullify the influence of the weaker jet, resulting in a mass transfer pattern close to a single strong jet.

Figure 8.8 shows the local Sherwood numbers for the cases of H = 4, S = 10 and flow ratios of 2 and 3. For a flow ratio of 2, the peak value due to the weaker jet is about 3 times smaller than that due to the stronger jet. For a flow ratio of 3, the peak due to the weaker jet nearly disappears. A comparison between these cases and those for H = 2 reveals that the secondary maximum and minimum values occur further downstream for a higher jet-to-plate spacing.

Figure 8.9 shows the local Sherwood numbers for the case of H = 4, S = 20 and a flow ratio of 2. Primary and secondary maximum values exist for both the stronger and weaker jets. A comparison between this case and the cases with S = 10 shows that the increased jet-to-jet spacing has the effect of flattening the peaks due to both the stronger and weaker jets.

Chapter 9

Conclusions

9.1 Mass Transfer due to One Confined Impinging Laminar Slot Jet

1. The local Sherwood number along the impingement plate exhibits a local minimum and a local maximum downstream from the stagnation region. The locations of the extrema are a function of the jet Reynolds number and the jet-to-plate spacing.

2. In the stagnation region, the jet-to-plate spacing has little effect on the local mass transfer rate when the jet-to-plate spacing is small (up to 4 in this study), and has much effect when the spacing is large.

3. In general, the numerical prediction for the local Sherwood numbers shows good agreement with the experimental results. Excellent agreement is obtained for the region between the stagnation point and the local minimum. In the stagnation region, the predicted Sherwood numbers are higher than the experimental data. In the region near the local maximum, the predicted Sherwood numbers are lower than the experimental values, with the discrepancy being larger for higher Reynolds numbers. Flow induced disturbances, which cannot be included into the numerical computation, may be

responsible for the discrepancy.

4. Good agreement is found between the experimental data of this study and the comparable data in the literature.

9.2 Mass Transfer due to Two Confined Impinging Laminar Slot Jets: Symmetrical Flow

1. There is a region of stagnation between the two jets. The average mass transfer rate in this region is about ten times lower than the maximum value for jet-to-plate spacings of 2 and 4. For a jet-to-plate spacing of 8, the average mass transfer rate in this region is about 5 times lower than the maximum value.

2. Because of the one-sided flow of the two counteracting jets, the maximum mass transfer rate (peak value) occurs downstream from the jet. The location depends mainly on the jet-to-plate spacing.

3. The combination of 3-D effect and flow induced disturbances may be responsible for the rather complex mass transfer pattern downstream from the peak value.

4. For the three jet-to-plate spacings studied, H = 2, 4 and 8, experimental results showed that H = 4 gave the highest peak values in mass transfer rate for all three Reynolds numbers, Re_b = 150, 300 and 450.

5. Apart from influencing the location of the peak values in mass transfer rate, the jet-to-jet spacing does not have much influence on the mass transfer pattern. With wider jet-to-jet spacings, there is more fluctuation on the lateral distribution of the local mass transfer rate in the central region, with the average remaining essentially unchanged.

6. In general, the numerical computation can predict both the location and the value of the maximum mass transfer rate accurately. The prediction for the central region is normally lower than the experimentally determined values. The largest discrepancy between the prediction and the experimental data occurs around the local maximum downstream from the peak for high Reynolds numbers. More research work is needed to determine the exact cause of the discrepancy.

9.3 Mass Transfer due to Two Confined Impinging Laminar Slot Jets: Asymmetrical Flow

1. The mass transfer pattern downstream from the stronger jet is much more complex than that downstream from the weaker jet.

2. Because of the cross-flow effect, the peak mass transfer rate downstream from the weaker jet is four times lower than that downstream from the stronger jet when the flow ratio between the two jets is only two. With a flow ratio of 3, the influence of the weaker jet is almost nullified by the flow from the stronger jet, and the mass transfer pattern of the whole system is similar to that due to a single jet.

Chapter 10

Recommendations

Further Studies

Because of the limitation of the experimental facility used in this study, no flow visualization was performed. The exact cause of the disagreement between the experimental results and the numerical prediction on the region downstream from the peak values was not known. In order to find out the cause for the strong secondary peaks for the case of single impinging slot jets and the complex mass transfer patterns for the case of two symmetrical jets, the following studies may be performed:

1. Flow visualization for the various cases;
2. Numerical analysis on a 3-dimensional domain. This can be achieved by running a commercial package, such as FLOW 3D.

Industrial Significance

From the industrial point of view, this study has shown the following important points:

1. For a single confined impinging slot jet, the secondary peak transfer rate could be very high;
2. Two confined symmetrical impinging slot jets will form a stagnant zone between the jets and the transfer rate in this zone is very low. This situation should be avoided in the design of a multiple jet system.

References

Abramson, N., "The holo-diagram: a practical device for making and evaluating holograms", *Appl. Opt.*, **8**, 1235-1240 (1969).

Abramson, N., "The holo-diagram. II: A practical device for information retrieval in hologram interferometry", *Appl. Opt.*, **9**, 97-101 (1970a).

Abramson, N., "The holo-diagram. III: A practical device for predicting fringe pattern in hologram interferometry", *Appl. Opt.*, **9**, 2311-2320 (1970b).

Adcock, J.N., "The laminar jet system for cooling hot steel strip", *Journal of Iron and Steel Institute*, **200**, 909-913 (1962).

Akfirat, J.C., "Transfer of heat from an isothermal flat plate to a two-dimensional wall jet", *Proc. 3rd Int. Heat Transfer Conf.*, Chicago, **2**, 274-279 (1966).

Al-Sanea, S., "A numerical study of the flow and heat-transfer characteristics of an impinging laminar slot-jet including crossflow effects", *Int. J. Heat Mass Transfer*, **35**, 2501-2513 (1992).

Ammari, H.D., Hay, N., Lampard, D., "The effect of density ratio on the heat transfer coefficient from a film cooled flat plate", *Gas Turbine and Aeroengine Congress and Exposition*, Toronto, ASME paper 89-GT-176, 1989a.

Ammari, H.D., Hay, N. and Lampard, D., "Simulation of cooling film density ratios in a mass transfer technique", *Gas Turbine and Aeroengine Congress and Exposition*, Toronto, ASME paper 89-GT-200, 1989b.

Andrews, G.E. and Hussain, C.I., "Full coverage impingement heat transfer: The influence of channel height", *Heat Transfer 1986*, **3**, 1205-1211 (1986).

Baines, W.D. and Keffer, J.F., "Shear stress measurements for an impinging air jet", *Transactions of the Technical Section*, Canadian Pulp and Paper Association, June, 39-44 (1979).

Bird, R.B., Stewart, W.E. and Lightfoot E.N., *Transport Phenomena*, John Wiley and Sons, New York, 1960.

Button, B.L. and Wilcock, D., "Impingement heat transfer -- A bibliography 1890-1975", *Previews of Heat and Mass Transfer*, **4**, No.3, 83-98 (1978).

Chaudhury, Z.H., "Heat transfer in a radial liquid jet", *J. Fluid Mech.*, **20**, 501-511 (1964)

Chen, J., Wang, T. and Zumbrunnen, D.A., "Numerical analysis of convective heat transfer from a moving plate cooled by an array of submerged planar jets", *Heat Transfer in Metals and Containerless Processing and Manufacturing*, ASME, Heat Transfer Division, 28th National Heat Transfer Conference, Minneapolis, HTD-Vol. **162**, 25-34 (1991).

Chilton, T.H. and Colburn, A.P., "Mass transfer coefficients", *Ind. Eng. Chem.*, **26**, 1183-1187 (1934).

Chong, Y.K., Hammond, G.P., Macaskill, C. and Ward, J., "An experimental study of two-dimensional jet-impingement heat/mass transfer in a confined cross-flow", *Heat Transfer 1986*, **3**, 1225-1230 (1986).

Chuang, S.H., "Numerical simulation of an impinging jet on a flat plate", *Int. J. Numerical Methods in Fluids*, **9**, 1413-1426 (1989).

Chuang, S.H. and Wei, C.Y., "Computations for a jet impinging obliquely on a flat surface", *Int. J. for Numerical Methods in Fluids*, **12**, 637-653 (1991).

Dawson, D.A. and Trass, O., "Mass transfer in a turbulent radial wall jet", *CJChE*, **44**, 121-129 (1966).

Deshpande, M.D. and Vaishnav, R.N., "Submerged laminar jet impingement on a plane", *J. Fluid Mech.*, **114**, 213-236 (1982).

Downs, S.J. and James, E.H., "Jet impingement heat transfer - a literature survey", *ASME Paper* No. 87-H-35, ASME, New York, 1987.

Fairweather, M., Kilham, J.K. and Nawaz, S., "Stagnation point heat transfer from laminar, high temperature methane flames", *Int. J. Heat and Fluid Flow*, **5**, 21-27 (1984).

Fechner, G., *Warmeubergang bei senkrecht auftreffendem strahl an der platte und am rotor*, Dissertation, T.U. Munchen, 1971.

Gardon, R. and Akfirat, J.C., "The role of turbulence in determining the heat-transfer characteristics of impinging jets", *Int. J. Heat Mass Transfer*, **8**, 1261-1272 (1965).

Gardon, R. and Akfirat, J.C., "Heat transfer characteristics of impinging two-dimensional air jets", *J. Heat Transfer*, Transactions of ASME, **88**, 101-108 (1966).

Gardon, R. and Cobonpue, J., "Heat transfer between a flat plate and jets of air impinging on it", *International Development in Heat Transfer*, 1961 Int. Heat Transfer Conf., Boulder, Part II, 454-460 (1961).

Gerhart, P.M. and Gross R.J., *Fundamentals of Fluid Mechanics*, Addison-Wesley Publishing Comp., Reading, 1985.

Glauert, M.B., "The wall jet", *J. Fluid Mech.*, **1**, 625-643 (1956).

Goldstein, R.J., Behbahani, A.I. and Heppelmann, K.K., "Streamwise distribution of the recovery factor and the local heat transfer coefficient to an impinging circular air jet", *Int. J. Heat Mass Transfer*, **29**, 1227-1235 (1986).

Goldstein, R.J. and Franchett, M.E., "Heat transfer from a flat surface to an oblique impinging jet", *J. Heat Transfer*, **110**, 84-90 (1988).

Goldstein, R.J. and Seol, W.S., "Heat transfer to a row of impinging circular air jets including the effect of entrainment", *Int. J. Heat Mass Transfer*, **34**, 2133-2147 (1991).

Goldstein, R.J. and Timmers, J.F., "Visualization of heat transfer from arrays of impinging jets", *Int. J. Heat Mass Transfer*, **25**, 1857-1868 (1982).

Hariharan, P., *Optical Holography: Principles, Techniques and Applications*, Cambridge University Press, Cambridge, 223-225 (1984).

Harper A.J. and Macleod N., "Hot spots in heat transfer", *Physics Bulletin*, **29**, Jan. 13-14 (1978).

Haslar, F. and Krizek, F., "Mass transfer of impact flow from slit nozzles on rotating drying cylinder", Presented at the 8th Int. Congress of Chemical Eng., *Chemical Equipment Design and Automation*, Praha, Czechoslovakia, Sept. 3-7, 1984.

Hay, N., Lampard, D. and Saluja, C.L., "Application of the swollen polymer technique to the study of heat transfer on film cooled surfaces", *Proc. 7th Int. Heat Transfer Conf.*, Munich, **4**, 503-508 (1982).

Hay, N., Lampard, D. and Saluja, C.L., "Effects of the condition of the approach boundary layer and of mainstream pressure gradients on the heat transfer coefficient on film-cooled surfaces", *J. Engng. for Gas Turbines and Power*, **107**, 99-104 (1985a).

Hay, N., Lampard, D. and Saluja, C.L., "Effects of cooling films on the heat transfer coefficient on a flat plate with zero mainstream pressure gradient", *J. Engng. for Gas Turbines and Power*, **107**, 105-110 (1985b).

Hay, N., Lampard, D., Maali, R. and Burns, I., "Simultaneous determination of heat transfer coefficient and adiabatic wall effectiveness on a film cooled surface using the swollen polymer technique", *8th Int. Heat Transfer Conf.*, San Francisco, 489-494 (1986).

Hollworth, B.R. and Berry, R.D., "Heat transfer from arrays of impinging jets with large jet-to-plate spacing", *J. Heat Transfer*, **100**, 352-357 (1978).

Hrycak, P., "Heat transfer from a row of jets impinging on concave semi-cylindrical surface", *Proc. 6th Int. Heat Transfer Conf.*, Toronto, **2**, 67-72 (1978).

Huang, B., Douglas, W.J.M. and Mujumdar, A.S., "Heat transfer under a laminar swirling impinging jet — a numerical study", *Proc. 6th Int. Heat Transfer Conf.*, Toronto, **5**, 311-316 (1978).

Huang, G.C., "Investigations of heat transfer coefficients for air flow through round jets impinging normal to a heat-transfer surface", *J. Heat Transfer*, **85**, 237-245 (1963).

Ichimiya, K. and Hosaka, N., "Experimental study of heat transfer characteristics due to confined impinging two-dimensional jets (heat transfer experiment for three slot jets)", *Experimental Heat Transfer, Fluid Mechanics, and Thermodynamics*, J.F. Keffer, R.K. Shah, and E.N. Ganic, Eds., 771-775 (1991).

Inada, S., Miyasaka, Y. and Izumi, R., "A study on the laminar-flow heat transfer between a two-dimensional water jet and a flat surface with constant heat flux", *Bull. JSME*, **24**, 1803-1810 (1981).

Inoue, S., Eguchi, K., Imamoto, T. and Kishi M., "Impinging jet dryer", *Drying Technology*, **10**, 679-714 (1992).

Ishigai, S., Nakanishi, S. and Ochi, T., "Boiling heat transfer for a plane water jet impinging on a hot surface", *Heat Transfer 1978*, **1**, 445-450, Hemisphere Publishing Corp., Washington, 1978.

Jambunathan, K, Lai, E., Moss, M.A. and Button, B.L., "A review of heat transfer data for single circular jet impingement", *Int. J. Heat and Fluid Flow*, **13**, 106-115 (1992).

Jaussaud, J.P., Douglas, W.J.M. and Mujumdar, S.S., "Evaporation under an obliquely impinging laminar ducted slot jet--A numerical study", *Int. Comm. Heat Mass Transfer*, **11**, 335-344 (1984).

Kapur, D.N. and Macleod, N., "Determination of local mass transfer coefficients by holography", *Nature Phys. Sci.*, **237**, 57-59 (1972).

Kapur, D.N. and Macleod, N., "The determination of local mass-transfer coefficients by holographic interferometry - I", *Int. J. Heat Mass Transfer*, **17**, 1151-1162 (1974).

Kapur, D.N. and Macleod, N., "Holographic determination of local mass transfer coefficients at a solid-liquid boundary", *AIChE J.*, **21**, 184-187 (1975).

Kapur, D.N. and Macleod, N., "Vapour pressure determination for certain high-boiling liquids by holography", *Ind. Eng. Chem., Prod. Res. Dev.*, **15**, 50-54 (1976a).

Kapur, D.N. and Macleod, N., "The estimation of local heat transfer coefficients for two-dimensional surface-roughness elements by holographic interferometry", *The Engineering Uses of Coherent Optics*, 615-630, Cambridge Univ. Press, Cambridge, 1976b.

Knowles, K. and Bray, D., "Computation of normal impinging jets in cross-flow and comparison with experiment", *Int. J. for Num. Methods in Fluids*, **13**, 1225-1233 (1991).

Kohring, F.C., "Waterwall water-cooling systems", *Iron and Steel Engineering*, June, 30-36 (1985).

Koopman, R.N. and Sparrow, E.M., "Local and average transfer coefficients due to an impinging row of jets", *Int. J. Heat Mass Transfer*, **19**, 673-683 (1976).

Korger, M. and Krizek, F., "Mass-transfer coefficient in impingement flow from slotted nozzles", *Int. J. Heat Mass Transfer*, **9**, 337-344 (1966).

Korger, M. and Krizek, F., "Die stoffübergangszahlen beim aufprall schräger flachstrahlen auf eine platte", *Verfahrenstechnik*, **6**, 223-228 (1972).

Law, H.S., *Mass transfer due to a confined laminar impinging two-dimensional jet*, Ph.D. thesis, University of Alberta, Edmonton, 1982.

Law, H.S. and Masliyah, J.H., "Mass transfer due to a confined laminar impinging two-dimensional jet", *Int. J. Heat Mass Transfer*, **27**, 529-539 (1984a).

Law, H.S. and Masliyah, J.H., "Mass transfer due to a confined laminar impinging axisymmetric jet", *Ind. Eng. Chem. Fundam.*, **23**, 446-454 (1984b).

Law, H.S. and Masliyah, J.H., "Coherent optical measurement techniques in profilometric determination of local mass transfer coefficients", *Optics and Lasers in Eng.*, **5**, 211-229 (1984c).

Law, H.S. and Masliyah, J.H., "Numerical prediction of the flow field due to a confined laminar two-dimensional submerged jet", *Computers and Fluids*, **12**, 199-215 (1984d).

Liu, X., Gabour, L.A. and Lienhard, J.H., "Stagnation point heat transfer during impingement of laminar liquid jets: analysis with surface tension effects", *General Papers in Heat Transfer, ASME paper* HTD-Vol.**204**, 173-182 (1992).

Livingood, J.N.B., and Hrycak, P., "Impingement heat transfer from turbulent air stream jets to flat plates - a literature survey", *NASA* TM X-2778, 1973.

Macleod, N. and Todd, R.B., "The experimental determination of wall-fluid mass transfer coefficients using plasticized polymer surface coatings", *Int. J. Heat Mass Transfer*, **16**, 485-504 (1973).

Martin, H., "Heat and mass transfer between impinging gas jets and solid surfaces", *Advances in Heat Transfer*, **13**, 1-60, Academic Press, New York, 1977.

Martynenko, O.G., Korovkin, V.N. and Sokovishin, Y. A., "A swirled jet problem", *Int. J. Heat Mass Transfer*, **32**, 2309-2317 (1989).

Masliyah, J.H. and Nguyen, T.T., "Qualitative study in mass transfer by laser holography", *CJChE*, **52**, 664-665 (1974).

Masliyah, J.H. and Nguyen, T.T., "Holographic determination of mass transfer due to impinging square jet", *CJChE*, **54**, 299-304 (1976).

Masliyah, J.H. and Nguyen, T.T., "Experimental study of mass transfer due to an impinging rectangular jet", *CJChE*, **55**, 156-160 (1977).

Masliyah, J.H. and Nguyen, T.T., "Mass transfer due to an impinging slot jet", *Int. J. Heat Mass Transfer*, **22**, 237-244 (1979).

McMurray, D.C., Myers, P.S. and Uyehara, O.A., "Influence of impinging jet variables on local heat transfer coefficients along a flat surface with constant heat flux", *Proc. 3rd Int. Heat Transfer Conf.*, 292-299 (1966).

McNaughton, K.J. and Sinclair, C.G., "Submerged jets in short cylindrical flow vessels", *J. Fluid Mech.*, **25**, 367-375 (1966).

Mikhail, S., Morcos, S.M., Abou-Elllail, M.M.M. and Ghaly, W.S., "Numerical prediction of flow field and heat transfer from a row of laminar slot jets impinging on a flat plate", *Proc. 7th Int. Heat Tr. Conf.*, **3**, Munchen, 377-382 (1982).

Miyasaka, Y. and Inada, S., "The effect of pure forced convection on the boiling heat transfer between a two-dimensional subcooled water jet and a heated surface", *J. Chem. Eng. Japan*, **13**, 22-28 (1980).

Miyazaki, H. and Silberman, E., "Flow and heat transfer on a flat plate normal to a two-dimensional laminar jet issuing from a nozzle of finite height", *Int. J. Heat Mass Transfer*, **15**, 2097-2107 (1972).

Mujumdar, A.S., Li, Y.K. and Douglas, J.M., "Evaporation under an impinging jet: a numerical study", *CJChE*, **58**, 448-453 (1980).

Obot, N.Y., Mujumdar, A.S. and Douglas, W.J.M., "The effect of nozzle geometry on impingement heat transfer under round turbulent jet", *ASME paper* No. WA/HT-53, ASME, New York, 1979.

Obot, N.Y., Mujumdar, A.S. and Douglas, W.J.M., "Effect of semi-confinement on impingement heat transfer", *Proc. 7th Int. Heat Transfer Conf.*, Munchen, Germany, September 6-19, **3**, 395-400 (1982).

Obot, N.T. and Trabold, T.A., "Impingement heat transfer within arrays of circular jets: part 1 - effects of minimum, intermediate, and complete crossflow for small and large spacings", *J. Heat Transfer*, **109**, 872-879 (1987).

Pan, Y, Stevens, J. and Webb, B.W., "Effect of nozzle configuration on transport in the stagnation zone of axisymmetric, impinging free-surface liquid jets: Part 2 — local heat transfer", *J. Heat Transfer*, **114**, 880-886 (1992).

Patankar, V.S., *Numerical heat transfer and fluid flow*, Hemisphere Publishing Corp., Washington, 1980.

Patankar, V.S. and Spalding, D.B, "A calculation procedure for heat, mass and momentum transfer in three-dimensional parabolic flows", *Int. J. Heat Mass Transfer*, **15**, 1787-1806 (1972).

Paterson, W.R., Colledge, R.A., Macnab, J.I. and Joy, J.A., "Solid-gas mass transfer measurement by the swollen polymer method: proving of swelling agents", *Int. J. Heat Mass Transfer*, **30**, 279-287 (1987).

Perry, K.P., "Heat transfer by convection from a hot gas jet to a plane surface", *Proc. Inst. Mech. Eng. (Lond.)*, **168**, 775-784 (1954).

Perry, R.H. and Chilton, C.H., Chemical Engineers' Handbook, 5th Eds., McGraw-Hill Book Comp., New York, 1973.

Polat, S., *Transport phenomena under jets impinging on a moving surface with throughflow*, Ph.D. thesis, McGill University, Montreal, 1988.

Polat, S. and Douglas, W.J.M., "Heat transfer under multiple slot jets impinging on a permeable moving surface", *AIChE J.*, **36**, 1370-1378 (1990).

Polat, S., Huang, B., Mujumdar, A.S., and Douglas, W.J.M., "Numerical flow and heat transfer under impinging jets: a review", *Annual review of numerical fluid mechanics and heat transfer*, **2**, 157-197, Hemisphere Publishing Corp., New York, 1989.

Polat, S., Mujumdar, A.S. and Douglas, W.J.M., "Impingement heat transfer under a confined slot jet. Part I: Effect of surface throughflow", *CJChE*, **69**, 266-273 (1991a).

Polat, S., Mujumdar, A.S. and Douglas, W.J.M., "Impingement heat transfer under a confined slot jet. Part II: Effect of surface motion and throughflow", *CJChE*, **69**, 266-273 (1991b).

Polat, S., Mujumdar, A.S., van Heiningen, A.R.P. and Douglas, W.J.M., "Numerical model for turbulent jets impinging on a surface with throughflow", *J. Thermophysics and Heat Transfer*, **5**, 172-180 (1991c).

Polat, S., van Heiningen, A.R.P. and Douglas, W.J.M., "Sensor for transient heat flux at a surface with throughflow", *Int. J. Heat Mass Transfer*, **34**, 1515-1523 (1991d).

Popiel, C.O. and Boguslawski, L., "Mass or heat transfer in impinging single, round jets emitted by a bell-shaped nozzle and sharp-ended orifice", *Heat Transfer 1986*, **3**, 1187-1192 (1986).

Popiel, C.O. and Boguslawski, L., "Effect of flow structure on the heat or mass transfer on a flat plate in impinging round jet", *2nd UK National Conf. on Heat Transfer*, University of Strathclyde, UK, September 14-16, **1**, 663-685 (1988).

Reid, R.C., Prausnitz, J.M. and Poling B.E., *The properties of Gases and Liquids*, 4th Eds., McGraw-Hill Book Comp., New York, 1987.

Roache, P.J., *Computational Fluid Dynamics*, Hermosa Publishers, Albuquerque, 154-161, 1982.

Rao, V.V. and Trass, O., "Mass transfer from a flat surface to an impinging turbulent jet", *CJChE*, **42**, 95-99 (1964).

Saad, N.R., *Flow and heat transfer for multiple turbulent impinging slot jets*, Ph.D. thesis, McGill University, Montreal, 1981.

Saad, N.R., Douglas, W.J.M. and Mujumdar, A.S., "Prediction of heat transfer under an axisymmetric laminar impinging jet", *Ind. Eng. Chem., Fundam.*, **16**, 148-154 (1977).

Saad, N.R., Polat, S. and Douglas, W.J.M., "Confined multiple impinging slot jets without crossflow effects", *Int. J. Heat and Fluid Flow*, **13**, 2-14 (1992).

Saluja, C.L., Lampard D., Hay N. and Burns I., "The determination of heat transfer coefficients on film cooled flat surfaces using the swollen polymer technique", *First UK National Heat Transfer Conf.*, Leeds, 893-906 (1984).

Schlichting, H., *Boundary-Layer Theory*, 7th Eds., McGraw-Hill Book Comp., New York, 1979.

Scholtz, M.T. and Trass, O., "Mass transfer in the laminar radial wall jet", *AIChE J.*, **9**, 548-554 (1963).

Scholtz, M.T. and Trass, O., "Mass transfer in a nonuniform impinging jet", *AIChE J.*, **16**, 82-96 (1970).

Schwarz, W.H. and Caswell, B., "Some heat transfer characteristics of the two-dimensional laminar incompressible wall jet", *Chem. Eng. Sci.*, **16**, 338-351 (1961).

Sparrow, E.M., Goldstein, R.J. and Rouf, M.A., "Effect of nozzle-surface separation distance on impingement heat transfer for a jet in a crossflow", *J. Heat Transfer*, **97**, 528-533 (1975).

Sparrow, E.M. and Lee, L., "Analysis of flow field and impingement heat/mass transfer due to a nonuniform slot jet", *J. Heat Transfer*, Transactions of ASME, **97**, 191-197 (1975).

Sparrow, E.M. and Lovell, B.J., "Heat transfer characteristics of an obliquely impinging circular jet", *J. Heat Transfer*, **102**, 202-209 (1980).

Sparrow, E.M. and Wong, T.C., "Impingement transfer coefficients due to initially laminar slot jets", *Int. J. Heat Mass Transfer*, **18**, 597-605 (1975).

Stevens, J. and Webb, B.W., "The effect of inclination on local heat transfer under an axisymmetric, free liquid jet", *Int. J. Heat Mass Transfer*, **34**, 1227-1236 (1991a).

Stevens, J. and Webb, B.W., "Local heat transfer coefficients under an axisymmetric, single-phase liquid jet", *J. Heat Transfer*, **113**, 71-78 (1991b).

Subba Raju, K. and Schlunder, E.U., "Heat transfer between an impinging jet and a continuously moving flat surface", *Warme und Stoffubertragrung*, **10**, 131-136 (1977).

Unterseher, F., Hansen, J. and Schlesinger B., *Holography Handbook*, Ross Books, Berkeley, 1982.

Vader, D.T., Incropera, F.P. and Viskanta, R., "Local convective heat transfer from a heated surface to an impinging, planar jet of water", *Int. J. Heat Mass Transfer*, **34**, 611-623 (1991).

van Heiningen, A.R.P., *Heat transfer under an impinging slot jet*, Ph.D. thesis, McGill University, Montreal, 1982.

van Heiningen, A.R.P., Mujumdar, A.S. and Douglas, W.J.M., "Numerical Prediction of the flow field and impingement heat transfer caused by a laminar slot jet", *J. Heat Transfer*, Transactions of ASME, **98**, 654-658 (1976).

van Heiningen, A.R.P., Mujumdar, A.S. and Douglas, W.J.M., "A high sensitivity, fast response heat flux sensor", *Int. J. Heat Mass Transfer*, **28**, 1657-1667 (1985).

Vest, C.M., *Holographic Interferometry*, John Wiley and Sons, New York, 1979.

Viskanta, R., "Heat transfer to impinging isothermal gas and flame jets", *Experimental Thermal and Fluid Science*, **6**, 111-134 (1993).

Viskanta, R. and Incropera, F.P., "Quenching with liquid jet impingement", *Heat and Mass Transfer in Materials Processing*, I. Tanasawa and N. Lior, Eds., 455-476, Hemisphere Publishing Corp., New York, 1992.

Wang, X.S., Dagan, Z. and Jiji, L.M., "Heat transfer between a circular free impinging jet and a solid surface with non-uniform wall temperature or wall heat flux - 1. Solution for the stagnation region", *Int. J. Heat Mass Transfer*, **32**, 1351-1360 (1989a).

Wang, X.S., Dagan, Z. and Jiji, L.M., "Conjugate heat transfer between a laminar impinging liquid jet and a solid disk", *Int. J. Heat Mass Transfer*, **32**, 2189-2197 (1989b).

Wang, Y.B., Chaussavoine, C. and Teyssandier, F., "Two-dimensional modelling of a non-confined circular impinging jet reactor -- fluid dynamics and heat transfer", *Int. J. Heat Mass Transfer*, **36**, 857-873 (1993).

Watson, E.J., "The radial spread of a liquid jet over a horizontal lane", *J. Fluid Mech.*, **20**, 481-499 (1964).

Wenyon, M., *Understanding holography*, Arco Pub. Inc., New York, 1985.

Yuan, T.D. and Liburdy, J.A., "Application of a surface renewal model to the prediction of heat transfer in an impinging jet", *Int. J. Heat Mass Transfer*, **35**, 1905-1912 (1992).

Zumbrunnen, D.A., Viskanta, R. and Incropera, F.P., "The effect of surface motion on forced convection film boiling heat transfer", *J. Heat Transfer*, **111**, 760-766 (1989a).

Zumbrunnen, D.A., Incropera, F.P. and Viskanta, R., "Convective heat transfer distributions on a plate cooled by planar water jets", *J. Heat Transfer*, **111**, 889-896 (1989b).

Zumbrunnen, D.A., "Convective heat and mass transfer in the stagnation region of a planar jet impinging on a moving surface", General Papers: *Phase Change and Convective Heat Transfer, Proc. 5th AIAA/ASME Thermophysics and Heat Transfer Conference*, K. Vafai et al., ed., ASME, New York, HTD-Vol **129**, 11-20 (1990).

Appendix A

Physical Properties

The physical properties used in this study to determine local Sherwood numbers are given by Masliyah and Nguyen (1976, 1977, 1979). The physical data independent of the operating conditions are as follows:

density of swollen polymer:	$\rho_s = 1.01\times10^3$ kg/m^3
molar mass of ethyl salicylate:	$M_m = 166.17$ kg/kmol
wavelength of laser light:	$\lambda = 6.328\times10^{-7}$ m

The rest of the physical properties depend on the operating conditions and can be evaluated as follows:

Vapour Pressure of Ethyl Salicylate

The vapour pressure of ethyl salicylate, P^0, is a strong function of operating temperature, T, and can be evaluated from the following equation (Kapur and Macleod, 1976a):

$$P^0 = 133.3e^{20.318 - \frac{6790.7}{T}} \qquad \text{(A.1)}$$

where P^0 is in Pa and T is the operating temperature in K.

Molar Density of Gas Mixture

The molar density of gas mixture, ρ^0, can be approximated by the molar density of air at the operating conditions. Applying the ideal gas law, the molar density of gas mixture can be evaluated from the following equation:

$$\rho^0 = \frac{P}{8314T} \tag{A.2}$$

where ρ^0 is in kmol/m^3, P is the operating pressure in Pa and T is the operating temperature in K.

Viscosity of Air

The viscosity of air, μ, is almost independent of pressure at low pressure, but increases with increasing temperature. There is no easy relation between the viscosity of gases and temperature. However, the relation can be roughly approximated by a power-law with the power ranging from 0.6 to 1.0 (Bird et al., p21-24, 1960). The viscosity of air is 1.789×10^{-5} kg/(s·m) at T = 288.2 K and 1.852×10^{-5} kg/(s·m) at T = 301.2 (Gerhart and Gross, p821, 1985). If a power-law equation is used to approximate the relation between the viscosity of air and temperature, the following relation can be obtained:

$$\mu = 1.789\times10^{-5}\left(\frac{T}{288.2}\right)^{0.784} \tag{A.3}$$

where μ is in kg/(s·m) and T is in K.

Diffusion Coefficient of the Air-Ethyl Salicylate System

The diffusion coefficient of the air-ethyl salicylate system can be calculated from Chapman-Enskog equation (Equation 11-3.2 of Reid et al., 1987):

$$D_{AB} = \frac{0.00266\,T^{1.5}}{PM_{AB}^{0.5}\sigma_{AB}^2\Omega_D} \tag{A.4}$$

where D_{AB} is the diffusion coefficient of system A-B in cm^2/s; T is temperature in K;

P is pressure in bar (10^5 Pa); M_{AB} is defined by the molecular weights of A and B (see below); σ_{AB} is characteristic Lennard-Jones length in Å (10^{-10} m); Ω_D is dimensionless diffusion collision integral. The various quantities in the above equation can be evaluated as follows:

$$M_{AB} = \frac{2}{\frac{1}{M_A} + \frac{1}{M_B}} \tag{A.5}$$

where M_A and M_B are the molecular weights of A and B, respectively. For air-ethyl salicylate system, $M_A = 29$ and $M_B = 166.17$, and hence $M_{AB} = 49.4$.

$$\sigma_{AB} = \frac{\sigma_A + \sigma_B}{2} \tag{A.6}$$

where

$$\sigma = 1.18 V_b^{1/3} \tag{A.7}$$

for either A or B and V_b is the liquid molar volume, in cm^3/mol, estimated from Le Bas contributions in Table 3-8 of Reid et al. (1987). For ethyl salicylate ($C_9H_{10}O_3$), the liquid molar volume can be estimated as:

$$V_b = 9\times14.8 + 10\times3.7 + 3\times7.4 - 15.0 = 177.4 \text{ cm}^3/\text{mol}$$

and hence

$$\sigma = 1.18\times177.4^{1/3} = 6.63 \text{ Å}$$

For air, $\sigma = 3.62$ Å (Reid et al., p587, 1987). Therefore, for the air-ethyl salicylate system, from Equation A.6, $\sigma_{AB} = 5.125$ Å.

$$\Omega_D = \frac{A}{(T^*)^B} + \frac{C}{\exp(DT^*)} + \frac{E}{\exp(FT^*)} + \frac{G}{\exp(HT^*)} \tag{A.8}$$

where $T^* = kT/\varepsilon_{AB}$, A = 1.06036, B = 0.15610, C = 0.19300, D = 0.47635,

E = 1.03587, F = 1.52996, G = 1.76474, H = 3.89411. ε_{AB} is the interaction characteristic Lennard-Jones energy which can be calculated from the following equation:

$$\varepsilon_{AB} = (\varepsilon_A \varepsilon_B)^{1/2} \tag{A.9}$$

and

$$\frac{\varepsilon}{k} = 1.15 T_b \tag{A.10}$$

where T_b is the normal boiling point (at 1 atm) in K. For air, $\varepsilon/k = 97.0$. For ethyl salicylate, $T_b = 507$ K, and hence $\varepsilon/k = 583$ K. For the air-ethyl salicylate system,

$$\varepsilon_{AB} = \left(\frac{\varepsilon_A}{k} \frac{\varepsilon_B}{k} \right)^{1/2} = \sqrt{97 \times 583} = 237.8 K \tag{A.11}$$

For any given pressure and temperature, the diffusion coefficient of the air-ethyl salicylate system can be calculate from Equations A.4-11. The computer program for evaluating all the necessary physical properties can be found in Appendix C.

Appendix B

Calibration of Rotameters

Two identical rotameters are used in this work: Brooks, Model 1307EJ23CE1AA. Before they could be used in this work, careful calibration was conducted to obtain the calibration curve shown in Figure B.1 with the calibration conditions being: T_0 = 293 K and P_0 = 94.137 kPa. The subscript "0" is employed to denote the calibration conditions. The calibration data were also fitted to obtain a second order regression equation which is also shown in the figure. The regression equation is as follows:

$$Q_0 = 7.432\times10^{-5} + 2.184\times10^{-5}R + 3.4\times10^{-7}R^2 \qquad \text{(B.1)}$$

where Q_0 is the volumetric flow rate in m^3/s and R is the rotameter reading from the bottom of the float. From the calibration curve, it can be noted that to ensure an accurate flow rate, the float reading should not be below 10, where the corresponding Reynolds number is about 150.

The value of volumetric flow rate from the calibration curve or equation, Q_0, must be corrected for the actual experimental operating conditions using the following expression (Law, p290, 1982) which can be derived from Equation 5-25 of Perry and Chilton (1973):

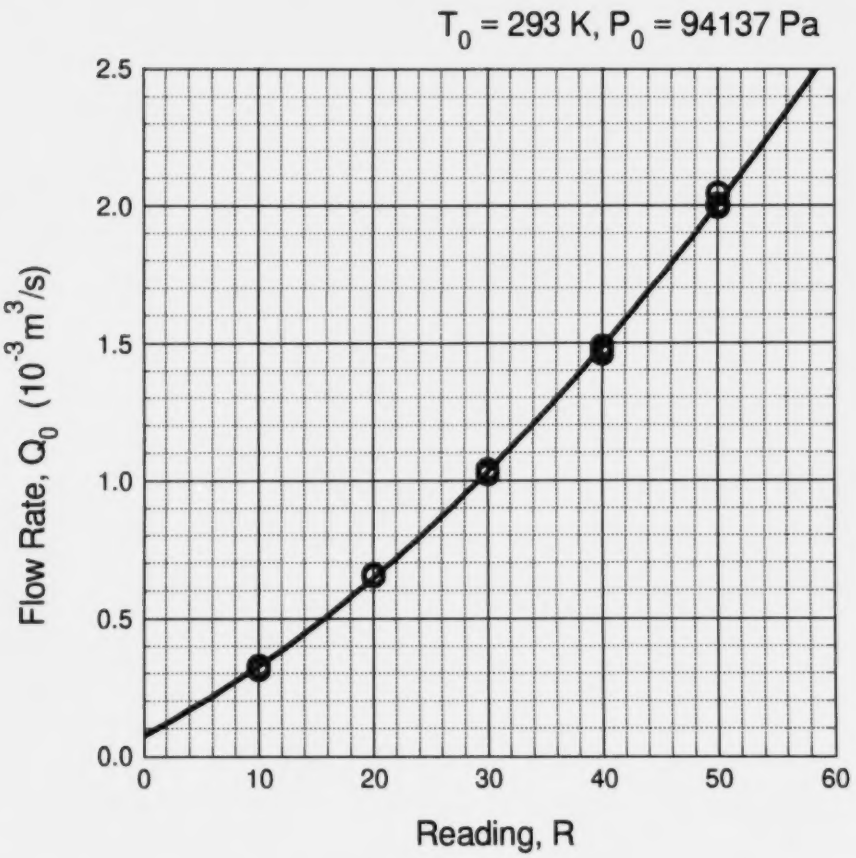

Figure B.1 Calibration Curve for the Rotameters

$$Q = Q_0\left(\frac{T}{T_0}\right)^{0.5}\left(\frac{P_0}{P}\right)^{0.5} \tag{B.2}$$

where Q is actual experimental volumetric flow rate, Q_0 is volumetric flow rate from calibration curve, T is operating temperature, T_0 is calibration temperature, P is operating pressure and P_0 is calibration pressure. All temperatures and pressures are in K and Pa, respectively.

Appendix C
Computer Program for Computing the Experimental Sherwood Numbers

The FORTRAN codes for evaluating the physical properties and the experimental Sherwood numbers are listed in this appendix.

```
*************************************************************************
*
*  This program computes the various parameters and Sherwood numbers
*  for an experimental run. The variables are:
*  INPUT:
*    FDAT = File name containing the experimental data
*    FRES = File name to which the program output goes
*    RUN  = The Run Number
*    DATE = The date when the experiment was conducted
*    TEMP = The temperature, K
*    PT   = The total pressure, Pa
*    X    = The array holding the nondimensional locations
*    FN   = The array holding the number of fringes
*    TSEC = The time elapsed to obtain FN fringes, sec
*  OUTPUT:
*    MU   = Air viscosity, kg/(sm)
*    RHO  = Air density, kg/m**3
*    P0   = Vapour pressure of ethyl salicylate, Pa
*    DAB  = Diffusivity of Air-ethyl salicylate system, m**2/s
*    SC   = Schmidt number of the experimental run
*
*************************************************************************
      PARAMETER (NDIM=50)
      CHARACTER*12 FDAT,FRES
      CHARACTER*16 RUN
      CHARACTER*20 DATE
      REAL X(NDIM),FN(NDIM),TSEC(NDIM),SHWD(NDIM),MU
C     ----------------------------------------------------------------
      OPEN (UNIT=3,FILE='datafile')
      READ (3,5) FDAT,FRES
 5    FORMAT(A12)
      OPEN(UNIT=7,FILE=FDAT)
      OPEN(UNIT=8,FILE=FRES)
C     ----------------------------------------------------------------
      READ(7,15) RUN
 15   FORMAT(A16)
      READ(7,16) DATE
 16   FORMAT(A20)
      READ(7,*) TEMP
      READ(7,*) PT
      READ(7,*)
      DO 20 I=1,100
        READ(7,*,END=111) X(I),FN(I),TSEC(I)
 20   CONTINUE
```

```
 111  NDAT=I-1
C  ------------------------------------------------------------------
C   Calculate air viscosity from μ(2)=μ(1)*(T2/T1)**0.784
C   where T is in K.
      MU=1.789E-5*(TEMP/288.2)**0.784
C  ------------------------------------------------------------------
C   Calculate air density from RHO=PT/R/TEMP
C   where R=287.
      RHO=PT/287.0/TEMP
C  ------------------------------------------------------------------
C   Calculate vapour pressure of ethyl salicylate:
      P0=133.3*EXP(20.318-6790.7/TEMP)
C  ------------------------------------------------------------------
C   Calculate diffusivity of the air-ethyl salicylate system by
C   the empirical correlation of Wilke and Lee

      AA=1.06036
      BB=0.1561
      CC=0.193
      DD=0.47635
      EE=1.03587
      FF=1.52996
      GG=1.76474
      HH=3.89411

      EPSDK = 237.8
      SIGAB = 5.125
      RMAB = 49.4
      SRM = RMAB**0.5
      TSTR=TEMP/EPSDK
      PBAR = PT*1.0E-5

      OMGD = AA/TSTR**BB+CC/EXP(DD*TSTR)+EE/EXP(FF*TSTR)
     &     + GG/EXP(HH*TSTR)

      DAB = 2.66E-7*TEMP**1.5/PBAR/SRM/SIGAB**2/OMGD
C  ------------------------------------------------------------------
C   Calculate Schmidt number for this run.
      SC = MU/RHO/DAB
C  ------------------------------------------------------------------
C   Calculate the Sherwood numbers for the identified points as given
C   by X, FN and TSEC in the data file

      CONST=1.2542E-5*TEMP/P0/DAB
```

```
      DO 200 I=1,NDAT
  200 SHWD(I)=CONST*FN(I)/TSEC(I)
C -----------------------------------------------------------------
C   Writing out the results.
      WRITE(8,205) RUN
  205 FORMAT(/T17,'Experimental Results of Run ',A16/)
      WRITE(8,207) DATE
  207 FORMAT(T20,'Date: ',T38,A20/)
      WRITE(8,209) TEMP
  209 FORMAT(T20,'Temperature:',T38,'T= ',T42,F7.2,' K')
      WRITE(8,211) PT
  211 FORMAT(T20,'Pressure:',T38,'P= ',T41,2P,E11.3,' Pa')
      WRITE(8,213) MU
  213 FORMAT(T20,'Air Viscosity:',T38,'Mu= ',T41,1P,E11.3,' kg/s/m')
      WRITE(8,215) RHO
  215 FORMAT(T20,'Air Density:',T38,'RHO= ',T41,F7.3,' kg/m**3')
      WRITE(8,217) P0
  217 FORMAT(T20,'Vapour Pressure:',T38,'P0= ',T41,F7.3,' Pa')
      WRITE(8,219) DAB
  219 FORMAT(T20,'Diffusivity:',T38,'DAB= ',T41,1P,E11.3,' m**2/s')
      WRITE(8,221) SC
  221 FORMAT(T20,'Schmidt No.:',T38,'Sc= ',T41,F7.3/)
      WRITE(8,223)
  223 FORMAT(T21,'X',T30,'FN',T37,'TSEC',T46,'SHWD'/)
  225 FORMAT(T19,F6.2,T29,F3.1,T35,F6.1,T42,1P,E11.3)
      DO 300 I=1,NDAT
  300 WRITE(8,225) X(I),FN(I),TSEC(I),SHWD(I)
      STOP
      END
```